UNIVERSITY OF SOUTHAMPTON
FACULTY OF ENGINEERING AND THE ENVIRONMENT
Aerodynamics and Flight Mechanics

Investigation of turbulent flow over irregular rough surfaces using direct numerical simulations

by

Manan Thakkar

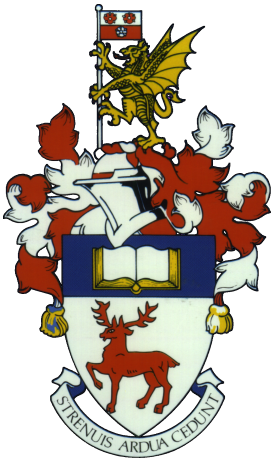

A thesis submitted for the degree of Doctor of Philosophy (PhD)

October, 2017

UNIVERSITY OF SOUTHAMPTON

ABSTRACT

FACULTY OF ENGINEERING AND THE ENVIRONMENT
Aerodynamics and Flight Mechanics

Doctor of Philosophy

INVESTIGATION OF TURBULENT FLOW OVER IRREGULAR ROUGH SURFACES USING DIRECT NUMERICAL SIMULATIONS

by Manan Thakkar

Incompressible turbulent flow in irregular rough channels is investigated using a finite-difference direct numerical simulation code which includes an iterative embedded boundary treatment to resolve the roughness. Seventeen industrially relevant rough surfaces with a wide variation in surface topography are considered. Various studies are conducted to understand the flow physics and the relationship between key flow parameters and surface topography. Studies at low values of friction Reynolds number, Re_τ, for a single surface, show that the flow is laminar up to $Re_\tau = 89$ and begins to develop quasi-periodic fluctuations at $Re_\tau = 89.5$. Fluctuations in the three velocity components continue to grow until $Re_\tau = 91$, and the flow is turbulent for $Re_\tau \geq 92$. Transition depends on the surface topography as some roughness peaks trigger fluctuations before others. For all the surfaces, mean and turbulent flow statistics are computed at $Re_\tau = 180$, for which the flow is fully turbulent but transitionally rough. All surfaces are scaled to the same physical roughness height. Nevertheless, a wide range of roughness function, ΔU^+, values is obtained, indicating that it depends not only on the roughness height but also on the detailed roughness topography. Other mean and turbulence flow statistics also vary considerably depending on the surface topography. Next, based on the simulation results database at $Re_\tau = 180$, a newly formulated method, that determines which surface topographical properties are important and how new properties can be added to an empirical model, is tested. Optimised models with several roughness parameters are systematically developed for ΔU^+ and profile peak turbulent kinetic energy. In determining ΔU^+, besides the known parameters of solidity and skewness, it is shown that the streamwise correlation length and rms roughness height are also significant. The peak turbulent kinetic energy is determined by the skewness and rms roughness height, along with the mean forward-facing surface angle and spanwise effective slope. A Reynolds number dependence study is conducted for a single surface, wherein the roughness height in viscous units, k^+, is varied from the transitionally rough to the fully-rough regime in the range $3.75 \leq k^+ \leq 120$. Excellent agreement with the experimental data of Nikuradse (Laws of flow in rough pipes, *NACA Technical Memorandum 1292*, 1933) is observed. The value of equivalent sand-grain roughness height, $k^+_{s,eq}$, thus obtained is close to the mean peak-to-valley height.

Contents

Nomenclature

u_τ	=	friction velocity of the fluid
δ	=	mean channel half-height
ν	=	kinematic viscosity of the fluid
Re_τ	=	friction Reynolds number $= u_\tau \delta / \nu$
ΔU^+	=	roughness function
k	=	roughness height of a given surface sample
$k_{s,eq}$	=	equivalent sand-grain roughness height

For a given flow quantity, ϕ,

ϕ	=	instantaneous quantity
$\overline{\phi}$	=	time-averaged quantity
ϕ'	=	fluctuations from the time average $= \phi - \overline{\phi}$
$\langle\overline{\phi}\rangle$	=	time- and spatially-averaged (in the streamwise and spanwise directions) quantity
ϕ^+	=	non-dimensionalisation by viscous (or wall) units, u_τ if ϕ is a velocity or ν/u_τ if ϕ is a length

x, y, z	=	streamwise, spanwise and wall-normal directions
M, N	=	number of data points discretising the rough surface samples in streamwise and spanwise directions
Δs	=	uniform spacing of points discretising the rough surface samples in streamwise and spanwise directions
k_x, k_y	=	streamwise and spanwise components of the 2D wave vector
k_c	=	Fourier filter cut-off wave number
$h(x,y)$, $h_{i,j}$	=	rough surface heights after filtering
L_x, L_y, L_z	=	streamwise, spanwise and wall-normal computational domain lengths
$k_c L_x$	=	maximum streamwise wave number
Δx, Δy	=	grid spacings in streamwise and spanwise directions
$\Delta z_{\min}$, $\Delta z_{\max}$	=	minimum and maximum grid spacings in the wall-normal direction
$\lambda_{\min}$	=	smallest Fourier wavelength in the rough surface topography

n_x, n_y, n_z	=	number of grid points in the streamwise, spanwise and wall-normal directions
ψ	=	embedded boundary signed distance function
f_{emb}	=	embedded boundary forcing function
n_Γ	=	embedded boundary normal vector (pointing into the solid boundary)
u, v, w	=	instantaneous streamwise, spanwise and wall-normal velocities
p	=	instantaneous pressure
ρ	=	density of the fluid
t	=	flow time unit
$\overline{h}$	=	mean roughness height of a given surface sample $= 0$

Rough surface topographical properties

$S_{z,5\times5}$	=	mean peak-to-valley height
S_a	=	average roughness height
S_q	=	root-mean-square (rms) roughness height
S_{sk}	=	surface sample skewness
S_{ku}	=	surface sample flatness (or kurtosis)
$S_{z,max}$	=	maximum peak-to-valley height
L_x^{cor}	=	streamwise correlation length
L_y^{cor}	=	spanwise correlation length
S_{sl}	=	longest correlation length
S_{al}	=	shortest correlation length
S_{tr}	=	surface texture aspect ratio $= S_{sl}/S_{al}$
S_{tr}^{flow}	=	flow texture ratio $= L_y^{\text{cor}}/L_x^{\text{cor}}$
ES_x	=	streamwise effective slope
ES_y	=	spanwise effective slope
S	=	surface sample planform area
S_f	=	frontal area of roughness elements
S_w	=	wetted area of roughness elements
S_f/S	=	solidity
Λ_s	=	Sigal-Danberg parameter
$\overline{\alpha}$	=	mean streamwise forward-facing surface angle
α_{rms}	=	root-mean-square (rms) of the streamwise surface angle
U_b	=	mean streamwise bulk velocity
U_c^+	=	mean centreline velocity
U^+	=	mean streamwise velocity profile
$\overline{u'^2}$, $\overline{v'^2}$, $\overline{w'^2}$	=	streamwise, spanwise and wall-normal Reynolds stress fields
$-\overline{u'w'}$	=	Reynolds shear stress field
$\langle\overline{u'^2}\rangle$, $\langle\overline{v'^2}\rangle$, $\langle\overline{w'^2}\rangle$	=	streamwise, spanwise and wall-normal Reynolds stress profiles

$-\langle\overline{u'w'}\rangle$	=	Reynolds shear stress profile
$(Re_\tau)_{\text{crit}}$	=	critical Reynolds number for transition
$(Re_\tau)_{\text{trans}}$	=	transition Reynolds number
$\langle u'_{\text{rms}}\rangle$, $\langle v'_{\text{rms}}\rangle$, $\langle w'_{\text{rms}}\rangle$	=	root-mean-square (rms) streamwise, spanwise and wall-normal Reynolds stress profiles
$P(\overline{u} < 0)$	=	volume fraction of negative time-averaged streamwise velocity
$b_{i,j}$	=	Reynolds stress anisotropy tensor
$\tilde{u}^2$, $\tilde{v}^2$, $\tilde{w}^2$	=	streamwise, spanwise and wall-normal dispersive stress fields
$\tilde{u}\tilde{w}$	=	dispersive shear stress field
$\langle\tilde{u}^2\rangle$, $\langle\tilde{v}^2\rangle$, $\langle\tilde{w}^2\rangle$	=	streamwise, spanwise and wall-normal dispersive stress profiles
$-\langle\tilde{u}\tilde{w}\rangle$	=	dispersive shear stress profile
κ	=	von Kármán constant
R_{uu}, R_{vv}, R_{ww}	=	velocity two-point correlations for the streamwise, spanwise and wall-normal velocities

Abbreviations

DNS	direct numerical simulation
LES	large-eddy simulation
RMS	root mean square
IBM	immersed boundary method
TKE	turbulent kinetic energy

List of Figures

List of Tables

Declaration of Authorship

I, Manan Thakkar, declare that the thesis entitled *Investigation of turbulent flow over irregular rough surfaces using direct numerical simulations* and the work presented in the thesis are both my own, and have been generated by me as the result of my own original research. I confirm that:

- this work was done wholly or mainly while in candidature for a research degree at this University;
- where any part of this thesis has previously been submitted for a degree or any other qualification at this University or any other institution, this has been clearly stated;
- where I have consulted the published work of others, this is always clearly attributed;
- where I have quoted from the work of others, the source is always given. With the exception of such quotations, this thesis is entirely my own work;
- I have acknowledged all main sources of help;
- where the thesis is based on work done by myself jointly with others, I have made clear exactly what was done by others and what I have contributed myself;
- parts of this work have been published as: Thakkar et al. [2017] and Busse et al. [2016]

Signed:.....

Date:.....

Acknowledgements

The last three-and-half years have been a roller coaster ride! My PhD journey, which began with eagerness and excitement, had its fair share of indifferences, breakthroughs and setbacks, and overall highs and lows, has taught me a lot of good things. This incredible journey would not have been completed without the support of the following people. Firstly, I would like to thank my supervisor, Prof. Neil Sandham; his guidance throughout the PhD was extremely helpful and his demanding approach always kept me on my toes for the next problem. Secondly, I would like to thank Dr. Angela Busse, whose research laid the foundation for my work. I am very grateful for her ad hoc guidance and unceasing patience in answering all my questions. Thirdly, Dr. Roderick Johnstone, whose initial support led to a deeper understanding of the work. I also acknowledge the IRIDIS high performance computing facility and associated support services at the University of Southampton, and the UK National Supercomputing facility, ARCHER, access to which was provided by the UK Turbulence Consortium. Both the above facilities were absolutely crucial to the research and aided in timely completion of the work. The feedback provided by my internal examiner, Dr. Zhengtong Xie, and second supervisor, Prof. Bharathram Ganapathisubramani, during the official PhD reviews and in general, motivated me to constantly better my work.

A PhD is not just about doing research in one's chosen field, the mind must be constantly stimulated and developed. Hence, my colleagues and friends must be mentioned here. I thank the 'office dudes', Arslan, Rafa, Saba, Jaime and Jorge, for those highly interesting brainstorming sessions, discussions and debates during lunch, which kept me sharp.

Lastly, none of this would have been possible without the support of my parents. Their untiring encouragement to focus on my 'goal' helped me tremendously, especially during the tough times.

Chapter 1

Introduction

The current work aims to investigate the turbulent fluid flow over irregular industrial rough surfaces using direct numerical simulations (DNS), with the aid of a previously developed code. This introductory chapter lays down the theoretical foundation and background for the rest of the thesis. A literature review, which describes the contribution of previous researchers in the field of fluid flow over roughness, follows. The review is followed by a description of the objectives of the work.

1.1 Theory and literature review

Rough surfaces are encountered in a large number of applications; from roughness in conjunction with industrial heat exchangers (Ligrani et al. [2003]), turbomachinery (Bons et al. [2001], Acharya et al. [1986]), ship propellers and hulls (Kirschner and Brennan [2012], Townsin [2003], Wahl [1989]) to roughness induced by plant canopies and structures in an urban environment exposed to atmospheric flows (Arnfield [2003], Finnigan [2000]). According to Wahl [1989], any solid surface in a marine environment will be affected by fouling. Marine fouling, which is caused by the accumulation of organic molecules, microorganisms, plants and animals on a body submerged in the water (Kirschner and Brennan [2012]), leads to an increase in roughness of the hull and hence its hydrodynamic drag. The drag penalty causes a decrease in ship speed and maneuverability and an increase in fuel consumption. Propeller fouling, although a small part of the fouling on the marine vehicle, is also important from the point of view of increased friction and fuel consumption which in turn hampers performance. Due to extended periods of service, turbines, compressors and other turbomachinery devices are adversely affected by roughness since their surface quality degrades due to phenomena such as erosion, corrosion and deposition (Acharya et al. [1986]). Heat exchangers utilise roughness to improve their efficiency (Ligrani et al. [2003]) as the increase in wall friction causes an increase in wall shear stress which enhances the heat transfer rate. Within the urban environment, roughness at different spatial scales is seen (Britter and Hanna [2003]). Increasing in size from the smallest roughness features, atmospheric flows are affected by the presence of trees, lawns and gardens, paved areas and streets, buildings and entities in between adjacent buildings, city blocks, neighbourhoods

and ultimately entire cities (Arnfield [2003]). The nature and topography of all these elements affects the aerodynamic characteristics of the air flow and energy transfer around them in a profound manner and their study is important in city planning. Urban roughness modelling is also useful in studies of pollutant dispersion (Bottema [1997]). Vegetation canopies play an important role in scalar exchange in the atmosphere due to winds (Finnigan [2000]). Many industrial surface finishing processes produce materials that are classified as rough. Examples of such processes include grinding, shotblasting, spark-erosion, casting etc. Previous work has been mostly limited to numerical and experimental studies on regular rough surfaces made from systematic arrangements of cubes, bars, cylinders, rods, spheres, etc. possessing a small number of characteristic length scales and whose surface properties could be easily evaluated. The main objective of the current work is to conduct direct numerical simulations of a range of well-characterised, scanned irregular rough surfaces seen in practical applications, to study the physics of the fluid flow and to methodically relate their surface parameters to various flow properties.

Studies of flow over rough walls have been undertaken since the mid-1800s when Darcy [1857] and Hagen [1854] performed the first experiments of flows through rough pipes. Many later researchers studied rough pipes of different materials, having circular cross section (with different diameters) and also rectangular pipes or channels with different channel widths and depths. These early studies culminated in the work of Nikuradse [1933], which is considered as one of the most comprehensive set of rough pipe flow experiments to date. For a range of Reynolds numbers, Nikuradse [1933] conducted measurements and analyses of water flow through circular pipes of different diameters. The roughness was introduced by coating the internal pipe surfaces with sand grains of uniform size. Experiments were also carried out for different grain sizes. Geometrical similarity between different pipe diameters was maintained by keeping a constant ratio of r/k where r was the pipe radius and k was the size (i.e. diameter) of the sand grains. Observations were made on the loss of head, velocity and pressure distributions, quantity of discharge and water temperature. The Reynolds number was defined as $Re = \overline{u}d/\nu$, where $\overline{u}$ was the average fluid velocity, d was the pipe diameter and ν was the fluid kinematic viscosity. Nikuradse [1933] also defined a resistance factor,

$$\lambda = \frac{dp}{dx}\frac{d}{\overline{q}},$$

where dp/dx was the pressure drop per unit length of the pipe and $\overline{q} = \rho\overline{u}^2/2$ was the dynamic pressure of the average flow, with ρ being the fluid density. It was observed that, depending on the Reynolds number, there existed three ranges of the flow over the roughness. In the first range, which existed at low Reynolds numbers, the roughness had no significant effect on λ. According to Nikuradse [1933], this was because the thickness of the laminar boundary layer was large compared to the roughness height and hence the value of λ was comparable to that of a smooth pipe. In the second range, which occurred at higher Reynolds numbers and which was termed as the transition range, the influence of roughness became more noticeable. An increase in Re led to an increase in λ. This was because the boundary layer thickness now became comparable to the roughness height. Within the

third range, which occurred at even higher Reynolds numbers, λ became independent of Re. Within this range the thickness of the boundary layer was so small that all the roughness projections extended through it. This classification exists till today and the ranges are termed as the hydraulically smooth regime, transitionally rough regime and fully rough regime respectively, denoting the first, second and third ranges of Nikuradse [1933]. One of the most important relations proposed was the generalised velocity distribution, given in the notation of the current work as

$$\frac{u}{u_\tau} = A + B \log\left(\frac{z}{k}\right),$$

where u/u_τ was the streamwise velocity normalised by the fluid friction velocity and z was the wall-normal coordinate. In the fully rough regime, $A = 8.48$ and $B = 5.75$ whereas in other regimes A and B depended on the non-dimensional quantity $u_\tau k/\nu$. Although the experiments were fairly comprehensive, the roughness considered was only of sand grain type, which does not apply to all engineering applications. However, the experimental data have served and continue to serve as benchmark for subsequent roughness studies.

The primary effect of roughness is an increase in the surface friction compared to a smooth wall, which is seen as a downward shift in the logarithmic region of the mean streamwise velocity profile when plotted in wall-units (refer Figure 1.1). This downward shift was first defined by Clauser [1954, 1956] as the roughness function, ΔU^+, also known as the roughness effect. Based on the smooth-wall log-law profile, this velocity deficit can

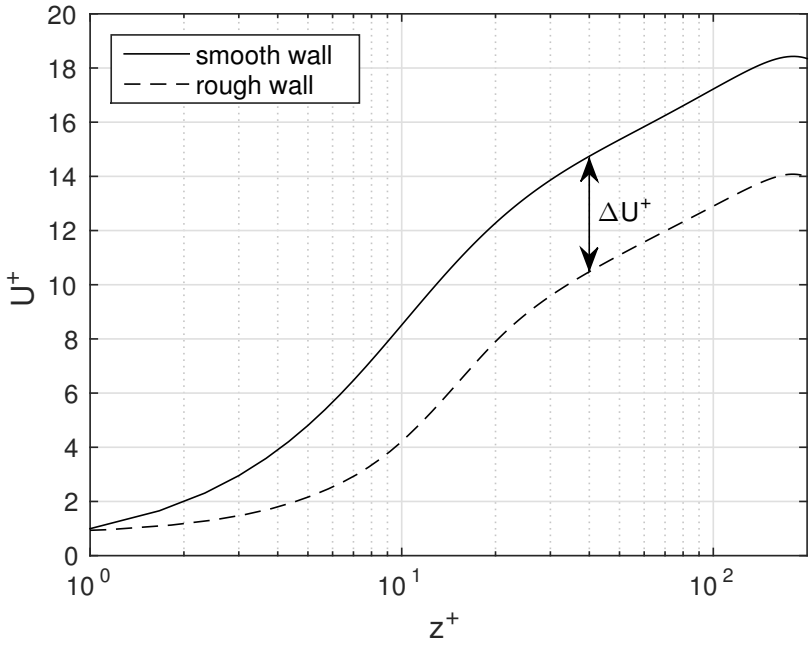

Figure 1.1: An example mean streamwise velocity profile showing the downward shift due to wall roughness. $U^+ = U/u_\tau$ is the mean streamwise velocity in wall-units, ΔU^+ is the roughness function and z^+ is the wall-normal direction in wall-units.

be represented as

$$U^+(z^+) = \frac{1}{\kappa}\ln(z^+) + A - \Delta U^+(k^+), \tag{1.1}$$

where '+' superscripts indicate viscous (wall) units, z^+ and k^+ are the wall-normal distance and roughness height in wall-units, κ is the von Kármán constant and A is the additive constant. Jiménez [2004] recommends $\kappa \approx 0.4$ and $A \approx 5.1$.

In general, the roughness effect depends on the surface topography and Reynolds number, which means $\Delta U^+ \sim k^+$. For relatively low k^+, $\Delta U^+ \approx 0$ and the flow is hydraulically smooth. Beyond a threshold value of k^+, the flow is considered to be fully rough, where ΔU^+ follows a universal behaviour, as mentioned by Jiménez [2004]. In between the hydraulically smooth and fully-rough regimes, the transitionally rough regime is observed, wherein the roughness function strongly depends on the nature of the surface and flow parameters.

Rough surfaces can be broadly classified as regular or irregular. A detailed review of previous studies is given below.

1.1.1 Studies on regular roughness

Regular roughness includes elements usually made up of a regular or periodic arrangement of known shapes such as spheres, cylinders, cones, cubes etc. on a surface. Such rough surfaces typically possess a small number of characteristic length scales and their surface properties such as roughness heights and spacing can be easily evaluated. It is also fairly simple to design or reproduce regular rough surfaces for the purpose of experimentation or computational simulations. Regular roughness is exhibited by heat exchanger applications (Ligrani et al. [2003]), some marine applications (for example, roughness introduced on ship hull panels due to rivets as studied by Schlichting [1936]) and may be seen in some types of urban flows where regularly spaced blocks of houses act as the roughness features (as seen in the field experiments of Dobre et al. [2005]).

Antonia and Krogstad [2001] conducted wind tunnel experiments to study the structure of turbulent boundary layers on two types of rough surface geometries: a regular three-dimensional mesh consisting of woven stainless-steel wire and an arrangement of circular rods aligned in the spanwise direction placed at regular intervals in the streamwise direction. The second geometry was considered two-dimensional. The experimental conditions were set up to obtain a similar value for the roughness function, ΔU^+, for both geometries. The Reynolds number based on the boundary layer displacement thickness (at a specific downstream distance) for the wire mesh and circular rods was $Re_\theta = 12800$ and 4810 respectively, whereas the ratio of the boundary layer thickness to roughness height was $\delta/k \approx 54.35$ and 46.25 respectively. Their main aim was to study differences in the boundary layer outer region Reynolds stresses for surfaces with similar ΔU^+. The agreement between the two geometries was good only for the streamwise components of Reynolds stress, whereas the wall-normal and shear stress components showed relatively poor agreement. They noted that the spanwise and shear stress showed the most significant differences, which implied that the wall-normal motion was most affected by the type of surface. Thus, ΔU^+ was

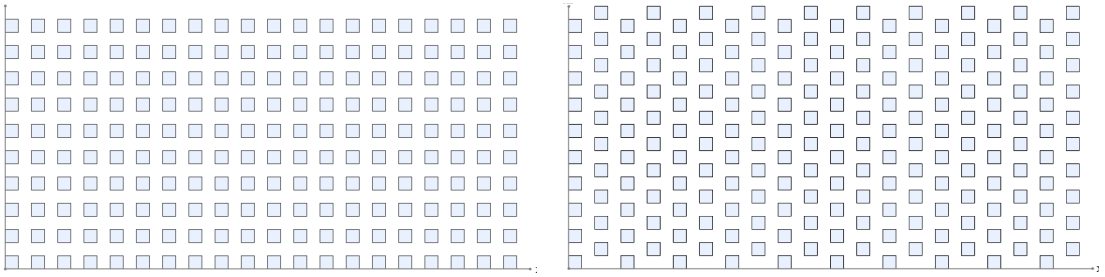

Figure 1.2: Schematic of the regular rough surface geometries (top view) used in the DNS of Orlandi and Leonardi [2006], in the form of aligned cubes (left) and staggered cubes (right). Flow is from left to right in both arrangements.

found to be useful in describing the effect of surface roughness only in the inner layer of the turbulent boundary layer. Also, relative to a smooth wall, flow over the wire mesh geometry exhibited a more isotropic behaviour compared to the circular rod geometry. They also concluded that the small scales of motion were more or less isotropic for three-dimensional roughness (based on their wire mesh geometry) as compared to two-dimensional roughness (their circular rod geometry) or a smooth wall.

In the context of two- and three-dimensional roughness, Orlandi and Leonardi [2006] conducted DNS studies on turbulent channels comprising of aligned and staggered cubes (Figure 1.2). Their focus was on closely spaced roughness elements because in such cases the shape of the roughness elements strongly influenced ΔU^+ and the emphasis was on the region close to the rough surface. Comparisons were made with a smooth channel and two basically two-dimensional (2D) geometries, consisting of transverse and longitudinal square bars. The Reynolds number based on the channel half-height and centreline velocity was $Re = 4200$. All cases had a streamwise separation to roughness height ratio of 1 (which was generally representative of the basic geometrical structure in urban areas) and channel half-height to roughness height ratio of $\delta/k = 5$. Detailed investigations of the near-wall flow physics were conducted by studying the velocity and vorticity. Also, the roughness function was parametrised with the rms of the wall-normal velocity on the crest plane of the cubes with a satisfactory collapse. The selection of the rms of wall-normal velocity was based on its more general validity compared to geometrical parameters (which are generally used to parametrise ΔU^+). It was concluded the parametrisation could be used in micro-meteorological applications.

Ashrafian and Andersson [2006] carried out DNS of a turbulent channel flow comprising of square rods aligned in the spanwise direction (Figure 1.3). The Reynolds number based on the friction velocity was $Re_\tau = 400$, for which the flow was in the upper transitionally rough regime. The ratio of rod streamwise separation to height was 7 and of channel half-height to rod height was $\delta/k \approx 29.5$. They investigated higher order statistics and the effect of roughness on the larger scales of motion away from the wall. Increased vorticity fluctuations were observed in the roughness sublayer (the layer of flow close to the wall where the flow is directly influenced by the roughness). Also, highly disrupted vortical structures in the near-wall regions recovered away from the wall to attain coherence similar to smooth

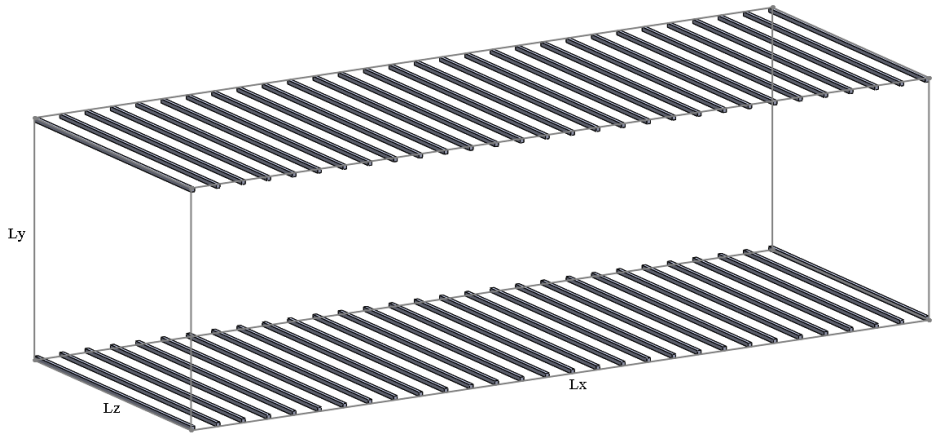

Figure 1.3: Schematic of the regular roughness geometry in the DNS studies of Ashrafian and Andersson [2006]. Lx, Ly and Lz are the domain lengths in the streamwise, wall-normal and spanwise directions respectively. Flow is from left to right the streamwise direction.

walls. The Reynolds stress anisotropy was unaffected in the outer layer (thus resembling the outer layer flow in the case of a smooth wall), whereas it was significantly reduced in the roughness sublayer. Overall, it was concluded that the nature of the flow in the vicinity of the rough wall did not significantly alter the flow in the outer regions and hence satisfied the wall-similarity hypothesis of Townsend [1976]. It was also concluded that factors such as geometry of the roughness elements and their arrangement as well as geometry of the flow itself (whether it was channel or boundary layer flow) might be responsible in producing different roughness effects.

To study the effects of dimensional differences between 2D and 3D roughness on wall-similarity, Lee et al. [2011] conducted direct numerical simulations of a spatially developing turbulent boundary layer over a wall roughened with regularly spaced staggered cubes of uniform size (Figure 1.4). Reynolds number based on the boundary layer momentum thickness varied from the inlet to outlet as $Re_\theta = 300 - 1300$ and the ratio of boundary layer thickness to cube height varied from $\delta/k \approx 6 - 19$. Cube streamwise separation was 8 times the cube height whereas spanwise separation was twice the cube height. Comparisons were made with DNS results of a turbulent boundary layer over an essentially 2D geometry

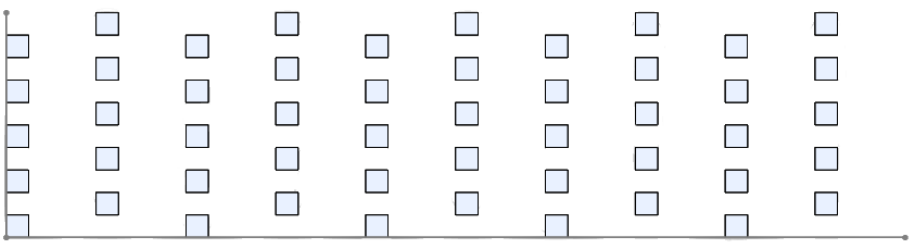

Figure 1.4: Schematic of the regular roughness geometry (top view) in the form of staggered cubes in the DNS studies of Lee et al. [2011]. Flow is from left to right.

consisting of an array of square rods aligned in the spanwise direction, with $\delta/k \approx 8 - 22$. The effects of the 3D roughness on the mean velocity distribution were weaker than those of the 2D roughness as the roughness function was lower for the 3D roughness compared to 2D. Mean velocity defect profiles for both types of roughness showed good collapse in the outer layer. The profile magnitudes of streamwise Reynolds stresses were similar for both 3D and 2D roughness in the outer layer but had larger values compared to the smooth wall. For the Reynolds wall-normal, spanwise and shear stresses, the 2D roughness exhibited higher values than the 3D roughness compared to the smooth wall. Overall, a lack of outer-layer similarity was observed for both types of roughness, thus proving its independence from dimensional variation. The differences between their findings and previous ones, which suggested wall-similarity for such cases, were attributed to differences in Reynolds number and strong blockage effects that created active upward motions.

Busse and Sandham [2012] studied channel-flow regular roughness by introducing an extra forcing term in the governing equations. The force term consisted of two parameters, related to the density and height of the roughness and a shape function that regulated the effect of the forcing term with respect to distance from the channel wall. The force term was meant to account for the additional pressure drag induced by the roughness elements. The effects of this forcing term on turbulent channel flow were investigated using a large number of parameter combinations and shape functions using direct numerical simulations at a friction Reynolds number of $Re_\tau = 180$. A selection of six shape functions was used to model different types of roughness. These included functions based on *i*) a box profile, *ii*) a triangular profile, *iii*) a parabolic profile, *iv*) an exponentially decaying profile, *v*) a

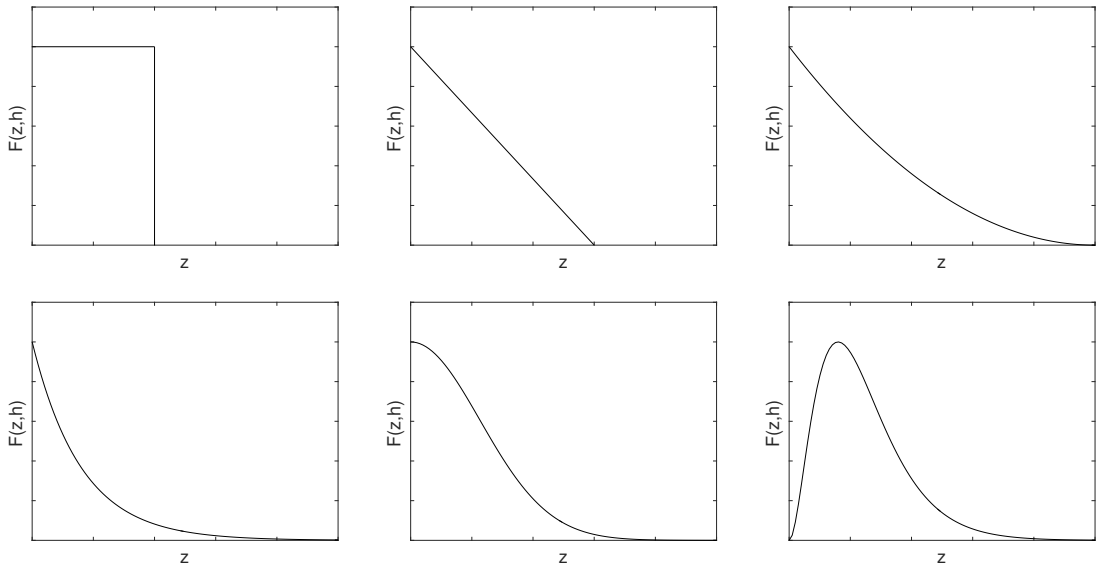

Figure 1.5: Shape function profiles used in the simulations of Busse and Sandham [2012]. Top row (left to right) - box profile, triangular profile and parabolic profile. Bottom row (left to right) - exponentially decaying profile, Gaussian profile and orbital profile. z = wall-normal coordinate, h = roughness height, F = shape function.

Gaussian profile and *vi*) an orbital profile, as shown in Figure 1.5. The main aims were to contribute to the development of a numerical model for rough surface flows and the classification of rough surfaces by the quantification of different parameters in the model. Qualitative comparisons were made, mainly in the near-wall regions, regarding the nature of the mean flow and roughness function, ΔU^+, and turbulent flow behaviour, especially pertaining to flow anisotropy. All cases except for the extremely rough ones showed a good collapse of the mean flow in outer layer scaling. Analysis of the Reynolds stress anisotropy and velocity two-point correlations suggested that with increasing wall-normal distance in the roughness sublayer the turbulence structure changed from rod-like to disc-like and showed a more mixing-layer-like behaviour. To justify the practical applicability of the approach, detailed quantitative comparisons were also made with fully-resolved rough wall data, with satisfactory agreement.

Chan et al. [2015] conducted investigations into various aspects of sinusoidal roughness in pipes (Figure 1.6) using DNS. Simulations were conducted at $Re_\tau = 180 - 540$, for which the flow was in the transitionally rough regime. Effects of the systematic variation of roughness height and wavelength on the flow were studied, thus enabling an understanding of the influence of surface solidity and effective slope. It was observed that the average roughness height had a more significant influence on ΔU^+ than the effective slope. To further study the variation of ΔU^+ with effective slope and the average roughness height (in viscous units), a simple linear relation was proposed, which showed a satisfactory fit to their data and several other studies. For all cases, profiles of velocity defect, radial, azimuthal and streamwise turbulence intensities and Reynolds shear stress (including those at the highest roughness height), collapsed in the outer layer. Hence, their results showed strong support for the outer-layer similarity hypothesis of Townsend [1976].

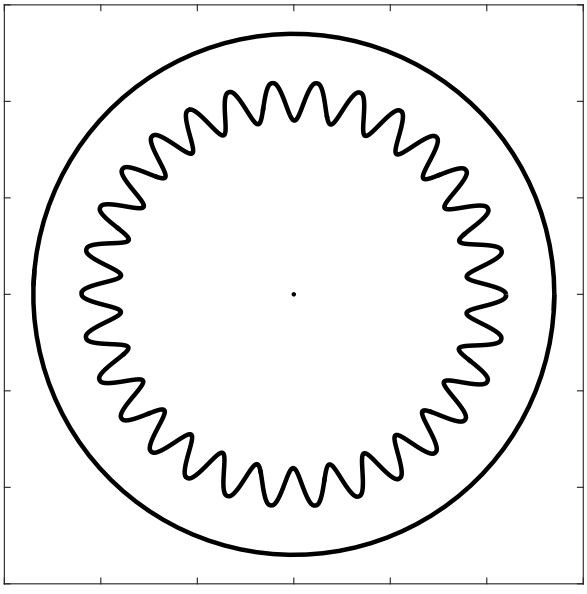

Figure 1.6: Schematic cross-section of the sinusoidal pipe roughness geometry in the DNS studies of Chan et al. [2015]. Flow is into the plane of the paper.

It can be seen that a large amount of work on regular roughness has been done and knowledge in the field has increased considerably in the past few decades. Experiments and computational simulations even on simple geometries such as cubes or square rods etc., which have been popular in the past decade or so, have given a fairly detailed insight into the fluid flow behaviour in terms of the effects on mean flow and roughness function, Reynolds stresses and its anisotropies as well as the skin friction drag of rough surfaces.

However, in most practical applications regular roughness is the exception and not the norm. They bear limited resemblance to their irregular counterparts and as such studies of only regular rough surfaces are not able to provide a complete picture of roughness.

1.1.2 Studies on irregular roughness

Most engineering rough surfaces seen and used in industrial applications exhibit irregular roughness distribution. Roughness seen in ship hull and propeller fouling phenomena, industrial finishing processes (such as gritblasting, spark-erosion, shotblasting) and most urban and plant canopy flows is irregular.

Far fewer studies on irregular rough surfaces exist compared to regular rough surfaces. These studies have mostly been dominated by experimental work and only recently have computational studies begun to be published. One of the most comprehensive and detailed experimental studies on irregular rough surfaces was conducted by Nikuradse [1933] as already mentioned at the beginning of Section 1.1. These experiments have served as a benchmark for many future studies and an analog to his definition of sand-grain roughness, called the equivalent sand-grain roughness, $k_{s,eq}$, is still used today to characterise rough surfaces. Effectively, $k_{s,eq}$ gives the size of the uniformly distributed sand grains that would obtain the same skin friction coefficient as the rough surface under consideration (as defined by Schlichting [1936]). Many researchers after Nikuradse performed similar experiments in order to understand the nature of irregular rough surface flows.

Grass [1971] conducted water channel flow experiments using special visualisation techniques to study the nature of the fluid flow over hydraulically smooth, transitionally rough and fully rough geometries. The hydraulically smooth geometry consisted of a polyurethane varnished marine plywood material, while the transitionally rough geometry was represented by sand grains of approximately 2mm diameter and the fully rough geometry consisted of pebbles of approximately 9mm diameter. The flow depth was maintained at 50mm and hence δ/k varied from approximately 6 (for the pebbles) to 25 (for the sand grains). The Reynolds number based on the average flow velocity and flow depth in the channel was approximately 7000 in all experiments. One of the primary objectives of the study was to obtain detailed turbulent velocity fluctuation measurements close to the roughness in order to study the flow physics. It was noted that there were intermittent phases of fluid transfer from the regions close to the wall to those away from it (fluid ejection) and vice versa (fluid inrush). It was quantitatively confirmed that fluid ejections corresponded with the transfer of low momentum fluid outwards from the boundary whereas fluid inrush was associated with transfer of higher momentum fluid towards the boundary. This cycle also

contributed a great deal to the Reynolds stresses and hence turbulent energy production close to the walls. It was also noted that the fluid transfer from regions close to the walls to regions away from it provided a dominant positive contribution to the Reynolds stresses in the outer regions. One of the important conclusions was the idea that an apparently universal ejection type momentum transport mechanism, possibly extending across the entire thickness of the boundary layer, existed in rough wall flows. An experimental study at similar δ/k ratio was carried out recently by Mohajeri et al. [2015], using particle image velocimetry (PIV) on gravel beds in an open channel, with $\delta/k \approx 7.5$ to 10.8. Longitudinal low- and high-momentum regions in the time-averaged velocity field, likely induced by secondary currents, were observed. Velocity cross-correlations suggested that upward and downward motions of the fluid were associated with upstream and downstream faces of the gravel particles. The relatively high δ/k ratio affected the wall-normal turbulence intensity the most.

Wu and Christensen [2007] conducted high-resolution PIV experiments and statistical analysis on an irregular rough geometry replicated from a turbine blade damaged due to the deposition of foreign materials, which consisted of a broad range of topographical scales. Experiments were conducted on a zero-pressure-gradient turbulent boundary layer at a Reynolds number, $Re_\theta = U_e\theta/\nu \approx 13000$, where U_e was the freestream velocity and θ was the boundary layer momentum thickness. Studies were conducted on two rough wall geometries, the roughness height of the first being twice that of the second. The main aim was to assess the validity of the wall-similarity hypothesis of Townsend [1976]. Comparisons were made with a corresponding smooth wall geometry and results indicated outer layer similarity in the turbulence structure. Data for the mean velocity defect profiles as well as Reynolds normal and shear stresses collapsed away from the rough wall. A similar collapse was observed when quadrant analysis was used to compute the contributions from various Reynolds stress producing events to the overall mean Reynolds shear stress. It was concluded that a roughness sublayer thickness of approximately $3 - 5k$ (where k was the average peak-to-valley height), as proposed by previous studies on idealised regular roughness, agreed well for more irregular roughness commonly seen in practical applications. Outer layer similarity was noted in both their roughness geometries despite one of them having $\delta/k = 28$ (where δ was the boundary layer displacement thickness) which was less than the criterion proposed by Jiménez [2004] ($\delta/k \geq 40$ for universal behaviour). However, in terms of $\delta/k_{s,eq}$, both geometries satisfied Jiménez's criterion. Thus it was stated that in some cases $\delta/k_{s,eq}$ might be more important than δ/k while assessing whether outer layer similarity should be expected in rough wall flow.

Mejia-Alvarez and Christensen [2010] conducted PIV experiments to study the behaviour of a zero pressure gradient developing and developed turbulent boundary layer. They utilised the same turbine surface geometry as Wu and Christensen [2007] but used singular value decomposition (SVD) to obtain lower order models of the geometry. SVD was used to decompose the highly inhomogeneous surface geometry into a set of topographical basis functions. The lower order models consisted of 5 and 16 SVD modes, respectively

containing about 71% and 95% of the surface content of the full rough surface. Their aim was to address the importance of the large scales of roughness over smaller scales in the context of flow over irregular rough surfaces. Hence only the most dominant topographical basis functions were considered to reconstruct the geometry, which meant that larger scale features were retained, whereas the smaller (and possibly less important) scales were removed. The Reynolds number was $Re_\theta = U_e\theta/\nu \approx 15000$ for developing and ≈ 13000 for developed flow (where U_e was the freestream velocity and θ was the boundary layer momentum thickness). For the case of developing flow, the 16-mode model accurately reproduced the flow characteristics of the full surface, including mean velocity profiles, Reynolds normal and shear stresses, probability density functions and quadrant contributions to the mean Reynolds shear stress. The 5-mode model, however, failed to reproduce these characteristics. For the case of developed flow, both 16- and 5-mode models satisfactorily reproduced the flow characteristics of the full surface outside the roughness sublayer, which meant the wall-similarity hypothesis of Townsend [1976] was satisfied. This implied that the smaller roughness scales (which had been removed from the geometries) had a relatively minor impact on the outer layer flow. However, neither model could reproduce bulk flow characteristics of the full surface, such as the value of the roughness function, ΔU^+. Within the roughness sublayer, both models showed differences with the full surface flow, especially in predicting the values of streamwise Reynolds stresses and contributions of intense ejection and sweep events. This meant that the smaller roughness scales played a small but measurable role in the development of the flow in the roughness sublayer.

Pailhas et al. [2008] conducted detailed wind tunnel experiments of developing turbulent boundary layers subject to adverse and zero pressure gradients over irregular rough surfaces. The Reynolds numbers based on the momentum thickness were in the range $Re_\theta = 2200$ to 5800 for the adverse pressure gradient cases and 3200 to 3800 for the zero pressure gradient cases. Their surface geometries included two types of sandpaper (with differing grain density), which consisted of roughness elements distributed in an inherently random manner. One of their main objectives was to look into the importance of the equivalent sand-grain roughness height, $k_{s,eq}$, in flows over rough surfaces. The goal was to assess the relevance of $k_{s,eq}$ and determine if it depended only on the geometrical surface parameters or on the parameters of the flow regime as well. It was observed that $k_{s,eq}$ was not constant for a given rough surface but varied depending on the flow regime (zero or adverse pressure gradient flow). Their main conclusion was that the equivalent sand-grain roughness height must take into account the surface geometrical parameters (such as roughness height and density) as well as the nature of the fluid flow (such as roughness regime and pressure gradient condition) and that the classical definitions of $k_{s,eq}$, which took into account mainly surface geometrical quantities, may not be justified for all types of rough surface flows.

De Marchis et al. [2010] analysed irregular 2D rough surfaces using wall-resolved large-eddy simulations (LES). A total of eight surfaces were constructed by superposing sinusoids with random amplitude and four different wavelengths, with simulations being carried out at $Re_\tau = 395$. The main goal was to check whether literature results over regular roughness

could be extended to irregular roughness. Peak streamwise and wall-normal velocity rms fluctuations showed a decrease with an increase in roughness height. High values of streamwise and wall-normal fluctuations were observed in similar regions around the roughness. A significant contribution from dispersive shear stress due to inhomogeneities introduced by the roughness was observed. An increase in roughness height produced a corresponding increase in the Reynolds and dispersive shear stress but a decrease in the viscous shear stress. This was attributed to the recirculation of flow beyond the roughness height which promoted vertical mixing and hence a reduction in the viscous contribution. A reduction in the streamwise turbulent intensity with a corresponding increase in the spanwise and wall-normal components indicated a tendency towards isotropy of the near-wall turbulence. This tendency also increased with increasing roughness height. Overall, results satisfied the wall-similarity hypothesis of Townsend [1976]. Although many observations agreed with those seen for regular roughness, a unique length scale representing the irregularity of the roughness was not found because the flow was greatly influenced by individual roughness elements. The detailed analysis conducted in this study makes it an important reference for the flow physics studies in the current work (especially in Chapter 6).

In a recent work, Cardillo et al. [2013] studied a zero pressure gradient turbulent boundary layer over irregular roughness using DNS at Reynolds numbers based on the boundary layer momentum thickness of $Re_\theta = 2077$ to 2439. The irregular rough surface was a 24-grit sandpaper with the roughness height (based on the mean peak-to-valley height) in wall-units, $k^+ = ku_\tau/\nu \simeq 11$, which was in the transitionally rough regime, and the inlet $\delta/k = 71$. Fourier transforms were utilised to determine which wavelengths of the surface contributed most to the overall spectrum. In order to reduce computational cost, only the most dominant wavelengths of the surface topography were considered whereas the remaining were filtered out. Comparisons were made with smooth wall DNS as well as laser Doppler anemometry experiments performed on similar geometries under similar conditions. Mean velocity profiles, Reynolds stresses and flow parameters such as skin friction coefficient, boundary layer and momentum thicknesses showed good agreement with the experiments. Iso-contours of the instantaneous velocity field quantitatively demonstrated that the surface roughness caused the turbulent boundary layer to thicken overall. Roughness also caused improved mixing of fluid across the boundary layer and hence changes in the velocity field were seen throughout. It was also noted that effects of roughness for the Re_θ considered were scale-dependent, whether inner or outer scaling units were considered. Peak values of Reynolds stresses increased when considering outer units whereas they decreased when considering inner units. However, significant differences were observed between the smooth and rough wall cases in the outer regions of the boundary layer for the Reynolds wall-normal and shear stresses.

Some of the irregular rough surfaces studied in the current work were first studied in a conference paper by Busse et al. [2013]. The aim was to perform simulations of realistic surfaces commonly seen in engineering applications in industry (as opposed to artificially constructed surfaces which have been extensively studied in previous fundamental research

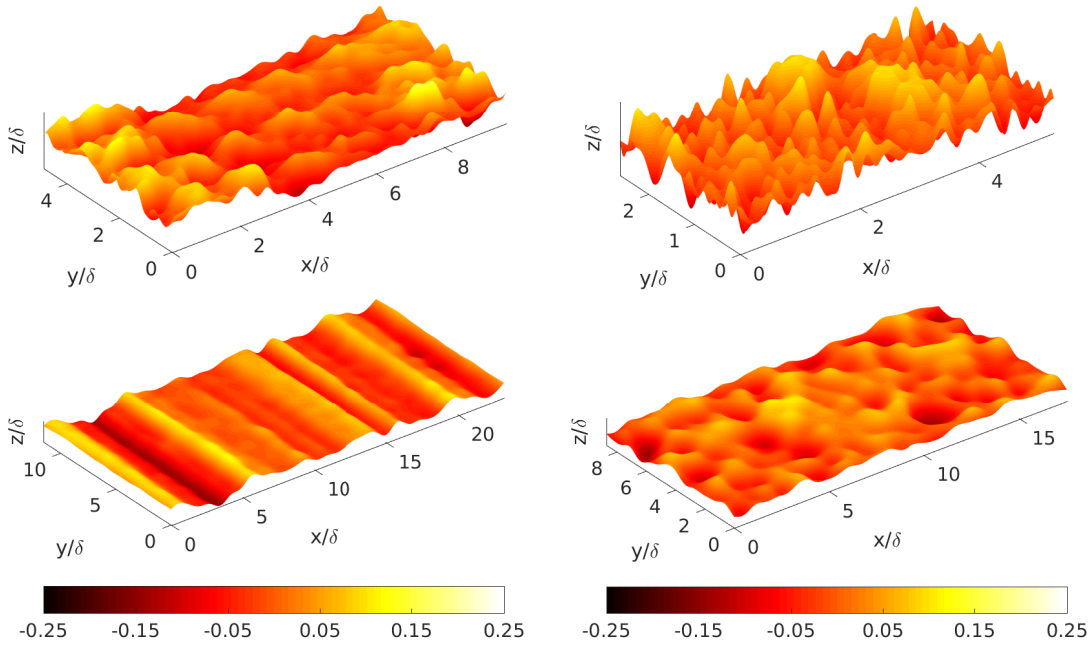

Figure 1.7: Rough surface samples considered in the studies of Busse et al. [2013]: carbon-carbon composite (top left), graphite (top right), ground steel (bottom left) and shotblasted steel (bottom right). Surfaces coloured by roughness height, k/δ.

of flow over rough walls). A three-step numerical methodology, consisting of surface scanning, pre-processing (Fourier filtering) and DNS of rough channel flow, was developed. An immersed boundary method was used to resolve the roughness. Simulations were conducted at $Re_\tau = 180$ with $\delta/k = 6$, where k was the mean peak-to-valley height. Four irregular rough surfaces were considered: graphite, carbon-carbon composite, shotblasted and ground steel (surface plots shown in Figure 1.7), which are typical of industrial applications. Despite all surfaces being scaled to the same roughness height, the roughness function, ΔU^+, varied significantly, thus proving that, along with the roughness height, the roughness topography also had a significant influence on roughness effects. It was also observed that ΔU^+ roughly increased with surface skewness, S_{sk} and the streamwise effective slope, ES_x. It was concluded that numerous surface parameters affected the aerodynamic behaviour of rough surfaces and recommendations were made on conducting future studies of a larger number of surfaces to establish reliable correlations relating the surface parameters to roughness effects. Busse et al. [2015] explained the numerical methodology in further detail and conducted a more thorough study on the graphite sample, including numerical validation studies for the mesh resolution, computational domain size and variation of Fourier filter width.

1.1.3 Studies on roughness correlations

Formulating correlations relating roughness topography to flow properties, such as skin friction, has been a topic of extensive research. Flack and Schultz [2010], in their review of roughness correlations, state that, “The most important unresolved issue regarding surface

roughness in fluids engineering practise is how frictional drag (for external flows) or pressure drop (for internal flows) relates to the particular roughness topography. In other words, which roughness scales best typify a surface hydraulically?" The main aim of such work is usually to characterise irregular roughness based purely on geometrical considerations. According to van Rij et al. [2002], industrial benefits of this include reduction in design uncertainties, lower costs of parts and increased life of components, as well as providing a useful reference to formulate other numerical roughness prediction models. Unlike regular roughness, which usually contains a small number of geometric length scales that can be easily defined, characterising irregular roughness is a non-trivial task due to the presence of a large number of length scales. A single parameter is hardly ever able to fully define the topography of an irregular rough surface. Hence researchers have made numerous attempts to formulate a robust set of topographical parameters and relate them to flow properties.

The earliest benchmark study on roughness correlations, which also laid the foundation for many future studies, was carried out by Schlichting [1936]. A series of experiments on regular rough surfaces, that included staggered arrangements of spheres, spherical segments, cones and angular plates, in the fully rough regime, were performed. The experiments were carried out in rectangular channels at $Re = \overline{u}d/\nu = 4.3 \times 10^5$ where $\overline{u}$ was the mean velocity of the flow and d was the channel hydraulic diameter. One of the most important objectives of the study was to develop a model to predict the surface friction for rough surfaces similar to those used in the experiments but at other Reynolds numbers and roughness ratios, k/r_h, where k was the absolute height of the roughness elements from the plate on which they were mounted and r_h was the hydraulic radius. This involved determining an equivalent sand-grain roughness, $k_{s,eq}$, which was the equivalent size of sand grains as used in the experiments of Nikuradse [1933] that had the same resistance as the geometry under consideration. Schlichting proposed that the surface resistance depended not only on the relative roughness, r_h/k, but also on the roughness density, S_f/S, where S_f was the total projected area of the roughness elements on a plane normal to the direction of the flow (or the frontal area of the roughness elements) and S was the surface area of the plate on which the roughness elements were mounted. The quantity S_f/S is also known as the solidity. He also proposed a resistance coefficient for rough surfaces as $C_f = 2W_r/(\rho u_k^2 S_f)$, where $W_r = W - W_g$ was the resistance due to the roughness elements alone, W was the total resistance of the rough plate, W_g was the resistance of the smooth areas between the roughness elements and u_k was the velocity at a distance from the wall $y = k$. It was found that C_f was independent of S_f/S for small values of roughness density and decreased rapidly for large values of roughness density.

The equivalent sand-grain roughness, $k_{s,eq}$, of Nikuradse [1933], subsequently became the "universal currency of exchange", as mentioned by Bradshaw [2000], in the study of rough surfaces and many researchers have aimed at its prediction by using correlations to surface parameters. Sigal and Danberg [1988, 1990] conducted a study to determine a suitable geometric correlation relating to the roughness density effect. Their relation was based on a database of results consisting of the experimental data of Schlichting [1936] and

twelve other regular roughness studies (refer Sigal and Danberg [1988, 1990] and references therein). The new parameter was given as

$$\Lambda_s = \left(\frac{S}{S_f}\right)\left(\frac{A_f}{A_s}\right)^{-1.6}, \tag{1.2}$$

where S was the planform area of the corresponding smooth surface, S_f was the total frontal area of all roughness elements (S and S_f were equivalent to those used by Schlichting [1936]), A_f was the frontal area of a single roughness element and A_s was the wetted area of a single roughness element. Within this correlation, (S/S_f) represented a roughness density parameter and (A_f/A_s) represented a roughness shape parameter. A relation between Λ_s and $k_{s,eq}$ for 2D roughness was proposed as

$$\frac{k_{s,eq}}{k} = \left\{ \begin{array}{lcl} 0.003215\Lambda_s^{4.925} & , & 1.4 \leq \Lambda_s \leq 4.89 \\ 8.0 & , & 4.89 \leq \Lambda_s \leq 13.25 \\ 151.71\Lambda_s^{-1.1379} & , & 13.25 \leq \Lambda_s \leq 100.0 \end{array} \right\}$$

and for 3D roughness as

$$\frac{k_{s,eq}}{k} = \quad 160.77\Lambda_s^{-1.3376} \quad , \quad 16.0 \leq \Lambda_s \leq 200.0,$$

where k was the absolute height of the roughness elements from the surface on which they were mounted (which was the same as that used by Schlichting [1936]). The scarcity of data for three-dimensional roughness prevented the authors from developing a completely general model and as such their parameter is known to be better suited for two-dimensional roughness.

Through a series of channel flow experiments on smooth, patterned rough and completely rough surfaces, van Rij et al. [2002] proposed a more generalized form of the Sigal-Danberg parameter which could be applied to three-dimensional irregular roughness. In case of irregular three-dimensional roughness, A_f/A_s is replaced by S_f/S_w, the ratio of the total frontal area to the total wetted area for all the roughness elements. Hence, the modified version of the parameter was given as

$$\Lambda_s = \left(\frac{S}{S_f}\right)\left(\frac{S_f}{S_w}\right)^{-1.6}, \tag{1.3}$$

where S_w was the total area of all forward-facing roughness elements wetted by the flow and the other parameters are same as in equation (1.2). A modified equation for the equivalent sand-grain roughness was also proposed as

$$\frac{k_{s,eq}}{k} = \left\{ \begin{array}{lcl} 1.583 \times 10^{-5}\Lambda_s^{5.683} & , & \Lambda_s \leq 7.842 \\ 1.802\Lambda_s^{0.03038} & , & 7.842 \leq \Lambda_s \leq 28.12 \\ 255.5\Lambda_s^{-1.454} & , & 28.12 \leq \Lambda_s \end{array} \right\}, \tag{1.4}$$

where k was the average roughness element height of the surface (S_a in the notation of the

current work, refer Appendix A for definition).

The work of Bons [2005] is important in the field of turbomachinery roughness correlations as he defined a streamwise forward-facing surface angle, α_i, of roughness elements (refer Appendix A for definition). Based on experimental data for six types of turbine blade roughness, he also proposed a correlation as

$$\frac{k_{s,eq}}{k} = 0.0191\overline{\alpha}^2 + 0.0736\overline{\alpha}, \tag{1.5}$$

where k was again the average roughness element height of the surface and $\overline{\alpha}$ was the average streamwise forward-facing surface angle (in degrees).

Napoli et al. [2008] conducted wall-resolved LES in channels comprising of irregular two-dimensional roughness at $Re_\tau = 395$. The rough surface geometries were formulated by superposition of sinusoidal functions with differing wavelengths and random amplitudes. A variety of irregular roughness was constructed by using a combination of different amplitudes, wavelengths and number of sinusoids. It was noted that the roughness function, ΔU^+, depended not only on the roughness height but also on the density of the roughness features and its variations across the geometry. In order to take into account both the roughness height and density variations, a new parameter, called the effective slope, ES, of wall corrugations was introduced as

$$ES = \frac{1}{L}\int_L \left|\frac{\partial h}{\partial x}\right| dx, \tag{1.6}$$

where L was the domain length and $\partial h/\partial x$ was the gradient of a roughness element, both in the streamwise direction (h represented the roughness element height and x represented the streamwise direction). It was identified that ΔU^+ depended on ES irrespective of the specific geometry under consideration. ΔU^+ increased linearly up to $ES \approx 0.15$, then followed a non-linear trend for larger values up to $ES \approx 0.55$ and then weakly decreased. It was concluded that, despite the rough surfaces being characterised by features of different amplitudes and spatial density of corrugations, they exhibited similar behaviour in terms of the shift in the mean velocity profile, ΔU^+, if they had similar values of effective slope. The effective slope has subsequently become an important rough surface topography parameter and has been studied by many researchers (for example, Schultz and Flack [2009], Yuan and Piomelli [2014]), including in the current work.

The review by Flack and Schultz [2010] on previously proposed roughness correlations in various roughness regimes covered many experiments on different types of regular roughness, including mesh, spheres, pyramids and square bars, and irregular roughness including different types of sandpaper, honed surfaces, uniform sand and turbine blades subject to pitting and corrosion. It was suggested that correlations proposed in the past were useful only for a subset of rough surfaces and could not be applied to roughness in general, especially irregular roughness. Hence, the aim was to propose a suitable new correlation that could be used more generally and that could be applied to a wider selection of irregular and three-dimensional rough surfaces and hence provide a method to enable drag predic-

tion based solely on the surface topography. Flows mainly in the fully-rough regime were considered, due to the availability of a large quantity of experimental results. A statistical analysis on various roughness scaling parameters indicated that the rms roughness height, S_q, and the skewness, S_{sk}, of the surface elevation probability density function correlated strongly with $k_{s,eq}$. The proposed correlation was given by

$$k_{s,eq} \approx 4.43 S_q (1 + S_{sk})^{1.37}. \tag{1.7}$$

This relation accurately predicted $k_{s,eq}$ values for most of the surfaces considered by the authors, although complete generality was not achieved with it.

Flack et al. [2016] conducted an experimental investigation of the skin-friction for grit-blasted surfaces (blasted with different grades of grit) in turbulent channel flow. The Reynolds number based on the bulk mean velocity and channel height was in the range $Re_m = 10000$ to 300000. A total of fifteen surfaces were tested, out of which six reached the fully-rough regime. Subsequently, based on the data for the six surfaces, a correlation for the equivalent sand-grain roughness height based on S_q and S_{sk} was formulated as

$$k_{s,eq} \approx 2.91 S_q (2 + S_{sk})^{-0.284}. \tag{1.8}$$

Although this correlation showed a good collapse for the surfaces considered, it did not work nearly as well when applied to compute $k_{s,eq}$ for the remaining nine surfaces. To obtain a ΔU^+ collapse in the entire Reynolds number range, the surfaces that did reach the fully-rough regime were assigned the experimentally measured value of $k_{s,eq}$ whereas the remaining surfaces were assigned an effective length scale that gave the best collapse in the transitionally rough regime. In order to predict the roughness function in the entire range, it was concluded that more complex models incorporating additional scales would be required. However, when combined with the model of Flack and Schultz [2010], the above model did a remarkable job of predicting $k_{s,eq}$ for many of the considered surfaces.

There have been other notable contributions in the study of hydrodynamic drag prediction using surface property correlations. Musker [1980] proposed a new relation for an effective roughness height and correlated it with the roughness function using seven surfaces representative of a variety of ship-hull roughness. The surface geometric properties included in the relation were the rms roughness height, surface skewness, kurtosis and the average slope of roughness elements. Waigh and Kind [1998] formulated relations for the roughness effect, based on 16 experimental studies comprising of various types of regular roughness geometries of differing shape and distribution in the fully-rough regime. Their relations included a roughness spacing parameter, ratio of the roughness height to spanwise length for a single element and ratio of the wetted area to frontal area of a single roughness element. In the field of urban roughness and the atmospheric boundary layer, Wieringa [1993] and Grimmond and Oke [1998] have provided a number of empirical correlations.

It must be noted that all studies mentioned above were experimental. More recently, it has been possible to conduct numerical simulations that complement the experimental

database. Yuan and Piomelli [2014] conducted studies to estimate and predict the roughness function and $k_{s,eq}$ on realistic surfaces. They carried out large-eddy simulations in turbulent open-channel flows over sand-grain roughness and realistic roughness replicated from hydraulic turbine blades. Both transitionally rough and fully rough regimes were covered by considering different roughness heights at two $Re_\tau = 400$ and 1000. They evaluated the performance of three existing correlations, proposed by van Rij et al. [2002], Bons [2005] and Flack and Schultz [2010], to predict $k_{s,eq}$. These correlations have already been displayed in equations (1.4), (1.5) and (1.7) respectively above. Data collapse was obtained for the first two correlations, which are slope-based whereas the third correlation, which is moment-based, showed data scatter. The reason for this scatter was that moments did not contain slope information and thus did not scale with $k_{s,eq}$ in cases where surface slope was an important parameter. Surface slope was influential in the studies of Yuan and Piomelli [2014] because their surfaces were in the waviness regime (as described by Schultz and Flack [2009]), which meant there was a dependence of ΔU^+ on the effective slope, ES.

Yang et al. [2016] carried out extensive LES studies on rectangular-prism roughness with the aim of examining the mean flow in the roughness layer (which was defined as the region between the surface and top of the roughness elements). An exponential form for the mean velocity profile in the roughness layer was assumed as

$$\frac{U(z)}{U_h} = \exp\left[a\left(\frac{z}{h} - 1\right)\right], \tag{1.9}$$

where $U(z)$ was the spatially/temporally averaged fluid velocity, z was the wall-normal distance, h was the height of the roughness elements and U_h was the velocity at $z = h$. The attenuation factor, a, depended on the density of the roughness element distribution and details of the roughness distribution on the wall. Simulation results showed validity of the assumption and it was subsequently used to formulate an analytical model for the effective drag exerted by an array of rectangular-prism roughness elements on the flow. Wake interactions among roughness elements were also accounted for by using the concept of flow sheltering, which meant the model would perform reasonably well for different solidities of roughness. Results from the model showed reasonable agreement with studies from literature when applied to aligned and staggered cube arrays, transverse ribs and rectangular roughness with non-uniform and Gaussian distribution. Although this study formulates a model based on an assumed velocity profile behaviour, which is different from the others described above (wherein flow parameters were directly related back to the rough surface topography), it gives an insight into another approach to rough surface characterisation.

1.2 Objectives

The foundation of the current work lies in the work carried out by Busse et al. [2015] and Busse et al. [2013]. An incompressible turbulent channel flow DNS code with an immersed boundary method to resolve roughness was formulated and validated. Studies were conducted on a selection of irregular industrially relevant rough surfaces and a small

database consisting of surface topographical properties and simulation results was prepared. Broadly, the goals of the current work relate to expanding this database by performing several other irregular rough-wall simulations using the above mentioned code. Overall, the objectives of the present work are:

(1) To develop a database of rough surface flows based on simulations covering surfaces with a wide range of topographical properties. All surfaces are replicas of realistic industrial roughness seen in engineering applications.

(2) Based on the above database, to develop a method that relates key flow properties to the surface topographical properties which will also enable studying the varying influence of different properties on the roughness effects.

(3) To investigate laminar to turbulent transition of flow over a typical irregular rough surface.

(4) To study the Reynolds number dependence of the flow and to show that a Reynolds number sweep using direct numerical simulations over a typical irregular rough surface is feasible.

1.3 Thesis outline

The thesis is organized into 9 chapters. Chapter 1 above has provided an introduction, with a fairly extensive literature review of work already done in the field. Chapter 2 gives a detailed explanation of the numerical methodology adopted to conduct a rough surface simulation. This includes pre-processing (Section 2.2), a description of the geometry and boundary conditions (Section 2.3.1), an explanation of meshing (Section 2.3.2) and an overview of the DNS code and immersed boundary method (Section 2.4). Chapter 3 gives a detailed description of the rough surface samples studied in the current work, along with their surface topographical properties (Section 3.2). Validation studies with respect to the computational mesh resolution, domain size and sensitivity to the channel blockage ratio are carried out in Chapter 4. Due to the large number of rough-wall simulations conducted, the results are split into four chapters: Chapter 5 describes the laminar to turbulent transition of the flow over a single rough surface sample, Chapter 6 describes the results of simulations conducted at $Re_\tau = 180$ (for all seventeen samples), along with the variation of certain flow quantities with certain surface properties, Chapter 7 describes a method to conduct full surface property parametrisation (of all seventeen samples) with key flow quantities, and Chapter 8 describes results of a Reynolds number sweep from the transitionally rough to the fully-rough regime for a single surface sample. Finally, the thesis is summarised along with important conclusions in Chapter 9 and recommendations for future work are provided in Section 9.3.

1.4 Standard practises and conventions

The following standard practises and conventions are obeyed throughout the thesis, unless alternative descriptions are provided otherwise.

1.4.1 Representation of the roughness height, k

The roughness height, k, is represented by the mean peak-to-valley height, $S_{z,5\times5}$. To compute this quantity, a surface is first partitioned into 5×5 sections of equal size and the maximum and minimum roughness height for each section is computed. $S_{z,5\times5}$ is then the difference between the mean of the maxima and mean of the minima (Appendix A).

1.4.2 Non-dimensionalisation of velocities

Velocity terms in the governing equations for DNS are non-dimensionalised by the friction velocity, u_τ. Hence, all velocity quantities, mentioned throughout the thesis (in the text, figures, tables and captions), are non-dimensional. For convenience, however, the denominator signifying non-dimensionalisation is skipped. For example, the time-averaged streamwise velocity is denoted as $\overline{u}$ instead of $\overline{u/u_\tau}$, the spanwise Reynolds stress is denoted as $\overline{v'^2}$ as opposed to $\overline{(v/u_\tau)'^2}$, and so on.

1.4.3 Computing ΔU^+

The roughness function, ΔU^+, is generally computed as the vertical shift in the log region of the mean streamwise rough-wall velocity profile from the corresponding smooth-wall profile, plotted on a semilogarithmic scale. However, many studies in this work are conducted at relatively low Reynolds number, and hence no clearly defined log region is present. ΔU^+ is thus computed by subtracting the centreline velocity for a given rough-wall simulation from the corresponding smooth-wall centreline velocity (as in Busse and Sandham [2012]). Although some studies are conducted at higher Reynolds numbers (for example, Chapter 8), for consistency, the same method to compute ΔU^+ is maintained throughout.

It is also important to note that for all simulations conducted in this work, statistics are obtained after considerably large durations of time averaging. Hence, the uncertainty in the value of ΔU^+ is small.

1.4.4 Computing dispersive stresses

In general, for rough walls, unlike smooth walls, the flow is locally statistically inhomogeneous in wall-parallel planes. The instantaneous velocity vector may thus be decomposed as (Coceal et al. [2006]),

$$u_i = U_i + \widetilde{u_i} + u_i',$$

where $U_i = \langle\overline{u_i}\rangle$ is the temporally (overbar) and streamwise-spanwise spatially averaged (triangular bracket) velocity and u_i' represents the turbulent fluctuations. $\widetilde{u_i}$ represents the

spatial variation of time-averaged velocity and is given as $\widetilde{u_i} = \overline{u_i} - U_i$. The total stress tensor, τ_{ij}, thus comprises of three terms (Coceal et al. [2006]),

$$\tau_{ij} = -\langle\overline{u_i' u_j'}\rangle - \langle\widetilde{u_i}\widetilde{u_j}\rangle + \nu\frac{\partial\langle\overline{u_i}\rangle}{\partial x_j},$$

The terms on the right hand side represent the Reynolds, dispersive and viscous stresses respectively. The dispersive stresses arise due to the inhomogeneity of the flow in each wall-parallel plane and represent transport of momentum by spatial variations in the horizontal planes.

1.4.5 Computing the mean streamwise bulk velocity, U_b

In the current work, the mean streamwise bulk velocity, U_b, is computed for a smooth wall as

$$U_b = \frac{1}{2\delta}\int_0^{2\delta}\langle\overline{u}\rangle \; dz,$$

where δ is the channel half-height and $\langle\overline{u}\rangle$ is the time- and spatially-averaged (in the streamwise and spanwise directions) streamwise velocity, and for a rough wall as

$$U_b = \frac{1}{H_{\text{chan}}}\int_{(h_{\min})_{\text{bw}}}^{(h_{\min})_{\text{tw}}}\langle\overline{u}\rangle \; dz,$$

where $H_{\text{chan}} = (h_{\min})_{\text{tw}} - (h_{\min})_{\text{bw}}$, with $(h_{\min})_{\text{bw}}$ as the minimum roughness height of the bottom channel wall and $(h_{\min})_{\text{tw}}$ as the minimum roughness height of the top channel wall.

Chapter 2

Numerical methodology

This chapter describes the numerical methodology adopted for the rough surface simulations in the present work. A three-step methodology, as formulated by Busse et al. [2015] and detailed here for completeness, is used to conduct the simulations. The first step involves obtaining data from the physical roughness sample using a variable focus microscope and is called surface data acquisition. The second step involves pre-processing (section selection, section scaling and filtering) which makes the data suitable for simulation. The third and final step involves conducting DNS of the flow over the rough surface sample.

2.1 Surface data acquisition

A number of techniques exist for surface data acquisition, ranging from contact measurements using stylus instruments, electron microscopes and non-optical comparators (Sherrington and Smith [1988a]) to optical instruments (Sherrington and Smith [1988b]). The data acquisition technique used for a particular surface depends on its material surface properties. The surface data for all samples in this work has been obtained using an Alicona Infinite Focus microscope which measures the surface height by focus variation. The data is obtained in the form of a height map of surface z coordinates (i.e. roughness heights from the mean reference plane) as a function of its x and y (lateral) coordinates. Also, the surfaces in this work are such that data contains no overhangs i.e. for each (x, y) coordinate, there is one z coordinate. All surfaces were scanned during the work of Busse et al. [2015] and Busse et al. [2013] and no new scans were generated as part of the current work.

2.2 Surface data pre-processing

For all rough surfaces, the surface scan is obtained as a discrete height map on a regular cartesian grid in x and y; $x = 0, \Delta s, 2\Delta s, \ldots, (M-1)\Delta s$ and $y = 0, \Delta s, 2\Delta s, \ldots, (N-1)\Delta s$ where Δs is the spacing of the measurement points as obtained during the scan and M and N are the number of data points in the streamwise and spanwise directions respectively. Two pre-processing steps need to be performed on the surface data before it can be used as a rough boundary in DNS: section selection and filtering.

2.2.1 Section selection

The sample for simulation is obtained as a smaller subsection of the scan. In order to select a sample which is representative of the rough surface under consideration, the physical size of the subsection is initially determined based on a visual inspection of the surface scan. The subsection, which maintains a fixed $2:1$ (streamwise to spanwise domain width) aspect ratio, must be chosen to retain sufficient roughness features, but taking into account the computational cost. After selection, the subsection is checked, and if necessary re-selected, so that it maintains adequate roughness correlation lengths within the streamwise computational domain and (since the simulations are conducted in channels) adequate domain size in terms of channel half-heights. The smallest streamwise domain lengths have an extent of approximately 5 times the mean channel half-height. As was shown by Busse et al. [2015], this is sufficient to obtain domain size independent rough-wall mean flow and Reynolds stress statistics. The described technique can be adopted as the surfaces in the current study exhibit a reasonably homogeneous distribution of roughness features. The location of the subsection on the scan is determined based on rms errors in

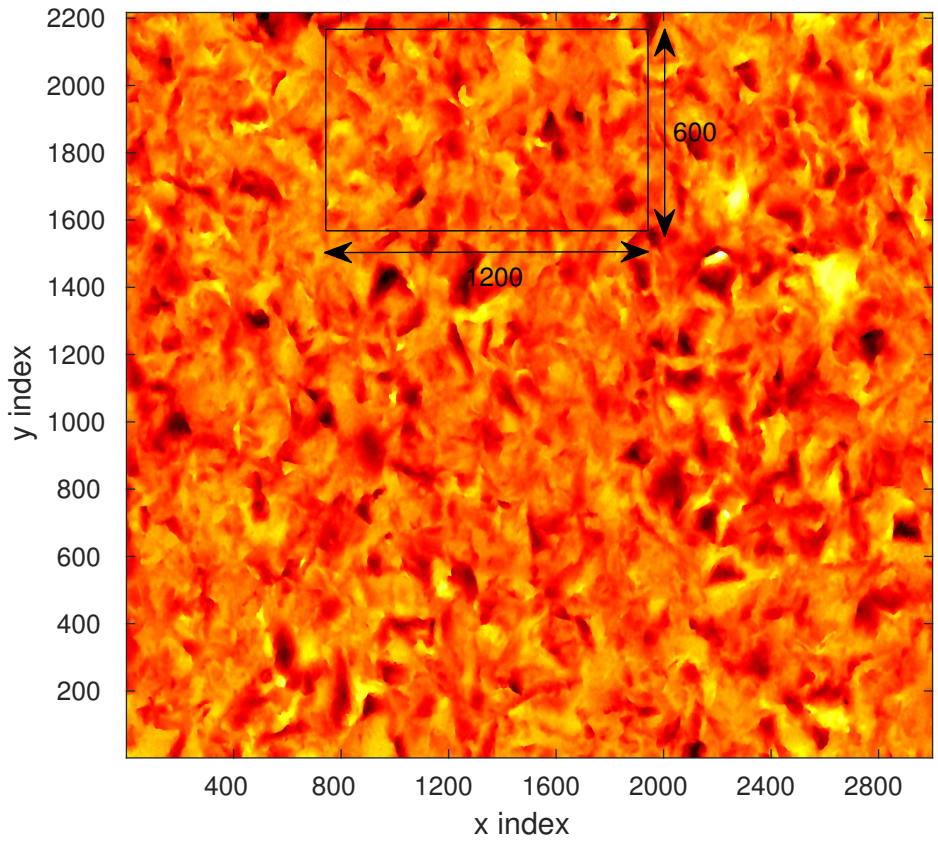

Figure 2.1: Roughness height contour plot of a full surface scan (top view) showing the optimum subsection selected on the basis of minimum RMS errors at the subsection boundaries. Subsection size in terms of streamwise and spanwise indices is also shown. Plot coloured by absolute roughness height. Colourbar: black to yellow - lower to higher roughness heights.

roughness heights at the lateral boundaries. In order to minimize non-periodicity in the lateral boundaries, the subsection with least rms errors in roughness heights between its streamwise boundaries and between its spanwise boundaries is selected. A combined error for the streamwise and spanwise boundaries is used to determine the best subsection. This process takes into account information only at the subsection boundaries and no information in the interior is used. Figure 2.1 shows an example surface sample with the optimum subsection.

It is important to note that the measurement technique used to obtain the surface data does at times obtain spurious roughness features such as spikes, which may be unphysical and may not actually be part of the surface sample. Hence these spikes need to be eliminated during section selection by rejecting sections containing them. Spikes are determined on the basis of the gradient between neighbouring measurement points, and sections with these gradients above a certain threshold are rejected. Although spikes may be smoothed out during the process of filtering (Section 2.2.2), removing them at the section selection stage will ensure no spurious features are part of the section. The section may have a mean slope across its length and/or width and a mean reference plane is subtracted before proceeding toward spike detection so that the mean height and slope of the section are zero.

After selecting a suitable subsection from the full surface sample, it needs to be scaled up from the physical domain into the computational domain, thus determining the computational domain extents. This scaling relates the roughness height and streamwise domain extent as

$$\frac{k_{\text{comp}}}{k_{\text{phys}}} = \frac{(L_x)_{\text{comp}}}{(L_x)_{\text{phys}}},$$

where k is a measure of the roughness height, given by the mean peak-to-valley height, $S_{z,5\times5}$ (refer Appendix A for its definition), L_x is the streamwise domain extent and the subscripts 'comp' and 'phys' represent quantities in the computational and physical domain respectively. k_{phys} and $(L_x)_{\text{phys}}$ can be evaluated from the subsection in the physical domain and k_{comp} is usually known in terms of the channel half-height, δ. Thus, the above equation can be solved for $(L_x)_{\text{comp}}$, which then gives the computational streamwise domain length. The computational spanwise domain length is then simply given as, $(L_y)_{\text{comp}} = (L_x)_{\text{comp}}/2$ (refer Section 2.3.1).

2.2.2 Filtering

The scaled subsection in its raw form is unsuitable for simulation and the surface data needs to be filtered. Filtering is done in Fourier space and is essentially a smoothing step, which needs to be carried out for the following reasons.

- The surface scan usually contains a finite amount of measurement noise which is typically on small spatial scales (Sherrington and Howarth [1988]). It is essential to remove this noise through filtering.

- Due to computational constraints, it is not possible to resolve all the length scales of roughness. From an aerodynamic perspective, the smallest roughness scales are

usually not relevant (Mejia-Alvarez and Christensen [2010]) and according to Jiménez [2004], the effect of roughness is known to be dominated by the largest features of a rough surface. Filtering removes the smallest scales, below a user-defined threshold.

- Periodic boundary conditions are used in the streamwise and spanwise directions to reduce computational cost and perform efficient simulation in reasonably small computational domains. Filtering makes the rough surface sample periodic. In the case of non-periodic boundary conditions, very large domains would be required in order to ensure independence of the flow parameters from the inlet and outlet boundary conditions, which would significantly increase computational cost. Also, in the case of non-periodic boundary conditions, there is a likelihood of the occurrence of unphysical jumps at the streamwise and spanwise boundaries.

The surface data is hence filtered in Fourier space using a low-pass filter to obtain an approximate model of the 3D surface topography. The discrete Fourier transform of the raw data is first found using a fast Fourier transform algorithm. The streamwise and spanwise components of the two-dimensional wave vector are given as

$$k_x = \frac{p}{\Delta s M}, \text{where } p = -\frac{M}{2}, -\frac{M}{2}+1, \ldots, \frac{M}{2}-1,$$
$$k_y = \frac{q}{\Delta s N}, \text{where } q = -\frac{N}{2}, -\frac{N}{2}+1, \ldots, \frac{N}{2}-1,$$

where M, N are the number of surface data points in the x and y directions respectively. In order to remove the contribution of the small scales i.e. high wave numbers, a circular low-pass filter is applied which removes all contributions above a certain wave number, k_c.

$$f_c(k_x, k_y) = \left\{ \begin{array}{lll} 1 & \text{for} & k_x^2 + k_y^2 \leq k_c^2 \\ 0 & \text{for} & k_x^2 + k_y^2 > k_c^2 \end{array} \right\}.$$

If the raw data is denoted as $\tilde{h}_{\text{raw}}(k_x, k_y)$ then after applying the above mentioned filter it becomes

$$\tilde{h}(k_x, k_y) = \tilde{h}_{\text{raw}}(k_x, k_y) \cdot f_c(k_x, k_y).$$

The final filtered data, $h(x, y)$, is the inverse Fourier transform of $\tilde{h}(k_x, k_y)$ and is thus described by a continuous and differentiable analytic function. Since filtering is done in Fourier space, the surface topography is essentially reconstructed using sinusoids, which are periodic over the given domain. Hence the resulting surface is periodic and varies smoothly across its boundaries. Figure 2.2 shows an example of a rough surface sample before and after filtering for an example surface. The 2D power spectrum of the unfiltered surface shown in the left of Figure 2.2 is shown in Figure 2.3. The low wavenumbers (represented by the small circle in the middle of the plot) have the highest contribution to the spectrum whereas higher wavenumbers contribute comparatively less.

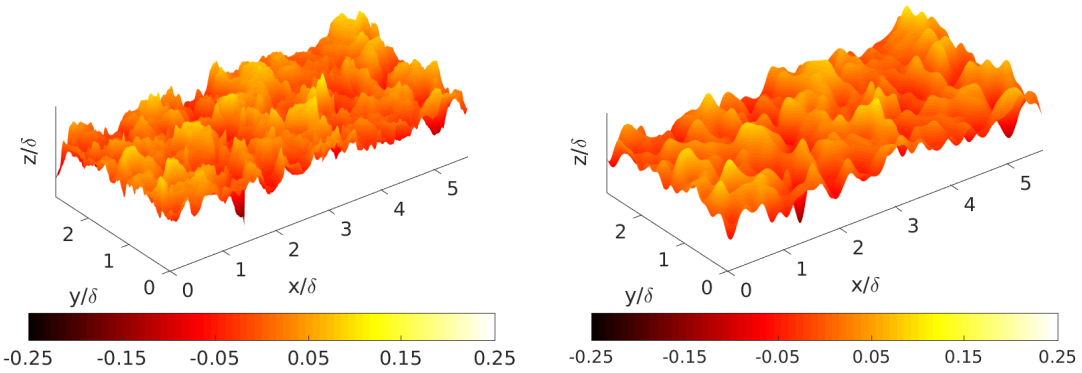

Figure 2.2: Example rough surface sample before filtering (left) and after filtering (right). Plots coloured by roughness height, k/δ. Scale of plots increased in wall-normal direction for clarity.

It is essential to choose an appropriate value for the cut-off wavenumber, k_c, above which all wavenumbers are filtered out. If k_c is too low, the filtered data will be too smooth and will not be an accurate representation of the original data. If it is too high, a lot of small and aerodynamically irrelevant scales would be preserved, which would significantly increase the computational cost. The value of k_c depends to a great extent on the topography of the rough surface and hence no general recommendations can be given. However, studies conducted by Busse et al. [2015] on one of the samples considered in the present work showed that a difference of 8% between the filtered and unfiltered values of the average and

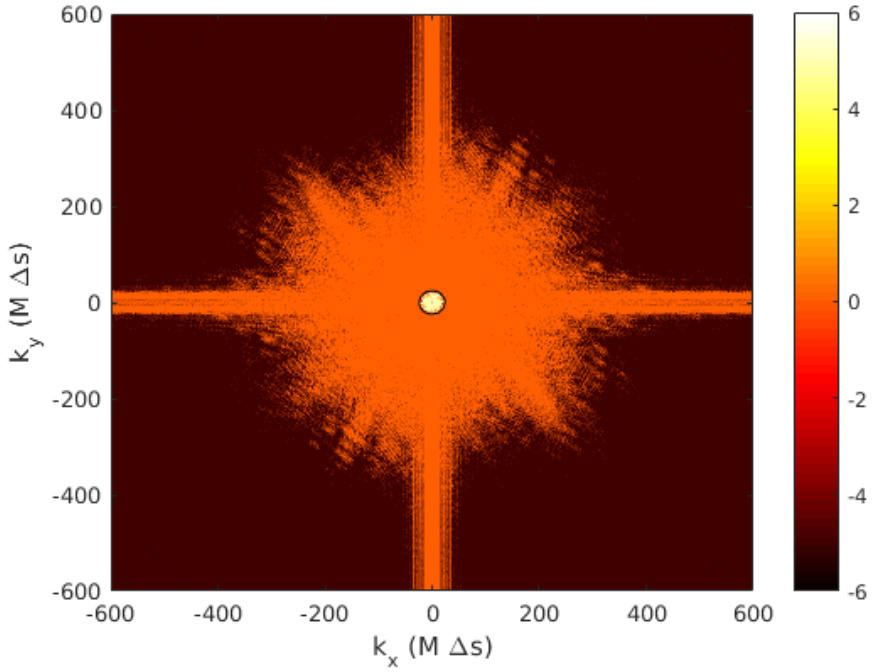

Figure 2.3: 2D power spectrum of the unfiltered surface sample shown in the left of Figure 2.2, coloured by the log of the power spectral density. The circle in the centre shows the extent of the low-pass filter used to obtain the filtered surface shown in the right of Figure 2.2.

rms roughness heights, S_a and S_q, retained most of the large scale surface topography and hence resulted in converged statistics. The same criterion is used in the present work to determine k_c, whose value depends on the sample.

Once k_c and the domain size are specified, the periodic sample is a precisely-defined representation of the original surface and can be used together with DNS in a rigorous manner.

2.3 DNS of turbulent channel flow

The rough-wall simulations are conducted using a channel flow approach, as described below.

2.3.1 Geometry description and boundary conditions

The rough surface samples are used as no-slip wall boundaries in incompressible turbulent channel flow. The streamwise, spanwise and wall-normal directions in the computational domain are denoted by x, y and z respectively, with corresponding domain lengths L_x, L_y and L_z. Considering the cut-off wavenumber criterion, mentioned in the previous section, in conjunction with the streamwise domain length, the maximum streamwise wavenumber is given as $k_c L_x$. The samples have an aspect ratio of 2 : 1, which means $L_x = 2L_y$. The rough surface on the upper channel boundary corresponds to a mirror image of that on the lower boundary but translated by $L_x/2$ and $L_y/2$ in the streamwise and spanwise directions respectively. This is done to reduce local blockage effects. The mean surface height is set as the mean reference plane, $z = 0$ at the bottom boundary and $z = 2\delta$ at the top boundary, where δ is the channel half-height. The channel height of 2δ is measured as the distance between the bottom and top mean reference planes. The domain length in the wall-normal direction, L_z, is slightly larger than 2δ to take into account the

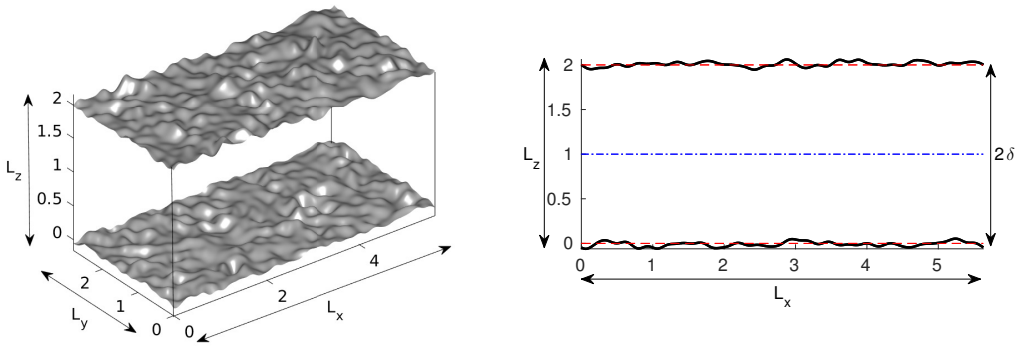

Figure 2.4: Schematic representation of the computational domain in 3D (left) and in the $x-z$ direction (right). L_x, L_y, L_z are the streamwise, spanwise and wall-normal domain lengths respectively, 2δ is the mean channel height, red dashed lines represent the bottom and top mean reference planes, blue dash-dot line represents the channel centreline. The flow is from left to right.

height of the roughness features. Figure 2.4 shows a schematic representation of the computational domain. The Reynolds number for channel flow is defined on the basis of the friction velocity, u_τ, and δ, and is also known as the friction Reynolds number.

$$Re_\tau = \frac{u_\tau \delta}{\nu},$$

where ν is the kinematic viscosity of the fluid.

2.3.2 Meshing

Meshing criteria for the wall-normal and lateral directions are defined in this section. In the wall-normal direction, a stretched mesh is used. In the region of the roughness features, $\min(h(x,y)) \leq z \leq \max(h(x,y))$, uniform mesh spacing (which is also the minimum mesh spacing in the wall-normal direction) is used with $\Delta z^+_{\text{min}} < 1$ and gradual stretching is applied towards the channel centre with $\Delta z^+_{\text{max}} \leq 5$ ('+' superscripts indicate non-dimensionalisation with ν/u_τ i.e. viscous- or wall-units). Figure 2.5 shows a schematic diagram of the mesh in an $x-z$ plane.

In the streamwise and spanwise directions, a uniform mesh spacing is used. There are two criteria governing the mesh, one based on the Reynolds number of the flow and the other based on the minimum wavelength (after filtering) of the rough surface sample. For the Reynolds number criterion, the mesh must have $\Delta x^+ = \Delta y^+ \leq 5$. Thus (considering

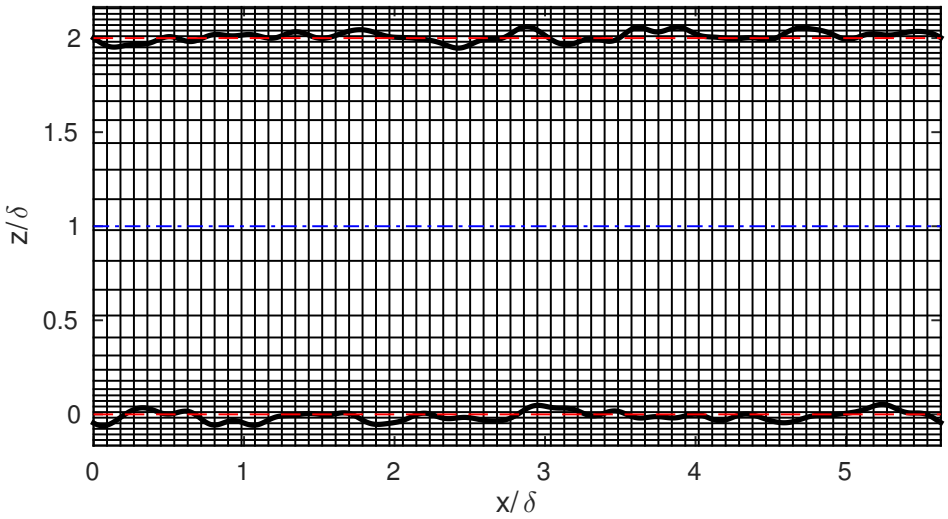

Figure 2.5: Schematic diagram ($x-z$ view) of the wall-normal mesh showing uniform grid spacing in the region of the roughness features and stretched spacing away from the walls. Black solid lines (thick) represent the rough surface boundary, red dashed lines represent the bottom and top mean reference planes and the blue dash-dot line represents the channel centreline. The schematic is for illustrative purpose only and does not represent an actual simulation mesh.

only Δx^+),

$$\begin{aligned}
\Delta x^+ &= \frac{\Delta x}{\nu/u_\tau} \leq 5, \\
&= \frac{L_x/n_x}{\nu/u_\tau}\frac{\delta}{\delta} \leq 5, \\
&= \frac{L_x/n_x}{\delta} Re_\tau \leq 5, \\
n_x &\geq \frac{L_x/\delta}{5} Re_\tau. \\
n_y &= n_x/2.
\end{aligned}$$

For the minimum wavelength criterion, the mesh must have $\Delta x = \Delta y \approx \lambda_{\min}/12$, where $\lambda_{\min}$ is the smallest wavelength of the rough surface after filtering, defined as the inverse of the filter cut-off wavenumber, k_c. Thus (considering only Δx),

$$\begin{aligned}
\frac{L_x}{n_x} &\leq \frac{L_x/(k_c L_x)}{12}, \\
n_x &\geq 12(k_c L_x). \\
n_y &= n_x/2.
\end{aligned}$$

where $k_c L_x$ is the maximum streamwise wavenumber (which is essentially the number of Fourier modes used to reconstruct the surface topography). Depending on the rough surface sample, either the Reynolds number criterion or the minimum wavelength criterion would be dominant. The mesh resolution criteria have been formulated and validated by Busse et al. [2015] on the basis of a mesh refinement study and further details are given there.

In summary, for the wall-normal mesh; $\Delta z^+_{\min} < 1$ and $\Delta z^+_{\max} \leq 5$ and for the mesh in the streamwise and spanwise directions; $\Delta x^+ = \Delta y^+ \leq 5$ and $\Delta x = \Delta y \approx \lambda_{\min}/12$, taking the criterion which gives the more stringent grid spacing. The procedure to generate a valid mesh for an example rough surface sample is described in Appendix B.

2.4 Overview of the immersed boundary method (IBM) and DNS code

The DNS code is of finite-volume type, has been written in Fortran and parallelized using the message passing interface (MPI) standard during the work of Busse et al. [2015], Busse et al. [2013] and Busse and Sandham [2012]. The important features of the code are given below.

2.4.1 Immersed boundary method

Immersed boundary methods (IBMs) fall into a category of meshing techniques called non-boundary conforming methods in which the mesh does not necessarily align with the solid boundary. In such techniques, flow variables in the grid cells close to solid bound-

aries need special treatment to capture the effect of the boundary on the flow and they are generally employed in the case of highly complex geometries where it is usually difficult to obtain good quality body-fitted meshes. The basic idea behind immersed boundary methods is to represent the effect of an object on the flow through a set of body forces, as was first proposed by Peskin [1972]. These methods have the advantage of straightforward implementation into existing codes. However, a drawback is that the forcing function is spread over several grid cells close to the solid boundary and the need for a smooth transition between fluid and solid regions leads to blurring. This may decrease the accuracy near the solid region or increase resolution requirements. A class of methods that does not suffer from blurring are called cut-cell methods where the solid boundary is tracked as an interface and the grid cells at this interface are modified depending on their intersections with the underlying cartesian grid. The disadvantage of these methods for complex geometries is the presence of very small and irregularly shaped cells which may adversely affect the conservation and stability properties of the solver. To overcome these problems, a new method has been formulated recently by Fadlun et al. [2000], which is known as an embedded-boundary method. This method has features of both immersed boundary and cut-cell methods; it incorporates a forcing approach to enforce boundary conditions and involves a local reconstruction of the solution close to the solid boundary. The current work uses the embedded-boundary method of Yang and Balaras [2006], as modified by Busse et al. [2015].

In this method, grid points are differentiated depending on their location inside or outside the solid boundary. All grid points within the solid region are called solid points, grid points in the fluid region with no direct neighbour in the solid region are called bulk points and points in the fluid region with one or more direct neighbours in the solid region are called forcing points. The solid boundary is implicitly defined as the zero level-set, Γ, of a signed distance function, $\psi(x, y, z)$. The solid points have $\psi < 0$ whereas the bulk (and forcing) points have $\psi > 0$. Points located on the solid boundary have $\psi = 0$. Thus, forcing points are defined in terms of ψ as points with $\psi > 0$ that have at least one neighbour with $\psi < 0$. Values of $\psi(x, y, z)$ are obtained using a minimization algorithm which computes the minimum distance for each wall-normal plane from the rough wall. Powell's method from Press et al. [2007] as modified by Brent [1973] is used for this purpose. This is done after filtering but before the actual DNS. Figure 2.6 shows a schematic diagram of the immersed boundary and related terminology, using a 2D example for clarity. A forcing function, f_{emb}, that enables correct enforcement of boundary conditions is added to the governing equations. At the bulk points, the original governing equations without the forcing function are applied and $f_{\text{emb}} = 0$. At the solid points, the forcing is obtained after setting the velocity to zero. At the forcing points, velocities (and other fluid quantities) are computed based on a linear interpolation from the three nearest points in the fluid domain and the velocity at the projection of the forcing point on the boundary (which in the context of this study is 0).

An important concept in this method is the normal vector to the solid surface, which

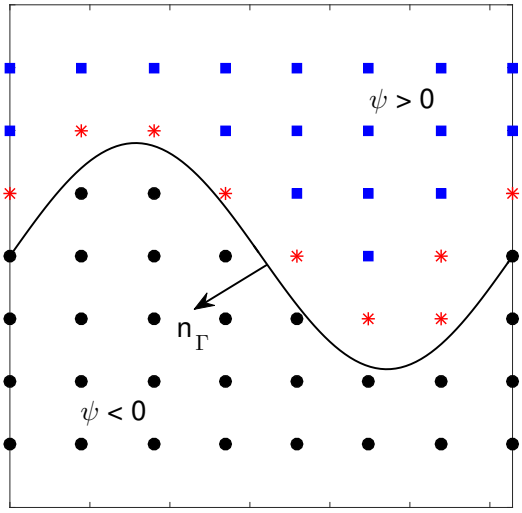

Figure 2.6: Schematic diagram of the immersed boundary mesh. Black solid line - rough surface boundary, blue squares - bulk points, black circles - solid points, red asterisks - forcing points. n_Γ is the normal vector to the surface and ψ is the signed distance function with values in the fluid and solid regions as shown. A 2D example is shown for clarity.

is crucial to performing the interpolation at the forcing points. If n_Γ is the normal vector pointing into the solid boundary then $-n_\Gamma$ is the normal vector pointing out of the solid boundary and into the fluid domain. To obtain the interpolation weights for linear reconstruction at a given forcing point, the system of linear equations formed by the bulk points in x, y and z immediately neighbouring the forcing point in the direction of $-n_\Gamma$ and the projection of the given forcing point on the solid boundary along n_Γ is solved. Figure 2.7

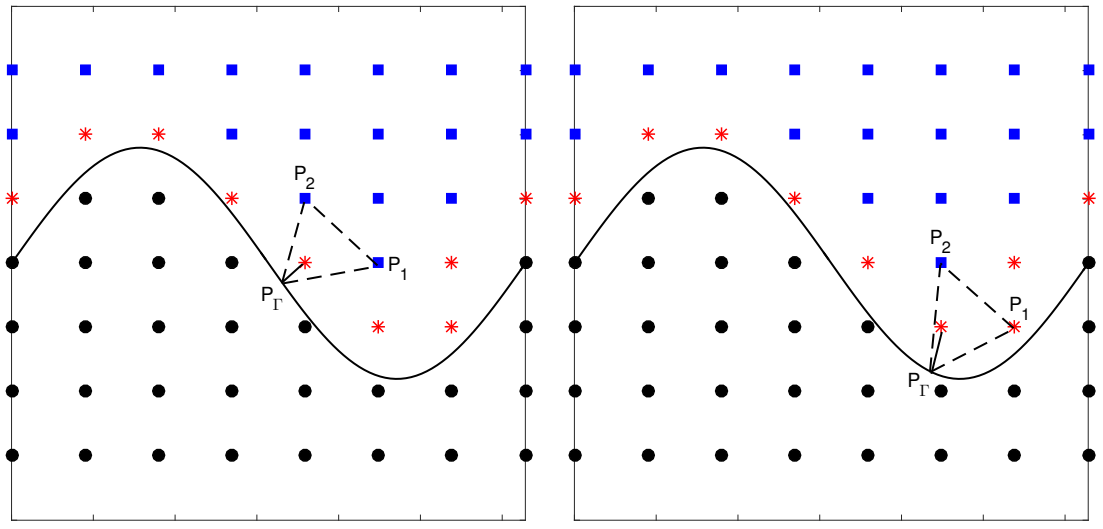

Figure 2.7: Schematic diagram showing regular interpolation stencil for a forcing point (left) and an ambiguous stencil wherein one of the neighbouring points is also a forcing point (right). Colour scheme of points same as Figure 2.6.

(left) shows a schematic representation of the interpolation stencil in 2D. Let the concerned forcing point be denoted as $P_f(x_f, y_f)$, its projection on the solid boundary as $P_\Gamma(x_0, y_0)$ and its two neighbouring points as $P_1(x_1, y_1)$ and $P_2(x_2, y_2)$. A flow quantity at the given forcing point, ϕ_f, can be represented in 2D as a linear combination of its coordinates as

$$\phi_f = w_0 + w_1 x_f + w_2 y_f, \tag{2.1}$$

where w_0, w_1 and w_2 are the interpolation weights. The values of ϕ at P_0, P_1 and P_2 are known (as ϕ_0, ϕ_1 and ϕ_2 respectively) and hence we get the following system of equations.

$$\phi_0 = w_0 + w_1 x_0 + w_2 y_0, \tag{2.2}$$
$$\phi_1 = w_0 + w_1 x_1 + w_2 y_1, \tag{2.3}$$
$$\phi_2 = w_0 + w_1 x_2 + w_2 y_2, \tag{2.4}$$

which in matrix-vector form gives

$$\begin{bmatrix} \phi_0 \\ \phi_1 \\ \phi_2 \end{bmatrix} = \begin{bmatrix} 1 & x_0 & y_0 \\ 1 & x_1 & y_1 \\ 1 & x_2 & y_2 \end{bmatrix} \begin{bmatrix} w_0 \\ w_1 \\ w_2 \end{bmatrix}, \tag{2.5}$$

which is of the form

$$\begin{aligned} \phi &= Aw \\ w &= A^{-1}\phi. \end{aligned} \tag{2.6}$$

Let

$$A^{-1} = \begin{bmatrix} a_{00} & a_{01} & a_{02} \\ a_{10} & a_{11} & a_{12} \\ a_{20} & a_{21} & a_{22} \end{bmatrix}.$$

Substituting A^{-1} in equation (2.6) gives on expansion

$$w_0 = a_{00}\phi_0 + a_{01}\phi_1 + a_{02}\phi_2, \tag{2.7}$$
$$w_1 = a_{10}\phi_0 + a_{11}\phi_1 + a_{12}\phi_2, \tag{2.8}$$
$$w_2 = a_{20}\phi_0 + a_{21}\phi_1 + a_{22}\phi_2 \tag{2.9}$$

and when these equations are substituted in equation (2.1),

$$\begin{aligned} \phi_f = (a_{00} + a_{10}x_f + a_{20}y_f)\phi_0 + (a_{01} + a_{11}x_f + a_{21}y_f)\phi_1 \\ + (a_{02} + a_{12}x_f + a_{22}y_f)\phi_2, \\ \phi_f = W_0\phi_0 + W_1\phi_1 + W_2\phi_2 \end{aligned} \tag{2.10}$$

is ultimately obtained and W_0, W_1 and W_2 are the updated interpolation weights. Hence ϕ_f is obtained as a linear combination of its neighbours, ϕ_0, ϕ_1 and ϕ_2. Extension of the

above procedure to three dimensions is straightforward and equation (2.5) becomes

$$\begin{bmatrix}\phi_0\\ \phi_1\\ \phi_2\\ \phi_3\end{bmatrix} = \begin{bmatrix}1 & x_0 & y_0 & z_0\\ 1 & x_1 & y_1 & z_1\\ 1 & x_2 & y_2 & z_2\\ 1 & x_3 & y_3 & z_3\end{bmatrix} \begin{bmatrix}w_0\\ w_1\\ w_2\\ w_3\end{bmatrix} \tag{2.11}$$

and the same steps as described above are followed.

Since the values of interpolation weights depend only on the coordinates of the forcing point, its projection on the solid boundary, and its neighbouring points (through the matrix A^{-1}), they need to be computed only once at the beginning of the program execution. During the interpolation of velocity at the forcing points, the no-slip condition is implicitly imposed on the wall as $u(x, y, z) = v(x, y, z) = w(x, y, z) = 0$ at P_Γ.

The above case shows a scenario where both the neighbouring points, P_1 and P_2 are bulk points. However, there may be a scenario where one of the neighbouring points is also a forcing point. This is shown in Figure 2.7 (right), where P_1 is a forcing point. In such cases, although the interpolation weights are not recomputed, computation of fluid quantities (for example, velocity) is iterated for all forcing points until the maximum resulting change in the concerned quantity between consecutive iterations is below a user-defined threshold, ϵ. A value of $\epsilon = 1 \times 10^{-8}$ has been used in this study. To simplify the code, however, this approach is used for all forcing points, irrespective of the neighbouring points (bulk or forcing) of a given forcing point.

2.4.2 Governing equations and numerical schemes

The governing equations for fluid flow are the incompressible Navier-Stokes equations. They are non-dimensionalised by δ and u_τ, after which they take the form (Busse and Sandham [2012]),

$$\frac{\partial u_j}{\partial x_j} = 0, \tag{2.12}$$

$$\frac{\partial u_i}{\partial t} + \frac{\partial}{\partial x_j}(u_i u_j) = \delta_{1i} - \frac{\partial p}{\partial x_i} + \frac{1}{Re_\tau}\frac{\partial}{\partial x_j}\left(\frac{\partial u_i}{\partial x_j} + \frac{\partial u_j}{\partial x_i}\right) + f_{\text{emb}}, \tag{2.13}$$

where the i index denotes directionality; x, y or z and the j index denotes summation over the three directions. The pressure gradient is split into the constant mean streamwise component, $-\delta_{1i}$ (which is the Kronecker delta), which drives the channel-flow, and the fluctuating component $\partial p/\partial x_i$. The friction velocity and length scales are based on the mean streamwise pressure gradient,

$$u_\tau^2 = -\frac{\delta}{\rho}\frac{dP}{dx} = 1,$$

which is in dimensional form, and where ρ is the fluid density. This expression comes essentially from a streamwise force balance, equating the force due to the pressure difference

across a given control volume with the friction force due to shear stress in the rough wall. f_{emb} is the embedded-boundary forcing function.

The governing equations are solved in space using a standard 2^{nd} order central finite difference scheme which operates on a staggered cartesian grid. The time integration is carried out using a 2^{nd} order Adams-Bashforth method.

2.4.3 Code flowchart and explanation

Figure 2.8 shows a flowchart depicting various stages in the DNS Fortran code. It shows only the most important stages and does not cover the details of each stage (for example, details of the multigrid method). The code was not significantly modified in this work and hence only an overview of each stage is given. It must be noted that since the code uses MPI, each stage in the flowchart after computational domain and mesh decomposition (which is done at the 'Initialise MPI' stage just after 'START') is carried out by every MPI process.

The stages in the flowchart are mostly self-explanatory but a short description follows. The code consists of roughly two phases: initialisation and time integration. Initialisation is a preparatory phase wherein a number of parameters required for the second phase, of time integration, are set up. The first stage is MPI parallel environment initialisation, where sections of the computational domain and mesh are assigned to each MPI process. The next five stages consist of reading files containing various input parameters (such as the time step length, number of time steps), computing global x-, y- and z-coordinates based on the domain and mesh sizes, assigning the global boundary conditions (such as no-slip walls and periodicity), allocating memory for the various global fields that will be required in the next phase and reading the initial flow field file (which contains time, velocity and pressure data). The next stage consists of immersed boundary initialisation, wherein the mesh points are classified as solid, forcing or bulk (for appropriate treatment in subsequent stages), computing the interpolation weights for the forcing points (which is done only once, at this stage) and computing the bulk volume of the rough channel. The first phase ends after immersed boundary initialisation.

The next phase is time integration. The code in this phase starts by computing the fluid advection and diffusion terms from the governing equations. The mean pressure gradient term (which drives the channel flow) is added in the next stage. This leads on to the stages of the pressure solver which form a large part of the time integration phase. The first two steps in the pressure solver perform a time integration step to obtain a provisional velocity and apply the velocity boundary conditions in the fluid domain. The next step involves applying the immersed boundary forcing function to compute the velocities at the forcing points, which is an iterative procedure. After the iterative procedure has converged, the velocity boundary conditions must be re-applied in the fluid domain. At this stage, the velocities of points inside the solid domain are also set to zero. The pressure Poisson equation is solved in the next stage, using a multigrid method and the iterative Stabilised Bi-Conjugate Gradient (BiCGStab) method. Applying a pressure correction after convergence of this

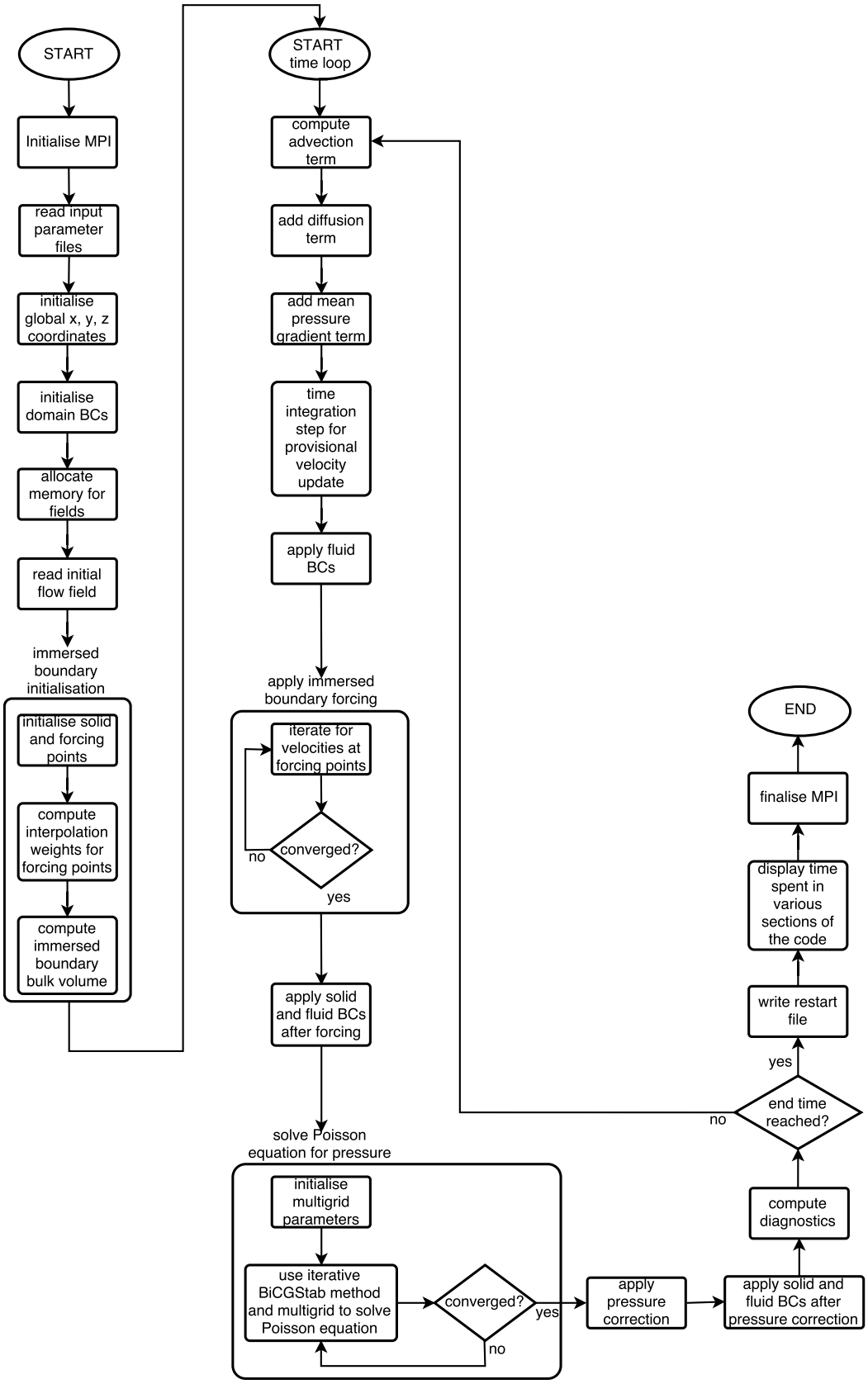

Figure 2.8: Flowchart showing the various stages in the DNS code. Only the most important stages are shown. BCs stands for boundary conditions.

iterative process signifies the end of the pressure solver. The velocity boundary conditions in the fluid and solid domain are then re-applied. The next stage involves computation and output of various flow diagnostics (such as mean forces and velocities, velocity correlations, spatially averaged profiles), after which the first loop of time integration comes to an end. The time integration phase is carried out in a loop which repeats for a given number of time steps. The loop ends when the set number of time steps is reached.

After the end of the time integration loop, the next two stages of the code are closing stages, wherein a restart field file is written out to serve as the initial flow field for the next simulation run and output of time spent in various important sections of the code (such as the immersed boundary forcing, pressure solver) is displayed. The last stage consists of finalising the MPI parallel environment after which the code comes to an end.

2.5 Time averaging procedures and Convergence

In the study of turbulent flows, ultimately the quality of the statistics determine the reliability of the final solution. Statistically averaged flow quantities are obtained through field time averaging. An initial transient phase is usually present in the flow, wherein the flow properties develop towards a statistically steady state. Field time averaging is performed after the transient phase has passed. The flow time, t, is non-dimensionalised by the ratio δ/u_τ as

$$t = \frac{t^*}{\delta/u_\tau},$$

where t^* is the dimensional time.

For the current study, a number of spatially-averaged flow quantities are studied in order to gauge the passage of the initial transient phase. Examples include the mean mass flow rate, mean streamwise velocity and mean and rms pressure. The mean mass flow rate is a bulk flow quantity and hence its evolution with time is studied. In most cases, it either rises or falls with time in the early stages of the simulation and eventually oscillates about a mean value, which indicates the flow has attained a statistically steady state. Figure 2.9 (top left) shows the time history of the mean mass flow rate for an example rough-wall simulation. It is observed that the initial transient lasts until $t \approx 30$.

In case of other flow quantities, profiles in the wall-normal direction are studied. These profiles, which are spatially averaged in the streamwise and spanwise directions, are accumulated from $t = 0$. This, however, is done only for the purpose of transient phase check and these statistics are not used in the final results. If the profiles between consecutive runs show only small differences, it is an indication of the flow reaching a statistically steady state. Figure 2.9 (top right, bottom left and bottom right) show profiles of time- and spatially-averaged streamwise velocity, $\langle\overline{u}\rangle$, pressure, $\overline{p/(\rho u_\tau^2)}$ and rms pressure, $[p/(\rho u_\tau^2)]_{\mathrm{rms}}$ between two consecutive runs. For all three quantities, both profiles show small differences, which indicates the flow has reached a statistically steady state. The pressure profiles show differences in the near-wall region, which is regarded as normal for rough wall simulations. These

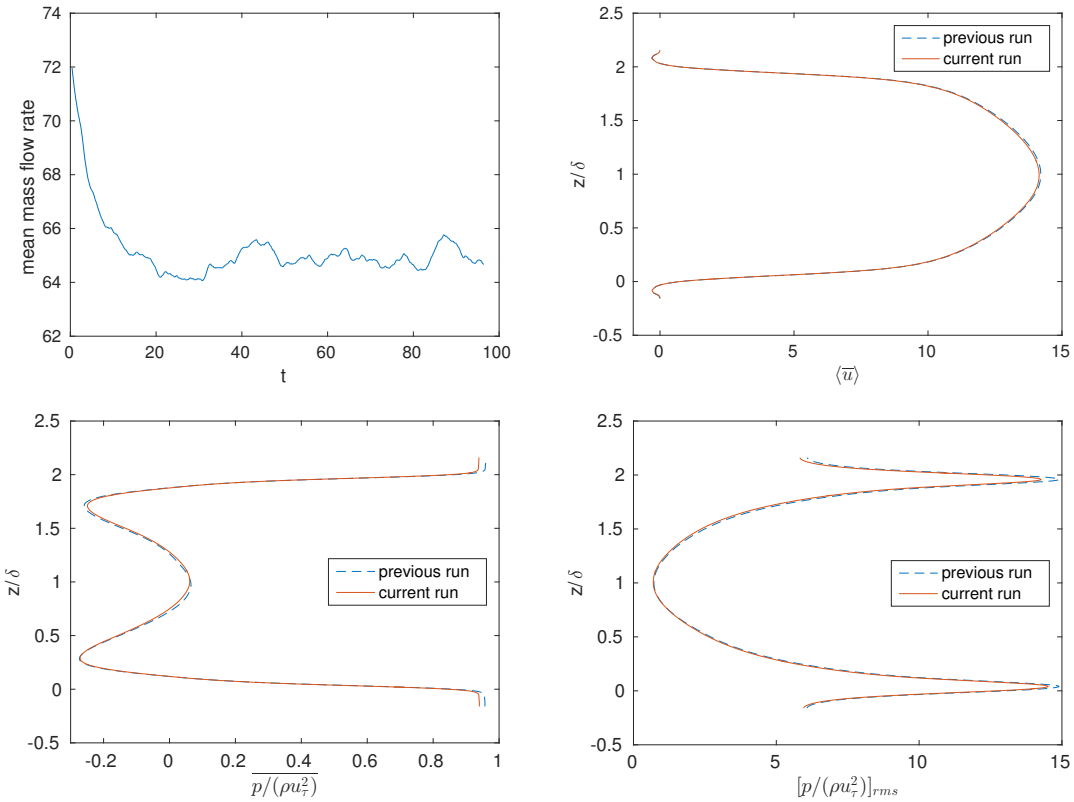

Figure 2.9: Various checks performed to gauge passage of flow initial transient phase. Time history of mean mass flow rate (top left) and wall-normal profiles of time- and spatially-averaged streamwise velocity, $\langle\overline{u}\rangle$ (top right), pressure, $\overline{p/(\rho u_\tau^2)}$ (bottom left) and rms pressure, $[p/(\rho u_\tau^2)]_{\mathrm{rms}}$ (bottom right), between consecutive runs. z/δ is the wall-normal distance.

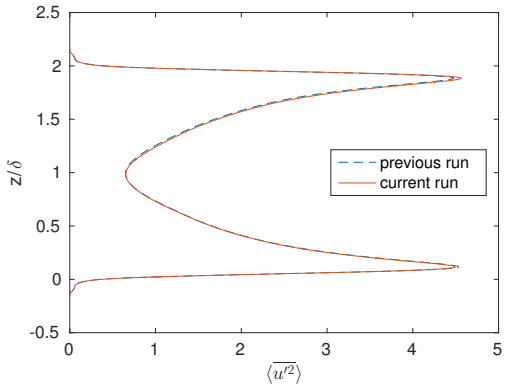

Figure 2.10: Check for flow statistical convergence using profiles of streamwise Reynolds stress, $\langle\overline{u'^2}\rangle$, in the wall-normal direction between two consecutive runs. z/δ is the wall-normal distance.

differences are observed for most rough-wall simulations in the current work and are understood to have an insignificant impact on the process of the flow reaching its statistically steady state.

For the studies conducted in this work, the initial transient phase for a typical case lasts for $(20 - 30)t$, after which field time averaging is performed for a further $(80 - 100)t$. In order to check for statistical convergence, profiles of turbulent flow quantities (for example, streamwise Reynolds stress) spatially-averaged in the streamwise and spanwise directions for consecutive runs are plotted against the wall-normal coordinate. If the profiles show only small differences and also exhibit symmetry about the channel centre, it is an indication of statistical convergence. Figure 2.10 shows profiles of time- and spatially-averaged streamwise Reynolds stress, $\langle\overline{u'^2}\rangle$, between two consecutive runs for an example rough-wall simulation. Both profiles show small differences and are symmetric about the channel centre, which indicates that the flow has reached a statistically converged state and the statistics are no longer expected to vary significantly.

Chapter 3

Rough surface samples

Since one of the main goals of this work is to build a database of commonly seen industrial rough surfaces along with their surface properties and simulation results, a study dedicated to the description of the surfaces is presented in this chapter. A total of seventeen rough surface samples have been considered in this work. A physical description of the samples is given first, followed by a description of some of their important surface topographical properties.

3.1 Description of the surface samples

The database includes two carbon-carbon composite surfaces, a concrete surface, a graphite surface, as well as surfaces subject to the processes of casting, hand filing (2 cases), gritblasting, grinding, shotblasting, spark-erosion (5 cases) and replicas of two ship

sample	type
s1	cast
s2	composite_1
s3	composite_2
s4	concrete
s5	filed_1
s6	filed_2
s7	graphite
s8	gritblasted
s9	ground
s10	ship-propeller_1
s11	ship-propeller_2
s12	shotblasted
s13	spark-eroded_1
s14	spark-eroded_2
s15	spark-eroded_3
s16	spark-eroded_4
s17	spark-eroded_5

Table 3.1: Rough surface sample naming convention.

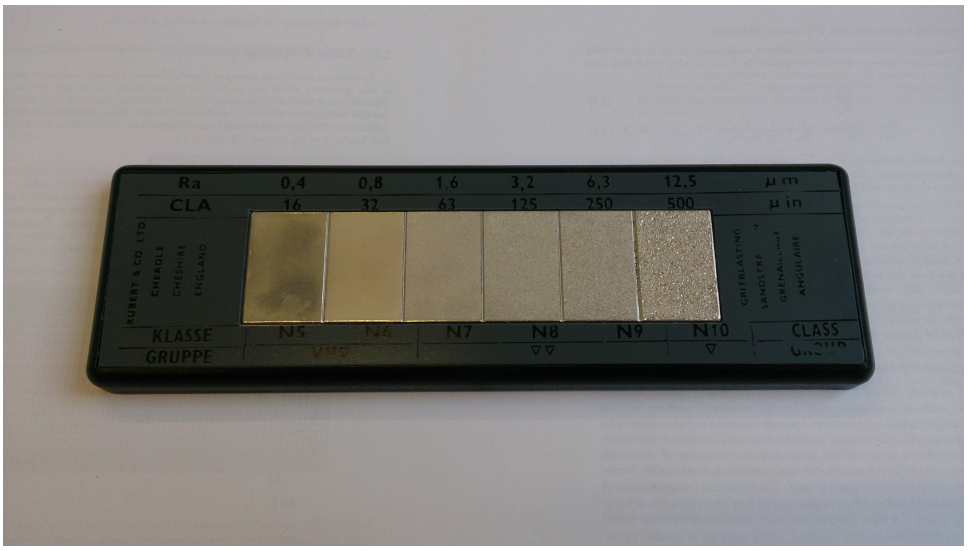

Figure 3.1: A standard roughness comparator showing patches of different grades of roughness (increasing from left to right).

propeller surfaces eroded by periods of service. In order to simplify naming, samples are assigned names as given in Table 3.1. These are the names used henceforth. Samples s2, s7, s9 and s12 were simulated by Busse et al. [2013] and the data, along with data for samples s4 and s13, were kindly provided by Dr. Angela Busse. The remaining samples were simulated in the present work. The composite and graphite samples (supplied by Gas Dynamics Ltd., UK) were exposed to arc-heating in order to simulate the environment experienced by space vehicles while re-entering the atmosphere. The cast, filed, gritblasted, ground, ship propeller, shotblasted and one of the five spark-eroded samples (spark-eroded_5 from Table 3.1) were taken from standard roughness comparators. The remaining four spark-eroded samples were taken from a spark-eroded surface provided by an industrial third-party. These four samples were selected as different subsections from the same larger rough surface scan. The concrete sample was taken from a larger block of concrete. Standard roughness comparators have been obtained from Rubert & Co. Ltd.*. A roughness comparator for one of the samples is shown in Figure 3.1. In general, a comparator consists of five to eight patches of the surface with different roughness grades. Although scans for each roughness grade for each surface have been obtained, grades representative of the roughness of each sample have been selected for the simulations. This means the non-dimensional RMS roughness height, S_q/δ, for the samples lies in the range 0.03 to 0.05.

Marine phenomena cause the surface of ship propellers to undergo various changes during extended periods of service and this increases their roughness (Kirschner and Brennan [2012], Townsin [2003], Wahl [1989]) due to, for example, corrosion. The ship propeller samples, s10 and s11, are replicas of such propeller surfaces. The two samples have similar average roughness height, S_a, but show differences in other surface properties (refer Table 3.2). The spark-eroded samples s13 to s16 were obtained as different subsections from the same larger surface scan. s13 was obtained by visual inspection of the roughness height

*Rubert & Co. Ltd. (Precision Engineers), Cheadle, Cheshire, England.

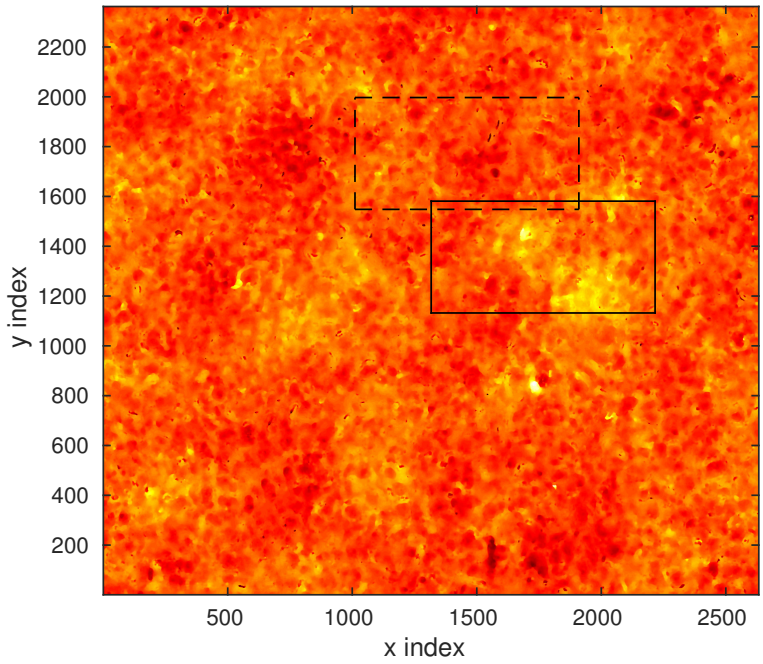

Figure 3.2: Contour plot of the full spark-eroded surface scan showing the placement of s13 (black dashed lines) and s14 (black solid lines). Plot coloured by absolute roughness height. Colourbar: black to yellow - lower to higher roughness heights.

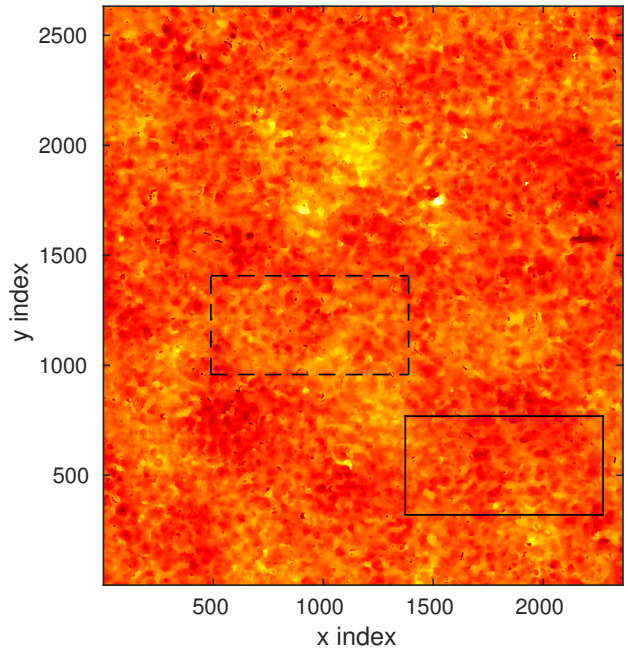

Figure 3.3: Contour plot of the full spark-eroded surface rotated by 90° showing the placement of the s15 (black solid lines) and s16 (black dashed lines) samples. Plot coloured by absolute roughness height. Colourbar: black to yellow - lower to higher roughness heights.

contour plot of the full surface scan whereas s14 was obtained by the automated section selection method based on minimum RMS errors in roughness heights at the section boundaries (as described in Section 2.2.1). The placement of s13 and s14 on the full surface scan is shown in Figure 3.2 for comparison. The s15 and s16 samples are obtained by rotating the full spark-eroded surface scan by 90° and then applying the automated section selection method. These two samples differ in terms of their topographical properties, especially in values of their surface skewness, with s15 showing a positive whereas s16 showing a negative value of skewness (refer Table 3.2). The placement of s15 and s16 on the rotated full surface scan is shown in Figure 3.3.

Surface plots of all 17 rough surface samples are shown in Figures 3.4 and 3.5. The composite and filed samples have strong directional alignment of their roughness features. In order to study this phenomenon, two samples of each are evaluated, with one having features aligned in the streamwise direction and the other having features aligned in the spanwise direction. Figures 3.4 (b) and (c) show the composite samples (s2 and s3), with features aligned in the streamwise and spanwise directions respectively and Figures 3.4 (e) and (f) show the filed samples (s5 and s6), with features aligned in the spanwise and streamwise directions respectively. The ground sample, s9 also shows strong directional alignment of features in the spanwise direction, as shown in Figure 3.4 (i).

3.2 Surface topographical properties of the samples

Mainsah et al. [2001] describe a large number of parameters that can be used to characterise rough surfaces. Table 3.2 (at the end of the chapter) displays a broad list of parameters for the current dataset of seventeen samples, whose description and computation is given in Appendix A. Since simulations are performed on smaller subsections of the full surface samples, surface properties of only those subsections are computed. The mean reference plane of a sample is set at $z = 0$ and hence the mean roughness height of the sample, $\overline{h}$, is zero.

$$\overline{h} = \frac{1}{MN} \sum_{i,j}^{M,N} h_{i,j} = 0,$$

where $h_{i,j}$ are the coordinates of the roughness height obtained after filtering and M, N are the number of points discretising the surface in x, y respectively.

Since the surface roughness height, k, has the strongest influence on the aerodynamic fluid flow parameters, the surfaces are scaled to the same roughness height (unless stated otherwise), which is represented by mean-peak-to-valley height, $S_{z,5\times5}$. It must be noted that k is always represented by $S_{z,5\times5}$ unless stated otherwise. The value chosen for $S_{z,5\times5}$ for the current study (unless stated otherwise) is

$$k = S_{z,5\times5} = \frac{\delta}{6} \text{ or } \frac{\delta}{k} = \frac{\delta}{S_{z,5\times5}} = 6.$$

$S_{z,5\times5}$ has also been used as a measure of roughness height in the studies of Schultz and

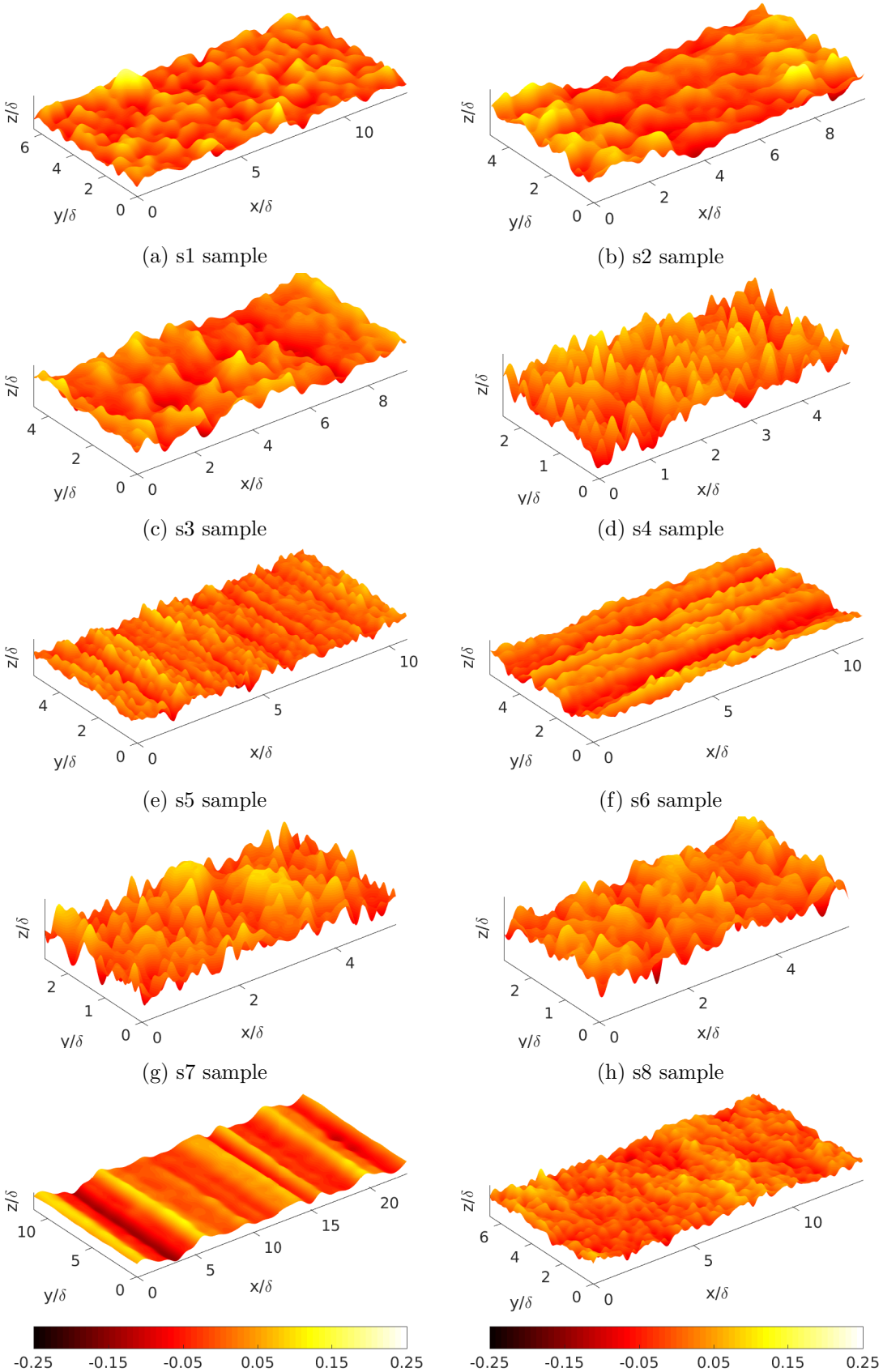

(a) s1 sample (b) s2 sample

(c) s3 sample (d) s4 sample

(e) s5 sample (f) s6 sample

(g) s7 sample (h) s8 sample

(i) s9 sample (j) s10 sample

Figure 3.4: Surface plots for samples s1 to s10. Plots coloured by roughness height, k/δ. Refer Table 3.1 for naming convention. All plots have the same colourbar, shown at the bottom.

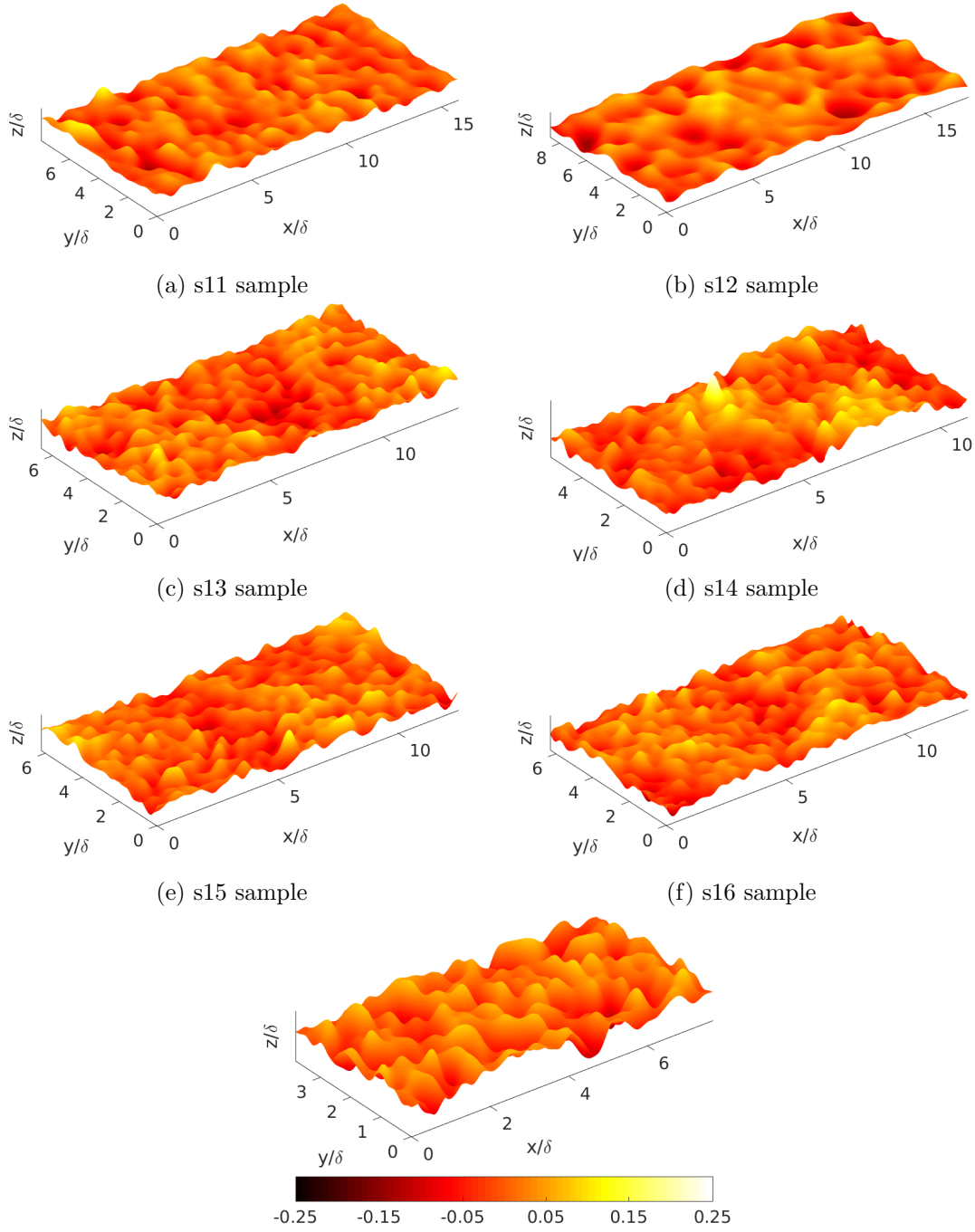

(a) s11 sample

(b) s12 sample

(c) s13 sample

(d) s14 sample

(e) s15 sample

(f) s16 sample

(g) s17 sample

Figure 3.5: Surface plots for samples s11 to s17. Plots coloured by roughness height, k/δ. Refer Table 3.1 for naming convention. All plots have the same colourbar, shown at the bottom.

Flack [2007], Wu and Christensen [2006] and Bons [2002]. The aerodynamic roughness flow parameters are most influenced by the highest features of the rough surface. In order to study universal roughness behaviour, k should be small compared to the channel half-height, δ and Jiménez [2004] recommends a ratio of δ/k (where k is based on the equivalent sand-grain roughness height) in excess of 40. In order to achieve a significant roughness effect for $\delta/k > 40$, very high Re_τ, in excess of 1000, would be required. This in turn would lead to extremely dense meshes as the small scales of motion, especially close to the rough walls, would need to be resolved. These factors lead to a prohibitively high computational cost. Hence a relatively low $\delta/k = 6$ is used, which leads to a clear roughness effect at relatively low Reynolds number, for example, $Re_\tau = 180$. Although this may be an obstacle to studying universal behaviour, studies at low δ/k are important, for example, in cases of water flow over gravel beds (Mohajeri et al. [2015], Grass [1971]) and flows in urban environments (Orlandi and Leonardi [2006]) and tree canopies (Sadeh et al. [1971]). It is also important to note that the reason for scaling all surfaces to the same roughness height is to enable a study of the influence of other surface characteristics, for example, skewness and correlation lengths, on the roughness effects.

An important geometrical parameter that is used to characterise the surfaces in this work is the generalised Sigal-Danberg parameter, Λ_s, as modified by van Rij et al. [2002],

$$\Lambda_s = \left(\frac{S}{S_f}\right)\left(\frac{S_f}{S_w}\right)^{-1.6}, \tag{3.1}$$

as also described in equation (1.3). Details of how to compute this parameter are described in Appendix A. S/S_f can be regarded as the inverse of the solidity which is defined as the total projected frontal roughness area per unit wall-parallel projected area. Λ_s provides information about the roughness density, shape as well as direction with respect to the mean flow.

According to Flack and Schultz [2010], skewness, S_{sk} is a quantitative way of describing whether a rough surface has more pronounced peaks or valleys. A negative value of skewness indicates that the surface is pitted, for example, due to corrosion or surface wear whereas a positive value indicates roughness due to isolated large peaks, for example, due to deposition of foreign materials (as in biological fouling). A surface skewness value close to zero indicates a more or less homogeneous distribution of peaks and valleys. The s1, s2, s7, s14 and s15 samples have a positive value of skewness whereas all other samples have a negative value. Also, s15 has a skewness value close to zero. The spark-eroded samples, s13, s14, s15 and s16, although taken from the same larger surface scan, show significantly different skewness values. Their values are -0.30, 0.43, 0.05 and -0.17 for s13, s14, s15 and s16 respectively. Hence a wide range of skewness, which means differing distributions of peaks and valleys, is obtained for these samples.

The largest correlation lengths are exhibited by the s5, s6 and s9 samples in their respective spanwise, streamwise and spanwise directions. This is attributed to the strong anisotropy of their roughness features, which can clearly be seen from the surface plots

(refer Figure 3.4 (e), (f) and (i)). The directionality of the features of a given rough surface can be obtained from the surface texture aspect ratio, S_{tr}, which is given by the ratio of the shortest to longest correlation lengths of the sample; $S_{tr} = S_{al}/S_{sl}$. If $S_{tr} > 0.5$ then the sample is regarded as statistically isotropic whereas anisotropic samples have $S_{tr} < 0.3$ (refer Appendix A). All samples with the exception of s2, s3, s5, s6, s9 and s10 have $S_{tr} > 0.5$ and hence are statistically isotropic. The s10 sample has $S_{tr} = 0.41$ and can be considered weakly anisotropic. Both the composite samples, s2 and s3, are anisotropic with $S_{tr} = 0.28$ for s2, with its dominant features oriented in the streamwise direction, and $S_{tr} = 0.21$ for s3, with its dominant features oriented in the spanwise direction (refer Figure 3.4 (b) and (c)). A major difference between s2 and s3 is observed in the surface skewness, their respective values being 0.24 and -0.19, indicating that s2 is peak dominated whereas s3 is valley dominated.

A parameter called the flow texture ratio, S_{tr}^{flow}, which depends on the streamwise and spanwise correlation lengths of the samples, has been defined as $S_{tr}^{\text{flow}} = L_y^{\text{cor}}/L_x^{\text{cor}}$. This parameter is another indicator of the anisotropy of the roughness features. If $S_{tr}^{\text{flow}} \gg 1$, for example, $S_{tr}^{\text{flow}} = 29.9664$ for the s5 sample, its roughness features have strong directional preference in the spanwise direction (refer Figure 3.4 (e)) and if $S_{tr}^{\text{flow}} \ll 1$, for example, $S_{tr}^{\text{flow}} = 0.0345$ for the s6 sample, its roughness features have strong directional preference in the streamwise direction (refer Figure 3.4 (f)). For values of S_{tr}^{flow} close to 1, the roughness features of the sample have a relatively homogeneous distribution and no specific directional preference is seen.

The effective slope, ES, as introduced by Napoli et al. [2008], represents the overall gradient of the roughness elements of an irregular rough surface. Higher values of ES indicate dense roughness whereas lower values are obtained for relatively sparse roughness. In the case of three-dimensional roughness, the effective slope is computed in the streamwise and spanwise directions and denoted by ES_x and ES_y respectively. From Table 3.2, most surfaces have similar values of ES_x and similar values of ES_y. Based on these values, s4, s7 and s8 can be considered relatively more densely rough whereas s9, s11 and s12 can be considered relatively sparsely rough. Another indication of roughness density is the solidity, S_f/S. According to Jiménez [2004], roughness is considered dense if its $S_f/S > 0.15$ and sparse otherwise. Based on this criterion, only one sample from the database, s4 ($S_f/S = 0.16$), is dense. A closer look at the values of S_f/S and ES_x from Table 3.2 shows that $2 \times S_f/S \approx ES_x$ for the current dataset. This relation was also pointed out by Napoli et al. [2008] from their studies on random 2D roughness and hence could be considered applicable to different types of roughness. Figure 3.6 (left) shows a plot of the two quantities and clearly establishes this relationship as all points fall on the straight line given by $2 \times S_f/S = ES_x$. A relationship is also observed between Λ_s and ES_x (Figure 3.6 (right)), as $(S_f/S)^{-1}$ is an integral part of Λ_s (equation (3.1)).

Bons [2005] mentioned that the mean streamwise forward facing surface angle, $\overline{\alpha}$, is geometrically related to the Sigal-Danberg parameter. This is observed from Figure 3.7 (top left), which shows a semilogarithmic plot of the two quantities for the samples in this

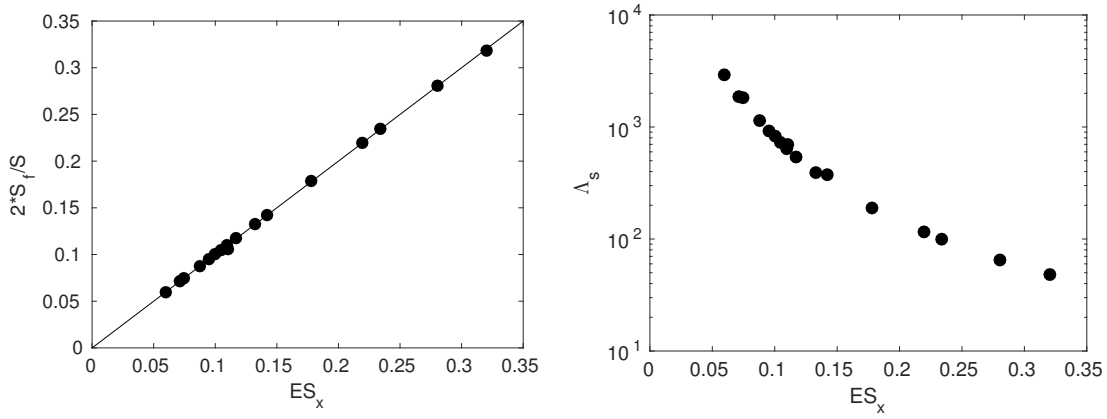

Figure 3.6: Variation of S_f/S with ES_x (left), with the straight line representing $2 \times S_f/S = ES_x$, and variation of Λ_s with ES_x (right).

study. From this, it is logical to follow that S_f/S is also related to $\overline{\alpha}$, Figure 3.7 (top right). The root-mean-square of the streamwise surface angle, α_{rms}, was proposed by Acharya et al. [1986] as an important parameter characterising real roughness in the context of turbine blades. Also established are relationships between α_{rms} and Λ_s (Figure 3.7 (bottom left)) and α_{rms} and S_f/S (Figure 3.7 (bottom right)). These relationships confirm that the

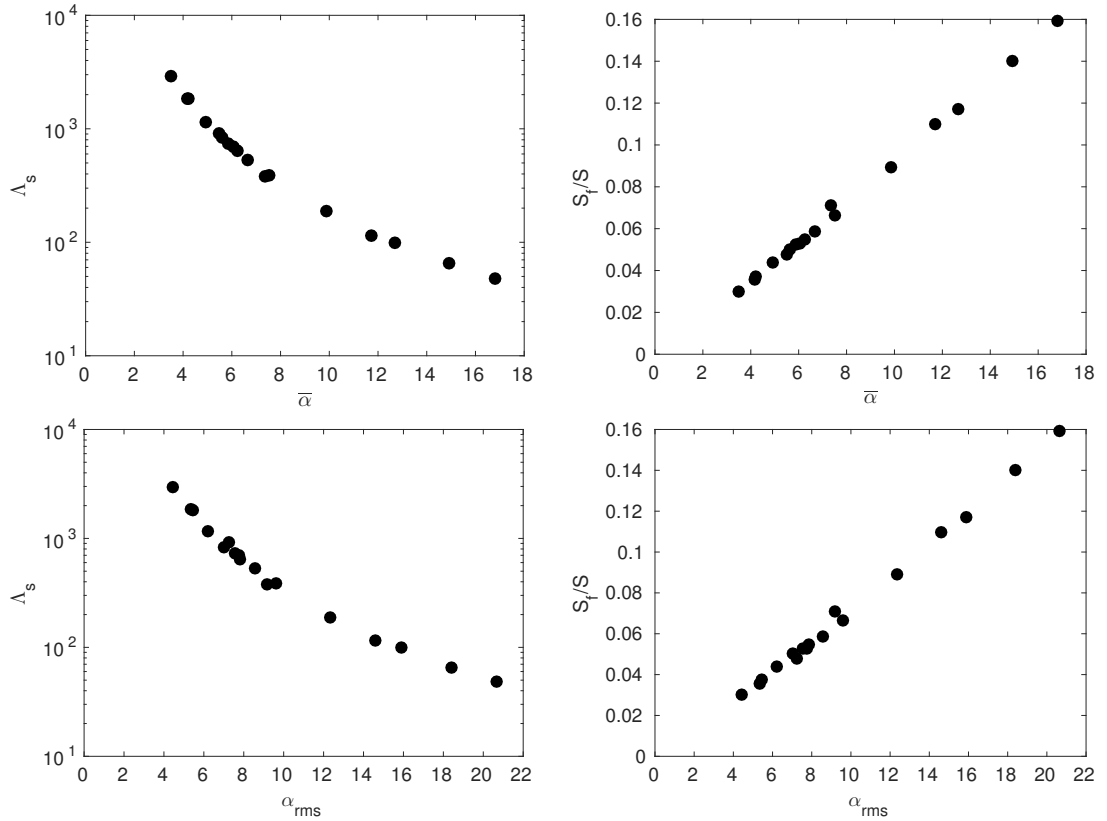

Figure 3.7: Variation of Λ_s and S_f/S with $\overline{\alpha}$ (top left and top right) and variation of Λ_s and S_f/S with α_{rms} (bottom left and bottom right). $\overline{\alpha}$ and α_{rms} are denoted in degrees.

streamwise forward facing surface angle is approximately linearly related to the solidity of the roughness elements. It is also worth noting that $\tan(\overline{\alpha}) \approx ES_x$, the tangent of the mean streamwise forward facing surface angle approximately represents the streamwise effective slope.

The above observations establish that ES_x, $\overline{\alpha}$ and α_{rms} are all closely linked to the solidity, S_f/S, for the current set of samples and as such cannot be regarded as independent parameters. This is particularly important for the parametric fitting studies conducted in Chapter 7 as, if one of the four properties enters the fit at a certain stage, none of the other three would provide any more useful information at a later stage.

It is also essential to note that the relationships depicted in Figures 3.6 (right) and 3.7 apply only to the current set of rough surfaces and may or may not be generalised to other types of roughness.

property	s1	s2	s3	s4	s5	s6	s7	s8	s9	s10	s11	s12	s13	s14	s15	s16	s17
k_cL_x	24	24	24	28	36	32	24	24	18	36	20	18	24	24	24	24	18
S_a	0.0304	0.0353	0.0323	0.0304	0.0243	0.0353	0.0294	0.0275	0.0412	0.0257	0.0274	0.0321	0.0312	0.0351	0.0284	0.0294	0.0308
S_q	0.0387	0.0436	0.0409	0.0379	0.0319	0.0427	0.0373	0.0358	0.0509	0.0328	0.0358	0.0409	0.0396	0.0441	0.0361	0.0372	0.0383
S_{sk}	0.5964	0.2434	-0.1852	-0.0531	-0.3686	-0.4132	0.2797	-0.5190	-0.1329	-0.2315	-0.4334	-0.4081	-0.3048	0.4355	0.0451	-0.1653	-0.3881
S_{ku}	4.006	2.869	3.012	2.708	3.912	2.514	2.974	3.844	2.817	3.504	4.430	3.379	3.394	3.626	3.229	3.101	2.871
$S_{\mathrm{z,max}}$	0.2949	0.3017	0.2644	0.2263	0.2622	0.2626	0.2290	0.2621	0.2660	0.2818	0.3147	0.2610	0.3185	0.3864	0.2674	0.2659	0.2314
L_x^{cor}	0.5347	2.0128	0.4676	0.2222	0.1786	11.2700	0.2139	0.2160	0.9450	0.7014	0.5192	0.9825	0.9912	1.5172	0.8190	0.6893	0.2808
L_y^{cor}	0.5131	0.5611	2.1821	0.1968	5.352	0.3886	0.3509	0.2958	11.6000	1.0971	1.0171	0.9211	1.3759	1.2848	0.4998	0.6471	0.3574
S_{sl}	0.5962	2.0174	2.1894	0.3507	5.352	11.2700	0.3591	0.3351	11.6000	1.4636	1.0727	1.0115	1.7411	1.7041	0.8357	0.8324	0.3613
S_{al}	0.4670	0.5748	0.4670	0.1871	0.1883	0.3890	0.2181	0.2153	0.9454	0.6019	0.5246	0.9361	0.9015	1.1952	0.5051	0.6001	0.2798
S_{tr}	0.7833	0.2849	0.2133	0.5336	0.0701	0.0688	0.6074	0.6427	0.1606	0.4112	0.4890	0.9255	0.5178	0.7014	0.6044	0.7219	0.7745
S_{tr}^{flow}	0.9595	0.2857	4.6666	0.8696	29.9664	0.0345	1.6364	1.3695	11.7172	1.5641	1.9591	0.9400	1.3762	0.8468	0.6102	0.9388	1.2728
ES_x	0.1098	0.0952	0.1418	0.3177	0.2194	0.0745	0.2798	0.2339	0.0710	0.1325	0.0877	0.0600	0.1057	0.1170	0.1000	0.1048	0.1781
ES_y	0.1162	0.1425	0.0963	0.3071	0.0990	0.1998	0.2791	0.2242	0.0105	0.1067	0.0583	0.0611	0.1062	0.1060	0.1133	0.1082	0.1465
S	84.50	48.02	43.62	12.10	57.28	63.51	13.78	15.85	269.12	90.86	126.12	153.12	88.45	60.50	77.88	79.96	29.29
S_f	4.644	2.293	3.100	1.928	6.297	2.370	1.934	1.856	9.590	6.028	5.541	4.601	4.684	3.548	3.901	4.201	2.612
S_w	42.940	24.290	24.261	6.887	30.840	32.210	7.709	8.580	131.620	46.051	64.418	75.630	44.530	30.630	40.180	41.190	15.310
S_f/S	0.0550	0.0477	0.0711	0.1593	0.1099	0.0373	0.1406	0.1171	0.0356	0.0663	0.0439	0.0300	0.0530	0.0586	0.0501	0.0525	0.0892
S_w/S	0.5082	0.5057	0.5562	0.5682	0.5383	0.5072	0.5594	0.5414	0.4891	0.5069	0.5108	0.4939	0.5035	0.5062	0.5194	0.5151	0.5225
Λ_s	639	914	378	48	116	1830	65	99	1854	390	1153	2934	693	537	838	734	190
$\overline{\alpha}$	6.245	5.493	7.357	16.801	11.711	4.213	14.913	12.674	4.167	7.521	4.937	3.494	6.070	6.663	5.616	5.871	9.861
α_{rms}	7.833	7.249	9.176	20.662	14.610	5.425	18.388	15.894	5.348	9.607	6.196	4.448	7.736	8.579	7.009	7.542	12.333

Table 3.2: Topographical properties of the rough surface samples in this study. $S_{z,5\times5} = \delta/6$, k_cL_x = maximum streamwise wavenumber. All length scales are non-dimensionalised by the mean channel half-height, δ. $\overline{\alpha}$ and α_{rms} are computed in degrees. Refer Appendix A for a description of each property and its calculation. Surface sample naming convention described in Table 3.1.

Chapter 4

Validation studies and smooth-wall simulations

The immersed boundary DNS code was first validated during the work of Busse et al. [2015] by performing dependence tests pertaining to the streamwise and spanwise mesh resolution, computational domain size and Fourier filter cut-off wavenumber. However, further dependence tests with respect to the mesh resolution and computational domain size have also been carried out as part of the current work. An additional study, investigating the sensitivity of the results to the channel blockage ratio, is also carried out by varying the k/δ ratio of the channel. Validation is performed by studying the mean and turbulent statistics for the different cases. All simulations in this chapter are performed on the s8 (gritblasted) sample.

The Reynolds number based on the roughness height, k^+, is given as

$$k^+ = \frac{ku_\tau}{\nu}, \tag{4.1}$$

where k is the roughness height, represented by $S_{z,5\times5}$ in this work. In principle, k^+ is also a representation of the roughness height in wall-units. Equation (4.1) can be converted into a form that includes Re_τ.

$$\begin{aligned} k^+ &= \frac{ku_\tau}{\nu}\frac{\delta}{\delta}, \\ &= \frac{k}{\delta}Re_\tau. \end{aligned}$$

For example, when $Re_\tau = 180$ and $k/\delta = 1/6$, then from the above, $k^+ = 30$.

4.1 Smooth-wall simulations

Smooth-wall simulations are required for comparison and for computing the roughness function, ΔU^+. These were performed using the same DNS code described in Section 2.4 but without the embedded boundary treatment. Periodic boundary conditions were enforced in the streamwise and spanwise directions and a constant mean streamwise pressure gradient

Re_τ	Δx^+	Δy^+	Δz^+_{min}	Δz^+_{max}	U_b	U_c^+
180	8.4	4.2	0.67	4.7	15.77	18.44
240	9.0	4.5	0.68	4.3	16.44	19.11
360	9.6	4.8	0.68	5.0	17.42	20.13
540	10.1	5.1	0.67	5.0	18.48	21.24
720	9.6	4.8	0.67	5.0	19.31	22.10

Table 4.1: Simulation parameters along with mean streamwise bulk velocity, U_b, and mean centreline velocity, U_c^+ for all smooth-wall simulations

was applied to drive the flow. The domain size for all smooth-wall simulations was $12\delta \times 6\delta \times 2\delta$ in the streamwise, spanwise and wall-normal directions respectively. The corresponding mesh resolution was $\Delta x^+ \leq 10$, $\Delta y^+ \approx \Delta x^+/2$, $\Delta z^+_{\text{min}} \approx 0.667$ and $\Delta z^+_{\text{max}} \leq 5$. Simulation parameters along with the mean streamwise bulk velocity, U_b, and mean centreline velocity, U_c^+, are given in Table 4.1. At $Re_\tau = 180$, Vreman and Kuerten [2014] conducted extensive comparisons of different DNS databases for smooth-wall channel flow to assess the accuracy and reproducibility of data. This Reynolds number is studied extensively in subsequent chapters. Comparisons of U_b and U_c^+ from the current work (first row in Table 4.1) with those of a refined finite difference DNS of Vreman and Kuerten [2014] show differences of approximately 1%.

4.2 Validation - variation of mesh resolution

This section describes the dependence of the mean and turbulent statistics on the mesh resolution. It is the aim of this section to test the limit of the mesh resolution against the requirements mentioned in Section 2.3.2.

Initially for this study, the sample is selected using the section selection procedure as described in Section 2.2.1. However, for quicker simulation turnaround times, the size of the physical sample is halved and the procedure of Section 2.2.1 is repeated within the larger sample. Figure 4.1 shows the full gritblasted surface scan and the position of the two sections on it. Figure 4.2 shows the final scaled sample in its unfiltered (left) and filtered (right) form.

Table 4.2 shows the computational domain size and simulation parameters for the study. All simulations are conducted at $Re_\tau = 180$. The mesh resolution is varied in the streamwise and spanwise directions only and all cases have the same wall-normal mesh parameters; $n_z = 288$, $\Delta z^+_{\text{min}} \approx 0.667$ and $\Delta z^+_{\text{max}} = 3.46$. Three different mesh resolutions, denoted as fine, medium and coarse, with reducing mesh resolution in that order, are studied. From the two meshing criteria described in Section 2.3.2, the λ_{min} criterion is dominant for the current sample at $Re_\tau = 180$, giving $n_x \geq 12(k_c L_x)$, $n_x \geq 144$, which gives $\Delta x^+ \lessapprox 3.52$. Hence, the fine mesh satisfies this criterion whereas both the medium and coarse meshes violate it (by approximately 11% and 33% respectively). In fact, the coarse mesh violates the Reynolds number criterion as well. Also, the quantity $\lambda_{\text{min}}/\Delta x$ shows how many cells are actually present per smallest wavelength of the sample, a value less than 12 indicates

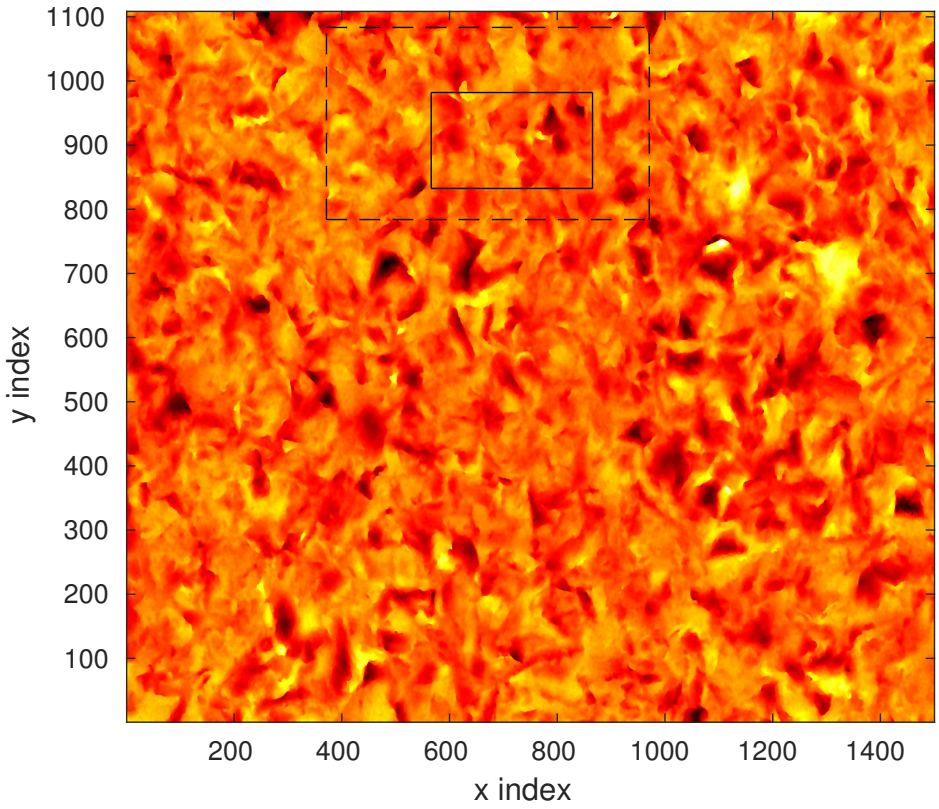

Figure 4.1: Section selection for the mesh dependence study. The larger box (dashed lines) represents the initial section whereas the smaller box (solid lines) represents the final section used in the study. Surface coloured by absolute roughness height. Colourbar: black to yellow - lower to higher roughness heights.

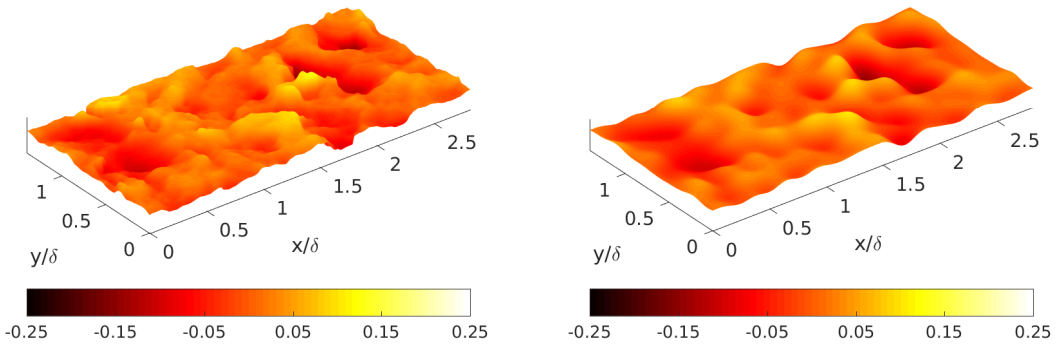

Figure 4.2: Final scaled sample before filtering (left) and after filtering (right). Surface plots coloured by scaled roughness height, k/δ.

	L_x/δ	L_y/δ	L_z/δ	k_cL_x	
	2.815	1.4075	2.2926	12	
name	n_x	n_y	$\Delta x^+, \Delta y^+$	$\lambda_{\min}/\Delta x$	ΔU^+
fine	160	80	3.17	14	5.33
medium	128	64	3.96	11	5.60
coarse	96	48	5.28	8	5.46

Table 4.2: Domain size and simulation parameters for the mesh dependence study. L_x/δ, L_y/δ and L_z/δ are the domain extents in the streamwise, spanwise and wall-normal directions while k_cL_x is the maximum streamwise wavenumber. n_x, n_y are mesh sizes in the streamwise and spanwise directions and Δx^+, Δy^+ are the mesh resolution in wall-units. $\lambda_{\min}/\Delta x$ represents how many cells are present per smallest wavelength of the sample.

that the $\lambda_{\min}$ criterion is violated.

4.2.1 Influence on the mean flow statistics

Figure 4.3 (left) shows time-averaged mean streamwise velocity profiles, U^+, against wall-normal distance in wall-units, z^+, on semilogarithmic axes for all three cases in the mesh dependence study. Smooth-wall profiles at $Re_\tau = 180$ are also shown for reference. All three rough-wall profiles show close agreement. Also, from Table 4.2, all ΔU^+ values are within 5% of each other. Figure 4.3 (right) shows the time-averaged mean streamwise velocity defect profiles against the wall-normal distance, z/δ, for the three rough-wall cases along with the smooth-wall profile. Overall, the rough-wall profiles are very similar and show good agreement with each other. Collapse of all three profiles with the smooth-wall profile is obtained beyond $z/\delta \approx 0.1$. The medium and coarse case profiles show only a small deviation for $0.1 \leq z/\delta \leq 0.4$.

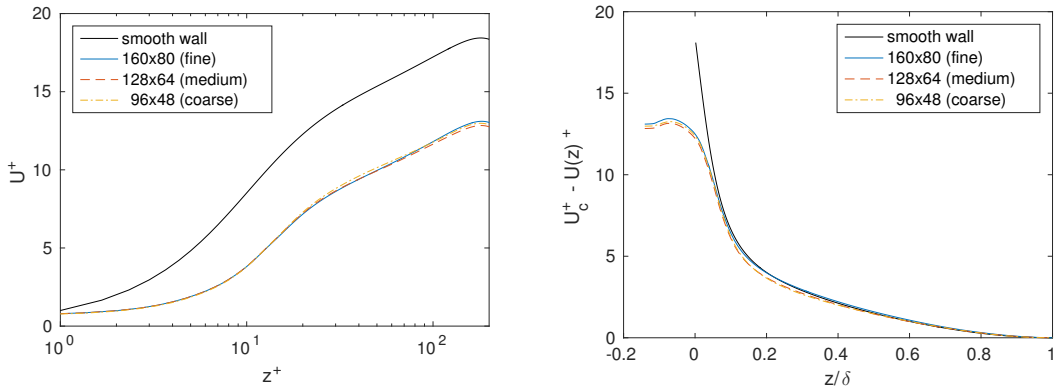

Figure 4.3: Mean streamwise velocity profiles, U^+, against wall-normal distance in wall-units, z^+ (left), and mean streamwise velocity defect profiles against wall-normal distance, z/δ (right). Also shown are smooth-wall profiles for reference. The legend shows number of mesh cells in the streamwise and spanwise directions along with the case name in brackets.

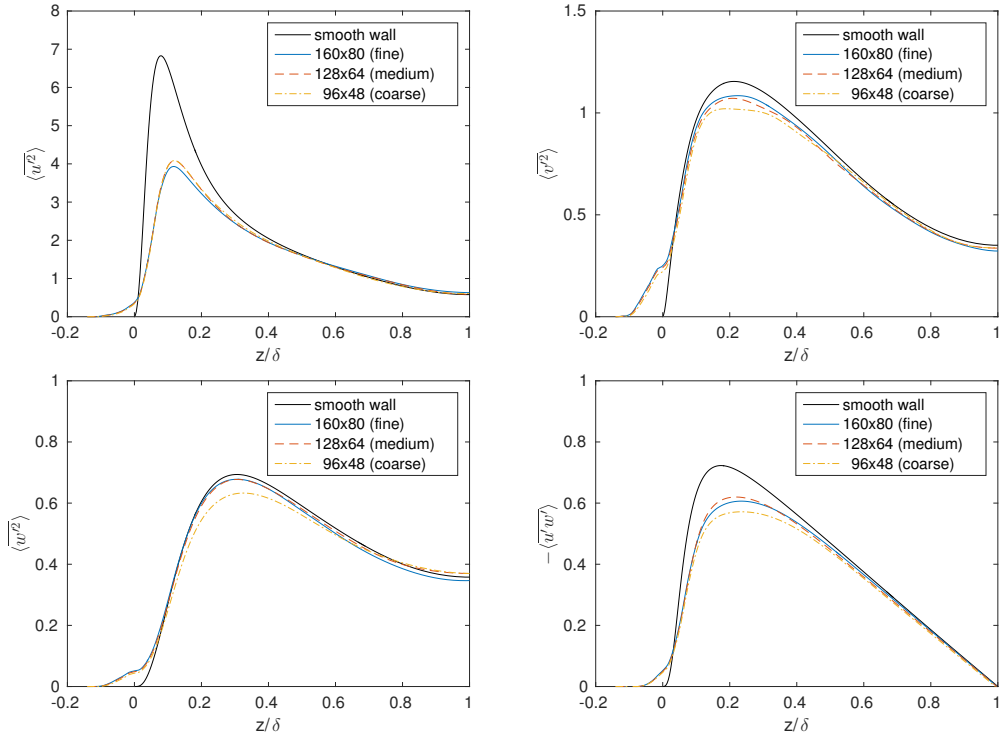

Figure 4.4: Reynolds stress profiles against z/δ: $\langle\overline{u'^2}\rangle$ (top left), $\langle\overline{v'^2}\rangle$ (top right), $\langle\overline{w'^2}\rangle$ (bottom left), $-\langle\overline{u'w'}\rangle$ (bottom right) along with corresponding smooth-wall profiles.

4.2.2 Influence on the turbulent flow statistics

Figure 4.4 shows the Reynolds stress profiles of the streamwise, $\langle\overline{u'^2}\rangle$ (top left), spanwise, $\langle\overline{v'^2}\rangle$ (top right), wall-normal, $\langle\overline{w'^2}\rangle$ (bottom left) and shear stress, $-\langle\overline{u'w'}\rangle$ (bottom right), against z/δ, which collectively depict the turbulent flow statistics. In general, profiles for the fine and medium mesh show close agreement, whereas profiles for the coarse mesh show differences. Peak streamwise fluctuations are slightly over predicted by the medium and coarse meshes whereas peak spanwise and wall-normal fluctuations, as well as the peak shear stress, are slightly under predicted by the coarse mesh.

From the mesh dependence study, it is seen that a small violation in the λ_{min} criterion may still give acceptable results, as in case of the medium mesh. However, all simulations henceforth will respect both meshing criteria from Section 2.3.2, $\Delta x^+ = \Delta y^+ \leq 5$ and $\Delta x \leq \lambda_{\text{min}}/12$.

4.3 Validation - variation of computational domain size

This section describes the dependence of mean and turbulent statistics on the size of the streamwise and spanwise computational domain. It is known that typically a large enough computational domain size is required for proper flow development to take place. The domain size requirements are strict for smooth channels, especially in the streamwise direction, due to the presence of long streamwise streaks (Kim et al. [1987], Kline et al.

[1967]). In rough channels, however, domain size requirements are slightly less stringent as the roughness breaks down the streamwise streaks (Ashrafian and Andersson [2006], Orlandi and Leonardi [2006], Smalley et al. [2002], Antonia and Krogstad [2001]). The concept of a minimal channel was introduced by Jiménez and Moin [1991] with reference to a smooth wall and utilised in various studies (for example, Chung et al. [2015], Hwang [2013]), wherein the basic building block of wall-bounded turbulence was isolated. Although this is the limiting case for domain size, it serves as a useful comparison for this study.

Two cases are considered as part of the study: one with a smaller domain size and the other with a larger domain size. Simulations for both cases are conducted at $Re_\tau = 360$, $k/\delta = 1/12$ and $k^+ = (k/\delta)Re_\tau = 30$. Re_τ is higher than the mesh dependence study so that validation is conducted for a wider range of Reynolds number. The roughness height, k/δ, scales with the sample computational domain size and the domain is either shrunk or enlarged depending on the required roughness height. For $k/\delta = 1/12$, the computational domain size is $L_x \times L_y = (2.815\delta \times 1.4075\delta)$, which in wall-units is $(1013.4 \times 506.7)^+$. This is significantly larger than the minimal channel criterion of Jiménez and Moin [1991], which was approximately $(300 \times 100)^+$. This case is classified as the smaller domain and is referred to as the 'untiled' sample. In order to obtain the larger domain sample, the smaller sample is simply copied in the streamwise and spanwise directions, thus obtaining 2×2 tiles, and is referred to as the 'tiled' sample. This can be done without issues as the sample is periodic in the streamwise and spanwise directions. The tiled sample thus has twice the domain extents of the untiled sample. It is important to note that in the process of tiling, the only parameters that change are the streamwise and spanwise domain sizes. This tiling process does not affect the flow field to a significant extent and its effects are discussed in detail in Chapter 8. Figure 4.5 shows surface plots in plan view of the two samples along with corresponding domain extents. Table 4.3 shows the simulation parameters for this study, including the values of ΔU^+ obtained for each case. The mesh resolution for the tiled case

Re_τ	360 (untiled)	360 (tiled)
L_x/δ	2.8150	5.630
L_y/δ	1.4075	2.815
L_x^+	1013.4	2026.8
L_y^+	506.7	1013.4
L_z/δ	2.1622	2.1622
n_x	384	720
n_y	192	360
n_z	448	448
$\Delta x^+, \Delta y^+$	2.6391	2.8150
$\Delta z^+_{\max}$	3.7336	3.7336
ΔU^+	4.26	4.28

Table 4.3: Simulation parameters for the domain dependence study. L_x/δ, L_y/δ and L_z/δ are the streamwise, spanwise and wall-normal domain extents, n_x, n_y and n_z are the streamwise, spanwise and wall-normal mesh sizes, Δx^+,Δy^+ and Δz^+ are the streamwise, spanwise and wall-normal mesh resolutions.

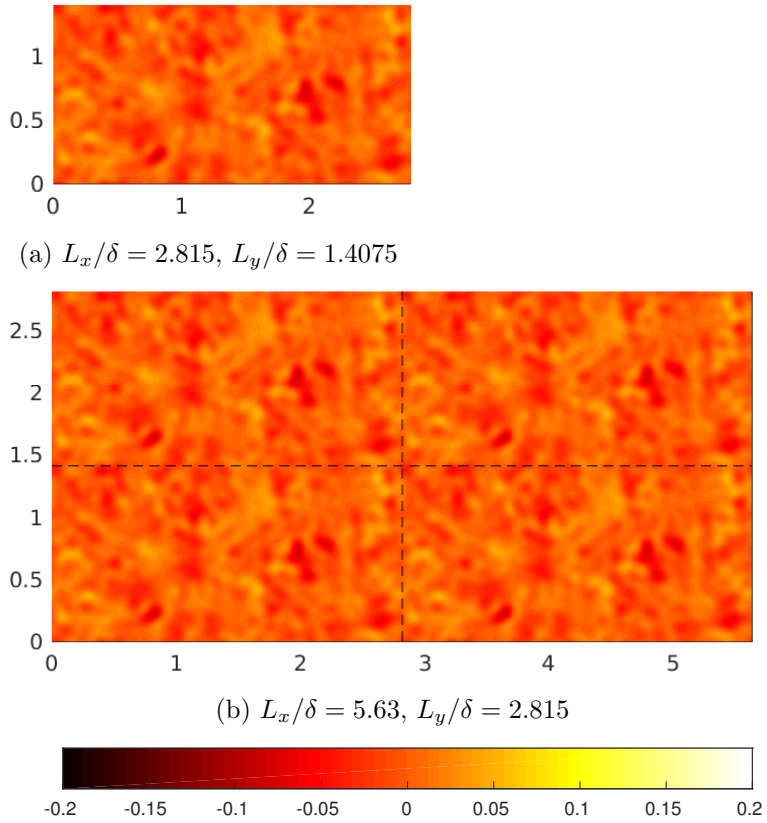

(a) $L_x/\delta = 2.815$, $L_y/\delta = 1.4075$

(b) $L_x/\delta = 5.63$, $L_y/\delta = 2.815$

Figure 4.5: Surface contour plots in plan view for the two samples. L_x/δ and L_y/δ are the streamwise and spanwise computational domain sizes. Dashed lines denote tile boundaries. Plot dimensions scaled by corresponding domain sizes. Plots coloured by roughness height, k/δ. Both plots have the same colourbar.

must remain approximately the same or higher than the untiled case. Both cases have $\Delta z^+_{\text{min}} \approx 0.667$.

4.3.1 Influence on the mean flow statistics

Values of ΔU^+ shown in Table 4.3 indicate very good agreement between both untiled and tiled cases and the difference is minor. Figure 4.6 (left) shows time-averaged mean streamwise velocity profiles, U^+, against wall-normal distance in wall-units, z^+ on semilogarithmic axes for both cases along with smooth-wall profiles at $Re_\tau = 360$. Profiles for both cases show only minute differences. Close agreement in ΔU^+ was also obtained in the DNS studies of Chung et al. [2015], on modelled and sinusoidal roughness, who showed that the minimal channel proposed by Jiménez and Moin [1991] was sufficient for predicting the roughness function. Figure 4.6 (right) shows time-averaged mean streamwise velocity defect profiles against the wall-normal distance, z/δ, for both the rough-wall cases, along with the smooth-wall profile. Almost no difference is seen in the profiles for the two rough-wall cases. Also, overall good agreement with the smooth-wall profile is observed.

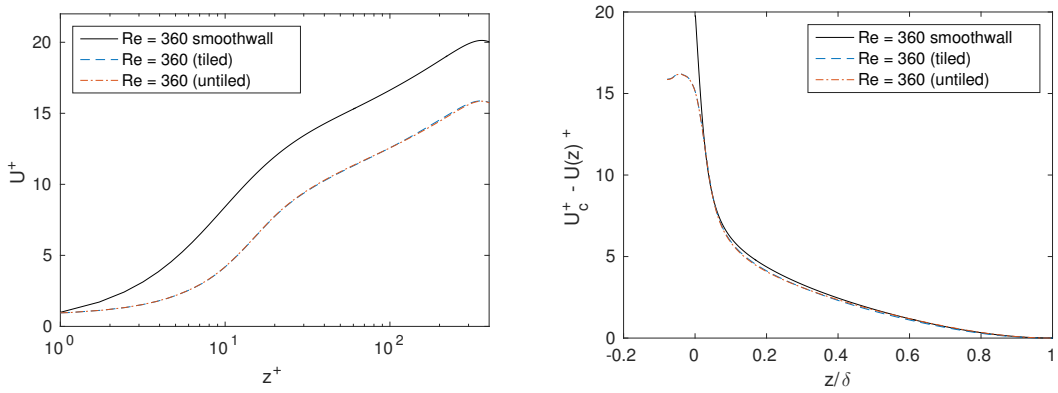

Figure 4.6: Mean streamwise velocity profiles, U^+, against wall-normal distance in wall-units, z^+ (left), and mean streamwise velocity defect profiles against wall-normal distance, z/δ (right). Also shown are smooth-wall profiles for reference.

4.3.2 Influence on the turbulent flow statistics

Figure 4.7 shows the Reynolds stress profiles of the streamwise $\langle\overline{u'^2}\rangle$ (top left), spanwise $\langle\overline{v'^2}\rangle$ (top right), wall-normal $\langle\overline{w'^2}\rangle$ (bottom left) and shear stress $-\langle\overline{u'w'}\rangle$ (bottom right), against z/δ, which collectively depict the turbulent flow statistics. In general, agreement between the two cases for the turbulent profiles is not as good as the mean profiles, probably because higher order statistics are more sensitive to the domain size. However, near-wall agreement of all profiles for both cases is very good, up to $z/\delta \approx 0.1$, beyond

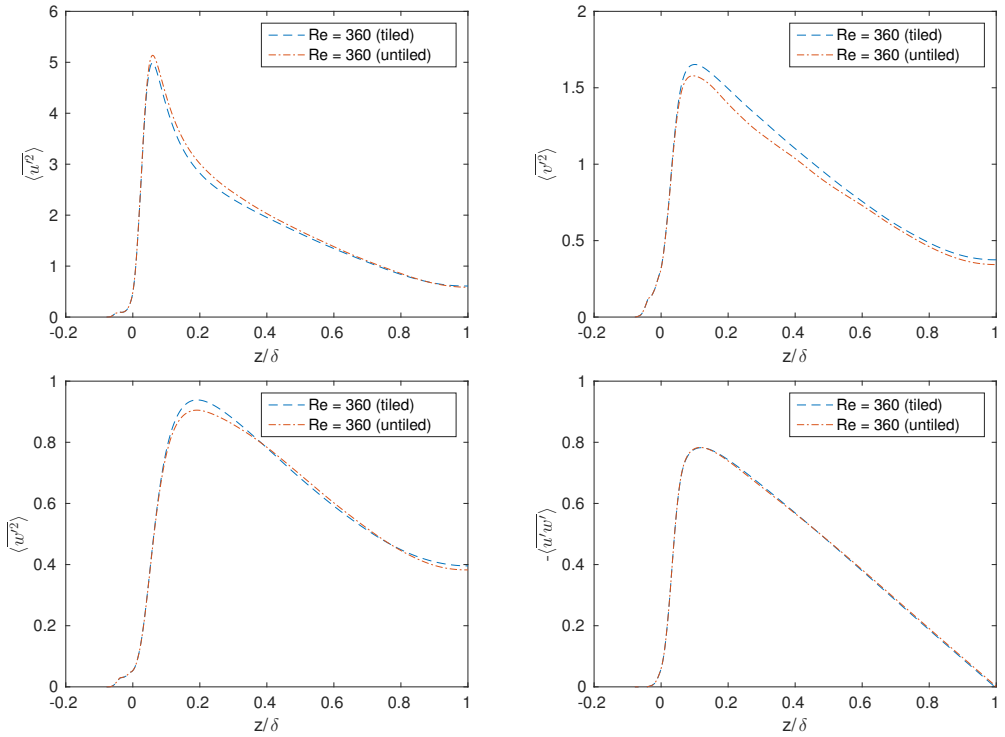

Figure 4.7: Reynolds stress profiles against z/δ: $\langle\overline{u'^2}\rangle$ (top left), $\langle\overline{v'^2}\rangle$ (top right), $\langle\overline{w'^2}\rangle$ (bottom left), $-\langle\overline{u'w'}\rangle$ (bottom right).

which differences begin to appear. Jiménez and Moin [1991] made similar observations in their smooth-wall minimal channel DNS studies and mentioned that the domain size might be too small to accommodate some of the large structures in the outer layer, thus leading to discrepancies in that region of the flow. Peak streamwise fluctuations for both cases are seen at $z/\delta \approx 0.05$, which was also observed by Hwang [2013] in his smooth-wall minimal span channel DNS studies. The peak values of $\langle\overline{u'^2}\rangle$ for both cases, which are quite similar, also agree with those of Hwang [2013]. Both these observations are slightly surprising as the peak of smooth-wall streamwise fluctuations is greater than that of rough walls and is usually located closer to the wall for a smooth wall. Hwang [2013] also mentioned that using a minimal span channel affects the spanwise fluctuations the most. In the current study, the greatest discrepancies are also observed in the spanwise fluctuations, probably, again due to the domain size constraining the large scale structures. Peak values between the two cases differ by less than 5% for the streamwise, spanwise and wall-normal fluctuations. Both cases, however, show excellent agreement in their shear stress profiles.

Busse et al. [2015] conducted a domain dependence study on the graphite sample (s7 from Table 3.1 and Figure 3.4 (g)) in a similar manner as the current section, by tiling the sample. Their small and large domain extents were $(5.25\delta \times 2.625\delta)$ and $(10.5\delta \times 5.25\delta)$ respectively. Their results showed almost no differences in the mean and turbulent profiles between the two cases and it is probable that their small domain was already large enough to obtain satisfactory results.

From computational studies on cube roughness, Coceal et al. [2007] and Coceal et al. [2006] showed that relatively small domains were enough to obtain satisfactory mean and turbulent statistics. It is understood from the above analysis that in the current study, although the mean profiles show good agreement between the small and large domains, the small domain constrains the flow to some extent and hence shows discrepancies in the turbulent statistics, up to a maximum of 5%, compared to the large domain.

4.4 Sensitivity to the channel blockage ratio, k/δ

It is commonly assumed that universal behaviour emerges only when the roughness height is considerably smaller than the macroscopic length scale of the flow, i.e. for small k/δ (Jiménez [2004]). The present validation study is conducted in order to check the sensitivity of the results to k/δ. The Re_τ and k/δ are varied but the roughness Reynolds number, $k^+ = (k/\delta)Re_\tau$, is kept constant for all cases. Since different flows having the same k^+ should produce the same ΔU^+ (Krogstad and Antonia [1999]), this study also serves to validate this statement. The roughness height and blockage ratio are equivalent as k is always non-dimensionalised by δ. Three Re_τ are considered for this study; $Re_\tau = 120$, 180 and 360. The Reynolds number is not reduced below $Re_\tau = 120$ due to the likely presence of low Reynolds number effects. $Re_\tau = 180$ serves as the reference case and the other cases are obtained by scaling the sample for this case. The value of $k/\delta = 1/6$ for $Re_\tau = 180$ gives a roughness Reynolds number, $k^+ = (k/\delta)Re_\tau = 30$, which remains constant for all cases. For the same k^+, a higher Re_τ would require a lower k/δ and hence lead to a smaller

Re_τ	120	180	360
k/δ	1/4	1/6	1/12
k^+	30	30	30
L_x/δ	8.4450	5.6300	2.8150
L_y/δ	4.2250	2.8150	1.4075
L_z/δ	2.4866	2.3244	2.1622
n_x	320	320	224
n_y	160	160	288
n_z	224	288	448
$\Delta x^+, \Delta y^+$	3.1669	3.1669	2.6391
$\Delta z^+_{\max}$	4.3926	3.7235	3.7336
ΔU^+	4.74	4.36	4.26

Table 4.4: Simulation parameters for the k/δ sensitivity study. L_x/δ, L_y/δ and L_z/δ are the streamwise, spanwise and wall-normal domain extents, n_x, n_y and n_z are the streamwise, spanwise and wall-normal mesh sizes, Δx^+,Δy^+ and Δz^+ are the streamwise, spanwise and wall-normal mesh resolutions.

domain size. Table 4.4 shows the simulation parameters for this study along with values of ΔU^+. k/δ at $Re_\tau = 180$ is twice the k/δ at $Re_\tau = 360$ and two-thirds the k/δ at $Re_\tau = 120$, in order to keep $k^+ = 30$ constant. For all cases, $\Delta z^+_{\min} \approx 0.667$. Surface plots of all cases in their plan view coloured by roughness height, corresponding streamwise and spanwise domain lengths along with values of k/δ are shown in Figure 4.8.

The domain extents for $k/\delta = 1/12$, $Re_\tau = 360$ may appear too small for proper flow development. However, it can be seen from Section 4.3 that the small domain size does not significantly affect the mean flow statistics at this Reynolds number. The turbulent profiles are affected only slightly.

4.4.1 Influence on the mean flow statistics

On initial inspection, values of ΔU^+ from Table 4.4 appear to be quite similar for all channel blockage ratios. The variance in ΔU^+ is approximately 5%, which is small. Figure 4.9 shows time-averaged mean streamwise velocity profiles in wall-units, U^+, against the wall-normal distance, z^+, on semilogarithmic axes. For comparison, this figure also shows smooth-wall profiles for $Re_\tau = 120$, 180 and 360. The profiles for all rough cases are remarkably similar all the way up to the log region of the corresponding case. The amount of downward shift in the rough-wall profiles from the corresponding smooth-wall profile also appears to be similar for all cases. Thus, the mean flow characteristics for all cases show similarity.

In order to understand the variation of ΔU^+ with k/δ, Figure 4.10 shows a plot of ΔU^+ against k/δ for all cases. Each symbol represents one case and since $Re_\tau = 180$ ($k/\delta = 1/6$) is the reference case, dashed lines are plotted above and below its ΔU^+ value to represent 5% tolerance bands. A 5% difference in ΔU^+ is considered reasonable and values falling within this difference are accepted. It is observed that ΔU^+ at $k/\delta = 1/12$ is within the tolerance. The ΔU^+ value at $k/\delta = 1/4$ is slightly outside the tolerance, by approximately

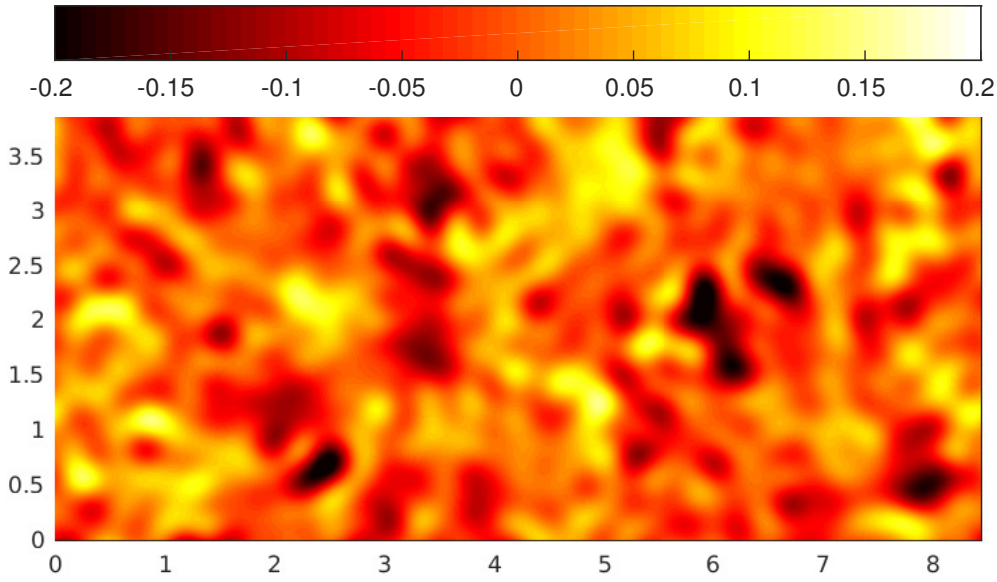

(a) $Re_\tau = 120$, $k/\delta = 1/4$, $L_x/\delta = 8.445$

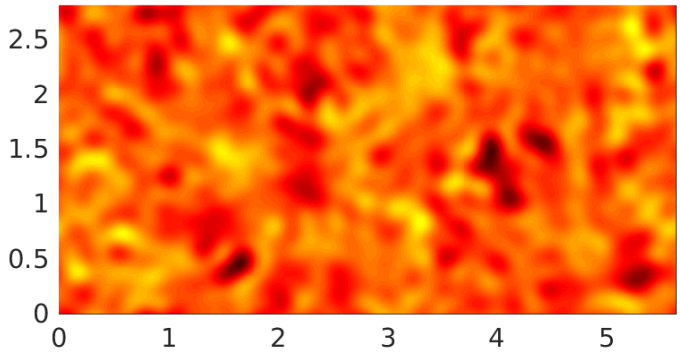

(b) $Re_\tau = 180$, $k/\delta = 1/6$, $L_x/\delta = 5.63$

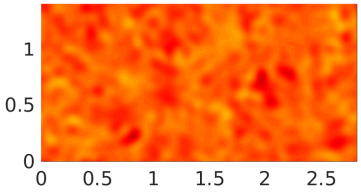

(c) $Re_\tau = 360$, $k/\delta = 1/12$, $L_x/\delta = 2.815$

Figure 4.8: Surface contour plots in plan view for the different samples. L_x/δ is the streamwise computational domain size. Plot dimensions scaled by corresponding domain sizes. Plots coloured by roughness height, k/δ. All plots have the same colourbar.

3%. Although this is accepted, the higher value of ΔU^+ is likely due to the high channel blockage of this case. It is also understood that the corresponding $Re_\tau = 120$ for this case may show the presence of low Reynolds number effects, which may be responsible for the slight disagreement. Despite the small number of cases, convergence in the value of ΔU^+ is achieved by $k/\delta = 1/6$. This means, for the same k^+, similar values of ΔU^+ can be expected for $k/\delta \leq 1/6$. Purely on the basis of ΔU^+, this ratio is much higher than that proposed by Jiménez [2004], who proposed $k/\delta \leq 1/40$ for similarity laws to apply.

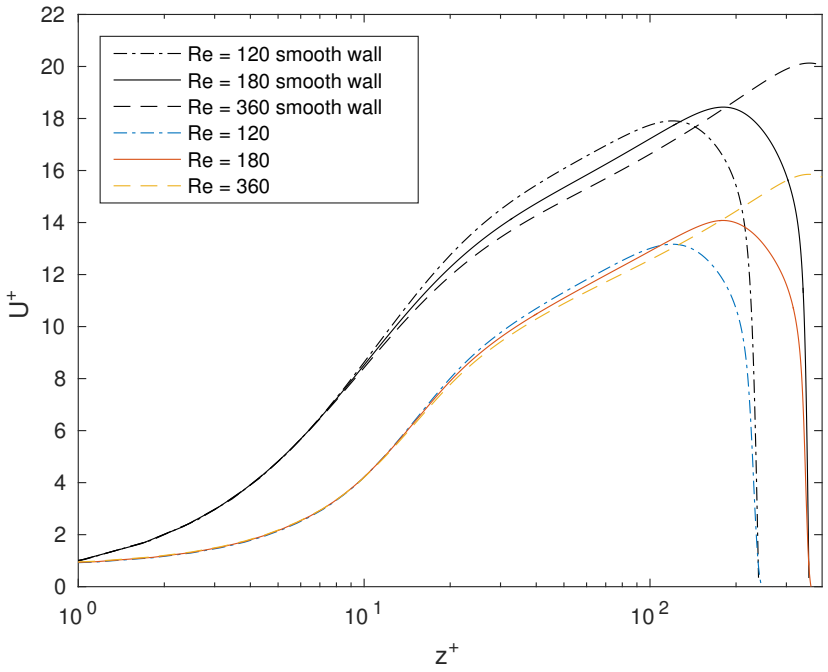

Figure 4.9: Mean streamwise velocity profiles, U^+, against wall-normal distance in wall-units, z^+, along with smooth-wall profiles.

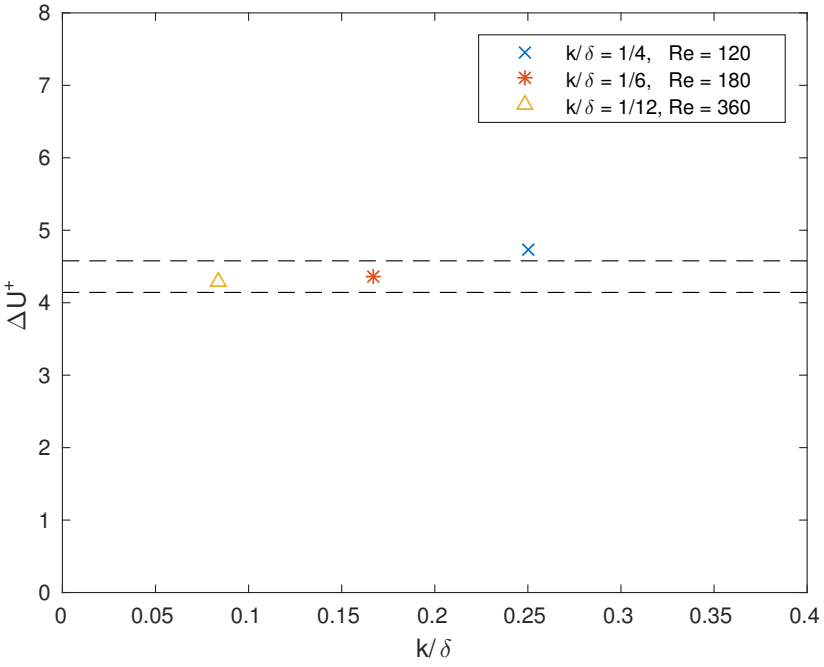

Figure 4.10: ΔU^+ against the channel blockage ratio, k/δ. The dashed lines above and below the $Re_\tau = 180$ case represent 5% tolerance bands.

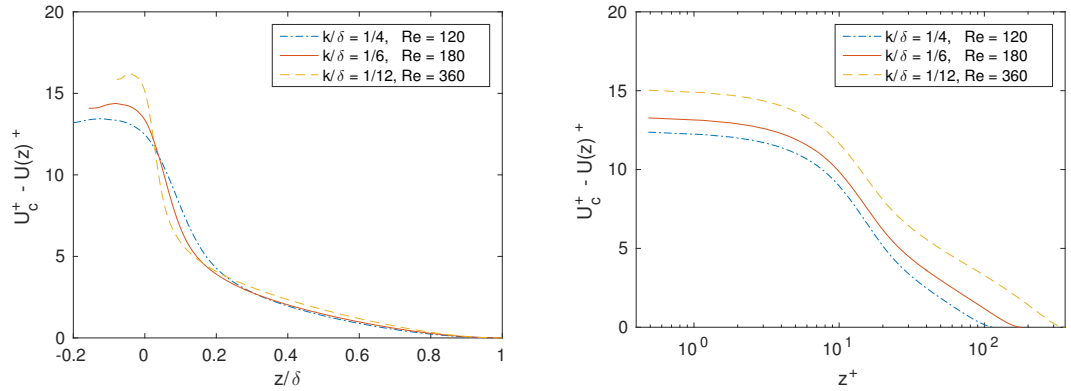

Figure 4.11: Mean streamwise velocity defect profiles against z/δ (left) and against z^+ (right).

Placidi and Ganapathisubramani [2015] conducted an experimental investigation of block roughness with $k/\delta \approx 0.1$. Based on a systematic variation of the frontal and plan solidities, it was mentioned that the criterion of Jiménez [2004] was unnecessarily restrictive for mean flow similarity.

Figure 4.11 shows time-averaged mean streamwise velocity defect profiles against the wall-normal coordinates, z/δ (left) and against z^+ (right). From the right plot, it is clear that profiles at lower k/δ (higher Re_τ) show higher values of velocity defect and hence are Re_τ dependent. From the left plot, profiles differ in the region close to the rough wall and up to $z/\delta \approx 0.2$. For $z/\delta \lessapprox 0$, a lower blockage ratio shows a higher velocity defect, because for a lower k/δ, the effects of roughness remain closer to the rough wall compared to a higher k/δ. Also, a higher Re_τ causes the mean centreline velocity, U_c^+, to be higher. The profiles then cross over in the region $0.03 \lessapprox z/\delta \lessapprox 0.04$. Above $z/\delta \approx 0.04$ and up to $z/\delta \approx 0.2$, lower k/δ show lower velocity defect values. Also in this region, lower k/δ show a steeper gradient of decrease in velocity defect. Beyond $z/\delta \approx 0.2$, profiles for $k/\delta = 1/4$ and $1/6$ collapse whereas $k/\delta = 1/12$ shows comparatively higher values. A collapse of all profiles is obtained for $z/\delta \gtrapprox 0.7$.

4.4.2 Influence on the turbulent flow statistics

Figure 4.12 shows Reynolds stress profiles (from top to bottom) of the streamwise, $\langle\overline{u'^2}\rangle$, spanwise, $\langle\overline{v'^2}\rangle$, wall-normal, $\langle\overline{w'^2}\rangle$ and shear stress, $-\langle\overline{u'w'}\rangle$, against z/δ (left) and z^+ (right), which collectively depict the turbulent flow statistics. A general dependence on Re_τ is observed. When plotted against z^+, all profiles for different k/δ show close similarity up to their peak magnitude, beyond which they start to drift apart, although still remaining similar. Profile peaks for all k/δ are observed at approximately the same z^+ for both the streamwise and spanwise fluctuations whereas peaks of the wall-normal fluctuations and shear stress show differences for different k/δ. In general, peak magnitudes for all profiles show an increasing trend with decreasing blockage (increasing Re_τ). When plotted against z/δ, peaks move closer to the rough wall with decreasing blockage. Not all profiles collapse close to the channel centre when plotted against z/δ; the shear stress profiles show the best

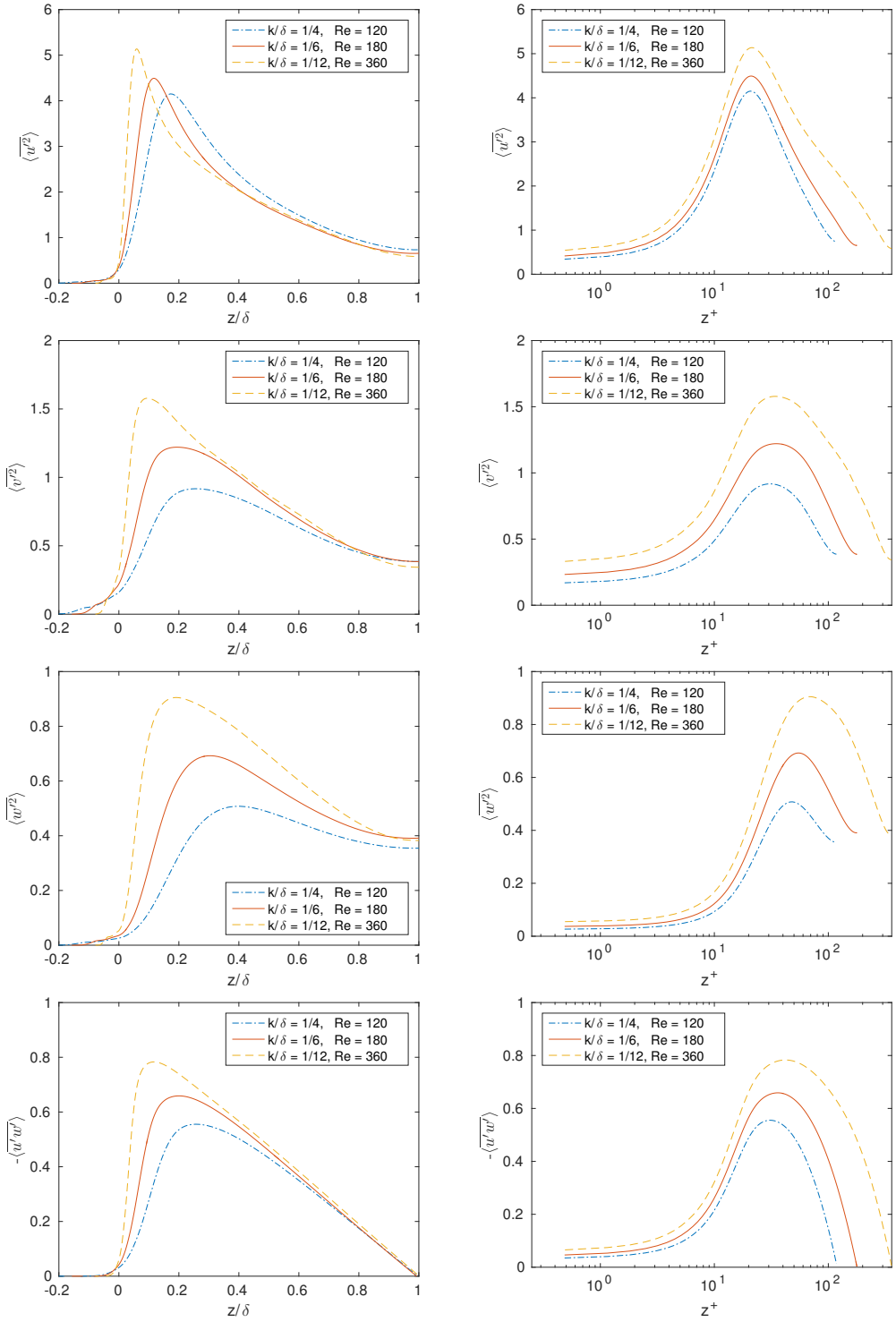

Figure 4.12: Reynolds stress profiles against z/δ (left) and z^+ (right). From top to bottom: $\langle\overline{u'^2}\rangle$, $\langle\overline{v'^2}\rangle$, $\langle\overline{w'^2}\rangle$, $-\langle\overline{u'w'}\rangle$.

collapse. As mentioned earlier, $Re_\tau = 120$ might show presence of low Reynolds number effects, which might manifest themselves in the turbulent statistics. It is interesting to note that all cases also have the same maximum and minimum roughness heights in wall-units; $h^+_{\text{max}} \approx 18.5$ and $h^+_{\text{min}} \approx -28.6$. With reference to these, streamwise fluctuation peaks for all k/δ are seen at $z^+ \approx 20$, which is very close to h^+_{max}, whereas peaks of spanwise and wall-normal fluctuations and shear stress are further away.

Thus, in general, the turbulent statistics show dependence on Re_τ and larger variation with the blockage ratio. This indicates greater sensitivity of higher order statistics. Although the present study does not investigate which parameter, Re_τ or k/δ, has a greater influence on the results, studying that aspect would provide further insight.

In summary, the studies conducted in this chapter have thus served to establish the validity of the DNS code for subsequent and more in-depth studies of the roughness considered in this work.

Chapter 5

Laminar to turbulent transition of flow over a rough surface sample

Before considering fully turbulent flow, this chapter gives a brief overview of the transition from laminar to turbulent flow over an irregular rough surface. Direct numerical simulations are performed for a range of relatively low Reynolds numbers and the overall flow behaviour is studied. A critical Reynolds number, $(Re_\tau)_{\text{crit}}$, at which the flow exhibits small and somewhat periodic fluctuations, and sustains an unsteady laminar behaviour, is identified. Beyond $(Re_\tau)_{\text{crit}}$, the flow is in a transitional phase after which it becomes turbulent. The Reynolds number at which transition is completed, $(Re_\tau)_{\text{trans}}$, is also identified. All studies in this chapter are performed on a modified version of the gritblasted sample (s8 from Table 3.1).

5.1 Brief description of previous studies

Most of the previous work investigating the influence of roughness on transition has been done on regular roughness elements. For example, Klebanoff and Tidstrom [1972] conducted measurements to study the mechanism of transition of a flat plate boundary layer due to the influence of an isolated 2D cylindrical rod. Emphasis was placed on the nature of disturbances in the region immediately downstream of the roughness (which was called the recovery zone), where the mean flow was distorted by the roughness. For a range of Reynolds numbers, based on measurements of intensity, disturbance spectra, growth and decay of velocity fluctuations and mean velocity distributions, it was observed that instabilities in the recovery zone triggered transition. It was concluded that disturbances introduced by the roughness were not significant enough to trigger transition but that roughness destabilized the flow in the recovery zone to existing disturbances, which was the main mechanism of transition.

Floryan [2006] studied three-dimensional instabilities of laminar flow over distributed roughness in the early stages of transition using linear stability theory. Global stability criteria for the critical Reynolds number and roughness amplitude were developed in the context of travelling-wave and vortex instabilities. Roughness was represented using Fourier

series and included wavy-walls (which required only a single Fourier mode and hence were the simplest geometry), rectangular grooves (which required many Fourier modes and hence were the most complex geometry) and triangular grooves (which required an intermediate number of Fourier modes and were intermediately complex). Truncation of the Fourier series representing the geometry also had an effect on transition. It was shown that, compared to the other geometries, rectangular grooves were the most effective in destabilising the flow. Overall, it was concluded that the flow remained laminar if the global stability criteria were satisfied.

Downs III et al. [2008] studied boundary layer transition induced by randomly distributed 3D roughness at different Reynolds numbers. The main goal was to study transition over realistic roughness and to provide data to develop a theoretical framework. Experiments were conducted for three Reynolds numbers, all of which exhibited transient growth of steady disturbances. Plots of mean and fluctuating velocity and disturbance-energy evolution in the streamwise direction showed that the lower two Reynolds numbers were laminar whereas the highest Reynolds number was turbulent. The highest Reynolds number case transitioned downstream of the roughness through a mechanism in which the unsteady-disturbance growth exceeded the stabilizing relaxation of the steady flow.

Orlandi [2011] conducted DNS over isolated as well as distributed roughness to demonstrate that the flow becomes turbulent only beyond a threshold value of rms wall-normal Reynolds stress computed at the crest of the roughness. This value was reached only when the roughness Reynolds number, $k^+ = ku_\tau/\nu$, was greater than 15. The threshold value was maintained for a variety of shape, density and distribution of regular wedge roughness. More specifically, the flow was laminar when the rms wall-normal Reynolds stress at the roughness crest was less than 0.3, transitional when it was between 0.6 and 1 and turbulent when it was close to 1. Thus an important conclusion was that the rms wall-normal Reynolds stress at the roughness crest was a fundamental quantity in establishing the status of wall-bounded flows.

Seddighi et al. [2015] conducted DNS in a transient channel flow with distributed pyramid roughness. An initially stationary turbulent flow was accelerated to a new flow rate and the transient flow behaviour after acceleration was studied. The equivalent sand-grain roughness heights for the initial and final flows were $k^+_{s,eq} = 14.5$ and 41.5 respectively. Through detailed studies of the near-wall flow physics of vortex formation, propagation and breakdown, wall shear stress and mean and fluctuating velocities, it was concluded that, despite the initial flow state being already turbulent, transient behaviour of the accelerated flow from the initial to final state resembled a roughness-induced laminar to turbulent transition.

The present study considers the transition of a realistic, irregular rough surface by conducting DNS over a range of Reynolds numbers. The main goal is to determine a critical Reynolds number, $(Re_\tau)_{\text{crit}}$, beyond which the flow over the surface shows small fluctuations which progressively increase with Reynolds number, and a transition Reynolds number, $(Re_\tau)_{\text{trans}}$, beyond which the flow is turbulent. Thus, subsequent simulations in

future chapters, which are all conducted at $Re_\tau > (Re_\tau)_{\text{trans}}$ can be confidently said to be in the fully turbulent regime. Care must be taken here to distinguish between the fully turbulent regime and the fully-rough regime, the latter being achieved only after the flow is fully turbulent and when $k^+_{s,eq} > 70$ (Nikuradse [1933]).

5.2 Rough surface sample and simulation parameters

Initially, the sample is selected using the section selection procedure described in Section 2.2.1. However, since this chapter is intended to provide only an overall picture of transition from laminar to turbulent flow, the size of the physical sample is halved with the procedure of Section 2.2.1 repeated within the larger sample. Consequently, this is the same sample as selected for the mesh dependence study in Section 4.2. This leads to quicker simulation turn around times. Figure 5.1 shows the full s8 surface sample and the position of the two sections on it. Figure 5.2 shows the final scaled sample in its unfiltered (left) and filtered (right) form.

Table 5.1 shows the topographical properties of the filtered surface sample. The properties are slightly different from the full s8 sample (Table 3.2). The maximum streamwise wavenumber, $k_c L_x$, is halved, which gives a roughness height, $S_{z,5\times5}/\delta = 0.1287$. The

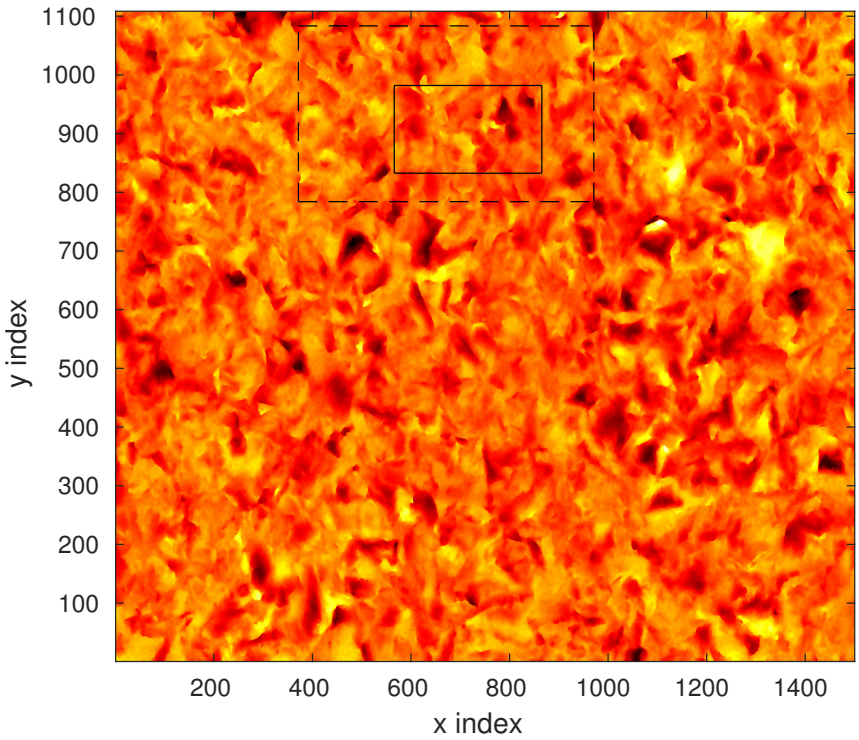

Figure 5.1: Section selection for the study on laminar to turbulent transition on the grit-blasted sample. The larger box (dashed lines) represents the initial section whereas the smaller box (solid lines) represents the final section used in the study. Surface coloured by absolute roughness height. Colourbar: black to yellow - lower to higher roughness heights. (Figure same as Figure 4.1.)

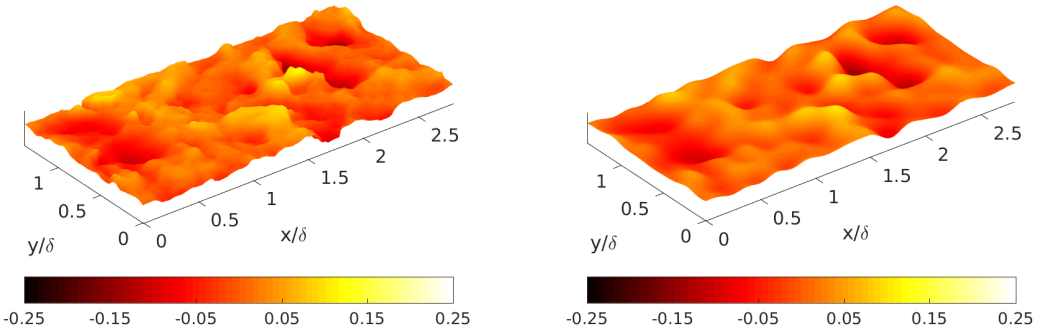

Figure 5.2: Final scaled sample before filtering (left) and after filtering (right). Plots coloured by scaled roughness height, k/δ. (Figure same as Figure 4.2.)

sample has a negative value of surface skewness, S_{sk}, which means it is valley-dominated (Flack and Schultz [2010]). Its surface texture aspect ratio, $S_{tr} = 0.4638$, is only slightly less than 0.5, which indicates that it is weakly anisotropic. Also, the flow texture ratio, $S_{tr}^{\text{flow}} = 1.8974$, is slightly greater than 1, which means roughness features have a weak spanwise directional preference.

Table 5.2 shows the computational domain extents and mesh parameters for all simulations in this study. The smaller domain size permits the use of a coarser mesh, as the priority here is to run a number of simulations to locate the critical Reynolds number, $(Re_\tau)_{\text{crit}}$. The grid spacings are normalised by Re_τ as it varies for each simulation. However, for all Re_τ simulated, both streamwise and spanwise grid spacings satisfy the meshing criteria from Section 2.3.2, i.e. $(\Delta x^+, \Delta y^+) < 5$. The wall-normal grid spacings vary depending on Re_τ as $0.3749 \leq \Delta z^+_{\text{min}} \leq 0.7916$ and $2.7878 \leq \Delta z^+_{\text{max}} \leq 5.8853$. The Reynolds number is increased from $Re_\tau = 45$ to $Re_\tau = 95$ in steps of 5.

Cases are presented that start from either a turbulent initial condition (obtained from a previously run turbulent simulation of the s8 sample), looking at laminarisation or reverse transition, or from a laminar initial condition (obtained from any of the laminar cases in the current study), looking at transition. The initial conditions also serve to check for hysteresis effects. Also, the relatively coarse mesh permits large simulation run times. Each case is

$k_c L_x$	$S_{z,5\times5}$	h_{max}	S_a	S_q	S_{sk}	S_{ku}	$S_{\text{z,max}}$
12	0.1287	0.1038	0.02839	0.03736	-0.6827	3.8018	0.2472
L_x^{cor}	L_y^{cor}	S_{sl}	S_{al}	S_{tr}	S_{tr}^{flow}	ES_x	ES_y
0.1833	0.3478	0.3795	0.1760	0.4638	1.8974	0.2564	0.2327

Table 5.1: Surface sample topographical properties. All length scales non-dimensionalised by δ.

L_x/δ	L_y/δ	L_z/δ	n_x	n_y	n_z	$\Delta x^+/Re_\tau$, $\Delta y^+/Re_\tau$	$\Delta z^+_{\text{min}}/Re_\tau$	$\Delta z^+_{\text{max}}/Re_\tau$
2.815	1.4075	2.2926	96	48	112	0.02933	0.008333	0.06195

Table 5.2: Domain extents and meshing parameters.

run up to a maximum of approximately 2000 time units, depending on the development of the flow.

5.3 Results - variation with Reynolds number

5.3.1 Time history of mean centreline velocity

Figure 5.3 shows time histories of the mean centreline velocity, $\langle U_c^+ \rangle$, over the range of Re_τ, except $Re_\tau = 50$, 60 and 70. All cases up to $Re_\tau = 90$ are provided with a turbulent initial condition obtained from a previous simulation of the full s8 sample at $Re_\tau = 180$ and interpolated onto the current mesh. If $\langle U_c^+ \rangle$ remains constant with time beyond a certain time, t, then it indicates a laminar flow solution has been reached. The lower values of $Re_\tau = 45$ and 55 show a monotonic rise in $\langle U_c^+ \rangle$ and attain a constant laminar value for large t. The intermediate values of $Re_\tau = 65$ and 75 show fluctuations in $\langle U_c^+ \rangle$ for small values of t but eventually attain a constant $\langle U_c^+ \rangle$ for large t. Larger values of $Re_\tau = 80$ and 85 show large fluctuations in $\langle U_c^+ \rangle$ for considerably larger time durations than $Re_\tau = 65$ and 75, but still achieve a constant $\langle U_c^+ \rangle$ beyond $t \approx 500$ and $t \approx 1200$ respectively. Hence, all cases up to $Re_\tau = 85$ undergo laminarisation. Table 5.3 shows the final laminar solution centreline velocities for all Re_τ except 90 and 95. These final values vary from $\langle U_c^+ \rangle \approx$ 21 to 26. Hence, if the final $\langle U_c^+ \rangle$ value for a given case lies in or close to this range, the simulation has reached a laminar solution. Although Table 5.3 does not show a clear trend of the final $\langle U_c^+ \rangle$ with Re_τ, the trend seen from $Re_\tau = 45$ to 85 is that the time duration of $\langle U_c^+ \rangle$ fluctuations increases with Reynolds number, but all cases ultimately laminarise, with constant $\langle U_c^+ \rangle$. For $Re_\tau = 90$, the initial behaviour of $\langle U_c^+ \rangle$ is similar to $Re_\tau = 85$. However, beyond $t \approx 900$, $\langle U_c^+ \rangle$ fluctuates about a mean value of approximately 26.8, and has a very similar rms value, which means the fluctuations are small. If the final $\langle U_c^+ \rangle$ is not constant but shows small fluctuations about a mean value, the solution is denoted as 'unsteady laminar'. To check for hysteresis effects, $Re_\tau = 90$ was restarted from $t = 0$, using its final solution as the initial condition, but remained unsteady laminar. The laminar initial condition for subsequent simulations (where required) was obtained from the final solution of $Re_\tau = 90$ above. $Re_\tau = 95$ remained turbulent when provided with a turbulent initial condition. In Figure 5.3, however, $Re_\tau = 95$ is provided with a laminar initial condition but becomes turbulent almost instantly. $\langle U_c^+ \rangle$ never achieves a constant value and fluctuates about a mean value of approximately 13.8, which is much less than what is observed for a laminar solution. Also, the above cases show no evidence of hysteresis.

To confirm the exact value of the critical Reynolds number, simulations closer to $Re_\tau =$ 90 but in smaller Reynolds number steps, including $Re_\tau = 89$, 91 and 92, are conducted. These cases are provided with a laminar initial condition to check whether the flow becomes

Re_τ	45	50	55	60	65	70	75	80	85
final $\langle U_c^+ \rangle$	21.15	23.17	24.74	25.48	24.86	23.80	23.37	23.92	25.26

Table 5.3: Final mean centreline velocities, $\langle U_c^+ \rangle$, for the laminar solutions.

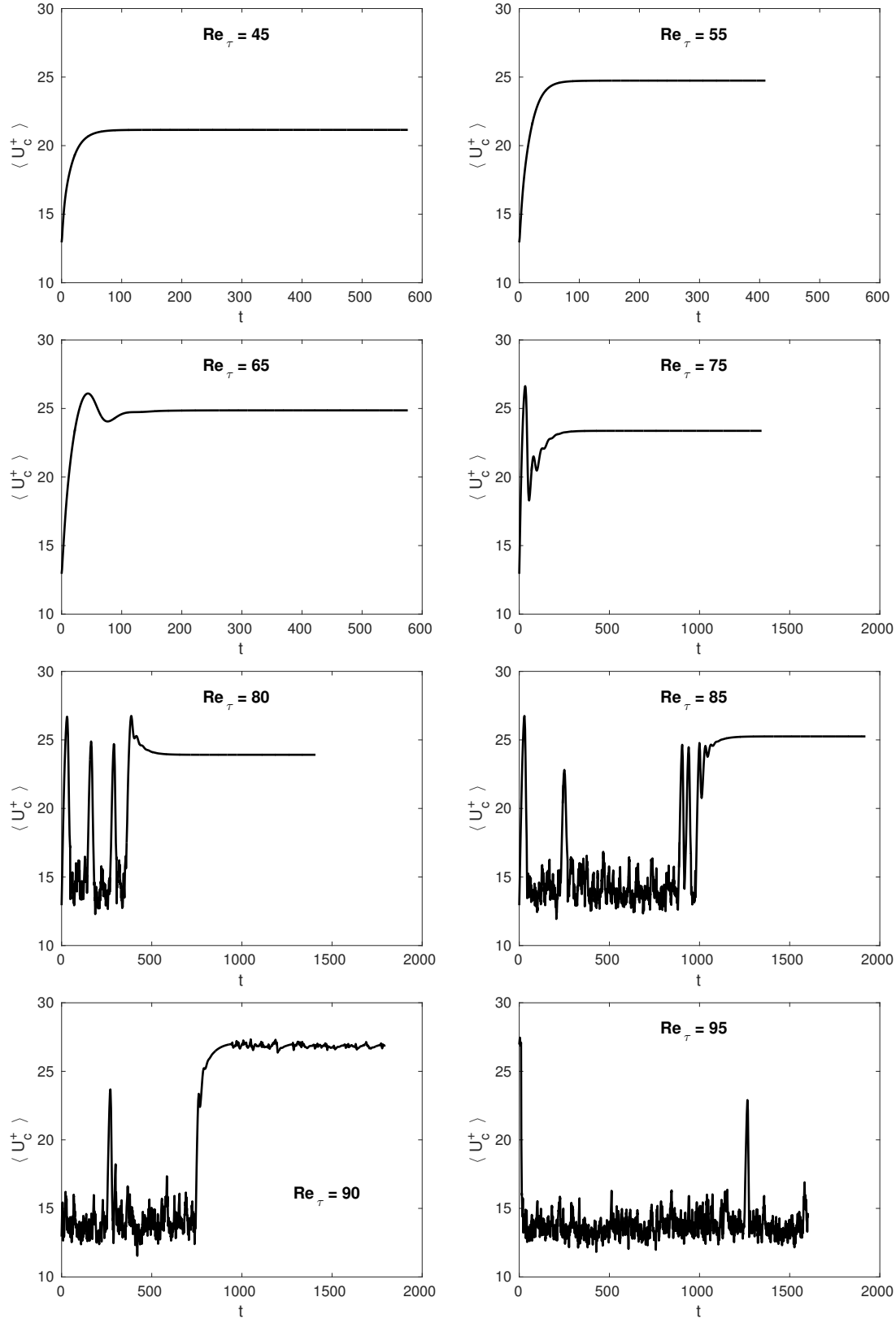

Figure 5.3: Time histories of mean centreline velocity, $\langle U_c^+ \rangle$, for the range of Re_τ.

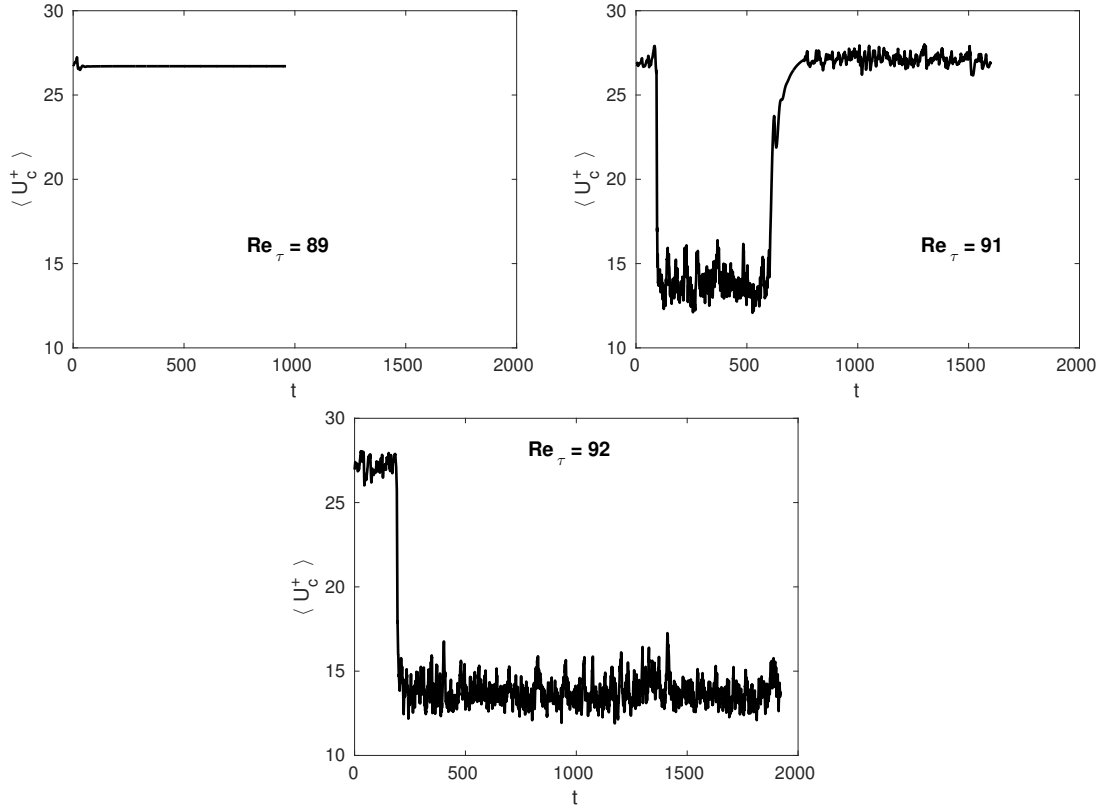

Figure 5.4: Time histories of mean centreline velocity, $\langle U_c^+ \rangle$, for $Re_\tau = 89$, 91 and 92.

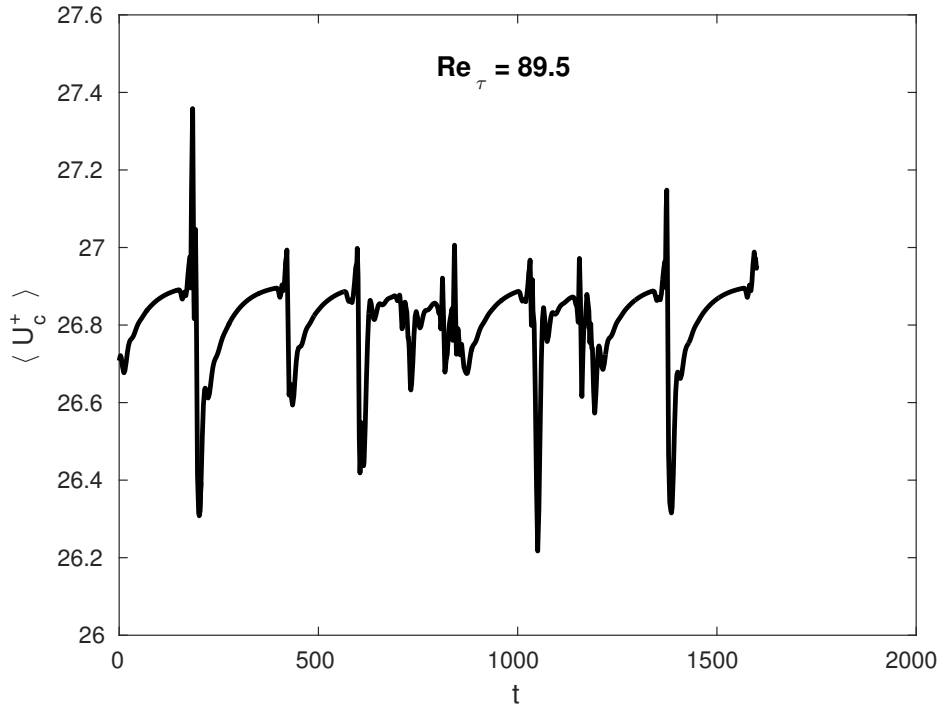

Figure 5.5: Time history of mean centreline velocity, $\langle U_c^+ \rangle$, for $Re_\tau = 89.5$ showing quasi-periodic behaviour.

turbulent and also to check for hysteresis effects. Time histories of $\langle U_c^+ \rangle$ for these Reynolds numbers are shown in Figure 5.4. It is clearly seen that $Re_\tau = 89$ remains laminar whereas $Re_\tau = 92$ becomes turbulent beyond $t \approx 200$. $Re_\tau = 91$, however, becomes turbulent (around $t \approx 100$) and then relaminarises to attain an unsteady laminar behaviour beyond $t \approx 750$. $\langle U_c^+ \rangle$ fluctuates about an approximate mean value of 27.1, which is close to $Re_\tau = 90$, but the fluctuations appear larger. This can be quantified using the standard deviation, σ, of the fluctuations in the unsteady laminar part, which gives $\sigma = 0.13$ for $Re_\tau = 90$ and $\sigma = 0.31$ for $Re_\tau = 91$. Hence the unsteadiness has increased from $Re_\tau = 90$ to 91, which indicates that the flow is at the start of transition. The above observations also indicate that $(Re_\tau)_{\text{trans}}$ is between 91 and 92.

Since $Re_\tau = 89$ is laminar and $Re_\tau = 90$ and 91 are both unsteady laminar, a final simulation was carried out at $Re_\tau = 89.5$. The time history of $\langle U_c^+ \rangle$ is shown in Figure 5.5. This case is also provided with a laminar initial condition and attains an unsteady laminar behaviour. Fluctuations are observed about a mean value of $\langle U_c^+ \rangle \approx 26.8$ with a standard deviation of 0.11, which is less than at $Re_\tau = 90$. The interesting feature of this case is that $\langle U_c^+ \rangle$ fluctuations show a somewhat repeating behaviour with time. From Figure 5.5, the behaviour is described by a gradual rise of $\langle U_c^+ \rangle$ for approximately 175 time units, followed by a sharp rise and fall over approximately 25 time units. This is possibly due to an emerging periodic instability at this Reynolds number. The time period of the instability is approximately 200 time units. The quasi-periodic behaviour and low standard deviation indicates that $(Re_\tau)_{\text{crit}}$ is between 89.0 and 89.5. $Re_\tau = 89$, 89.5, 91 and 92 also show no evidence of hysteresis.

5.3.2 Root-mean-square (rms) fluctuations

For the higher Reynolds numbers, $Re_\tau = 89.5$, 90, 91, 92 and 95, Figure 5.6 shows profiles of rms streamwise, $\langle u'_{\text{rms}} \rangle$, spanwise, $\langle v'_{\text{rms}} \rangle$, and wall-normal, $\langle w'_{\text{rms}} \rangle$, Reynolds stresses, against wall-normal coordinates in wall-units, z^+, on semilogarithmic axes. The statistics have been time-averaged and spatially averaged in the streamwise and spanwise directions. For the lower Reynolds numbers, up to $Re_\tau = 89$, rms fluctuations are negligible (order of 10^{-6} or less). Hence these cases can be regarded as laminar. At $Re_\tau = 89.5$, small rms fluctuations in all three components begin to appear close to the channel centre. Their magnitude progressively increases for $Re_\tau = 90$ and 91, with peaks still close to the channel centre. The appearance of early fluctuations near the channel centre is an indication of a large scale instability initiating transition. At $Re_\tau = 92$ and 95, rms fluctuations for all three components rise significantly, with peaks now closer to the rough wall. Through DNS studies on wedge roughness, Orlandi [2011] mentioned that a sudden rise in the magnitude of wall-normal rms fluctuations, $\langle w'_{\text{rms}} \rangle$, is an indication of the flow having transitioned to turbulence. This is consistent with the previous observations that $Re_\tau = 92$ and 95 are turbulent whereas $Re_\tau = 89.5$, 90 and 91 are in a transition phase. Figure 5.6 also shows that $\langle u'_{\text{rms}} \rangle$ has the highest magnitude.

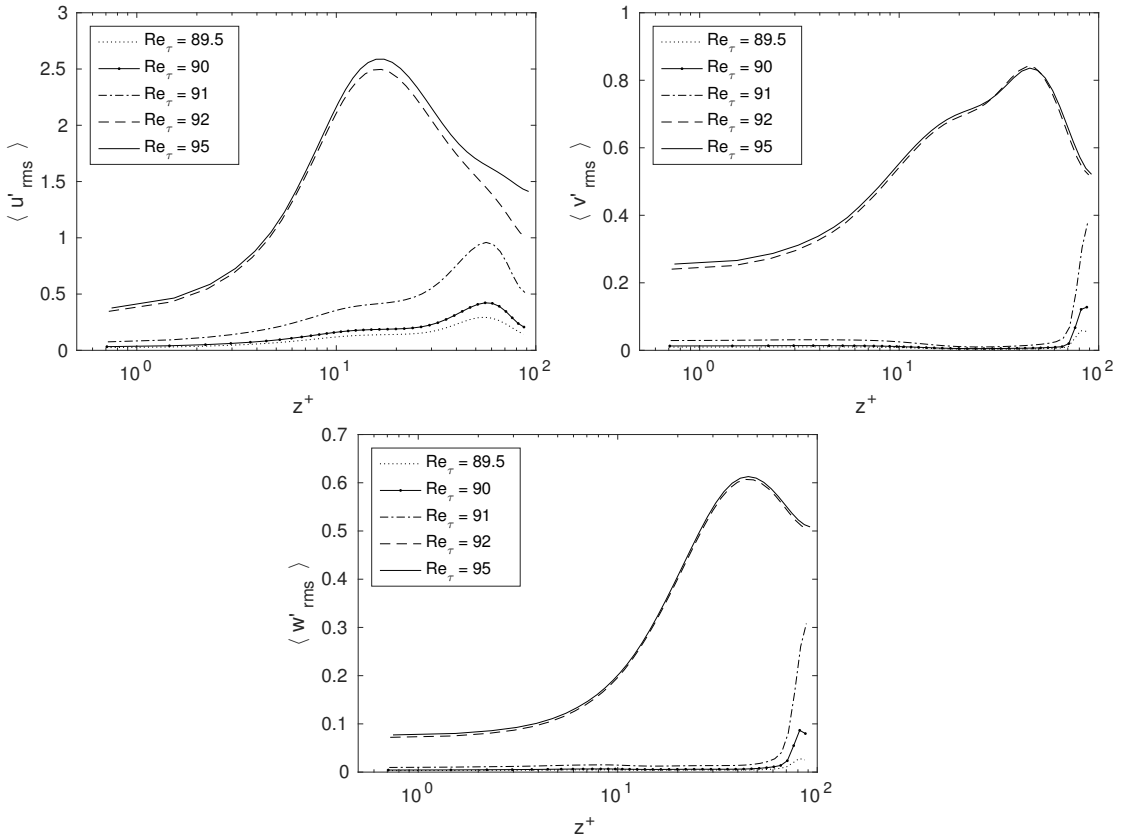

Figure 5.6: Profiles of rms streamwise, $\langle u'_{\mathrm{rms}} \rangle$, spanwise, $\langle v'_{\mathrm{rms}} \rangle$, and wall-normal, $\langle w'_{\mathrm{rms}} \rangle$, Reynolds stresses, for the transitional ($Re_\tau = 89.5, 90, 91$) and turbulent ($Re_\tau = 92, 95$) cases, against wall-normal coordinates in wall-units, $z^+ = zu_\tau/\nu$.

Orlandi [2011] also characterised the effects of roughness peaks by studying the value of $\langle w'_{\mathrm{rms}} \rangle$ at the crests of the wedges as a function of Reynolds number. Since the current study considers irregular roughness and there is no single roughness crest for all elements, the above-mentioned quantity is computed at the maximum roughness height, $h_{\mathrm{max}} = 0.1038$ (from Table 5.1) and is denoted as $\langle w'_{\mathrm{rms}} \rangle_{\mathrm{hmax}}$. A plot of $\langle w'_{\mathrm{rms}} \rangle_{\mathrm{hmax}}$ against Re_τ is shown

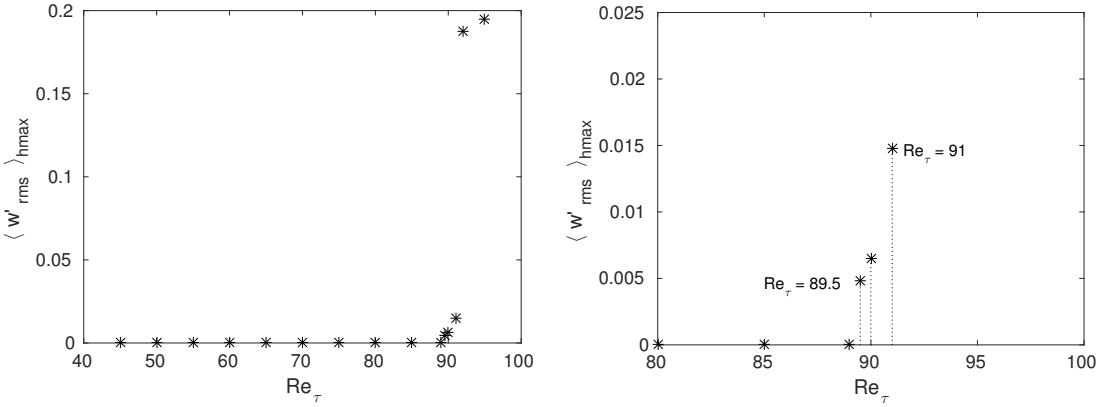

Figure 5.7: Behaviour of rms wall-normal fluctuations at h_{max}, $\langle w'_{\mathrm{rms}} \rangle_{\mathrm{hmax}}$, for all Reynolds numbers (left) and close-up of the transitional region (right).

Re_τ	$\langle w'_{\mathrm{rms}} \rangle_{\mathrm{hmax}}$	k^+
45	0	5.78
50	0	6.43
55	0	7.08
60	0	7.72
65	0	8.37
70	0	9.01
75	0	9.65
80	0	10.30
85	0	10.94
89	0	11.45
89.5	0.0048	11.52
90	0.0065	11.58
91	0.0148	11.71
92	0.1876	11.84
95	0.1946	12.23

Table 5.4: Values of rms wall-normal fluctuations at the maximum roughness height $\langle w'_{\mathrm{rms}} \rangle_{\mathrm{hmax}}$ and corresponding Re_τ along with k^+. $\langle w'_{\mathrm{rms}} \rangle_{\mathrm{hmax}}$ values up to $Re_\tau = 89$ are of the order of 10^{-6} or less and hence are approximated to 0. The horizontal line below $Re_\tau = 89$ splits the laminar and non-laminar (transitional or turbulent) regimes.

in Figure 5.7 (left), with corresponding values in Table 5.4. Also, Figure 5.7 (right) shows a close-up view of the transition region, which includes $Re_\tau = 89.5$, 90 and 91, and shows the trend in the departure of $\langle w'_{\mathrm{rms}} \rangle_{\mathrm{hmax}}$ from the laminar values. A gradual rise is observed from $Re_\tau = 89$ ($\langle w'_{\mathrm{rms}} \rangle_{\mathrm{hmax}} \approx 10^{-6}$) to $Re_\tau = 91$, after which $\langle w'_{\mathrm{rms}} \rangle_{\mathrm{hmax}}$ shows a steep rise from $Re_\tau = 91$ to 92. A sharp rise in $\langle w'_{\mathrm{rms}} \rangle_{\mathrm{hmax}}$, according to Orlandi [2011], is an indication of transition to turbulence. The value of turbulent $\langle w'_{\mathrm{rms}} \rangle_{\mathrm{hmax}} \approx 0.2$ is of the same order of magnitude as Orlandi [2011], however its value would depend on the type of roughness. Table 5.4 also shows corresponding values of k^+. The flow is laminar for $k^+ \lessapprox 11.45$ ($Re_\tau \leq 89$). This dividing k^+ value is only slightly different from Orlandi [2011], who showed for wedge roughness that the flow remains laminar for $k^+ < 14$ and becomes turbulent for $14 < k^+ < 40$.

From the above analyses, it is clear that $Re_\tau = 92$ and 95 are turbulent whereas $Re_\tau = 89.5$, 90 and 91 are in a state of transition and are classified as unsteady laminar. Fluctuations in the rms Reynolds stresses first begin to appear at $Re_\tau = 89.5$ and progressively increase with Re_τ. Thus, it can be confirmed that $89 < (Re_\tau)_{\mathrm{crit}} \leq 89.5$ and $91 < (Re_\tau)_{\mathrm{trans}} \leq 92$.

5.3.3 Flow visualisations

Visualisations of the flow field close to the rough wall explain the influence of roughness topography on the small scale fluctuations. Figure 5.8 shows slices of wall-normal Reynolds stress, $\overline{w'^2}$, at $z/\delta = 0.1$, for the transitional and turbulent cases. Also shown is $Re_\tau = 89$, which is laminar, to confirm that it exhibits fluctuations of negligible magnitude. For this

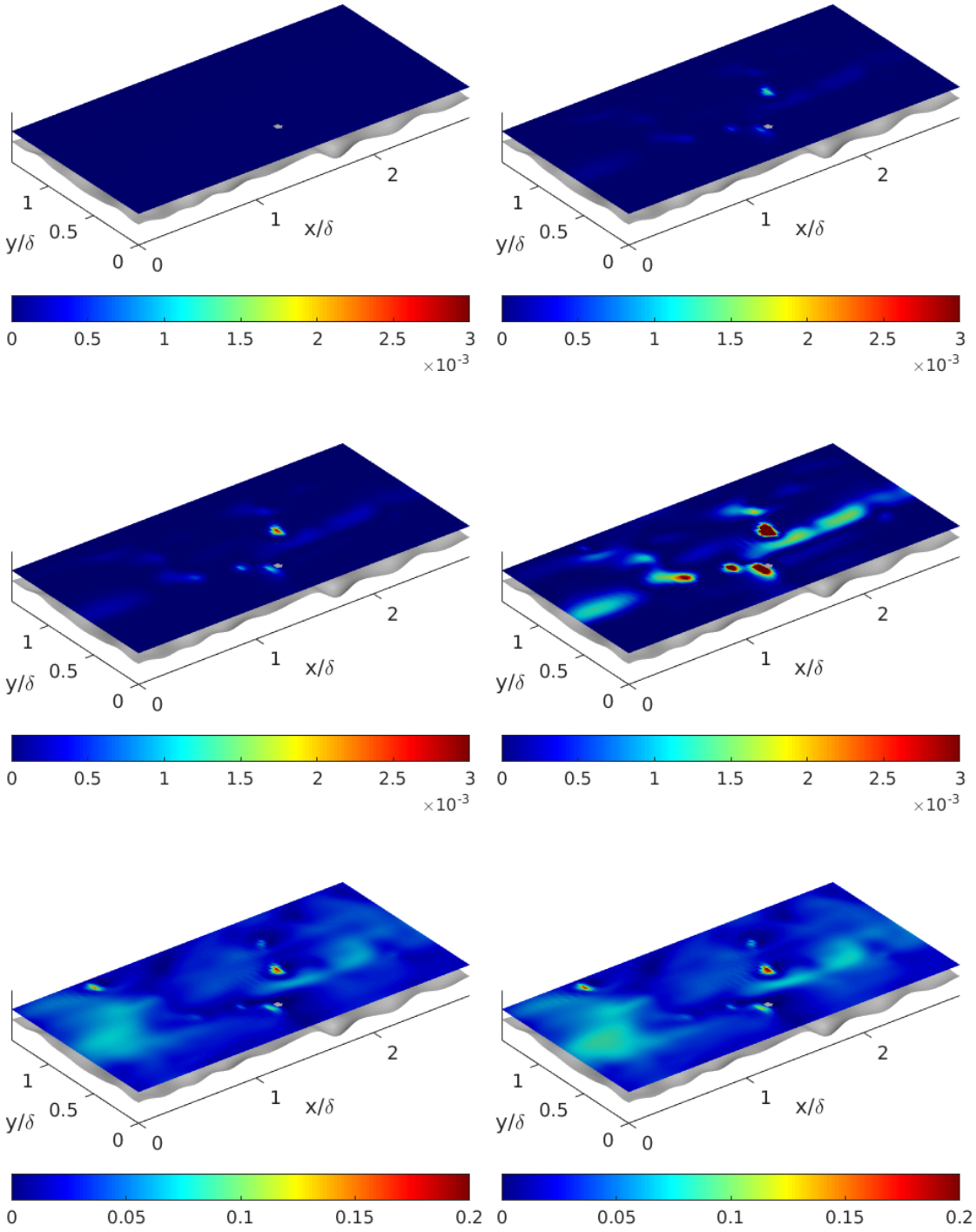

Figure 5.8: Slices of wall-normal Reynolds stresses, $\overline{w'^2}$, for the transitional and turbulent cases at $z/\delta = 0.1$. From left to right, then top to bottom, $Re_\tau = 89$, 89.5, $Re_\tau = 90$, 91, $Re_\tau = 92$, 95. Grey regions indicate the rough wall.

analysis, fluctuations are considered significant if their magnitude is greater than 10^{-3} and the colourbars in the figure are adjusted accordingly depending on the Reynolds number. Small scale wall-normal fluctuations first begin to appear close to the rough wall at $Re_\tau = 89.5$. Magnitude of $\overline{w'^2}$ then continues to increase with Re_τ until the flow reaches its turbulent state at $Re_\tau = 92$. Both the turbulent cases, $Re_\tau = 92$ and 95, have very similar magnitudes of wall-normal fluctuations.

The above slices enable a brief analysis of how the wall-normal fluctuations are affected by the roughness topography. Figure 5.9 (top) shows the $Re_\tau = 90$ case from Figure 5.8 along with a surface plot of the rough wall (Figure 5.9 bottom) indicating corresponding roughness features that are responsible for triggering early small scale fluctuations. Regions

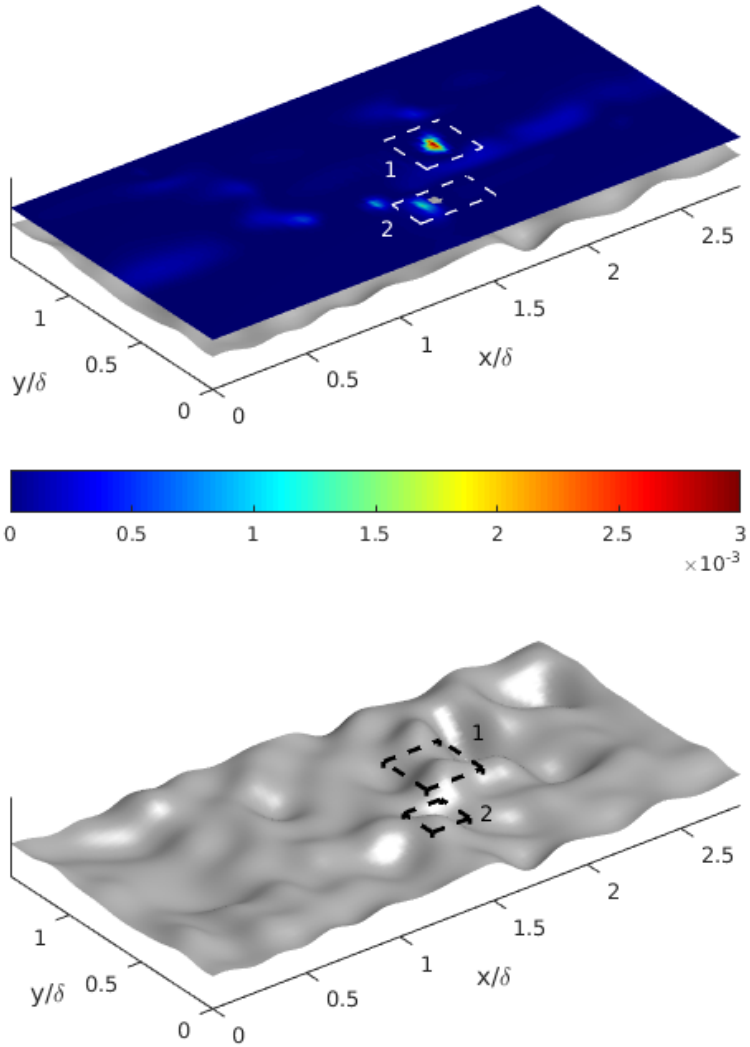

Figure 5.9: Slice of wall-normal Reynolds stress, $\overline{w'^2}$, for $Re_\tau = 90$ (top) at $z/\delta = 0.1$ indicating regions of early fluctuations (within white dashed lines) and the rough wall (bottom) indicating corresponding features (within black dashed lines) triggering those fluctuations. Numbers indicate the order in which fluctuations are observed (top plot) and corresponding peaks triggering them (bottom plot).

showing fluctuations are labelled in the order in which they first appear and are indicated within dashed lines (top plot), along with corresponding roughness features triggering them (bottom plot). It is understandable that wall-normal fluctuations are caused by roughness peaks, which protrude into the flow. Although the earliest fluctuations are observed at $Re_\tau = 89.5$, generated by peak 1 in Figure 5.9 (bottom), peak 2 triggers further fluctuations at $Re_\tau = 90$. It is interesting to note that peak 2 represents the maximum roughness height of the surface ($h_{\max}$ from Table 5.1) but does not trigger the earliest wall-normal fluctuations. Thus, generation of these early small scale fluctuations, and ultimately, transition to turbulence, depends significantly on the surface topography. As the Reynolds number increases, the flow reaches its turbulent state, which is then sustained due to continuous

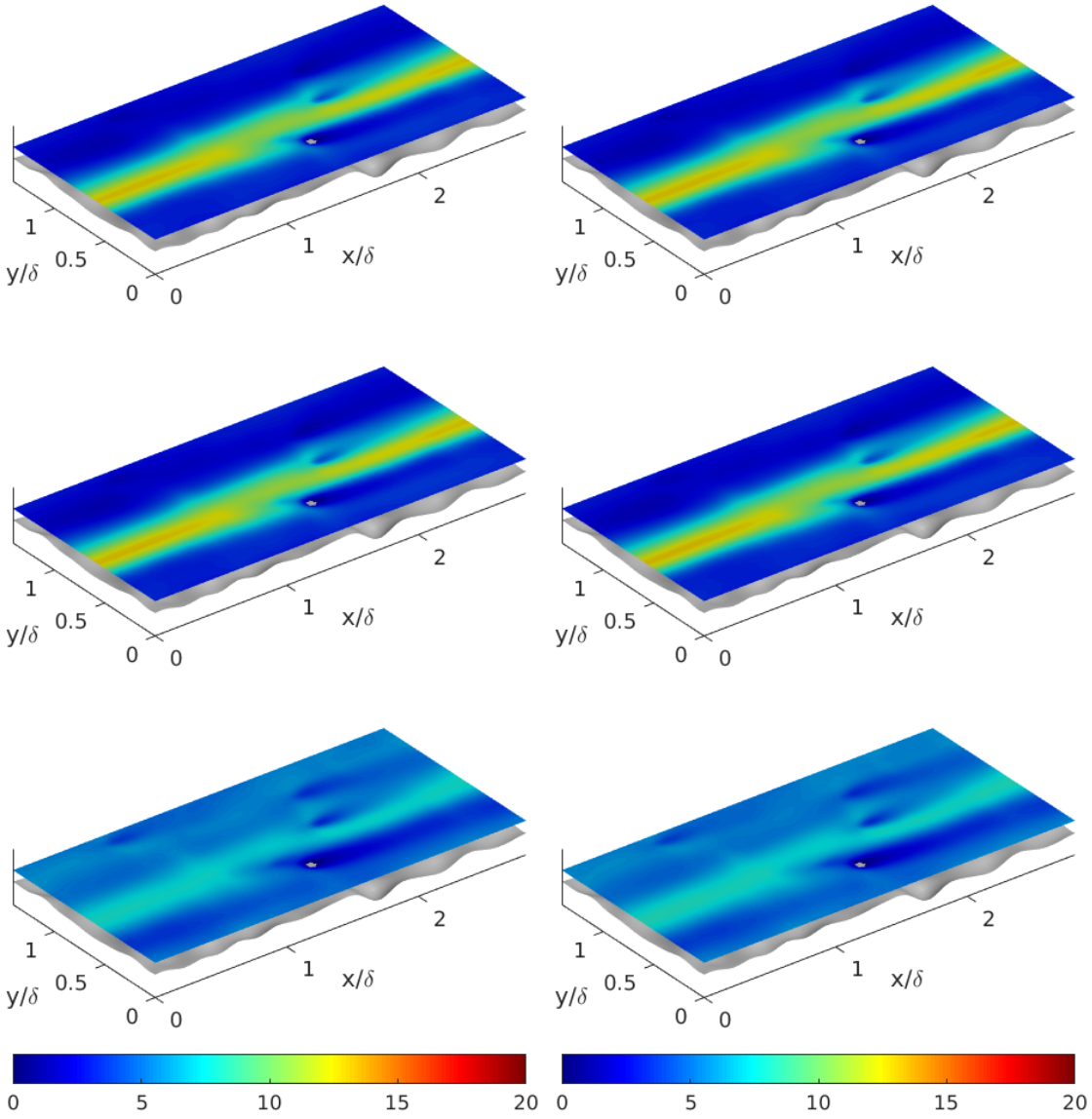

Figure 5.10: Slices of time-averaged streamwise velocity, $\overline{u}$, for the transitional and turbulent cases at $z/\delta = 0.1$. From left to right, then top to bottom, $Re_\tau = 89$, 89.5, $Re_\tau = 90$, 91, $Re_\tau = 92$, 95. Grey regions indicate the rough wall.

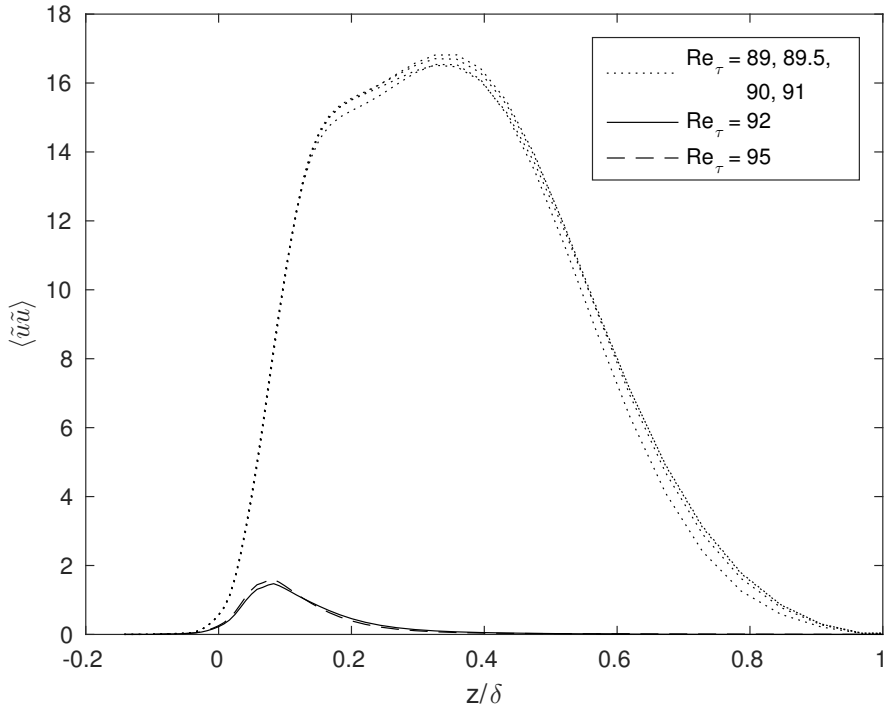

Figure 5.11: Profiles of streamwise dispersive stress, $\langle\tilde{u}\tilde{u}\rangle$, for $Re_\tau = 89$ (laminar), $Re_\tau = 89.5$, 90, 91 (transitional) and $Re_\tau = 92$, 95 (turbulent) cases. The laminar and transitional cases have been displayed using the same line style.

generation of fluctuations by the roughness peaks.

Figure 5.10 shows slices of time-averaged streamwise velocity, $\overline{u}$, at $z/\delta = 0.1$, for $Re_\tau = 89$ (laminar), $Re_\tau = 89.5$, 90 and 91 (transitional) and $Re_\tau = 92$ and 95 (turbulent). The laminar and transitional cases show comparatively higher $\overline{u}$ values than the turbulent cases. In order to sustain turbulence at $Re_\tau = 92$ and 95, the fluctuations extract energy from the mean flow, leading to a decrease in mean streamwise velocity compared to the laminar and transitional cases. This relatively high streamwise velocity also leads to large streamwise dispersive stress in the laminar and transitional cases, as seen from the streamwise dispersive stress profiles, $\langle\tilde{u}\tilde{u}\rangle$, shown in Figure 5.11. Profiles for the laminar and transitional cases are displayed using the same line style because they have very similar magnitudes. The turbulent profiles are almost an order of magnitude less than the laminar and transitional profiles.

It can thus be concluded that generation of early small scale fluctuations in the transition process is influenced by the roughness topography and certain roughness peaks trigger disturbances earlier than others. A large difference between the turbulent and non-turbulent (laminar or transitional) streamwise dispersive stress is also observed. Due to relatively large streamwise velocities, the laminar and transitional cases have much higher streamwise dispersive stress compared to the turbulent cases.

5.4 Summary

Overall, it can be summarised that all Reynolds numbers up to $Re_\tau = 89$ show laminar behaviour. The earliest fluctuations, generated by a large scale instability close to the channel centre, are seen at $Re_\tau = 89.5$, along with quasi-periodic behaviour of the mean centreline velocity, $\langle U_c^+ \rangle$, with time. Thus $89 < (Re_\tau)_{\text{crit}} \leq 89.5$. Beyond $Re_\tau = 89.5$ and up to $Re_\tau = 91$, there is an increase in the unsteadiness and the flow is in a state of transition. The flow is turbulent for $Re_\tau \geq 92$. Based on observations for $Re_\tau = 91$ and 92, it is confirmed that $91 < (Re_\tau)_{\text{trans}} \leq 92$. Based on a linear stability analysis, Orszag [1971] proved that for plane Poiseuille flow, the transition Reynolds number based on the centreline velocity is $(Re_{\text{cl}})_{\text{trans}} = 5772$, which gives $(Re_\tau)_{\text{trans}} = 107.4$. The transition Reynolds number for the given rough surface sample is lower than this value because the roughness is more effective at generating small scale disturbances, which leads to earlier transition. The study also shows that there is no evidence of hysteresis effects.

It is essential to note that the results and corresponding observations in this chapter are valid for the particular sample (Figure 5.2) at a specific maximum streamwise Fourier wavenumber, $k_c L_x$ (Table 5.1), and may change for other samples and values of $k_c L_x$. The results may also differ if a constant mean streamwise mass flow rate is used to drive the flow instead of a constant mean streamwise pressure gradient (Section 2.4.2).

All simulations in subsequent chapters are conducted at $Re_\tau > (Re_\tau)_{\text{trans}}$ and are hence classified as fully turbulent.

Chapter 6

Results - studies at $Re_\tau = 180$

One of the primary goals of this work is to prepare a database of industrially relevant rough surfaces and methodically relate their surface topographical properties to ΔU^+. This chapter describes the physical results for all seventeen samples in the database at $Re_\tau = 180$ and $\delta/k = 6$, and is followed by a mathematical treatment of surface properties in Chapter 7. In general, the influence of roughness topography on the results is significant.

Statistics of the time-averaged mean and turbulent flow quantities will be presented along with planar visualisations of the flow. Smooth-wall results will be included to serve as a comparison. Table 6.1 shows simulation parameters, which include computational domain and mesh sizes in the streamwise, spanwise and wall-normal directions, mesh spacings and the values of ΔU^+ and peak profile turbulent kinetic energy (TKE).

sample	L_x/δ	L_y/δ	L_z/δ	n_x	n_y	n_z	Δx^+, Δy^+	$\Delta z^+_{\max}$	ΔU^+	peak TKE
s1	13.00	6.50	2.236	480	240	272	4.8750	4.74	3.39	3.05
s2	9.80	4.90	2.290	384	192	288	4.5938	4.16	2.72	3.10
s3	9.34	4.67	2.287	384	192	288	4.3781	3.65	3.94	3.04
s4	4.92	2.46	2.238	384	192	256	2.3063	4.14	4.95	2.97
s5	10.70	5.35	2.298	448	224	288	4.3007	3.62	4.17	3.11
s6	11.27	5.64	2.292	448	224	288	4.5281	3.66	1.28	3.47
s7	5.25	2.63	2.232	384	192	256	2.4609	4.13	5.02	2.88
s8	5.63	2.82	2.324	320	160	288	3.1669	3.72	4.36	3.06
s9	23.20	11.60	2.292	768	384	256	5.4375	5.06	2.63	3.29
s10	13.48	6.74	2.342	512	256	288	4.7391	4.07	2.84	3.36
s11	15.88	7.94	2.387	576	288	288	4.9631	4.86	2.57	3.95
s12	17.50	8.75	2.308	640	320	256	4.9219	5.02	1.71	3.45
s13	13.30	6.65	2.388	512	256	288	4.6758	4.82	2.82	3.27
s14	11.00	5.50	2.300	512	256	320	3.8672	3.48	3.42	3.00
s15	12.48	6.24	2.248	512	256	288	4.3875	3.58	2.67	3.26
s16	12.65	6.32	2.300	512	256	288	4.4459	3.71	2.77	3.22
s17	7.65	3.83	2.282	320	160	256	4.3054	4.40	4.36	3.33

Table 6.1: Simulation parameters at $Re_\tau = 180$. n_x, n_y and n_z are the number of grid cells in the streamwise, spanwise and wall-normal directions respectively. Also shown are the values of ΔU^+ and peak profile TKE. $\delta/k = 6$ for all samples. Surface plots of all samples shown in Figures 3.4 and 3.5.

6.1 Influence of roughness topography on the mean flow statistics

Figure 6.1 shows time-averaged mean streamwise velocity profiles against wall-normal distance in wall-units, z^+, on semilogarithmic axes for all 17 samples. Smooth-wall profiles at $Re_\tau = 180$ have also been shown for comparison. Due to the large number of samples, results are spread out over 4 figures for clarity. The time-averaged flow field, $\overline{u}$, is spatially averaged in the x and y directions to obtain the profiles, U^+. Grid points in the fluid only are considered during spatial averaging. A clear roughness effect is seen for all samples, from the downward shift in the mean velocity profiles. ΔU^+ values for all samples are given in Table 6.1. There is a wide range, from $\Delta U^+ = 1.28$ (s6 sample) to $\Delta U^+ = 5.02$ (s7 sample), despite all samples being scaled to the same roughness height. This is a clear indication that the roughness function depends not only on the roughness height for a given sample but also on its detailed roughness topography. The s6 (filed_2) sample has the smallest roughness function value at $\Delta U^+ = 1.28$, probably because the roughness features of this sample are strongly aligned in the streamwise direction (refer Figure 3.4 (f)) and this anisotropic topography gives less resistance to the flow. This leads to a comparatively lower increase in surface friction and hence a smaller value of ΔU^+ compared to other samples. The s7 (graphite) and s4 (concrete) samples show some of the largest values of ΔU^+, at

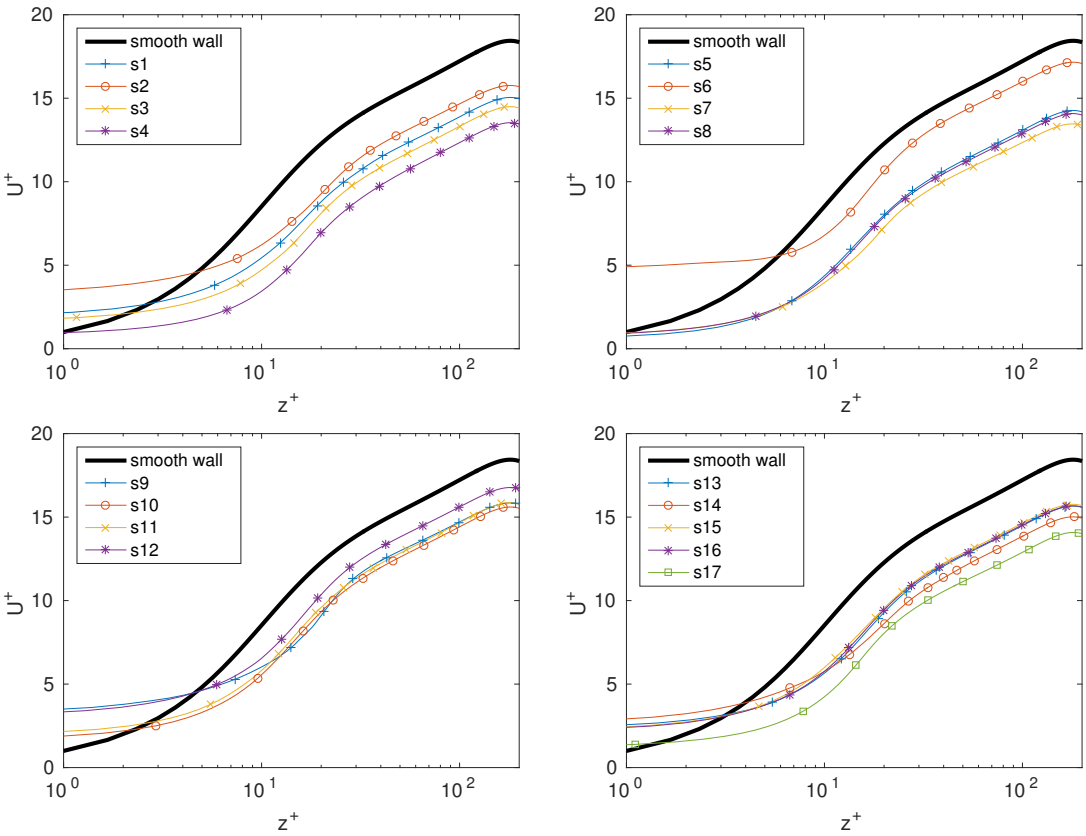

Figure 6.1: Mean streamwise velocity profiles in wall-units, U^+, for the 17 rough surface samples. $z^+ = zu_\tau/\nu$ is the wall-normal distance in wall-units.

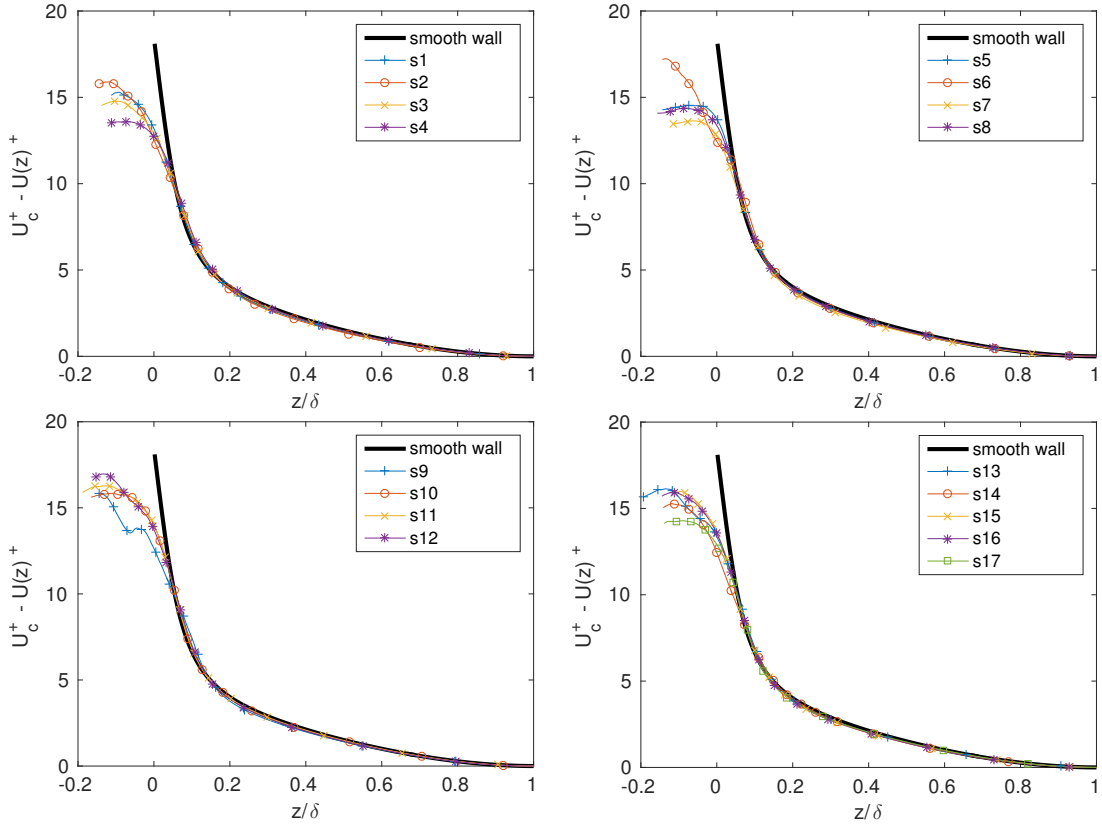

Figure 6.2: Mean streamwise velocity defect profiles for the 17 rough surface samples. U_c^+ is the mean streamwise centreline velocity in wall-units, $U(z)^+ = u(z)/u_\tau = U^+$ are the mean streamwise velocity profile values and z/δ is the wall-normal distance.

5.02 and 4.95 respectively. This closeness in ΔU^+ values between the two is possibly due to similar values of L_x^{cor}, S_f/S and Λ_s (Table 3.2). The ship-propeller samples, s10 and s11 also exhibit similar values of ΔU^+, despite their surface properties showing numerous differences. Three out of the five spark-eroded samples, s13, s15 and s16 also exhibit similar values of ΔU^+, possibly due to similar S_q and S_f/S.

Figure 6.2 shows time-averaged mean streamwise velocity defect profiles against wall-normal distance, z/δ for all samples. The behaviour of the velocity defect profiles also depends strongly on the topography of a given sample. Profiles for most samples decrease monotonically away from the rough walls. Some samples, such as s9 (ground) and s13 (spark-eroded_1), however, show a clear change in the direction of the profile gradient very close to their rough walls ($z/\delta < 0$). Close to the rough walls (roughly $z/\delta \leq 0.1$), all profiles show differences from each other and from the smooth-wall data. For $z/\delta > 0.1$, all profiles show good collapse with the smooth-wall data. This indicates that the outer layer similarity hypothesis of Townsend [1976] is satisfied in terms of the mean flow.

6.2 Influence of roughness topography on reversed flow

In the context of the mean flow, it is of interest to study reversed flow behaviour close to the rough walls. As a measure of reversed flow, the volume fraction of the negative time-averaged streamwise velocity, $P(\overline{u} < 0)$, is computed for each wall-normal location. Starting from the first wall-normal coordinate for each sample, the number of solid and fluid points (based on the value of ψ as mentioned in Section 2.4.1) at each wall-normal location are computed. At a given wall-normal location, if n_f denotes the total number of fluid points and $n_{f,(\overline{u}<0)}$ denotes the number of fluid points with $\overline{u} < 0$ then the volume fraction of negative time-averaged streamwise velocity is given as

$$P(\overline{u} < 0) = \frac{n_{f,(\overline{u}<0)}}{n_f}.$$

$P(\overline{u} < 0)$ is computed in this manner for all wall-normal locations.

Figure 6.3 shows the wall-normal variation of $P(\overline{u} < 0)$ for all samples. It is quite clear that the presence of reversed flow regions is strongly dependent on surface topography. For most samples, the volume fraction of reversed flow for $z/\delta \leq -0.1$, which is deep within the roughness valleys, is high (almost unity), indicating that areas of recirculating fluid dominate these regions. As wall-normal distance increases, the effect of roughness features

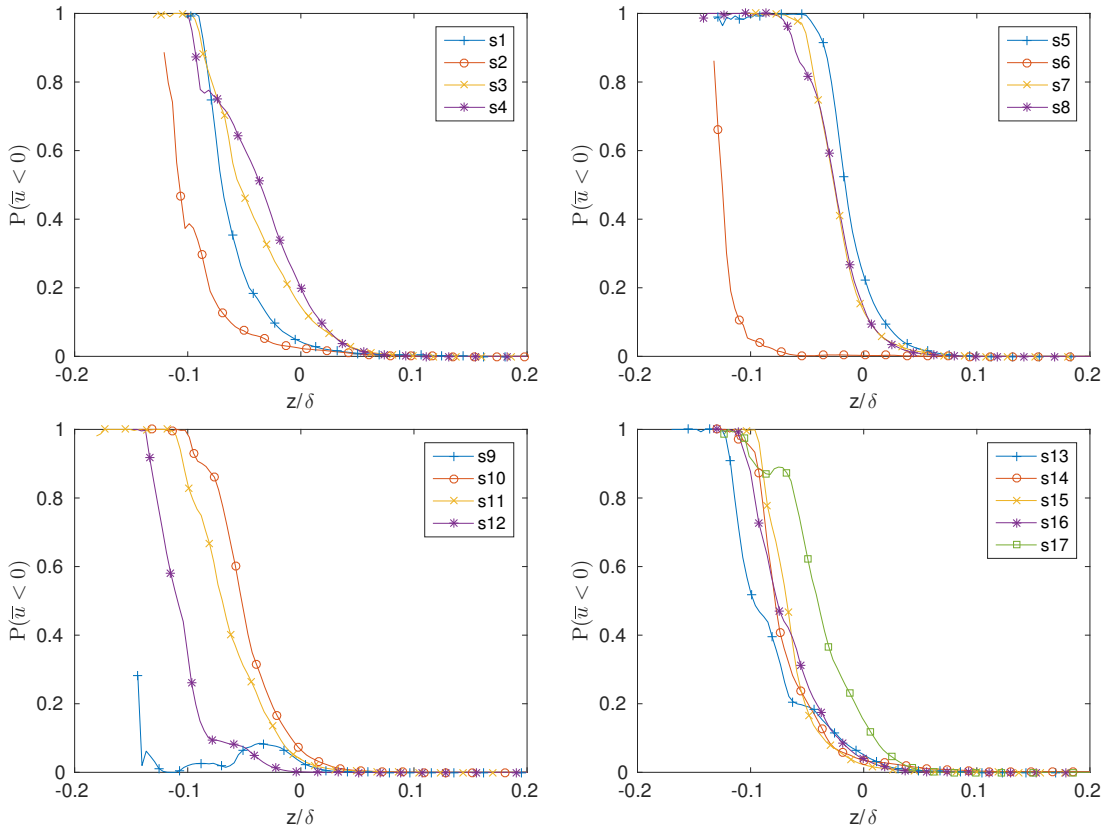

Figure 6.3: Volume fraction of negative time-averaged streamwise velocity, $P(\overline{u} < 0)$, for the 17 rough surface samples. z/δ is the wall-normal distance.

on the flow starts to decrease and hence $P(\overline{u} < 0)$ decreases monotonically for most samples. Qualitatively, these observations are consistent with Busse et al. [2015]. Some samples, such as s9 (ground) and s17 (spark-eroded_5), however, show a non-monotonic behaviour in $P(\overline{u} < 0)$.

Both filed samples, s5 and s6, are interesting as their volume fraction variation is opposite to each other. Sample s5, due to its anisotropic topography with features aligned in the spanwise direction (which evidently promotes flow accumulation and reversal), shows a high value of $P(\overline{u} < 0)$ almost up to $z/\delta = 0$, only after which it starts to decrease. The s6 sample on the other hand, with its features aligned in the streamwise direction, shows

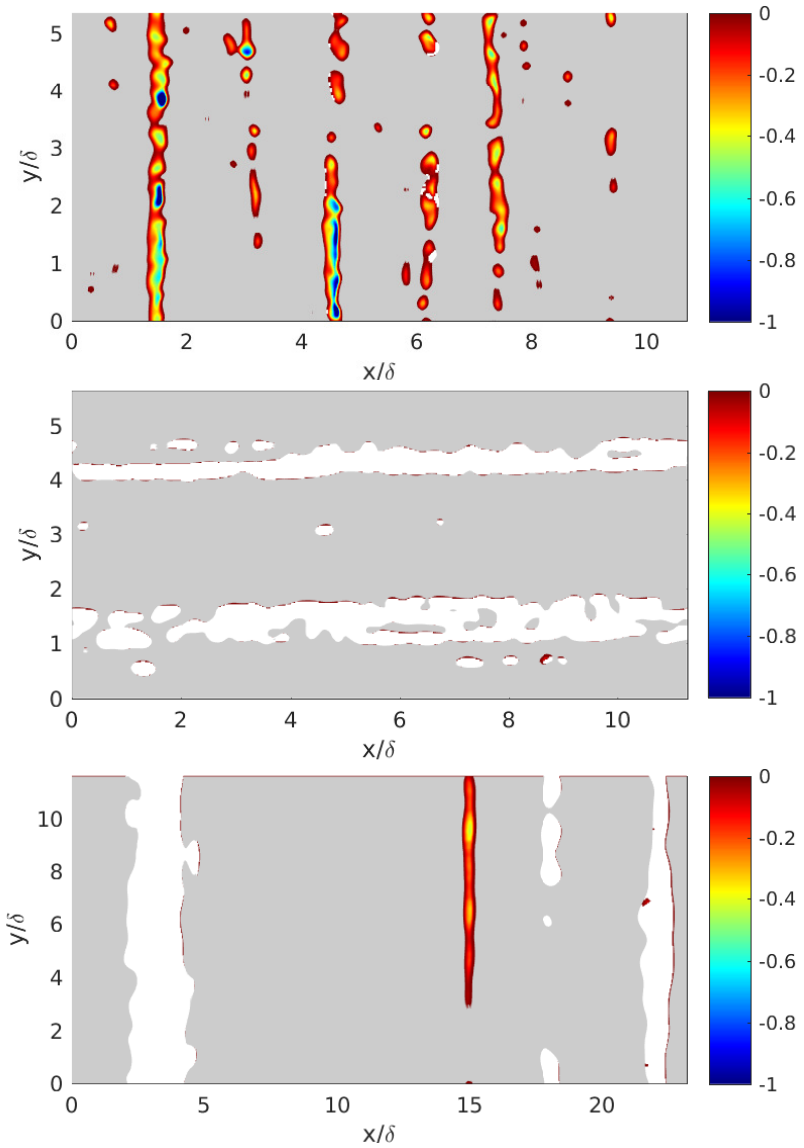

Figure 6.4: Contour plots of negative time-averaged streamwise velocity, $-\overline{u}$, at $z/\delta = -0.05$. The s5 sample (top) shows numerous regions of recirculating flow whereas the s6 sample (middle) shows almost no regions of recirculating flow. The s9 sample (bottom) has a very low volume fraction of reversed flow. Grey regions: rough wall, white regions: regions of non-reversed flow, coloured regions: regions of reversed flow.

a rapid decrease in $P(\overline{u} < 0)$ from the lowest wall-normal location itself. The behaviour of s2 (composite sample with features aligned in the streamwise direction) is similar to s6. Figure 6.4 shows contour plots of negative time-averaged streamwise velocity, $-\overline{u}$, at $z/\delta = -0.05$ for s5 (top) and s6 (middle). Almost all fluid regions in the s5 sample show flow reversal whereas almost no fluid regions in the s6 sample show flow reversal.

Sample s9 (ground) has a similar topography to s5, with features aligned in the spanwise direction. Its volume fraction behaviour, however, is similar to s6 and $P(\overline{u} < 0)$ at lower wall-normal locations is even lower. The contour plot of $-\overline{u}$ at $z/\delta = -0.05$ for s9 is shown in Figure 6.4 (bottom). Despite s5 and s9 having features aligned in the spanwise direction, s5 has much more small scale roughness than s9 (refer Figure 3.4 (e) and (i)). This leads to a comparatively higher S_f/S (s5 roughness is denser than s9), which is possibly responsible for the above-mentioned volume fraction behaviour.

6.3 Influence of roughness topography on the turbulent flow statistics

Profiles of second order turbulent statistics are studied in the following. These include the diagonal components of the Reynolds stress tensor, $\overline{u'^2}$, $\overline{v'^2}$ and $\overline{w'^2}$, termed as the streamwise, spanwise and wall-normal Reynolds stress respectively, which also represent fluctuations in the respective coordinate directions. They are also collectively termed as the Reynolds normal stresses. Also studied are statistics for the Reynolds shear stress, $-\overline{u'w'}$ and turbulent kinetic energy (TKE) given by TKE $= (\overline{u'^2} + \overline{v'^2} + \overline{w'^2})/2$. The time-averaged Reynolds stress fields are spatially averaged in the x and y directions to obtain the profiles. All profiles are plotted against the wall-normal direction normalised by the channel half-height, z/δ. Contour plots of spatial distribution of the streamwise, spanwise and wall-normal fluctuations are also studied for representative samples in a plane normal to the spanwise direction at $y = L_y/2$.

6.3.1 Influence on Reynolds stresses

Figure 6.5 shows profiles of the streamwise fluctuations, $\langle\overline{u'^2}\rangle$. For $z/\delta \leq 0$, streamwise fluctuations depend roughly on the streamwise correlation length, L_x^{cor}, of the corresponding sample. The variation of streamwise fluctuations at $z = 0$, $\langle\overline{u'^2}\rangle_{z=0}$, with L_x^{cor} is shown in Figure 6.6 (left). It appears that $\langle\overline{u'^2}\rangle_{z=0}$ roughly increases with L_x^{cor}, however, the trend is not clear. Though sample s5 (filed_1) has the smallest $L_x^{\text{cor}} = 0.18$ and smallest value of $\langle\overline{u'^2}\rangle_{z=0}$ and s6 (filed_2) has the highest $L_x^{\text{cor}} = 11.27$ and the highest value of $\langle\overline{u'^2}\rangle_{z=0}$. Streamwise fluctuations peak at $z/\delta \approx 0.15$ for all samples, although the peak magnitudes vary widely. A decrease in the peak streamwise fluctuations, $\langle\overline{u'^2}\rangle_{\max}$, with an increased amount of roughness has been noted by previous studies (Busse and Sandham [2012], De Marchis et al. [2010], Krogstad and Antonia [1999], Grass [1971]). Although the roughness height is constant in the current study, peak magnitudes show an inverse dependence on ΔU^+ (because in general an increased amount of roughness is characterised

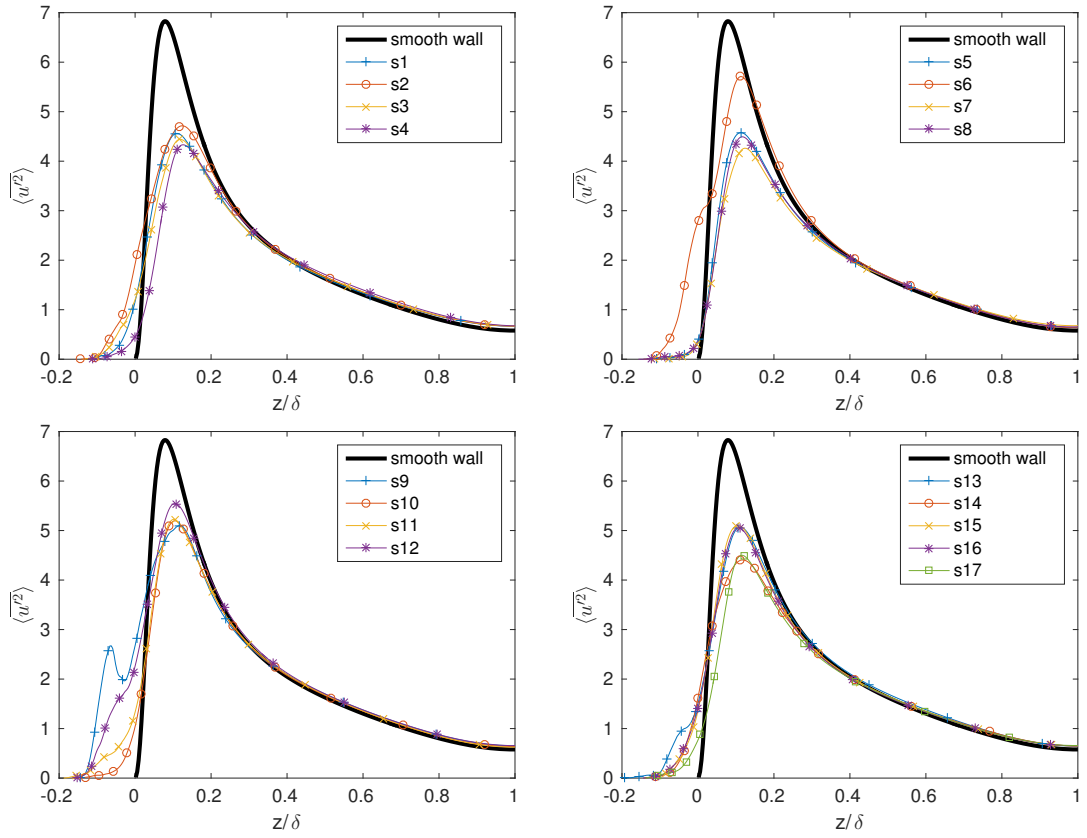

Figure 6.5: Streamwise Reynolds stress profiles, $\langle \overline{u'^2} \rangle$, for the 17 rough surface samples. z/δ is the wall-normal distance.

by a higher ΔU^+), as shown in Figure 6.6 (right). It is also worth noting that all rough wall peaks are less than the smooth-wall peak. Smooth walls are known to exhibit long streamwise streaks (Kim et al. [1987], Kline et al. [1967]) that increase the streamwise fluctuations whereas rough walls are known to break down the turbulence structures close to walls (De Marchis et al. [2010], Ashrafian and Andersson [2006], Orlandi and Leonardi [2006], Smalley et al. [2002], Antonia and Krogstad [2001]). Beyond $z/\delta \approx 0.4$ and closer

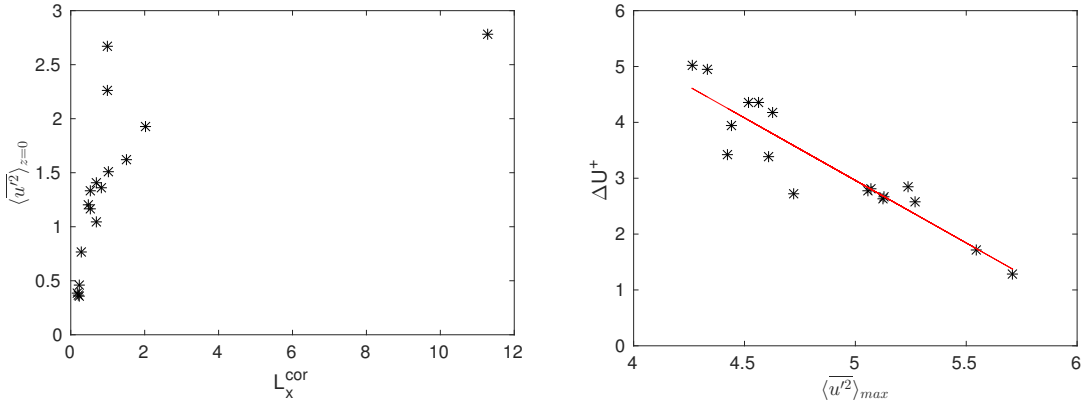

Figure 6.6: Variation of $\langle \overline{u'^2} \rangle_{z=0}$ with L_x^{cor} (left) and ΔU^+ with $\langle \overline{u'^2} \rangle_{\text{max}}$ (right). The red line in right plot shows a fit to the data.

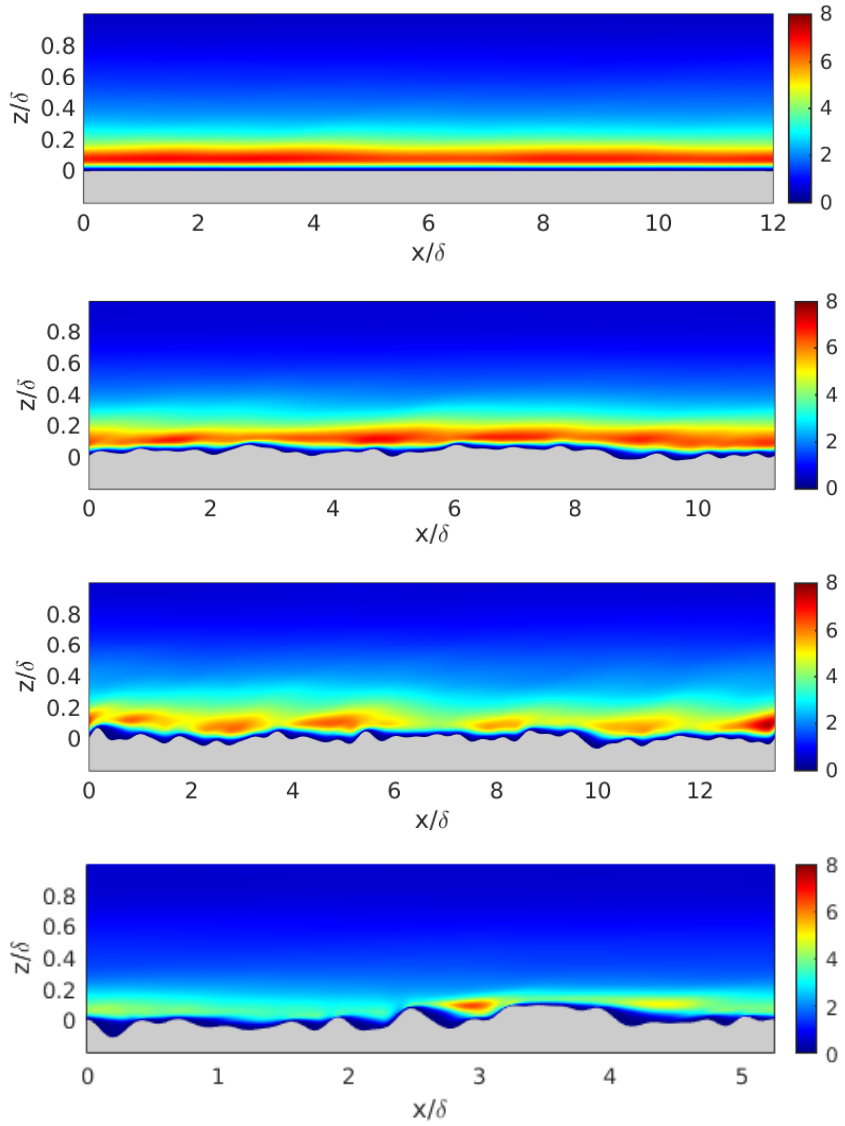

Figure 6.7: Spatial distribution of $\overline{u'^2}$ at $y = L_y/2$, from top to bottom, for the smooth-wall, s6 (filed_2), s10 (ship-propeller_1) and s7 (graphite) samples. The grey region represents the wall.

to the channel centre, all profiles collapse with the smooth-wall data.

The spatial variation of streamwise fluctuations, $\overline{u'^2}$, at $y = L_y/2$ is shown in Figure 6.7 for the smooth-wall case and three representative rough samples, which include s6 (filed_-2), s10 (ship-propeller_1), and s7 (graphite). From top to bottom, the slices represent cases with increasing ΔU^+. From the figure, streamwise fluctuation peak is confirmed at $z/\delta \approx 0.15$. From LES studies on irregular roughness, De Marchis et al. [2010] observed that with increasing roughness height, high intensity streamwise fluctuation regions close to the rough walls were progressively spread along the wall-normal direction and their streamwise length decreased. The same is observed for increasing ΔU^+ in the current study (from top to bottom in Figure 6.7). Also with increasing ΔU^+, peak magnitude of $\overline{u'^2}$ reduces, which was observed by De Marchis et al. [2010] for increasing roughness height. Close to

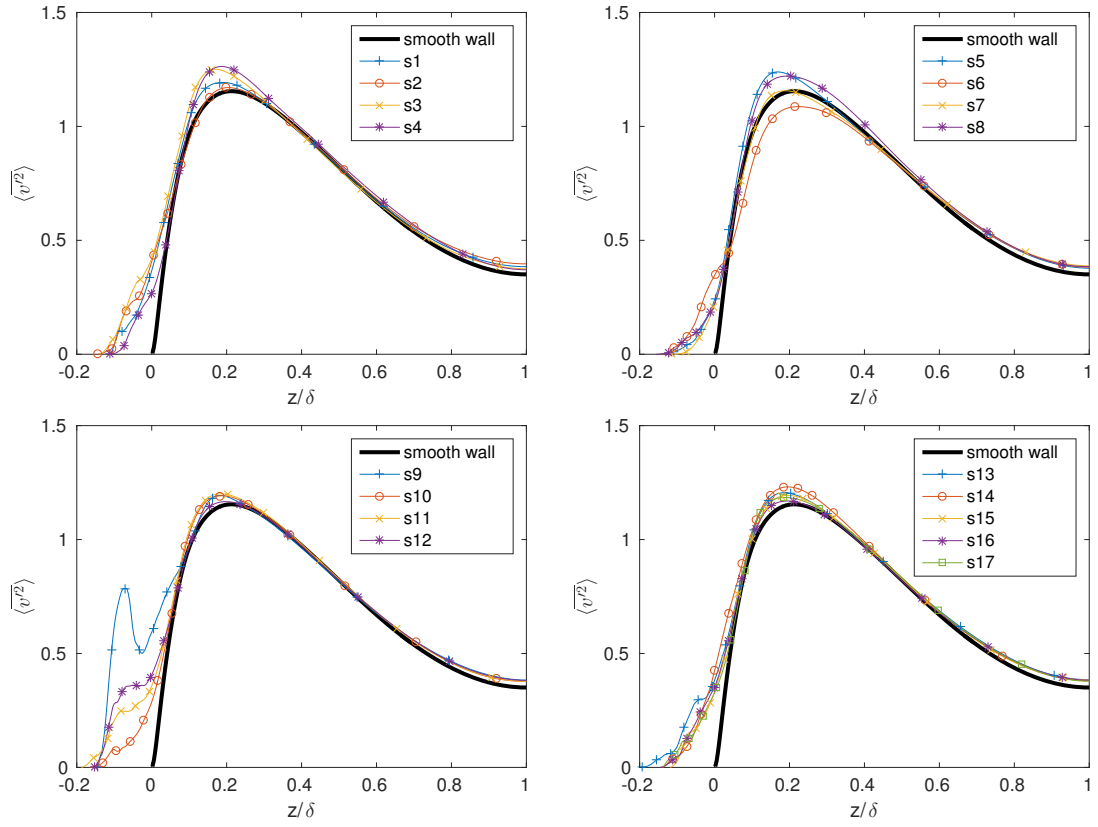

Figure 6.8: Spanwise Reynolds stress profiles, $\langle \overline{v'^2} \rangle$, for the 17 rough surface samples. z/δ is the wall-normal distance.

the channel centre, $\overline{u'^2}$ shows little variation and is similar to the smooth-wall data.

Spanwise Reynolds stress profiles, $\langle \overline{v'^2} \rangle$, are shown in Figure 6.8. For $z/\delta \leq 0$, spanwise fluctuations roughly depend on the spanwise correlation lengths, L_y^{cor}, of the corresponding sample. Figure 6.9 (left) shows the variation of spanwise fluctuations at $z = 0$, $\langle \overline{v'^2} \rangle_{z=0}$, with L_y^{cor}, where $\langle \overline{v'^2} \rangle_{z=0}$ roughly increases with L_y^{cor}, although the trend is not clear. Samples s7 (graphite) and s8 (gritblasted) have among the lowest L_y^{cor} and, consequently, the lowest

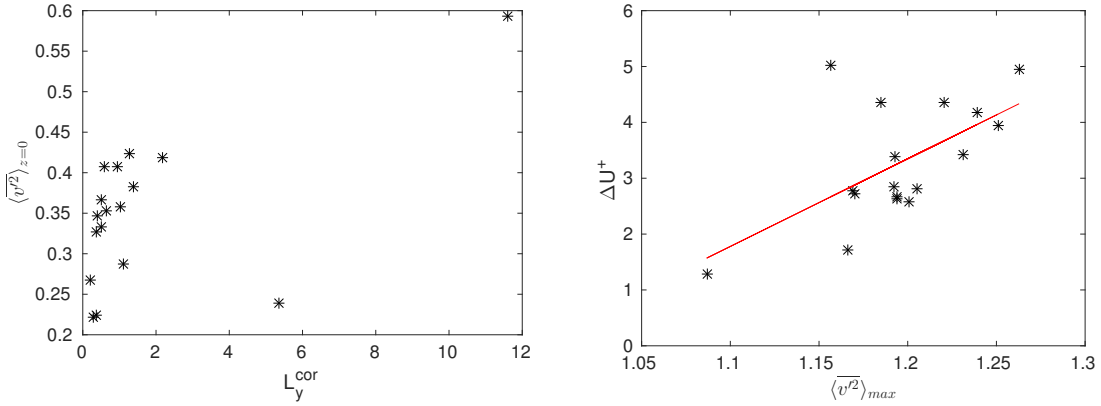

Figure 6.9: Variation of $\langle \overline{v'^2} \rangle_{z=0}$ with L_y^{cor} (left) and ΔU^+ with $\langle \overline{v'^2} \rangle_{\text{max}}$ (right). The red line in the right plot shows a fit to the data.

values of $\langle\overline{v'^2}\rangle_{z=0}$. Sample s9 (ground) has the highest $L_y^{\text{cor}} = 11.6$ and the highest value of $\langle\overline{v'^2}\rangle_{z=0}$. The highly anisotropic topography of s9, with features strongly aligned in the spanwise direction, is also responsible for high $\langle\overline{v'^2}\rangle_{z=0}$. Spanwise fluctuations peak at $z/\delta \approx 0.2$. Peak spanwise fluctuations, $\langle\overline{v'^2}\rangle_{\max}$, vary directly with ΔU^+ and hence with the amount of roughness. This is shown in Figure 6.9 (right), which is the opposite trend from $\langle\overline{u'^2}\rangle_{\max}$ (Figure 6.6 (right)). The highly anisotropic topography of s6 (filed_2), with features strongly aligned in the streamwise direction, leads to a relatively low $\langle\overline{v'^2}\rangle_{\max}$ (even lower than the smooth-wall data) compared to the other samples. Beyond $z/\delta \approx 0.4$ and closer to the channel centre, all profiles collapse with the smooth-wall data.

The spatial variation of spanwise fluctuations, $\overline{v'^2}$, at $y = L_y/2$ is shown in Figure 6.10 for the smooth-wall case and three representative rough samples, which include s9 (ground),

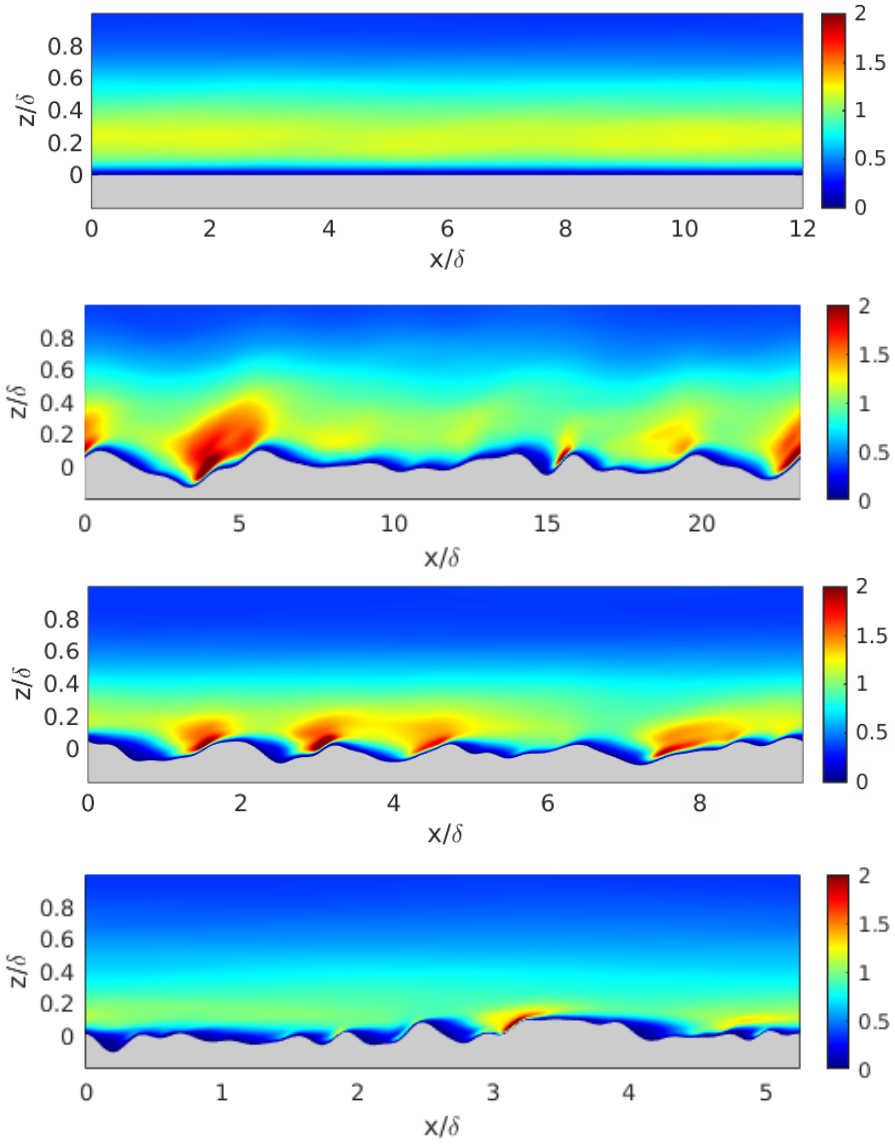

Figure 6.10: Spatial distribution of $\overline{v'^2}$ at $y = L_y/2$, from top to bottom, for the smooth-wall, s9 (ground), s3 (composite_2) and s7 (graphite) samples. The grey region represents the wall.

s3 (composite_1), and s7 (graphite). From top to bottom, the slices represent cases with increasing ΔU^+. Some roughness peaks exhibit high intensity $\overline{v'^2}$ on their windward faces. This is caused by the 'splat' phenomenon, also noted by De Marchis et al. [2010] and Ashrafian et al. [2004] (who studied DNS of regularly spaced square bars). This phenomenon occurs due to splitting of the high speed flow incident on the peaks. Close to the channel centre, $\overline{v'^2}$ shows little variation and is similar to the smooth-wall data.

The wall-normal Reynolds stress profiles, $\langle\overline{w'^2}\rangle$, are shown in Figure 6.11. For $z/\delta \leq 0$, wall-normal fluctuations roughly depend on the average roughness height, S_a, and rms roughness height, S_q, of the corresponding sample. Figure 6.12 shows the variation of wall-normal fluctuations at $z = 0$, $\langle\overline{w'^2}\rangle_{z=0}$, with S_a (left) and with S_q (right). $\langle\overline{w'^2}\rangle_{z=0}$ increases with both S_a and S_q. Sample s5 (filed_1) has the lowest S_a and S_q and consequently the lowest $\langle\overline{w'^2}\rangle_{z=0}$ whereas sample s9 (ground) has the highest S_a and S_q and the highest $\langle\overline{w'^2}\rangle_{z=0}$. Wall-normal fluctuations peak at $z/\delta \approx 0.3$. There is no clear trend of ΔU^+ with $\langle\overline{w'^2}\rangle_{\max}$, as seen in the case of peak profile streamwise and spanwise fluctuations. Beyond $z/\delta \approx 0.4$ and closer to the channel centre, all profiles collapse with the smooth-wall data, though there is some disagreement for $0.8 \leq z/\delta \leq 1$. The disagreement, which varies for different samples, is possibly due to an increase in the instantaneous wall-normal velocity induced by the roughness peaks that may increase the interaction between the roughness and the outer flow (De Marchis et al. [2010]).

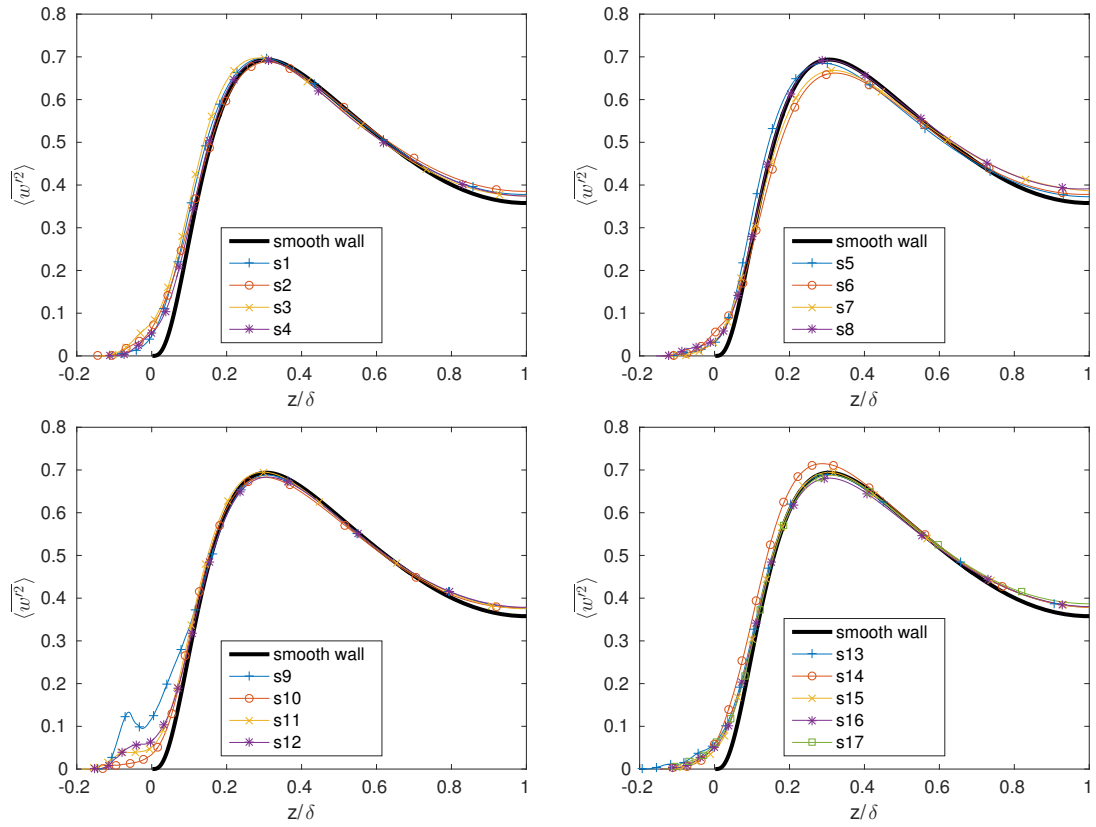

Figure 6.11: Wall-normal Reynolds stress profiles, $\langle\overline{w'^2}\rangle$, for the 17 rough surface samples. z/δ is the wall-normal distance.

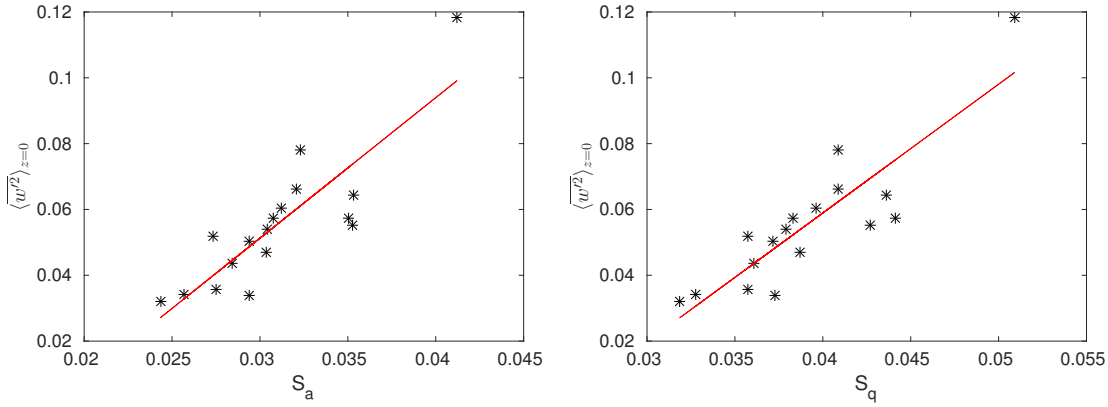

Figure 6.12: Variation of $\langle \overline{w'^2} \rangle_{z=0}$ with S_a (left) and with S_q (right). Red lines in both plots show fits to the data.

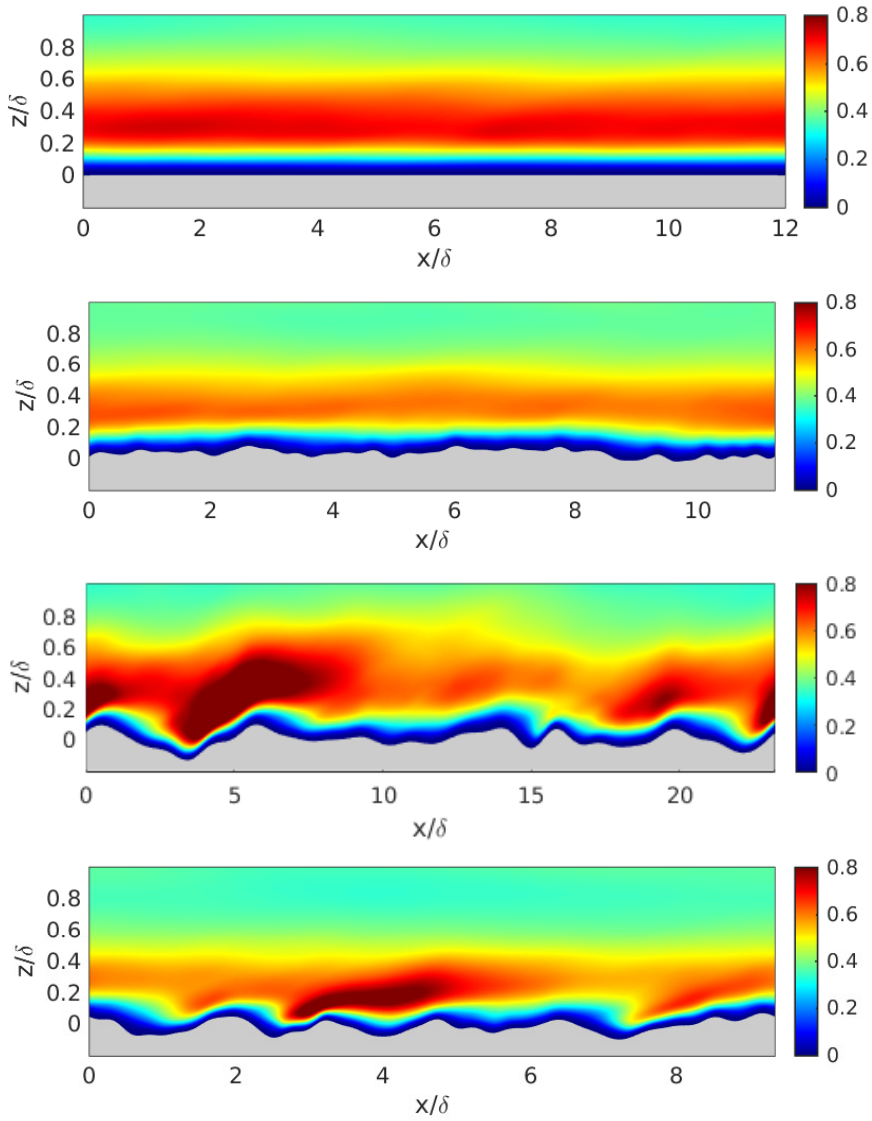

Figure 6.13: Spatial distribution of $\overline{w'^2}$ at $y = L_y/2$, from top to bottom, for the smooth-wall, s6 (filed_2), s9 (ground) and s3 (composite_2) samples. The grey region represents the wall.

The spatial variation of wall-normal fluctuations, $\overline{w'^2}$, at $y = L_y/2$ is shown in Figure 6.13 for the smooth-wall case and three representative rough samples, which include s6 (filed_2), s9 (ground) and s3 (composite_2). From top to bottom, the slices represent cases with increasing ΔU^+. Sample s6 is very similar to the smooth-wall data. De Marchis et al. [2010] observed that $\overline{w'^2}$ increased with increasing roughness height, which in the current study should roughly translate to increasing ΔU^+. However, it is not clear from Figure 6.13 whether $\overline{w'^2}$ increases with ΔU^+. Sample s9 shows larger regions of high intensity $\overline{w'^2}$ compared to s3 despite its ΔU^+ being less than for s3. In general, regions of high $\overline{w'^2}$ are observed upstream of larger roughness peaks, which in some cases (for example, sample s9 and s3) may also propagate downstream. Sample s9 shows relatively large regions of high $\overline{w'^2}$, which extend up to $z/\delta \approx 0.8$.

Some general observations are noted for the Reynolds normal stress profiles (Figures 6.5, 6.8 and 6.11) as follows. Within the roughness and up to $z/\delta \approx 0.05$, Reynolds normal stresses for all samples are greater than the smooth-wall value. Fluctuations over rough walls can occur very close to the roughness features, including at and below the mean wall location, $z/\delta = 0$, which is not possible in the case of smooth walls. In general, an increase in normal stresses close to the rough walls and a collapse with the smooth-wall data close the channel centre is observed, which was also noted by De Marchis et al. [2010]. For smooth walls, Hu et al. [2006] mentioned that peak location of streamwise fluctuations is closer to

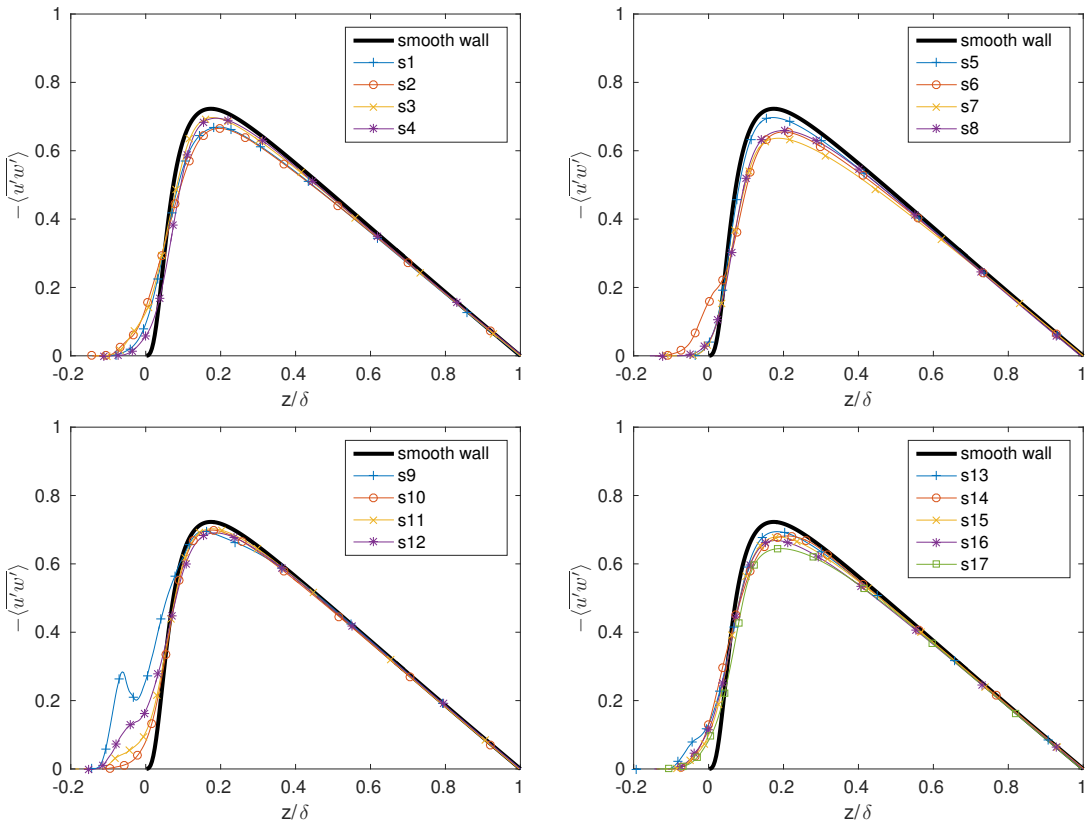

Figure 6.14: Reynolds shear stress profiles, $-\langle\overline{u'w'}\rangle$, for the 17 rough surface samples. z/δ is the wall-normal distance.

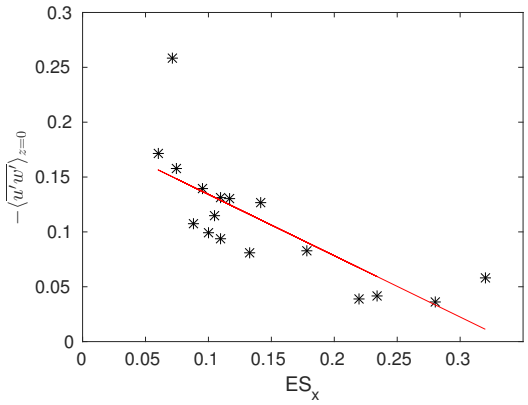

Figure 6.15: Variation of $-\langle\overline{u'w'}\rangle_{z=0}$ with ES_x. The red line shows a fit to the data.

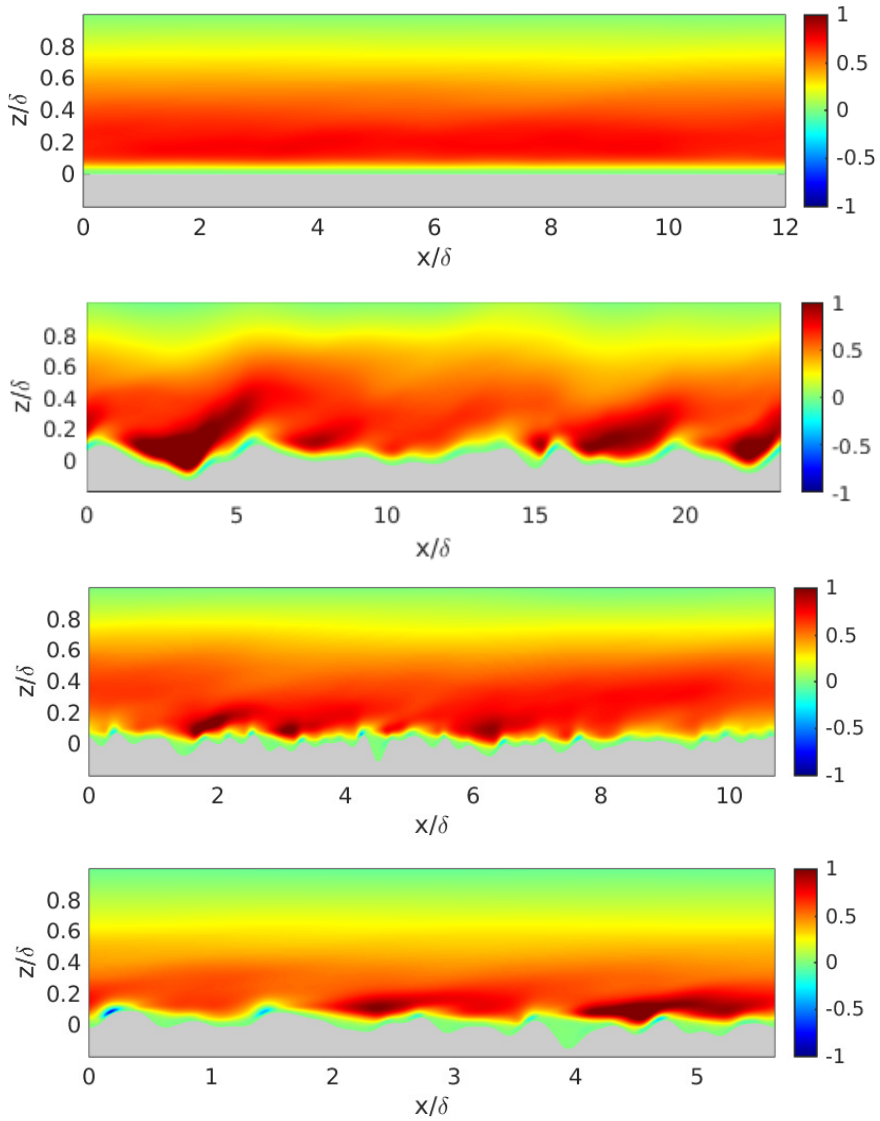

Figure 6.16: Spatial distribution of $-\overline{u'w'}$ at $y = L_y/2$, from top to bottom, for the smooth-wall, s9 (ground), s5 (filed_1) and s8 (gritblasted) samples. The grey region represents the wall.

the wall than for spanwise and wall-normal fluctuations, which is also observed from the current study for all samples. Streamwise fluctuation peaks are located at $z/\delta \approx 0.15$ (which is below the roughness height, $k/\delta = 1/6$) whereas spanwise and wall-normal fluctuation peaks are located at $z/\delta \approx 0.2$ and 0.3 respectively. Thus the roughness may interfere more with the streamwise fluctuations than with the spanwise and wall-normal fluctuations.

The Reynolds shear stress profiles, $-\langle\overline{u'w'}\rangle$, are shown in Figure 6.14. In general, the presence of the rough wall significantly increases the shear stress compared to the smooth-wall, as observed for $z/\delta < 0.1$. For $z/\delta \leq 0$, the Reynolds shear stress shows some dependency on the streamwise effective slope, ES_x. Figure 6.15 shows the variation of shear stress at $z = 0$, $-\langle\overline{u'w'}\rangle_{z=0}$, with ES_x. In general, $-\langle\overline{u'w'}\rangle_{z=0}$ decreases with ES_x. Shear stress peaks at $z/\delta \approx 0.2$ and $-\langle\overline{u'w'}\rangle_{\max}$ for all samples is less than the smooth wall data. Also, there is no clear trend of ΔU^+ with $-\langle\overline{u'w'}\rangle_{\max}$, as seen in the case of peak profile streamwise and spanwise fluctuations. Away from the rough walls, beyond $z/\delta \approx 0.6$, all profiles collapse with the smooth-wall data.

The spatial variation of Reynolds shear stress, $-\overline{u'w'}$, at $y = L_y/2$ is shown in Figure 6.16 for the smooth-wall case and three representative rough samples, which include s9 (ground), s5 (filed_1) and s8 (gritblasted). From top to bottom, the slices represent cases with increasing ΔU^+. De Marchis et al. [2010] observed that increasing roughness height caused higher shear stress regions to spread in the wall-normal direction, which is roughly seen with increasing ΔU^+ from top to bottom in Figure 6.16. This is seen as an increase in thickness of the lower shear stress (green) region immediately adjacent to the rough walls. With increasing roughness, De Marchis et al. [2010] also observed a change in sign of $-\overline{u'w'}$ on roughness peaks. Regions of negative shear stress are observed from Figure 6.16 on some peaks of the gritblasted sample.

6.3.2 Influence on turbulent kinetic energy (TKE)

Figure 6.17 shows the TKE profiles, $(\langle\overline{u'^2}\rangle + \langle\overline{v'^2}\rangle + \langle\overline{w'^2}\rangle)/2$, for all samples. Trends in the TKE are very similar to trends observed in case of the streamwise fluctuations. Figure 6.18 (left) shows profiles of streamwise, spanwise and wall-normal fluctuations for the s8 (gritblasted) sample, as an example, and for the smooth-wall data. This figure shows the contribution of each component to the TKE. For both s8 and the smooth-wall, the peak $\langle\overline{u'^2}\rangle$ is higher than both peak $\langle\overline{v'^2}\rangle$ and $\langle\overline{w'^2}\rangle$. Also, a higher peak $\langle\overline{u'^2}\rangle$ is observed for the smooth-wall than s8. The above two observations were made for all samples. To quantify the anisotropy of the velocity fluctuations and hence TKE, the diagonal components of the Reynolds stress anisotropy tensor, $b_{i,j}$, are computed at the peak profile value of TKE for all samples. Hence

$$b_{i,j} = \frac{\langle\overline{u_i' u_j'}\rangle_{\max}}{2 \times \langle \mathrm{TKE} \rangle_{\max}} - \frac{1}{3}\delta_{i,j}, \tag{6.1}$$

where $\delta_{i,j}$ is the Kronecker delta. It is known that $-1/3 \leq b_{i,j} \leq 2/3$ and hence a component with a positive value of $b_{i,j}$ indicates dominant contribution to the TKE. Figure 6.18 (right) shows data for $b_{1,1}$, $b_{2,2}$ and $b_{3,3}$ against $\langle \mathrm{TKE} \rangle_{\max}$ for all samples, along with associated

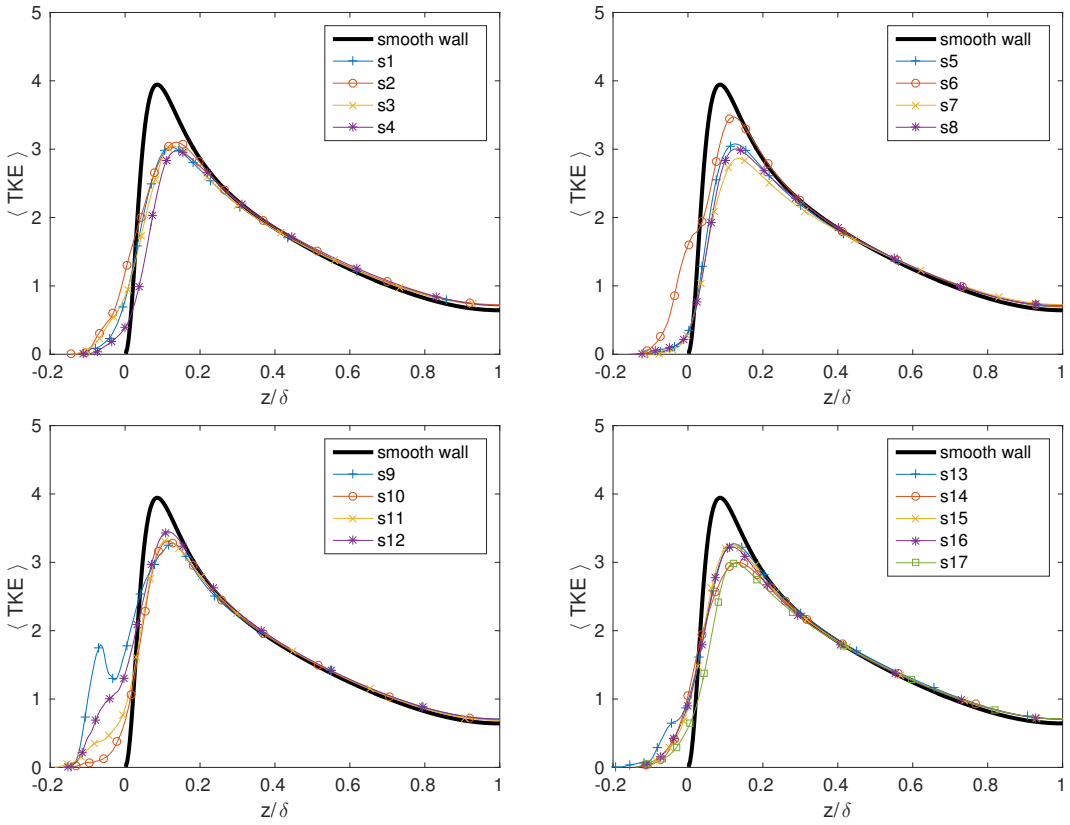

Figure 6.17: Turbulent kinetic energy profiles for the 17 rough surface samples. z/δ is the wall-normal distance.

linear fits. Firstly, all samples have a positive value of $b_{1,1}$ and negative value of both $b_{2,2}$ and $b_{3,3}$, which indicates that the streamwise component of velocity fluctuations plays a dominant role in determining the TKE. Secondly, the $b_{1,1}$ fits show an increasing trend whereas both $b_{2,2}$ and $b_{3,3}$ fits show a decreasing trend with $\langle \text{TKE} \rangle_{\text{max}}$. Hence larger streamwise fluctuations lead to larger $\langle \text{TKE} \rangle_{\text{max}}$. For the smooth wall data, $b_{1,1} = 0.53$,

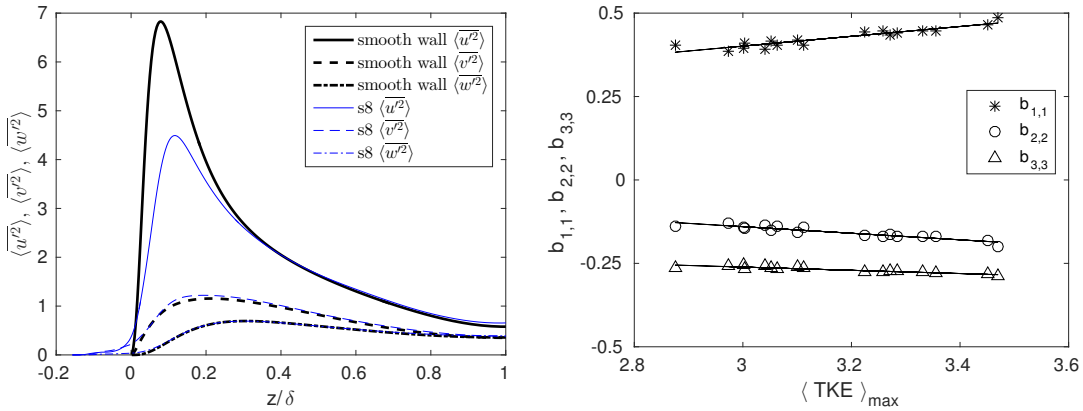

Figure 6.18: Profiles of streamwise, $\langle \overline{u'^2} \rangle$, spanwise, $\langle \overline{v'^2} \rangle$ and wall-normal, $\langle \overline{u'^2} \rangle$, fluctuations for the s8 (gritblasted) sample and smooth wall (left). Diagonal components of $b_{i,j}$ against $\langle \text{TKE} \rangle_{\text{max}}$ (right) with associated linear fits.

$b_{2,2} = -0.22$ and $b_{3,3} = -0.31$, which are greater in magnitude than for all rough samples. Hence, it is also proved that anisotropy for rough walls in all three coordinate directions is reduced compared to the smooth wall.

6.4 Influence of roughness topography on the dispersive stress statistics

Section 1.4.4 explained how the dispersive stresses are computed. In this section, dispersive stress profiles are discussed in conjunction with contour plots of time-averaged velocity in $x - y$ planes.

The streamwise dispersive stress profiles, $\langle \tilde{u}^2 \rangle$, are shown in Figure 6.19. All samples show peak streamwise dispersive stress, $\langle \tilde{u}^2 \rangle_{\max}$, at $z/\delta \approx 0.05$. The variation of $\langle \tilde{u}^2 \rangle_{\max}$ is high compared to peak streamwise Reynolds stress, $\langle \overline{u'^2} \rangle_{\max}$. For all samples, the peak streamwise Reynolds stress (srs) shows a standard deviation, $\sigma_{\text{srs}} \approx 0.44$ whereas peak streamwise dispersive stress (sds) shows $\sigma_{\text{sds}} \approx 2.61$. Figure 6.20 (left) shows a comparison of $\langle \tilde{u}^2 \rangle$ with the corresponding Reynolds stress for a typical case (for example, s7 (graphite)). It is observed that $\langle \tilde{u}^2 \rangle_{\max} < \langle \overline{u'^2} \rangle_{\max}$, which in general applies to all samples. Some samples, such as s2 (composite_1) and s6 (filed_2), however, show greater $\langle \tilde{u}^2 \rangle_{\max}$ than the corresponding $\langle \overline{u'^2} \rangle_{\max}$, as shown in Figure 6.20 (right). Both these samples are

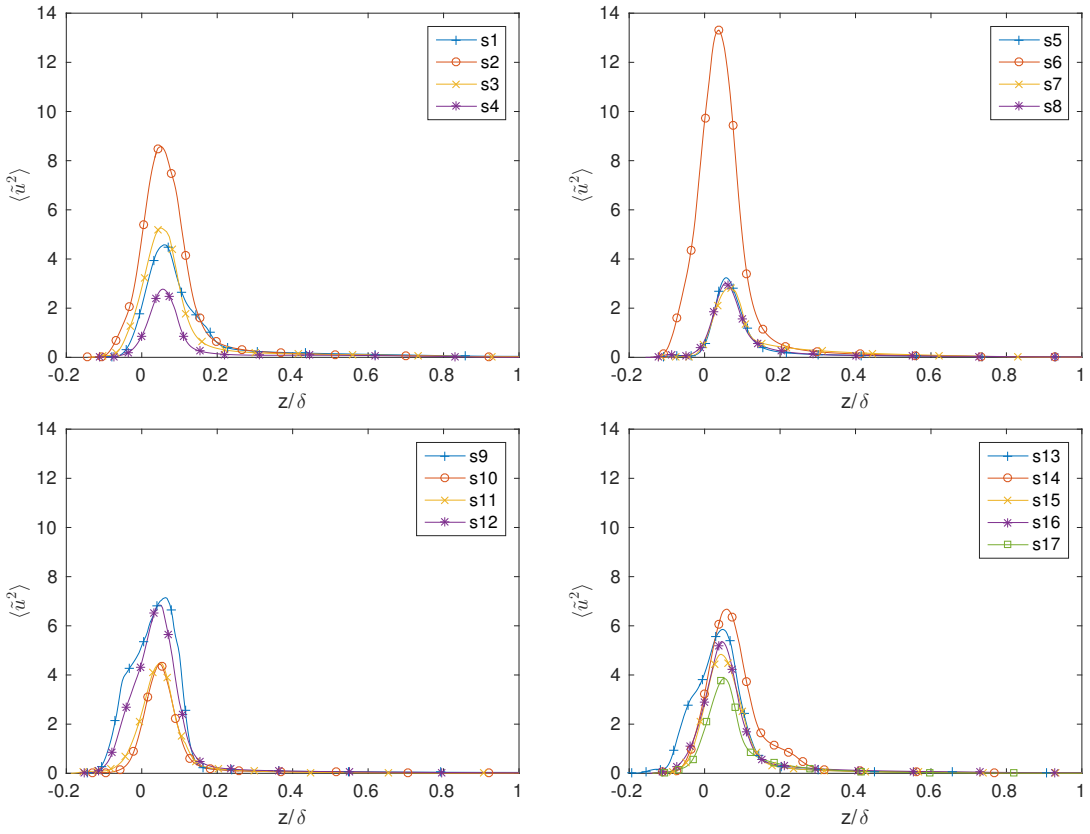

Figure 6.19: Streamwise dispersive stress profiles, $\langle \tilde{u}^2 \rangle$, for the 17 rough surface samples. z/δ is the wall-normal distance.

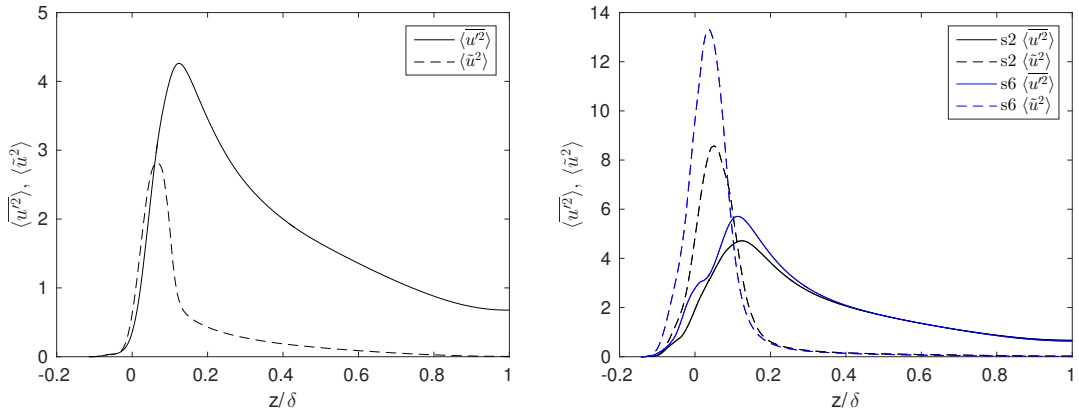

Figure 6.20: Comparison of the streamwise Reynolds stress profiles, $\langle\overline{u'^2}\rangle$, with the streamwise dispersive stress profiles, $\langle\tilde{u}^2\rangle$, for the s7 (graphite) sample (left), and s2 (composite_1) and s6 (filed_2) samples (right). z/δ is the wall-normal distance.

streamwise anisotropic with comparatively high values of streamwise correlation lengths, L_x^{cor}. The variation of $\langle\tilde{u}^2\rangle_{\max}$ with L_x^{cor} shows an increasing trend (Figure 6.21 (left)). Since $\sigma_{\text{sds}} > \sigma_{\text{srs}}$, a similar trend is observed when the variation of $\langle\tilde{u}^2\rangle_{\max} - \langle\overline{u'^2}\rangle_{\max}$ with L_x^{cor} is studied (Figure 6.21 (right)). These trends explain why samples with streamwise anisotropic topographies (such as s2 and s6) exhibit relatively high values of streamwise dispersive stress. However, spanwise anisotropic samples, such as s3 (composite_2) and s9 (ground), with relatively low L_x^{cor}, also exhibit $\langle\tilde{u}^2\rangle_{\max} > \langle\overline{u'^2}\rangle_{\max}$. The spatial variation of time-averaged streamwise velocity, $\overline{u}$, at $z/\delta = 0.05$ is shown in Figure 6.22 for three representative rough samples, s7 (graphite), s6 (filed_2) and s2 (composite_1). Samples s6 and s2 show relatively large regions of high streamwise velocity compared to s7. This high streamwise velocity leads to comparatively large dispersive stress. It is evident from Figure 6.22 that topographies providing little streamwise hindrance to the flow promote higher streamwise dispersive stress.

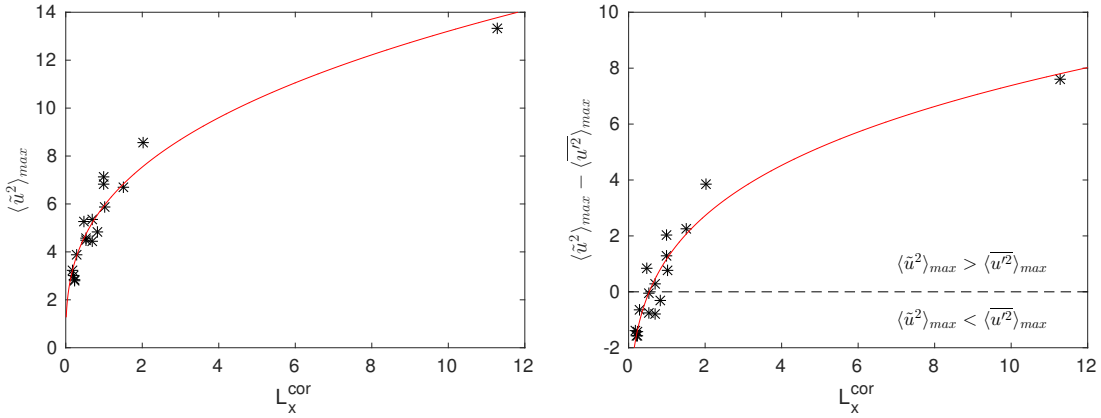

Figure 6.21: Variation of the peak streamwise dispersive stress, $\langle\tilde{u}^2\rangle_{\max}$, with L_x^{cor} (left) and variation of the difference between the peak streamwise dispersive stress and peak streamwise Reynolds stress, $\langle\tilde{u}^2\rangle_{\max} - \langle\overline{u'^2}\rangle_{\max}$, with L_x^{cor}. Red lines in both plots show fits to the data.

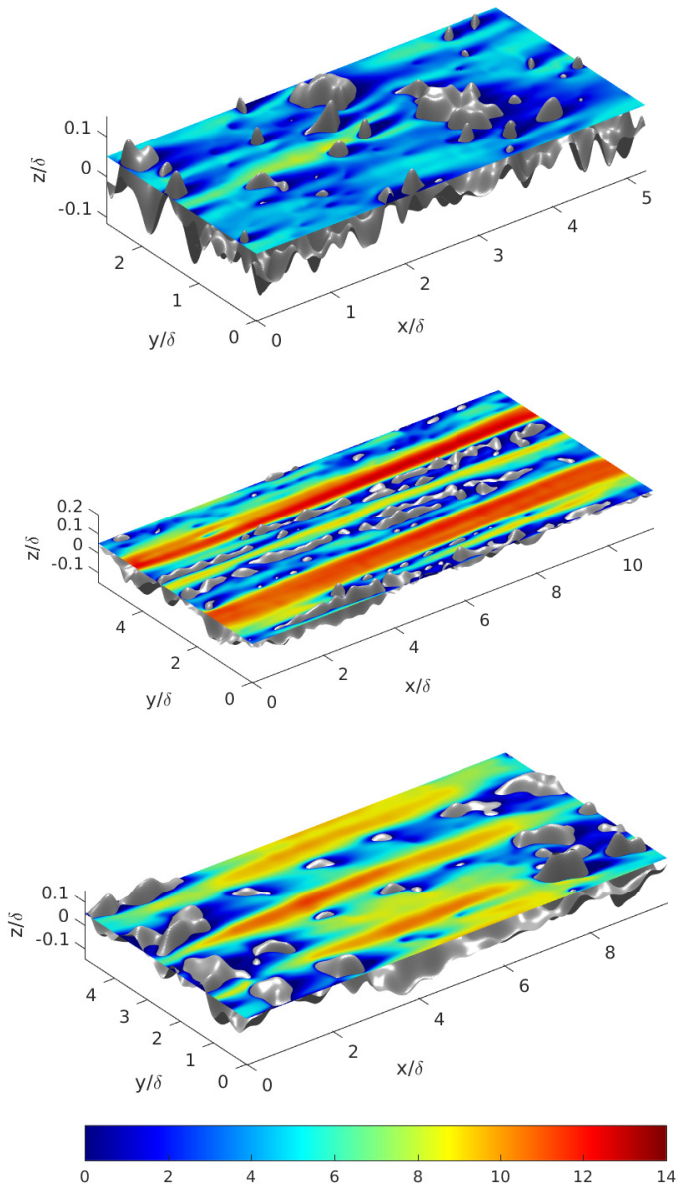

Figure 6.22: Spatial distribution of time-averaged streamwise velocity, $\overline{u}$, at $z/\delta = 0.05$, from top to bottom, for the s7 (graphite), s6 (filed_2) and s2 (composite_1) samples. The grey region represents the wall.

The spanwise dispersive stress profiles, $\langle \tilde{v}^2 \rangle$, are shown in Figure 6.23. In general for all samples, spanwise dispersive stress is significantly less than the corresponding spanwise Reynolds stress; a comparison for a typical case (s7 graphite) is shown in Figure 6.24. Spanwise dispersive stress is also much less than the streamwise dispersive stress. The highest peaks of spanwise dispersive stress, $\langle \tilde{v}^2 \rangle_{\max}$, are observed for the s1 (cast), s7 (graphite), s11 (ship-propeller_2) and s17 (spark-eroded_5) samples. The spatial variation of time-averaged spanwise velocity, $\overline{v}$, at $z/\delta = 0.05$ for s1 and s17 (Figure 6.25 (top and middle)) shows numerous regions of high spanwise velocity, which are responsible for high spanwise dispersive stress. The topographies of these samples exhibit closely spaced roughness features and hence promote spanwise variation of the flow. The lowest $\langle \tilde{v}^2 \rangle$ is observed for the s9

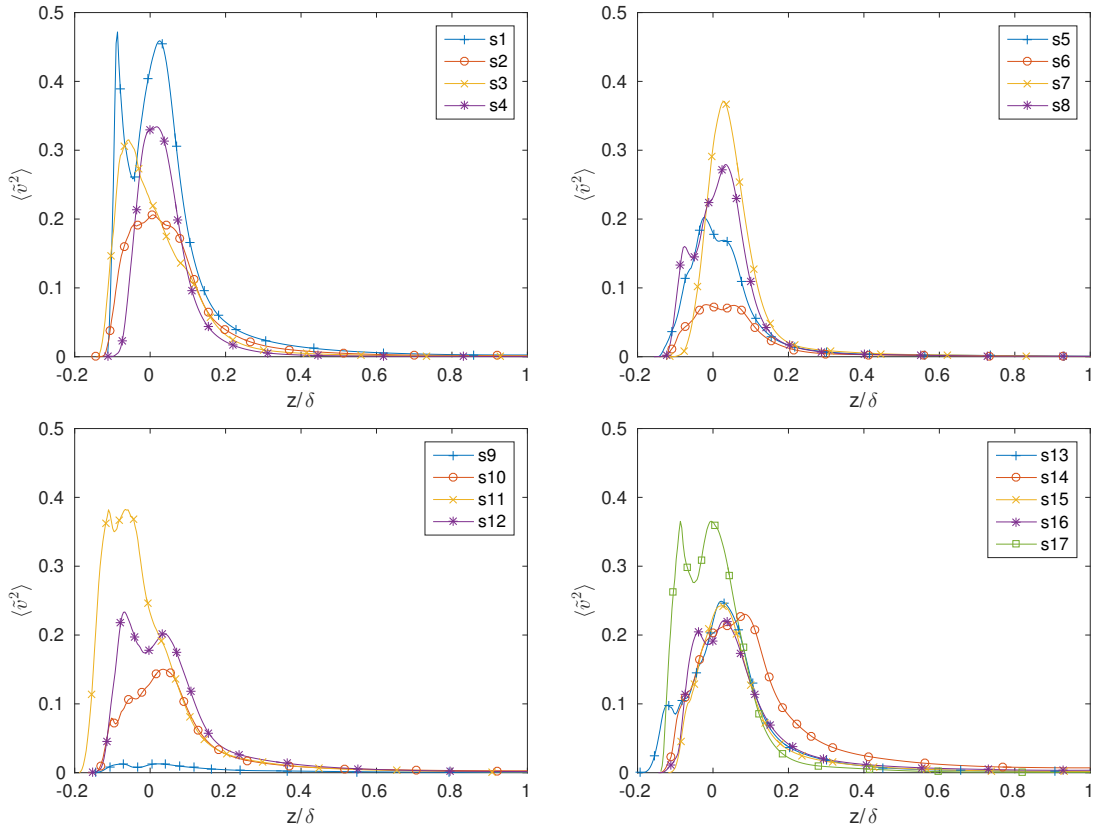

Figure 6.23: Spanwise dispersive stress profiles, $\langle \tilde{v}^2 \rangle$, for the 17 rough surface samples. z/δ is the wall-normal distance.

(ground) sample, due to very little spanwise velocity variation, as seen from Figure 6.25 (bottom).

The wall-normal dispersive stress profiles, $\langle \tilde{w}^2 \rangle$, are shown in Figure 6.26. In general for all samples, the wall-normal dispersive stress is significantly less than the corresponding wall-normal Reynolds stress; comparison for a typical case (s12 shotblasted) is shown in Fig-

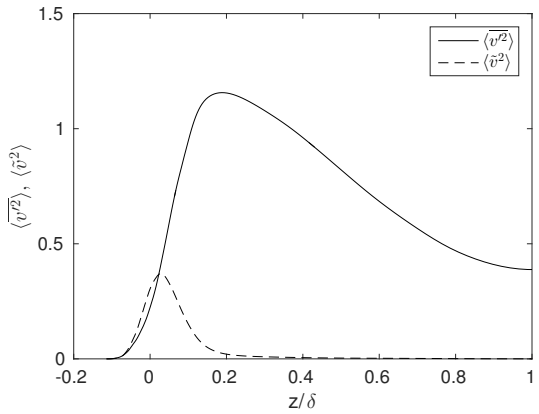

Figure 6.24: Comparison of the spanwise Reynolds stress profiles, $\langle \overline{v'^2} \rangle$, with the spanwise dispersive stress profiles, $\langle \tilde{v}^2 \rangle$, for the s7 (graphite) sample. z/δ is the wall-normal distance.

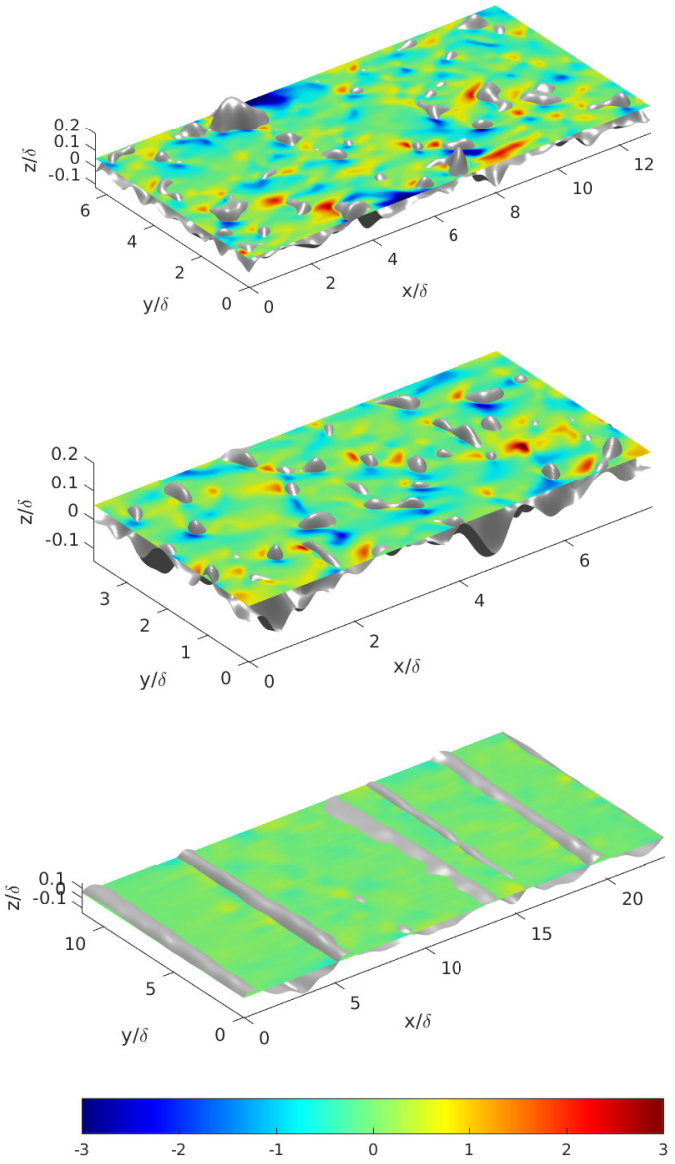

Figure 6.25: Spatial distribution of time-averaged spanwise velocity, $\overline{v}$, at $z/\delta = 0.05$, from top to bottom, for the s1 (cast), s17 (spark-eroded_5) and s9 (ground) samples. The grey region represents the wall.

ure 6.27 (left). Wall-normal dispersive stress is also much less than both the streamwise and spanwise dispersive stress. All samples show peak wall-normal dispersive stress, $\langle\tilde{w}^2\rangle_{\max}$, at $z/\delta \approx 0.1$, with most samples exhibiting $\langle\tilde{w}^2\rangle_{\max} \approx 0.1$. Sample s9 (ground), however, has $\langle\tilde{w}^2\rangle_{\max}$ more than twice this value. The variation of $\langle\tilde{w}^2\rangle_{\max}$ with the corresponding spanwise correlation length, L_y^{cor}, shown in Figure 6.27 (right). Although it appears that $\langle\tilde{w}^2\rangle_{\max}$ increases with L_y^{cor}, the trend is not clear. The spatial variation of time-averaged wall-normal velocity, $\overline{w}$, at $z/\delta = 0.1$ for s3 (composite_2), s6 (filed_2) and s9 (ground) (Figure 6.28) gives further insight into the behaviour of the wall-normal dispersive stress. Overall the lowest $\langle\tilde{w}^2\rangle$ is observed for the s6 sample because of very little wall-normal velocity variation (Figure 6.28 (middle)). Regions of high $\overline{w}$ are observed in case of the s3 and

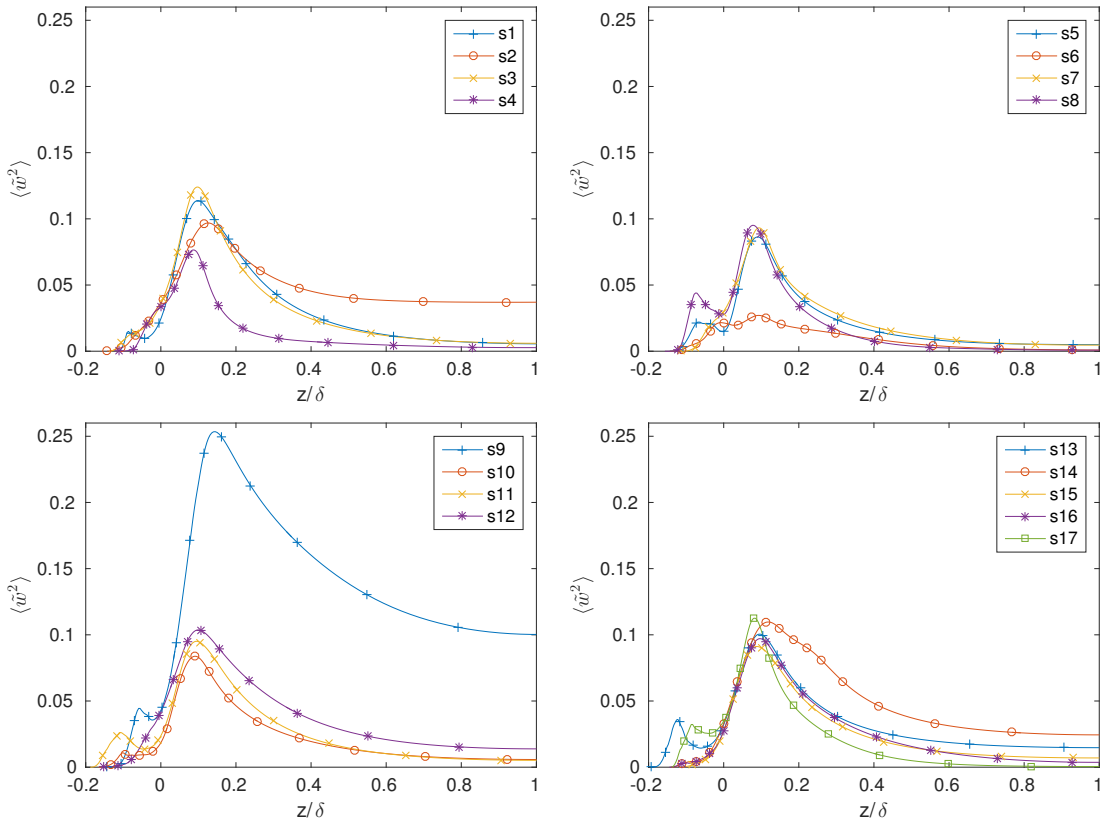

Figure 6.26: Wall-normal dispersive stress profiles, $\langle \tilde{w}^2 \rangle$, for the 17 rough surface samples. z/δ is the wall-normal distance.

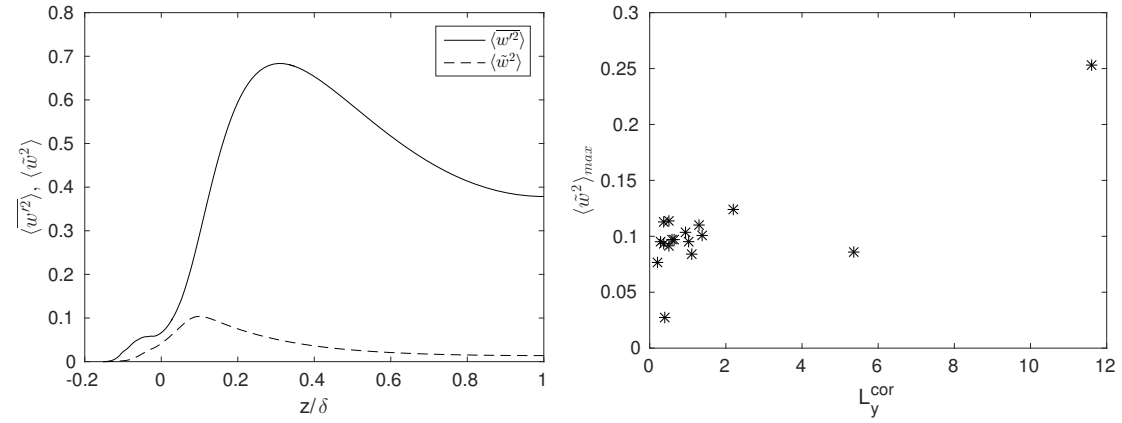

Figure 6.27: Comparison of the wall-normal Reynolds stress profiles, $\langle \overline{w'^2} \rangle$, with the wall-normal dispersive stress profiles, $\langle \tilde{w}^2 \rangle$, for the s12 (shotblasted) sample (left) and variation of the peak wall-normal dispersive stress, $\langle \tilde{w}^2 \rangle_{\max}$, with the spanwise correlation length, L_y^{cor} (right). z/δ is the wall-normal distance.

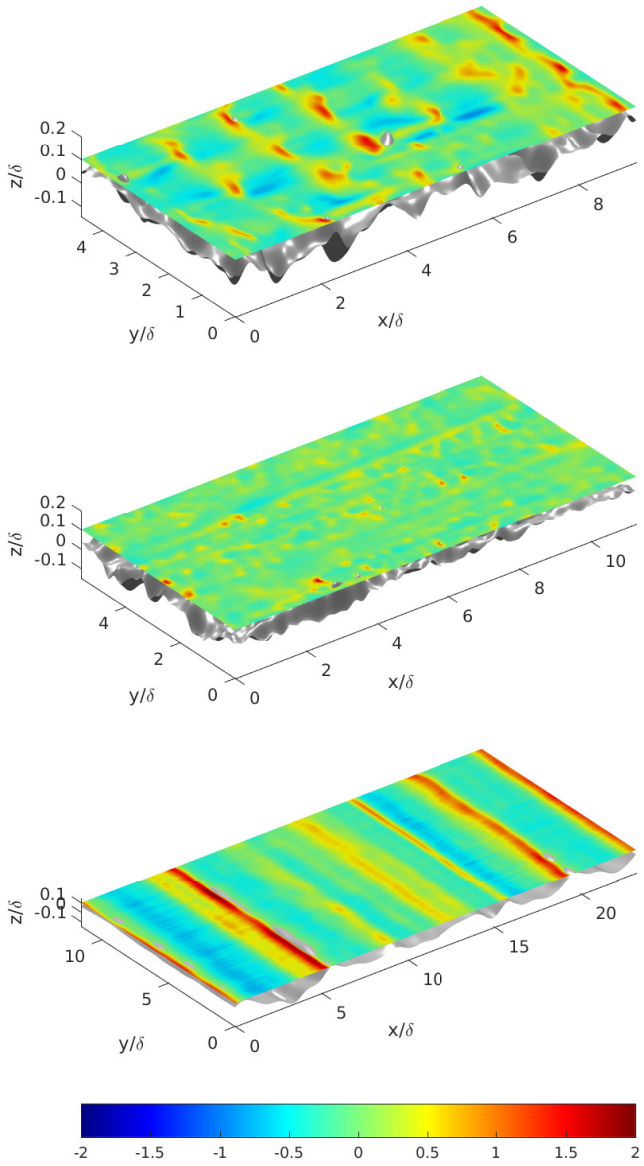

Figure 6.28: Spatial distribution of time-averaged wall-normal velocity, $\overline{w}$, at $z/\delta = 0.1$, from top to bottom, for the s3 (composite_2), s6 (filed_2) and s9 (ground) samples. The grey region represents the wall.

s9 samples (Figure 6.28 (top and bottom)). Both these samples are spanwise anisotropic and promote high wall-normal velocity as the flow incident on the windward faces of their roughness features undergoes an alternating upward and downward motion. The effect is stronger for s9 than for s3. This observation also justifies Figure 6.27 (right) as both these samples have comparatively high L_y^{cor}.

A few common observations are made from the streamwise, spanwise and wall-normal dispersive stress profiles, respectively shown in Figures 6.19, 6.23 and 6.26. In general, dispersive stress peaks are located closer to the rough wall than corresponding Reynolds stress peaks. Also, the rate of decay of dispersive stress with distance from the wall is higher than the corresponding rate of decay of Reynolds stress. $\langle \tilde{u}^2 \rangle$ and $\langle \tilde{v}^2 \rangle$ rapidly

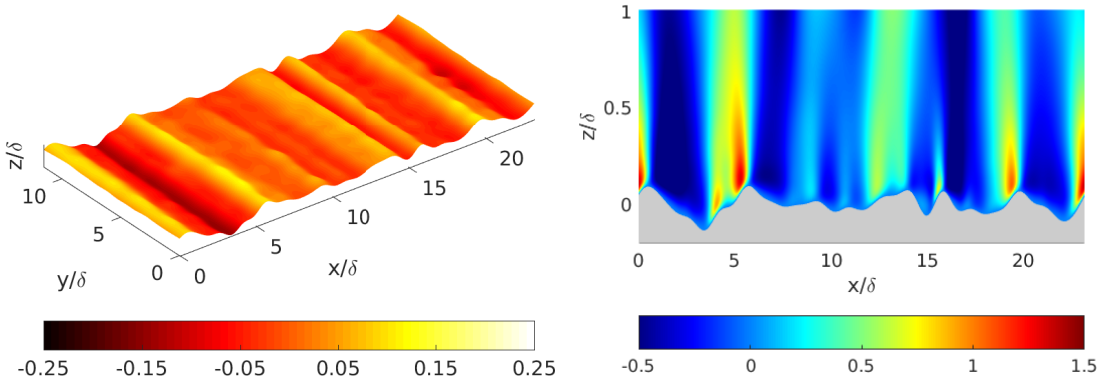

Figure 6.29: Surface plot of the s9 (ground) sample coloured by roughness height, k/δ (left), and spatial distribution of its time-averaged wall-normal velocity, $\overline{w}$, at $y = L_y/2$ (right). The grey region represents the wall.

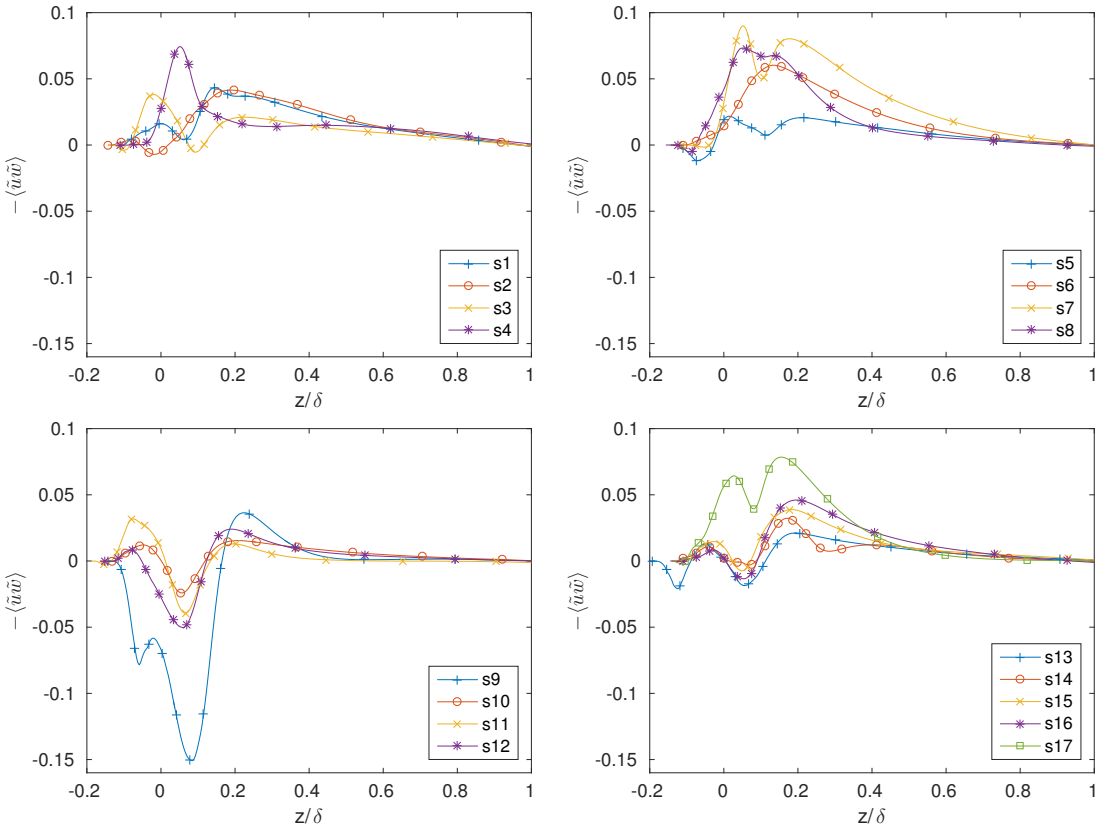

Figure 6.30: Dispersive shear stress profiles, $-\langle\tilde{u}\tilde{w}\rangle$, for the 17 rough surface samples. z/δ is the wall-normal distance.

decay to zero at a relatively short distance from the rough wall. However, the same is not observed for $\langle\tilde{w}^2\rangle$. Some samples, such as s2 (composite_1), s9 (ground) and s14 (spark-eroded_2), show relatively large values of wall-normal dispersive stress up to the channel centre. A possible cause of this is the relatively small channel half-height to roughness height, δ/k, ratio for the current study. This affects some samples more than others. For example, sample s9 (ground) shows the highest values of $\langle\tilde{w}^2\rangle$ away from the wall, chiefly due to its undulating topography and high spanwise correlation length. A surface plot of s9, coloured by its roughness height, is shown in Figure 6.29 (left) and a slice of time-averaged wall-normal velocity, $\overline{w}$, at $y = L_y/2$ is shown in Figure 6.29 (right). The topography promotes high $\overline{w}$ and its effects propagate all the way to the channel centre. This leads to a relatively high wall-normal dispersive stress. Mohajeri et al. [2015] made similar observations from open channel experiments on gravel beds at relatively high $\delta/k \approx 7.5$ to 10.8. In their experiments, wall-normal turbulence intensity was affected the most compared to the streamwise turbulence intensity. The wall-normal dispersive stress, however, rapidly decreased close to the channel centre.

The dispersive shear stress profiles, $-\langle\tilde{u}\tilde{w}\rangle$, are shown in Figure 6.30. The behaviour of $-\langle\tilde{u}\tilde{w}\rangle$ is more complex than the other dispersive stresses because most samples show the presence of multiple peaks. Spatial variation of dispersive shear stress for three representative samples, s3 (composite_2), s8 (gritblasted) and s9 (ground), at $z/\delta = 0.05$ and 0.1, is shown in Figure 6.31. $-\langle\tilde{u}\tilde{w}\rangle$ peaks are seen roughly around these wall-normal distances in Figure 6.30. In general, it is observed that valleys in the samples promote regions of high dispersive shear stress above them. Regions of low $-\tilde{u}\tilde{w}$ are observed close to and above some roughness peaks. Samples s3 and s8 show positive peaks of $-\langle\tilde{u}\tilde{w}\rangle$, which is confirmed from the spatial variation (Figure 6.31 (left)) with the presence of more regions of positive than negative dispersive shear stress. Sample s9 shows a large negative peak of $-\langle\tilde{u}\tilde{w}\rangle$, which from Figure 6.31 (left) is seen as large regions of negative dispersive shear stress. Comparing the spatial variations at $z/\delta = 0.05$ and 0.1 (Figure 6.31 left and right respectively), it is also observed that dispersive shear stress decreases rapidly with wall-normal distance for samples s3 and s8. However, it does not decrease as rapidly for sample s9 (ground). The relatively complex behaviour of the dispersive shear stress is attributed to the highly irregular topography of the samples with varying heights of roughness peaks. From LES studies on block roughness, Xie et al. [2008] observed that blocks of random height gave rise to higher dispersive stresses and larger variations of the flow within the roughness than blocks of uniform height.

To summarise, this chapter has discussed the mean and turbulent statistics, along with flow visualisations, at $Re_\tau = 180$, for the seventeen rough surface samples. Results show considerable variation depending on the surface topography. The simulation data along with surface topographical properties from Table 3.2 form the required database, which is utilised to conduct rough surface parametrisation in the next chapter.

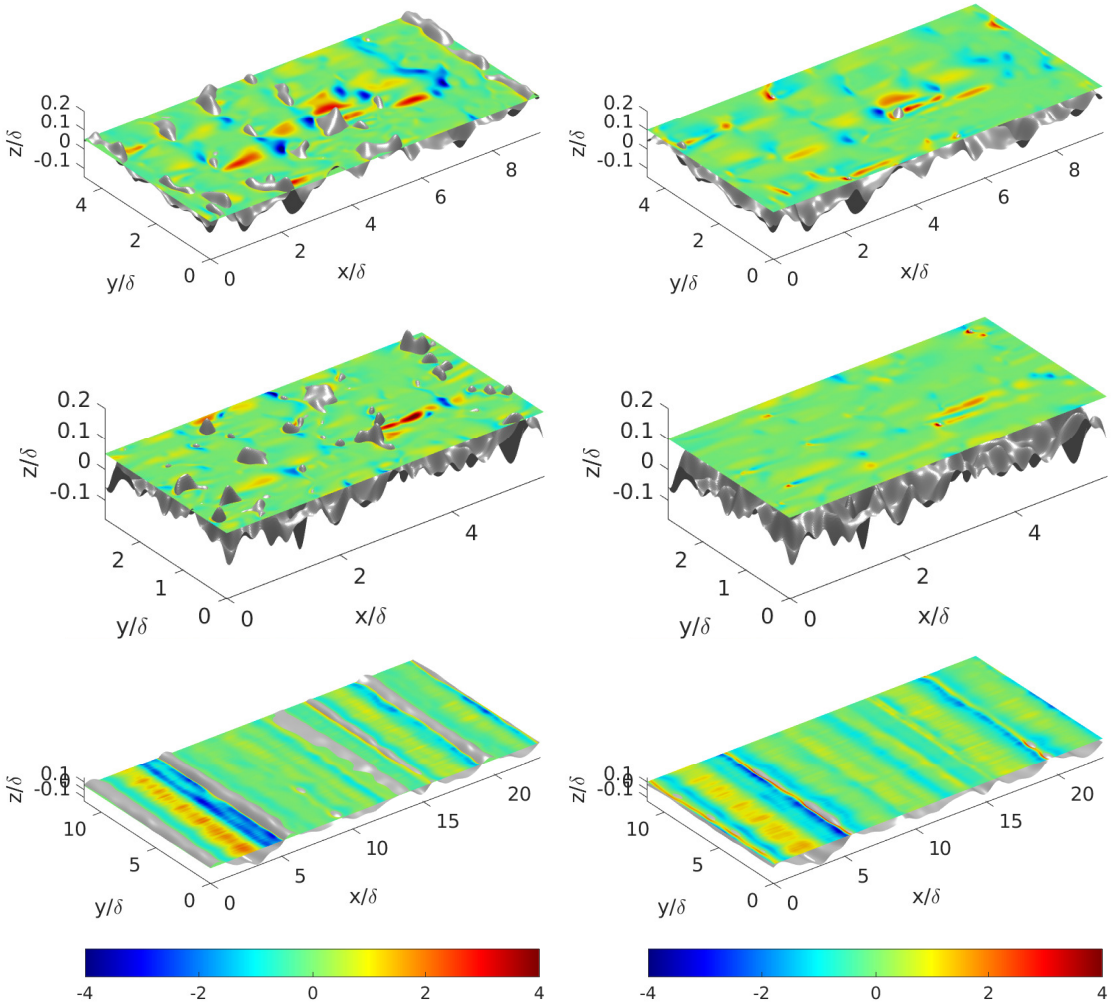

Figure 6.31: Spatial variation of dispersive shear stress, $-\tilde{u}\tilde{w}$, at $z/\delta = 0.05$ (left) and $z/\delta = 0.1$ (right), from top to bottom, for the s3 (composite_2), s8 (gritblasted) and s9 (ground) samples. The grey region represents the wall.

Chapter 7

Dependence on surface topographical properties and parametrisation at $Re_\tau = 180$

The variation of certain flow properties with certain surface topographical properties has been studied in the previous chapter (for example, Figures 6.6, 6.9 and 6.12). However, since one of the main aims of this work is to correlate the roughness function, ΔU^+, with the topographical properties of the surface, a more in-depth study on that is carried out here. Surface properties studied in particular include surface skewness, S_{sk} (also studied by Flack and Schultz [2010]), streamwise effective slope, ES_x (also studied by Napoli et al. [2008] and Schultz and Flack [2009]) and the Sigal-Danberg parameter, Λ_s (also studied by van Rij et al. [2002]). An extensive and methodical parametrisation of topographical properties, which takes into consideration all the properties from Table 3.2, is then presented.

7.1 Dependence of roughness function on surface skewness and effective slope

Skewness, S_{sk} and effective slope, ES are two properties that have been studied extensively in the past (refer to Flack and Schultz [2010], Napoli et al. [2008], Yuan and Piomelli [2014]). Flack and Schultz [2010] mentioned that surface skewness, S_{sk} is an indication of the distribution of peaks and valleys (as discussed in Section 3.2). Based on numerous experiments, they also formulated a relation to predict the equivalent sand-grain roughness based on S_{sk} and RMS roughness height, S_q, given as,

$$(k_{s,eq})_{\mathrm{FS}} \approx 4.43 S_q (1 + S_{sk})^{1.37}. \tag{7.1}$$

In general, ΔU^+ is directly proportional to the equivalent sand-grain roughness height for a particular type of roughness and hence it can be checked whether ΔU^+ correlates individually with S_{sk} or S_q. Figure 7.1 shows plots of ΔU^+ against S_{sk} (left) and ΔU^+

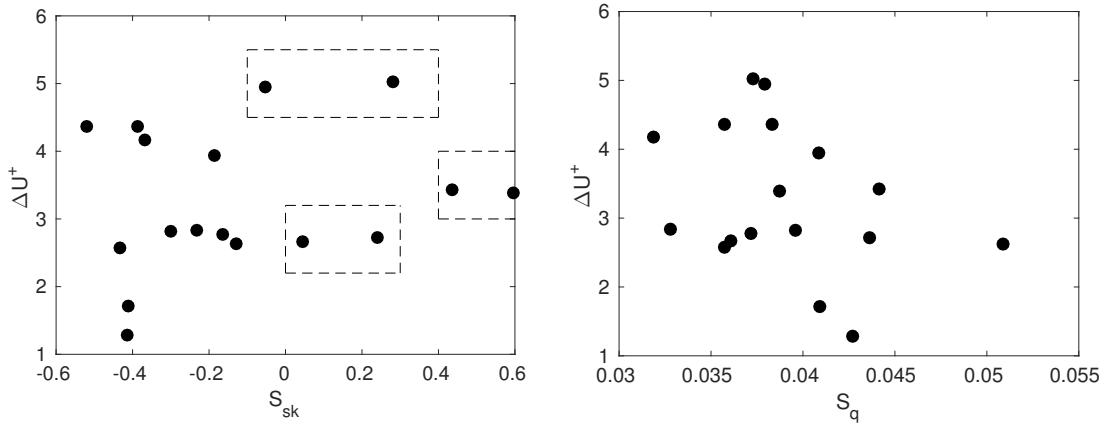

Figure 7.1: Dependence of ΔU^+ on S_{sk} (left) and on S_q (right).

against S_q (right). The correlation of ΔU^+ with both S_{sk} and S_q is poor. The data is quite scattered and no clear relationship can be obtained. Additionally, the plot on the left also shows 3 pairs of samples (data points within dashed black lines) which have approximately equal ΔU^+ but significantly different S_{sk}. These include s4 and s7 (top pair), s1 and s14 (middle pair) and s2 and s15 (bottom pair). It is thus clear that for the current study, neither RMS roughness height nor surface skewness on their own are enough to correlate with ΔU^+. Studies of Yuan and Piomelli [2014] also showed poor agreement between ΔU^+ and S_{sk}. They mentioned the reason for that as the skewness not including surface slope i.e. streamwise effective slope, ES_x, in its definition. Hence skewness is not a suitable parameter for surfaces whose ES_x is an important parameter (refer next paragraph), which include all 17 surfaces in the current study. Referring now to Figure 7.2, which shows the variation of ΔU^+ with the equivalent sand-grain roughness height proposed by Flack and Schultz [2010] given by equation (7.1), it can be seen that ΔU^+ does not correlate well with $(k_{s,eq})_{\mathrm{FS}}$ either and the expected increasing trend of ΔU^+ with the equivalent sand-grain roughness height is not clearly seen. Flack and Schultz [2010] formulated their correlation based on experiments conducted in the fully-rough regime whereas all surfaces at the current $Re_\tau = 180$ are in the transitionally rough regime, which may contribute to

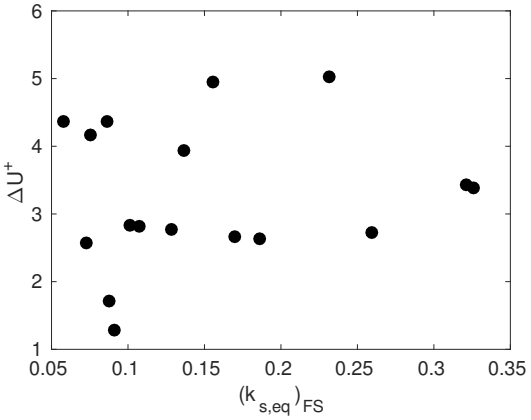

Figure 7.2: Dependence of ΔU^+ on $(k_{s,eq})_{FS}$

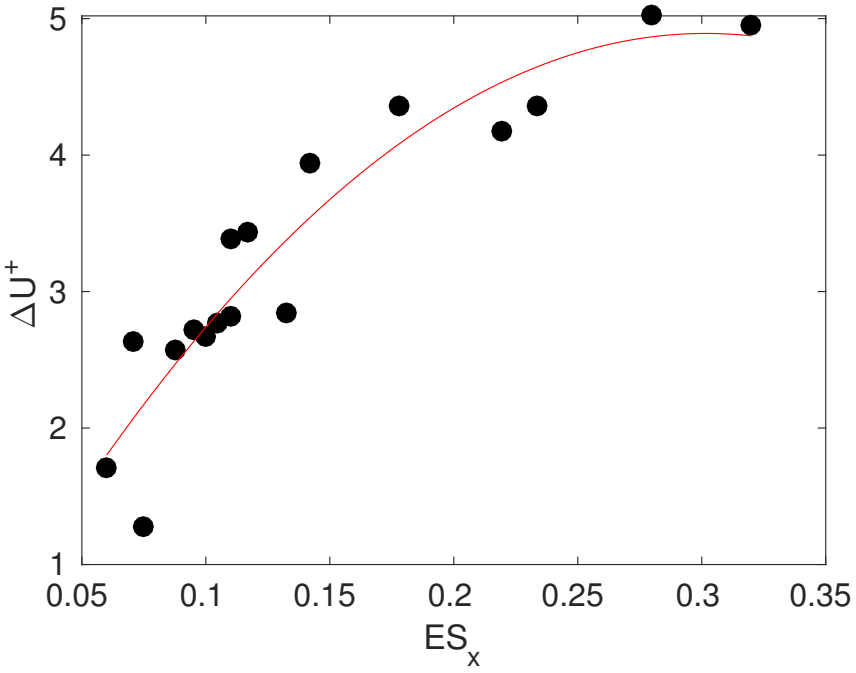

Figure 7.3: Dependence of ΔU^+ on the streamwise effective slope, ES_x. The red line shows a fit to the data.

the data scatter. Also, most surfaces considered by Flack and Schultz [2010] had positive skewness, whereas the current database contains surfaces with both positive and negative skewness.

Figure 7.3 shows a plot of ΔU^+ against the streamwise effective slope, ES_x. The dependence of the roughness function on the streamwise effective slope is evident. The relationship is not linear as seen from the curve fit to the data (red line) also shown. The effective slope was first identified as an important geometrical parameter by Napoli et al. [2008] who conducted DNS studies of irregular random rough surface geometries. Their geometries varied only in the streamwise direction and hence only a streamwise effective slope existed. On the relationship between ΔU^+ and ES_x, they mentioned that ΔU^+ increases linearly up to $ES_x \approx 0.15$, then follows a non-linear curve for larger values of ES_x up to $ES_x \approx 0.55$ and then weakly decreases. Most of these observations can be made from Figure 7.3 as well, though the maximum value of streamwise effective slope for the current set of surfaces is $ES_x \approx 0.32$. A weakly decreasing behaviour in ΔU^+ is observed for the last two data points in Figure 7.3.

Based on experimental studies conducted on close-packed pyramids, Schultz and Flack [2009] proposed the existence of a surface 'waviness' regime where ΔU^+ is strongly dependent on ES_x. This was also supported by Yuan and Piomelli [2014]. All surfaces in the current study appear to lie in the waviness regime as Figure 7.3 shows a strong dependence of ΔU^+ on ES_x. Surfaces whose ΔU^+ is relatively independent of ES_x fall under what Schultz and Flack [2009] termed the surface 'roughness' regime. In this regime, ΔU^+ scales solely on the roughness height. Schultz and Flack [2009] also mentioned that there is a

critical ES_x, which may depend on the type of roughness, separating the waviness and roughness regimes, which in their studies was $ES_x \approx 0.35$. This is the effective slope at which ΔU^+ becomes approximately constant with respect to ES_x. The fact that the current set of surfaces lies in the waviness regime is also responsible for the significant data scatter in the plot of ΔU^+ against $(k_{s,eq})_{\mathrm{FS}}$, shown in Figure 7.2 as this relation was intended for surfaces in the roughness regime.

Figure 7.4 (left) shows a comparison of the variation of ΔU^+ with ES_x for the current study with data from Napoli et al. [2008] and Schultz and Flack [2009]. For similar values of ES_x, values of ΔU^+ in the current study are in general less than those obtained by both references. This is probably because the current study comprises of samples only in the transitionally rough regime, whereas both Napoli et al. [2008] and Schultz and Flack [2009] studied samples in the transitionally rough as well as the fully-rough regimes. In order to make a comparison, values of ΔU^+ from the current study are scaled up to match with the other studies shown. The scale factor is determined by the ratio of the highest ΔU^+ value of Napoli et al. [2008] to the highest ΔU^+ value from the current study and has an approximate value of 2. This means the higher ΔU^+ values are almost half the values obtained by Napoli et al. [2008]. The resulting plot is shown in Figure 7.4 (right). Also shown is a vertical dashed line at $ES_x = 0.35$ which separates the surface waviness regime (on its left) from the surface roughness regime (on its right), as proposed by Schultz and Flack [2009] for their data. Beyond $ES_x = 0.35$, in the data of Schultz and Flack [2009], it is clearly seen that ΔU^+ remains more or less constant with ES_x and scales only with roughness height. For the same values of ES_x, the roughness height increases in the vertical direction in the data of Schultz and Flack [2009]. The plot also puts data from the current study in perspective with other studies in the literature and shows the range of effective slope, comprising a subset of the broad class of irregular roughness.

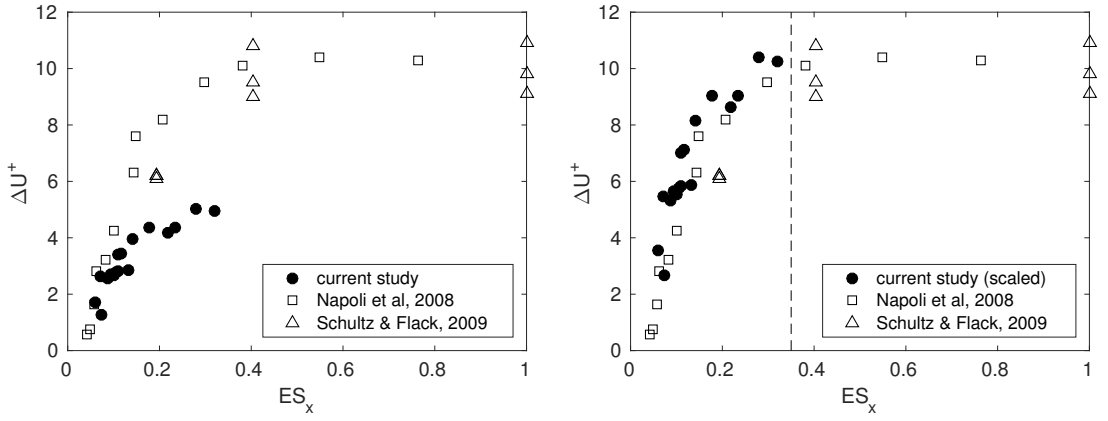

Figure 7.4: Comparison of the variation of ΔU^+ (left) and scaled values of ΔU^+ (right) with ES_x for the current study, Napoli et al. [2008] and Schultz and Flack [2009]. For Schultz and Flack [2009], only cases at their highest Reynolds numbers have been shown, with increasing roughness height in the vertical direction. The vertical dashed line represents the critical $ES_x \approx 0.35$ of Schultz and Flack [2009].

7.2 Dependence of roughness function on the Sigal-Danberg parameter

Next, the dependence of the roughness function on the generalized Sigal-Danberg parameter, Λ_s, is studied. Figure 7.5 shows a plot of ΔU^+ against Λ_s on semilogarithmic axes. This parameter is calculated for all 17 samples from the database using the relations given in Appendix A. The modified version of the parameter as proposed by van Rij et al. [2002],

$$\Lambda_s = \left(\frac{S}{S_f}\right)\left(\frac{S_f}{S_w}\right)^{-1.6},$$

is used in this study (refer to equation (3.1) in Section 3.2 or Appendix A for further details). Λ_s is heavily dependent on the surface topography and hence a broad range of values, spanning three orders of magnitude, is obtained. It is clear from the plot that ΔU^+ and Λ_s are inversely proportional to each other. For higher values of Λ_s, the effect of the rough surface on the flow decreases. It is observed from Table 3.2 that the wetted area parameter for the current set of surfaces is about half the planform area, and hence the value of Λ_s depends mainly on S_f. Effectively, as the frontal area of the roughness elements decreases (which means less roughness), Λ_s increases and hence ΔU^+ decreases. Λ_s takes into account roughness density, shape and direction with respect to the mean flow and hence the data scale very well with ΔU^+. The minimum least squares error fit given by

$$\Delta U^+ = \log(\Lambda_s^{-1.89}) + 8.32, \tag{7.2}$$

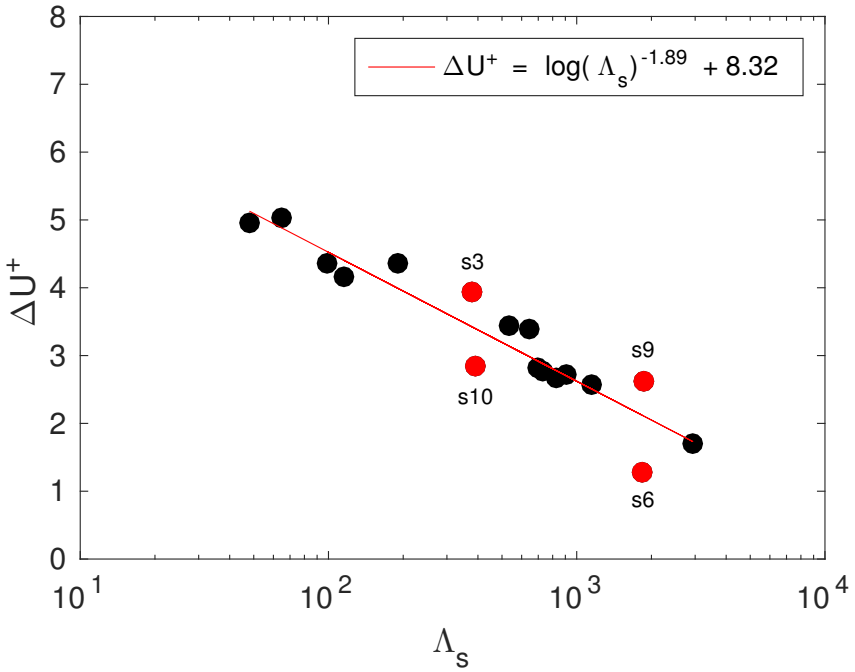

Figure 7.5: Dependence of ΔU^+ on the generalized Sigal-Danberg parameter, Λ_s. Outlier data points shown in red.

is also shown on the plot. The goodness of fit is given by the root mean squared error, $\sigma = 0.3753$ and coefficient of determination, $R^2 = 0.8836$. This is a reasonably good fit and is an indication of the importance of this parameter, despite a few outlier data points. On visual inspection, four samples; s3, s6, s9 and s10 (whose data points are coloured red), appear to be vertically furthest away from the fit. Hence, although the initial fit is good, its quality could be improved if the error in the outlier data points could be reduced. An initial attempt describing a simple mathematical procedure to achieve this follows.

7.2.1 Improving the correlation between ΔU^+ and Λ_s

Before the relationship between ΔU^+ and Λ_s can be improved, a means of quantifying the error in the values of ΔU^+ based on the fit must be decided. Values of Λ_s, ΔU^+ from the simulations (denoted as ΔU^+ (DNS)), ΔU^+ from equation (7.2), (denoted as ΔU^+ (fit)) and the percentage relative errors between the two ΔU^+ values are shown in Table 7.1. The % relative error in the above table is calculated as,

$$\% \text{ relative error} = \frac{|\Delta U^+(\text{DNS}) - \Delta U^+(\text{fit})|}{\Delta U^+(\text{DNS})} \times 100$$

As a first attempt, samples with relative error greater than 10% are selected as candidates for improvement. These include s3 (with relative error = 12.2509%), s6 (69.6037%), s9 (18.1736%) and s10 (20.9501%), as also mentioned previously based on visual inspection. The s1 sample with relative error = 10.7218% is regarded as being on the borderline and not selected.

The idea is to formulate a new parameter which will be a combination of Λ_s and other

sample	Λ_s	ΔU^+ (DNS)	ΔU^+ (fit)	% relative error
s1	639	3.4	3.02	10.7218
s2	919	2.7	2.72	0.7161
s3	378	3.9	3.45	12.2509
s4	48	4.9	5.14	4.9480
s5	116	4.2	4.42	6.2061
s6	1830	1.3	2.15	69.6037
s7	66	5.0	4.88	2.3788
s8	99	4.4	4.55	4.3176
s9	1890	2.6	2.13	18.1736
s10	390	2.8	3.49	20.9501
s11	1153	2.6	2.53	1.0491
s12	2960	1.7	1.76	3.4858
s13	696	2.8	2.95	5.2667
s14	537	3.4	3.16	8.3957
s15	832	2.7	2.80	5.2995
s16	734	2.8	2.90	5.2114
s17	190	4.4	4.01	7.7435

Table 7.1: Percentage relative errors for all samples between ΔU^+ (DNS) and ΔU^+ (fit). Boxed rows represent the outlier samples.

sample	S_{tr}	S_{tr}^{flow}
s3	0.21	4.6666
s6	0.07	0.0345
s9	0.08	11.7172
s10	0.41	1.5641

Table 7.2: S_{tr} and S_{tr}^{flow} values for the 4 outlier samples; s3, s6, s9 and s10.

surface topographical properties such that a plot of ΔU^+ and the new parameter will give a better fit to the data than the initial fit, equation (7.2), obtained from Figure 7.5. Based on all 17 samples, it is not trivial to select the topographical properties to formulate a new parameter. Hence attention is focussed on the properties of the four outliers selected above. From values of S_{tr} and S_{tr}^{flow}, all four samples are observed to be statistically anisotropic, as shown in Table 7.2. The s6 and s9 samples are strongly anisotropic with features aligned in the streamwise and spanwise directions respectively, s3 is anisotropic with features aligned in the spanwise direction and s10 is weakly anisotropic with features somewhat aligned in the spanwise direction as well. The four samples are outliers possibly due to the nature of these properties. The above observations immediately suggest S_{tr} and S_{tr}^{flow} as candidate surface properties to add to the new parameter along with Λ_s. An initial attempt is made at formulating a new parameter comprising of Λ_s, S_{tr} and S_{tr}^{flow}.

The basic idea of improving the fit is to bring the outliers closer to the fit line. The procedure used to incorporate this will undoubtedly change the fit equation but if the relative errors between ΔU^+ (DNS) and ΔU^+ (fit) for all samples are less than the previous fit, then an improvement will have been satisfactorily obtained. Since ΔU^+ will not change for the samples and a new parameter will be plotted on the x-axis, the outliers will shift in the horizontal direction to improve the fit. A graphical representation of this process is shown in Figure 7.6. The previous fit line has been greyed out because it will change after the procedure is complete. Although the new parameter will be formulated based only on the outliers, its value will be different from Λ_s for all samples. Hence, not only the outliers but all points in Figure 7.6 will be shifted in the horizontal direction, although some points will shift more than others.

Several previous studies have formulated surface property correlations based on a power law (for example, Flack and Schultz [2010], van Rij et al. [2002]) and this approach is also used in the current study. However, the surface properties may also be combined using other mathematical approaches, for example, an algebraic relationship (for example, Bons [2005]). Let the new parameter be called Φ and be represented as

$$\Phi = \Lambda_s (S_{tr})^a (S_{tr}^{\text{flow}})^b, \tag{7.3}$$

where a and b are fitting constants that need to be evaluated based on the available outlier data points. When this approach is applied to all data points, they will shift from their original locations in Figure 7.5 by an amount which will differ for each point. This amount is given by the ratio of the Λ_s obtained from equation (7.2) to the original Λ_s. It is clear

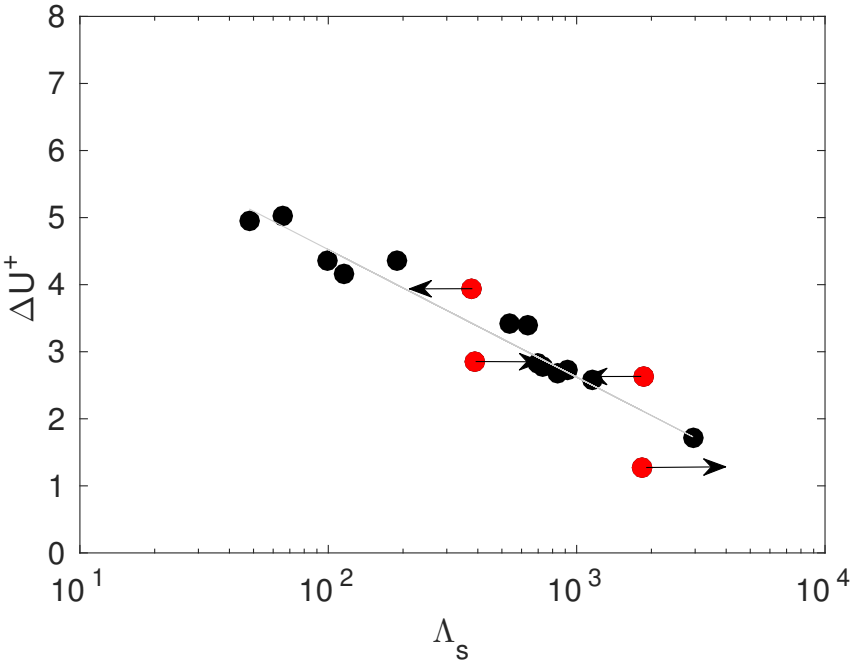

Figure 7.6: Improvement of the correlation between ΔU^+ and Λ_s by introducing S_{tr} and S_{tr}^{flow}. Shifting of only the outliers is shown.

that

$$(\Lambda_s)_{\text{fit}} = -\frac{\exp(\Delta U^+ - 8.32)}{1.89}, \tag{7.4}$$

from equation (7.2). Hence the above-mentioned ratio is given as $(\Lambda_s)_{\text{fit}}/\Lambda_s$. Hence equation (7.3) can also be written as

$$\Phi = \Lambda_s \frac{(\Lambda_s)_{\text{fit}}}{\Lambda_s}. \tag{7.5}$$

Then comparing equations (7.3) and (7.5),

$$(S_{tr})^a (S_{tr}^{\text{flow}})^b = \frac{(\Lambda_s)_{\text{fit}}}{\Lambda_s}. \tag{7.6}$$

$S_{tr}, S_{tr}^{\text{flow}}, (\Lambda_s)_{\text{fit}}$ and Λ_s are known and hence equation (7.6) can be solved to obtain the values of a and b. Since, in this initial attempt, only the outlier points mentioned above are desired to be improved, only their surface properties will be used to compute a and b, and hence Φ.

The parameters required to solve equation (7.6) for the four outliers are given in Table 7.3. Equation (7.6) has only two unknowns but four data points (corresponding to the four outliers) are available to solve it. Values of a and b were determined using all possible 2-point combinations from the four points, and the data was fitted with Φ on a new ΔU^+ against Φ curve for each 2-point combination. The values of a and b that obtained the best fit, determined from the lowest value of σ and highest value of R^2, were selected. A comparison of the relative errors between ΔU^+ (DNS) and ΔU^+ (fit) was also made for the final best fit. There are six 2-point combinations from the four data points to determine

sample	S_{tr}	S_{tr}^{flow}	Λ_s	$(\Lambda_s)_{\text{fit}}$	$(\Lambda_s)_{\text{fit}}/\Lambda_s$
s3	0.21	4.6666	378	210.26	0.5562
s6	0.07	0.0345	1830	5372.28	2.9357
s9	0.08	11.7172	1890	1062.81	0.5623
s10	0.41	1.5641	360	803.09	2.2308

Table 7.3: Parameters required to solve equation (7.6) for the 4 outlier samples; s3, s6, s9 and s10.

a and b. Values of a and b along with σ and R^2 for the six combinations are provided in Table 7.4. The lowest value of $\sigma = 0.3313$ and the highest value of $R^2 = 0.9093$ are obtained on utilising the surface properties of the s6 and s9 samples. Φ thus obtained is given as

$$\Phi = \Lambda_s (S_{tr})^{-0.0472} (S_{tr}^{\text{flow}})^{-0.2824}. \tag{7.7}$$

A plot of ΔU^+ against Φ is shown in Figure 7.7 with the corresponding equation of the new fit line, given as

$$\Delta U^+ = \log(\Phi)^{-1.677} + 7.699. \tag{7.8}$$

The plot shows the new fit as well as the previous fit (from equation (7.2)) to gain a visual understanding of how the fit has changed. The new values of σ and R^2 are an improvement (approximately 12% in σ and 3% in R^2) over the previous values and hence it can be conclusively said that an overall improvement in the fit is obtained.

The relative errors in ΔU^+ for all samples obtained from the new fit are given in Table 7.5. The errors for the four outlier points have reduced compared to Table 7.1. Since the properties of s6 and s9 ultimately obtained the best fit, their relative errors show the greatest decrease. This is also seen from the plot as the data points for s6 and s9 have moved horizontally closer to the new fit line. Although most samples other than the four outliers show an increase, albeit slight, in their relative errors, the final best values of σ and R^2 indicate an acceptable improvement in the fit.

Thus a procedure to improve the fit of ΔU^+ against Λ_s by introducing S_{tr} and S_{tr}^{flow} to formulate a new parameter, $\Phi = \Lambda_s (S_{tr})^{-0.0472} (S_{tr}^{\text{flow}})^{-0.2824}$, has been described. Although the procedure is crude and uses elementary mathematical concepts, an overall improvement

sample	a	b	σ	R^2
s6, s9	-0.0472	-0.2824	0.3313	0.9093
s9, s10	-2.1112	-2.4006	0.7520	0.5327
s3, s9	-6.3109	-6.7107	0.8669	0.3790
s6, s10	-0.7598	0.2842	0.7200	0.5716
s3, s6	0.0339	-0.3468	0.3781	0.8819
s3, s10	-2.2106	-2.5980	0.7650	0.5164

Table 7.4: Values of a and b along with σ and R^2 for the six 2-point combinations from the 4 outlier data points. The boxed row represents the combination giving the best values of σ and R^2.

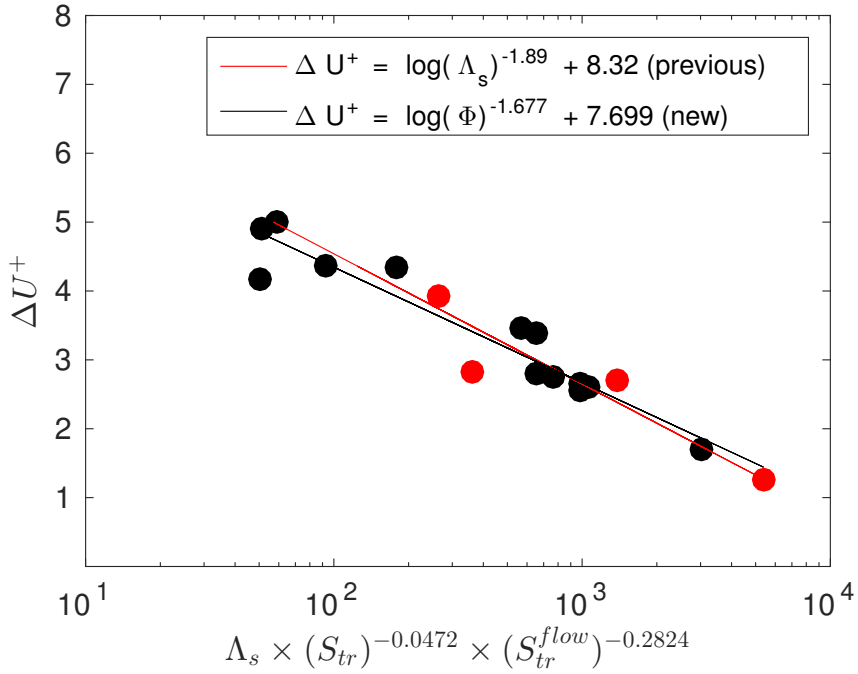

Figure 7.7: ΔU^+ against $\Phi = \Lambda_s(S_{tr})^{-0.0472}(S_{tr}^{\text{flow}})^{-0.2824}$ showing visual improvement in the outliers (red). The previous and new fit lines are also shown for comparison.

sample	Λ_s	ΔU^+ (DNS)	ΔU^+ (fit)	% relative error
s1	639	3.4	2.98	11.9152
s2	919	2.7	2.43	10.0704
s3	378	3.9	3.64	7.3725
s4	48	4.9	4.82	1.4492
s5	116	4.2	4.84	16.4627
s6	1830	1.3	1.44	13.6449
s7	66	5.0	4.73	5.3615
s8	99	4.4	4.40	0.9588
s9	1890	2.6	2.62	0.9126
s10	390	2.8	3.41	20.6798
s11	1153	2.6	2.68	4.6108
s12	2960	1.7	1.86	9.5759
s13	696	2.8	2.98	6.2553
s14	537	3.4	3.07	10.8857
s15	832	2.7	2.68	0.8661
s16	734	2.8	2.87	3.9504
s17	190	4.4	3.92	9.9230

Table 7.5: Percentage relative errors for all samples between ΔU^+ (DNS) and ΔU^+ (fit) obtained using Φ. Boxed rows represent the outlier samples.

of the fit is ultimately obtained, which shows the method is effective. However, a more robust and systematic method (which takes into account all properties of all samples and not just selected properties of the outliers) that correlates ΔU^+ with the surface topographical properties needs to be developed in order to have further confidence in the results.

7.3 Full parametrisation of topographical properties

This section describes a procedure that utilises all the available DNS simulation data and surface topographical properties of all 17 samples from the database to obtain parametric models that relate the effects of roughness on the flow to surface topography. The method has been published in Thakkar et al. [2017].

Although a general solution to the roughness problem must be delayed until a more complete dataset is available for fully rough cases and including a wider Reynolds number range, it seems sensible to try to make as much progress as possible with the present set of restricted data, first of all to find out the issues that arise in formulating a general empirical model and, secondly, to guide the next set of simulations to best exploit the available computational resources. As can be seen from Table 6.1, there is a large variation in the roughness function ΔU^+ that must be due to other parameters, besides the height, that govern the surface topography. To obtain surface properties that possibly influence the roughness function, a fitting process is employed whereby ΔU^+ is plotted against a combination of surface properties and the quality of the fit is improved by successively adding other properties. Additions are made based on a systematic testing of all available properties using specific mathematical forms (algebraic, exponential, logarithmic or power) and selecting the property and form that gives the best possible fit. In Table 7.6, all forms tried for this process are listed for an example surface property, p. The particular form for a property may not necessarily be optimal, since only the above-mentioned four mathematical forms are tested and there may be other forms which might influence the fitting process. Combinations of surface parameters are denoted by λ_n, where $n = 0$ for a baseline model, $n = 1$ for a 1-parameter model and so on. An example for $n = 2$ could be

$$\lambda_2 = \ln\left(\frac{S_f}{S}\right)\left(\frac{4S_q}{S_{z,5\times5}}\right)^{c_1} e^{(c_2 S_{sk})},$$

where c_1 and c_2 are fitting constants.

To measure the success of the method, the root-mean-square error, σ, between the data and a straight-line curve fit using the derived parameter, as well as the value of the coefficient of determination, R^2, of the fit are used. In order to maximise the number of

name of form	algebraic	exponential	logarithmic	power
equation of form	$1 + (c \cdot p)$	$e^{c \cdot p}$	$1 + c \cdot \ln(p)$	p^c

Table 7.6: Mathematical forms of properties tested during the fitting process. c is a fitting constant and p is the value of a given surface property.

property combinations tested, fits giving the 3 lowest values of σ (which means the 3 highest values of R^2) are retained for further improvement. This means, for example, in case of $n = 0$ (or the baseline model), where ΔU^+ is fitted with a single surface property, fits of those properties which obtain the 3 lowest values of σ are selected for further improvement by addition of more properties. However, in the following description, only the best fits are reported. The reason for selecting multiple property combinations is also because a given property combination that gives the lowest value of σ for $n = 1$, for example, may not necessarily give the lowest σ value for $n = 2$ because of the interactions between different surface properties. Parameters are continued to be added until no significant improvement of the fit is obtained and the fit with the final lowest value of σ is selected as the best.

As a start, for $n = 0$ to fit ΔU^+, the performance of a solidity parameter, expressed here in logarithmic form, is considered as

$$\lambda_0 = \ln\left(\frac{S_f}{S}\right). \tag{7.9}$$

Using just this parameter, the best fit to the data is $\Delta U^+ = a\lambda_0 + b$, with $a = 2.0438$ and $b = 8.9035$ and with $\sigma = 0.3807$ and $R^2 = 0.8802$. The resulting straight line is plotted in Figure 7.8 (top left) and already a reasonable fit to the data can be seen. Given the success

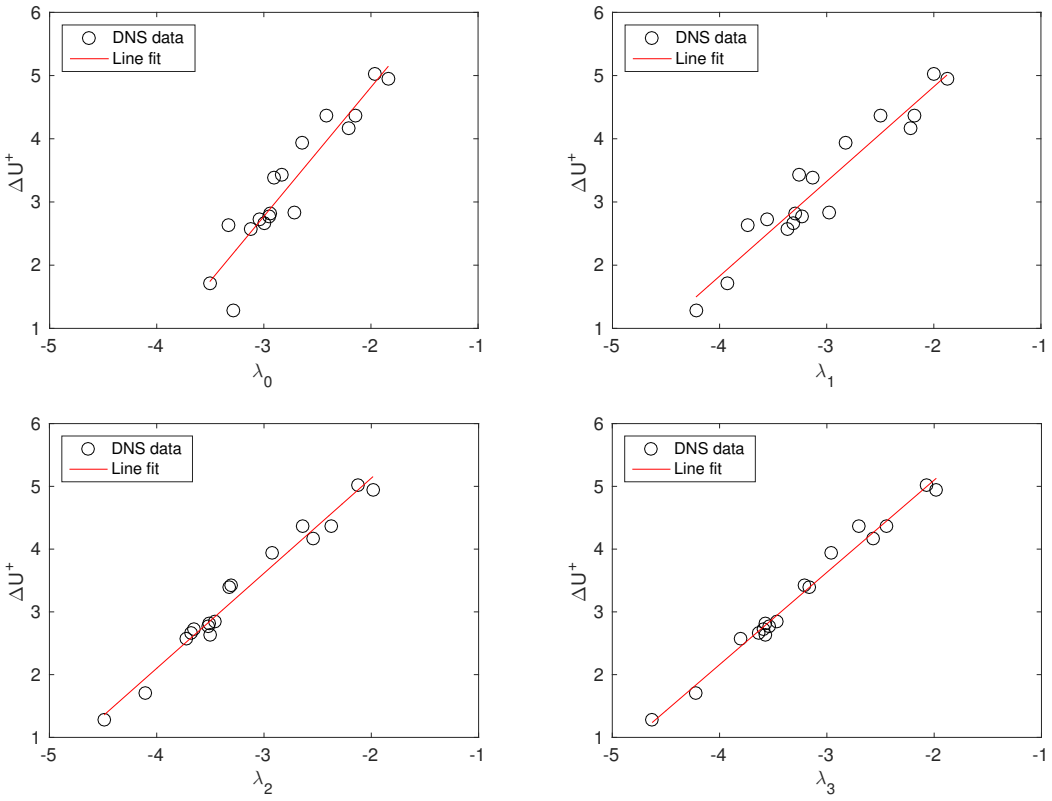

Figure 7.8: Linear fits to the DNS data, correlating the roughness function, ΔU^+, with different parameters λ_0 (top left), λ_1 (top right), λ_2 (bottom left) and λ_3 (bottom right), corresponding to equations (7.9), (7.11), (7.12), (7.13) in the text.

of the simplest measure, the strategy is to introduce modifications to the definition of λ_0 based on additional surface properties as shown in Table 3.2.

Extensions to the solidity parameter have already appeared in the literature and, for irregular surfaces, van Rij et al. [2002] redefined the parameter introduced by Sigal and Danberg [1990], previously given in equation (3.1). A generalisation of this approach is to set

$$\lambda_{SD} = \ln\left[\frac{S_f}{S}\left(\frac{S_f}{S_w}\right)^{\beta}\right], \tag{7.10}$$

where S_w is the wetted area of the forward-facing elements of the surface and Sigal and Danberg [1990] used $\beta = 1.6$ (note that Sigal and Danberg [1990] used the inverse of this parameter whereas the current study uses a definition where λ can be interpreted as the solidity or density of the roughness). However, using this value of β in the present study led to no improvement in the standard error. A separate exercise was undertaken to optimise the value of the exponent, giving $\beta = 0.18$, but with a barely measurable increase in R^2. The reasons for the failure of this additional term are clear from Table 3.2, since for the types of roughnesses considered the wetted area parameter is always about half the planform area i.e. there is an approximate symmetry (of forward-facing and rearward-facing roughness elements) in the roughness samples. Thus the term S_f/S_w introduces no additional useful information. One could continue using (7.10) as the reference parameter and get the same results, but this study prefers only to use parameters that are justified by the data and hence the simple solidity, λ_0, is taken as the baseline property.

The next step is to test each of the potential surface parameters as modifications to λ_0. The best two, with almost identical performance, were the streamwise correlation length parameter, $L_x^{\mathrm{cor}}/S_{z,5\times5}$, and the flow texture ratio, S_{tr}^{flow}. The success of both suggests that the spanwise correlation length is less important and the best-performing parameter, with a single optimised coefficient for $n = 1$, is retained to give

$$\lambda_1 = \lambda_0\left[1 + 0.067\ln\left(\frac{L_x^{\mathrm{cor}}}{S_{z,5\times5}}\right)\right]. \tag{7.11}$$

The improved fit to the data is shown in Figure 7.8 (top right), with $\sigma = 0.3073$ and $R^2 = 0.9220$. It is interesting that a streamwise correlation length enters as the next-most important parameter after the solidity since this type of parameter doesn't appear in many correlations. The parameter is additionally intriguing since dense roughness cases will have low values of $L_x^{\mathrm{cor}}/S_{z,5\times5}$ and from the correlation this would lead to lower λ_1 and hence lower ΔU^+, which is indeed what is observed (Jiménez [2004]). The absence of dense roughness cases ($S_f/S > 0.15$) from the current sample set means that this cannot be tested fully, and addressing this point would be a priority for future simulations.

The process is continued to define the best models for $n = 2$ and 3. The best model for $n = 2$ is found to include the relative rms roughness height parameter, S_q, as

$$\lambda_2 = \lambda_0\left[1 + 0.09\ln\left(\frac{L_x^{\mathrm{cor}}}{S_{z,5\times5}}\right)\right]\left(\frac{4S_q}{S_{z,5\times5}}\right)^{-0.50}, \tag{7.12}$$

parameter	a	b	σ	R^2
λ_0	2.0438	8.9035	0.3807	0.8802
λ_1	1.4988	7.8221	0.3073	0.9220
λ_2	1.5150	8.1607	0.1806	0.9731
λ_3	1.4699	8.0394	0.1383	0.9842

Table 7.7: Best fit parameters for λ_0, λ_1, λ_2 and λ_3, corresponding to equations (7.9), (7.11), (7.12), (7.13) in the text. $\Delta U^+ = a\lambda_n + b$, where a = slope of the fit and b = y-axis intercept. σ = rms error of the fit and R^2 = coefficient of determination.

with $\sigma = 0.1806$ and $R^2 = 0.9731$. The best model for $n = 3$ includes the skewness, S_{sk}, as

$$\lambda_3 = \lambda_0 \left[1 + 0.09 \ln\left(\frac{L_x^{\mathrm{cor}}}{S_{z,5\times5}}\right)\right] \left(\frac{4S_q}{S_{z,5\times5}}\right)^{-0.44} e^{(-0.074 S_{sk})}, \tag{7.13}$$

with $\sigma = 0.1383$ and $R^2 = 0.9842$. Figure 7.8 (bottom left) and (bottom right) show the continued improvements seen with the λ_2 and λ_3 representations. The largest remaining errors in the fit to the data are less than $0.1u_\tau$. Additional parameters were tested, but with no significant further improvements found. Fit parameters for λ_0, λ_1, λ_2 and λ_3 are summarised in Table 7.7. Tests were also run by removing parameters individually, confirming that a ranking in order of importance is (i) solidity, (ii) streamwise correlation length non-dimensionalised by the mean peak-to-valley height, (iii) rms roughness height non-dimensionalised by the mean peak-to-valley height and (iv) skewness. Note that the roughness height is not one of these parameters since all the cases were run for the same $S_{z,5\times5}$. Had the simulations been in the fully-rough regime, the equivalent sand-grain roughness, $k_{s,eq}^+$, would be determined as a constant (dependent on all the above parameters) multiplied by some suitable measure of the roughness height, for example S_q^+ or $S_{z,5\times5}^+$. Both rms roughness height and skewness are part of the model formulated by Flack and Schultz [2010] and Flack et al. [2016] so it is no surprise to see them here. Also, it has been pointed out in Section 3.2 that the streamwise effective slope, mean and rms streamwise forward-facing surface angles are proportional to the solidity for these surfaces, and hence cannot be considered as independent parameters.

A point of caution is that the above analysis is only the first step. As more samples are added covering different types of roughnesses (dense, for example) it is expected that additional parameters might be required. What is important is that we now have a systematic method to incorporate additional parameters. It is important to note that the models in equations (7.9) to (7.13) should not be used for $k_{s,eq}^+$ since the current data were all taken in the transitionally rough regime. Nevertheless, a number of parameters that contribute significantly to the roughness function in this regime have been identified and it is likely that the same parameters contribute to the determination of $k_{s,eq}^+$. The same numerical coefficients would only be found if all the samples followed the same path through the transitionally rough regime, which is unlikely.

A similar approach as above was also utilised to fit surface property data to the value

of peak TKE from Table 6.1. Different parameters are seen to appear in the model as the fluctuations behave differently with property combinations as compared to ΔU^+. The various models obtained for this process are given below.

$n = 0$:

$$\lambda_0 = \ln(\overline{\alpha}). \tag{7.14}$$

$n = 1$:

$$\lambda_1 = \lambda_0 e^{(0.38 S_{sk})}. \tag{7.15}$$

$n = 2$:

$$\lambda_2 = \lambda_0 e^{(0.24 S_{sk})} \left[1 + 0.70 \ln\left(\frac{4S_q}{S_{z,5\times5}}\right)\right]. \tag{7.16}$$

$n = 3$:

$$\lambda_3 = \lambda_0 e^{(0.19 S_{sk})} \left[1 + 0.64 \ln\left(\frac{4S_q}{S_{z,5\times5}}\right)\right](1 - 0.70 E S_y). \tag{7.17}$$

The fits for the above models are shown in Figure 7.9 (λ_0: top left, λ_1: top right, λ_2: bottom left and λ_3: bottom right) and fit parameters are summarised in Table 7.8. Although fits are reported only up to $n = 3$, further improvements, following the same systematic fitting approach as described for ΔU^+, are seen up to $n = 5$. Values up to $\sigma = 0.0244$ and $R^2 = 0.9820$ are obtained when the average roughness height, S_a, in its algebraic form and

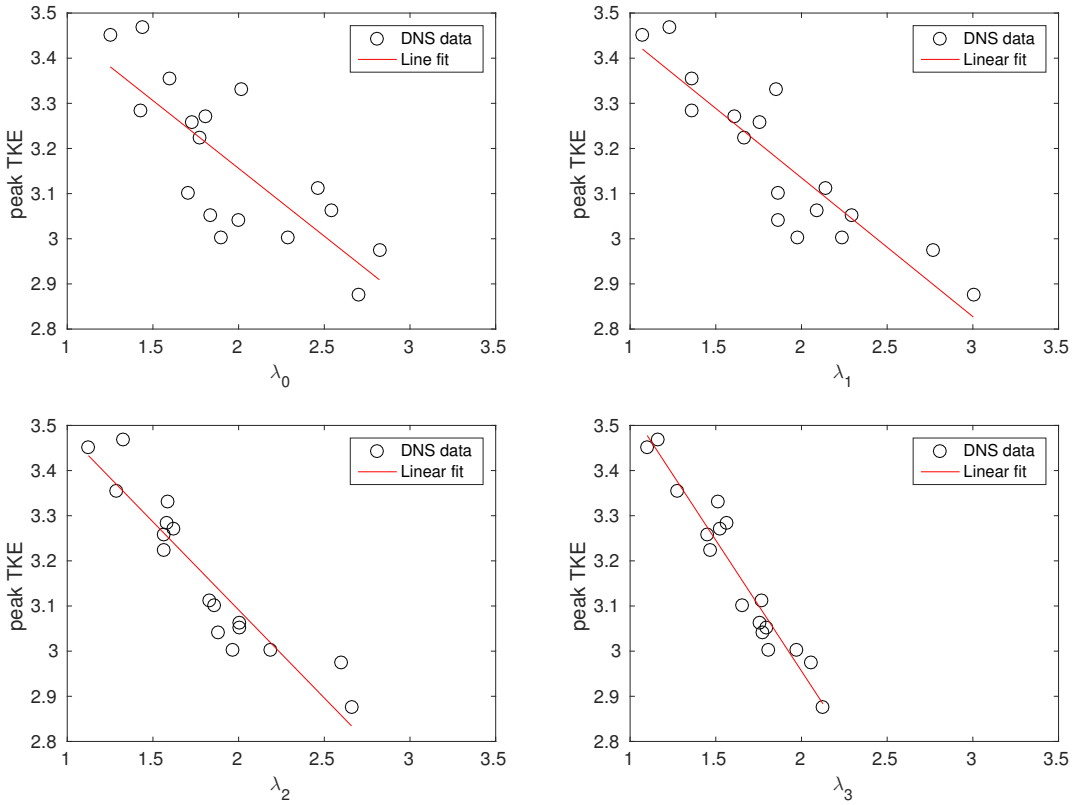

Figure 7.9: Linear fits to the DNS data, correlating the peak TKE, with different parameters λ_0 (top left), λ_1 (top right), λ_2 (bottom left) and λ_3 (bottom right), corresponding to equations (7.14), (7.15), (7.16) and (7.17) in the text.

parameter	a	b	σ	R^2
λ_0	-0.3004	3.7568	0.1897	0.6169
λ_1	-0.3074	3.7498	0.0966	0.8048
λ_2	-0.3901	3.8716	0.0653	0.8681
λ_3	-0.5765	4.1149	0.0352	0.9288

Table 7.8: Best fit parameters for λ_0, λ_1, λ_2 and λ_3, corresponding with equations (7.14), (7.15), (7.16), (7.17), in the text. Peak TKE $= a\lambda_n + b$, where a = slope of the fit and b = y-axis intercept. σ = rms error of the fit and R^2 = coefficient of determination.

shortest correlation length, S_{al}, in its power form (both properties non-dimensionalised by $S_{z,5\times5}$) are included in the model. However, due to the relatively small size of the sample database for fitting purposes, the influence of these properties is probably not as significant as the ones seen up to $n = 3$. For $n < 3$, property combinations other than equation (7.16) may give lower values of σ. But since equations (7.15) and (7.16) finally lead to equation (7.17), which ultimately gives the lowest σ value of all final fits tested, it is selected as the best fit and is discussed here. The baseline parameter is the mean forward-facing surface angle, $\overline{\alpha}$, which is an angle parameter as opposed to S_f/S, which is an area parameter, seen in the case of ΔU^+. However, it has been shown in Figure 3.7 that S_f/S and $\overline{\alpha}$ are approximately linearly related. Also, higher values of $\overline{\alpha}$ in general correspond to a higher roughness effect (from higher values of ΔU^+, refer Tables 3.2 and 6.1 and Figure 7.10) and hence its influence on the fluctuations would be significant. Other baseline parameters that gave σ values comparable to $\overline{\alpha}$ include α_{rms}, S_f/S, and ES_x, all in logarithmic form. This is not too surprising as the four parameters are interrelated. Surface skewness, S_{sk}, is the next important parameter and after that comes the rms roughness height non-dimensionalised by the mean peak-to-valley-height, $S_q/S_{z,5\times5}$, both of which also appear in λ_1 and λ_2 respectively for the other baseline parameters, albeit in different forms. Spanwise effective slope, ES_y, is the next parameter to enter the fit, the appearance of which could relate to how the streamwise flow navigates around the roughness features. It would be interesting

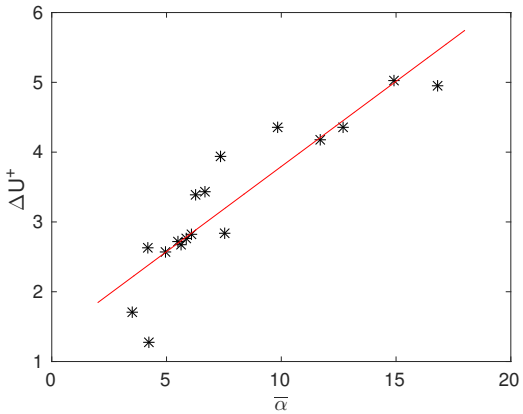

Figure 7.10: Variation of the mean forward-facing surface angle, $\overline{\alpha}$ (degrees), with ΔU^+. The red line shows a fit to the data.

in the future to understand why certain parameters enter the fit as opposed to others, which is not considered in this study. The baseline TKE fit is not as good as the fit for ΔU^+ but significant improvement is obtained until λ_3. A separate fitting study conducted for the profile peak streamwise fluctuations, $\langle\overline{u'^2}\rangle_{\max}$, alone also gave the same properties influencing the fit, although in a slightly different order.

Thus a methodical procedure to correlate the roughness function, ΔU^+, and peak TKE to the surface topography has been described. Although the procedure does not achieve complete generality due to the simulation data being in the transitionally rough regime and the relatively low effective slope of the samples, it does give a very good indication of which topographical properties influence roughness effects. Extension to the fully-rough regime is straightforward but requires larger computational resources. Increasing the size of the dataset by introducing more surfaces having different properties would serve to increase the generality of the fitting process.

Chapter 8

Results - Reynolds number dependence

It is common to carry out experimental studies for a given rough surface or a selection of rough surfaces over a range of Reynolds number, Re_τ. In some cases, the Reynolds number spans the entire range of roughness regimes: hydraulically smooth, transitionally rough and fully-rough. The best known example of such an experimental investigation is the extensive study carried out by Nikuradse [1933] on sand-roughened pipes. More recent studies include experiments by Ligrani and Moffat [1986] on close-packed spheres, Schultz and Flack [2009] on pyramids, Shockling et al. [2006] and Schultz and Flack [2007] on honed roughness and Flack et al. [2016] on gritblasted surfaces. Only a few computational studies exist in this area and the most recent one is the DNS work of Chan et al. [2015] for sinusoidal roughness in pipes.

To show that a Reynolds number sweep using numerical simulations is possible for a highly irregular rough surface, the gritblasted sample (s8 from Table 3.1 and Figure 3.4 (h)) is subject to DNS for a wide Reynolds number range, where $180 \leq Re_\tau \leq 720$ and the roughness Reynolds number, $3.75 \leq k^+ \leq 120$. The mean flow statistics are studied for all cases. Also studied is the behaviour of the roughness function with varying k^+, which then leads to a characterisation of the surface in the entire Reynolds number range. A similar study was also performed on the graphite sample (s7 from Table 3.1 and Figure 3.4 (g)) by Busse et al. [2016] but with the lowest $k^+ = 15$ and with a focus on near-wall flow physics, where a comparative study of the results for the graphite and gritblasted samples was conducted.

8.1 Simulation parameters and sample construction

Table 8.1 shows the simulation parameters for the Reynolds number dependence study. The lowest Reynolds number simulated is $Re_\tau = 180$, as the presence of low-Reynolds number effects is seen at lower Re_τ. For example, simulations were conducted at $Re_\tau = 120$ ($k^+ = 20$) and $Re_\tau = 90$ ($k^+ = 15$). The plot of ΔU^+ against k^+ on semilogarithmic axes showed a different trend at these lower k^+ and the expected behaviour of $\Delta U^+ \to 0$

k^+	3.75	7.5	15	30	40	60	90	120
Re_τ	180	180	180	180	240	360	540	720
k/δ	1/48	1/24	1/12	1/6	1/6	1/6	1/6	1/6
tiles	8×8	4×4	2×2	1×1	1×1	1×1	1×1	1×1
n_x	2304	1152	640	320	320	432	720	864
n_y	1152	576	320	160	160	216	360	432
n_z	192	192	288	288	352	576	864	1056
Δx^+,Δy^+	0.4398	0.8797	1.5834	3.1669	4.2225	4.6917	4.2225	4.6917
$\lambda_{\min}/\Delta x$	12	12	13	13	13	18	30	36
$\Delta z^+_{\max}$	3.2827	3.7635	2.3095	3.7235	4.7549	4.3628	3.7239	4.7556

Table 8.1: Simulation parameters for the Reynolds number dependence study.

as $k^+ \to 0$ was not seen. This is shown in Figure 8.1 which also shows the Colebrook interpolation formula and the data of Nikuradse [1933] for reference. Hence $Re_\tau = 120$ and 90 were discarded and lower k^+ values were obtained by an alternative tiling method.

The computational domain size for the s8 sample is $(5.63\delta \times 2.815\delta)$ for $k/\delta = 1/6$, which gives $k^+ = 30$ at $Re_\tau = 180$. To increase k^+ beyond this value, Re_τ is simply increased, while maintaining $k/\delta = 1/6$. However, to obtain lower values of $k^+ < 30$, while keeping a minimum $Re_\tau = 180$, the roughness height must be decreased. Since the roughness height scales with the domain size, a lower k/δ is obtained through a smaller domain. However, in order to maintain a minimum domain size (in conjunction with the streamwise domain requirement of at least 5δ, as mentioned in Section 2.2.1), the smaller domain for a particular k/δ is tiled (or replicated) in the streamwise and spanwise directions to obtain the minimum required domain size. For example, to obtain the sample for $k^+ = 15$, the sample at $k^+ = 30$ (Figure 8.2 (left)) is shrunk to half its domain size to reduce the roughness height from $k/\delta = 1/6$ to $k/\delta = 1/12$ and is then replicated to obtain 2×2 tiles (Figure 8.2 (right)). Hence, the new sample domain size is $(5.63\delta \times 2.815\delta)$ and has $k^+ = 15$ at $Re_\tau = 180$. The same approach is adopted to obtain samples for lower k^+. The 'tiles' parameter, along with k/δ, from Table 8.1 shows how each sample is constructed

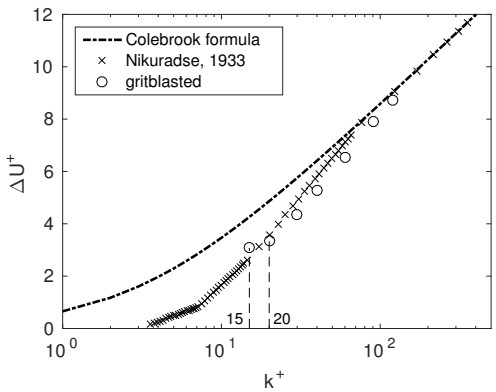

Figure 8.1: ΔU^+ data for the Reynolds number dependence study showing low Reynolds number effects at $k^+ = 20$ and 15 (data points indicated by vertical dashed lines).

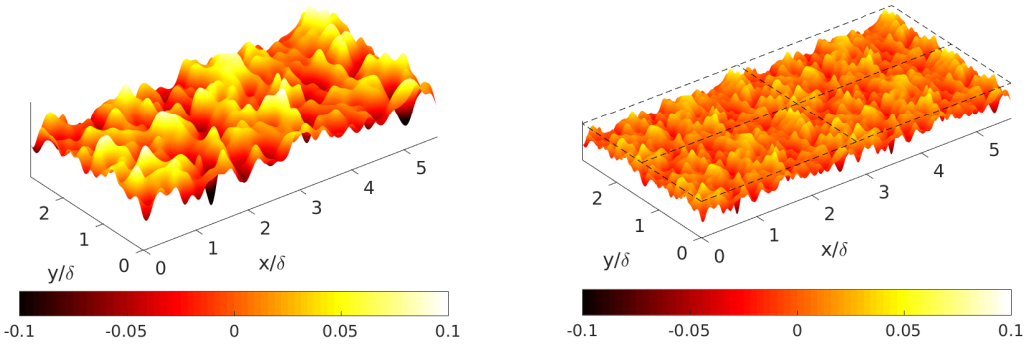

Figure 8.2: Surface plots showing the tiling procedure; original sample for $k^+ = 30$ (left) and tiled sample for $k^+ = 15$ (right). The dashed lines denote tile boundaries. Samples coloured by roughness height, k/δ. Scale of plots increased in the wall-normal direction for clarity.

for the corresponding k^+. This approach is possible because the sample is periodic in the streamwise and spanwise directions and hence no discontinuity will be present at the tile boundaries.

From the meshing criteria described in Section 2.3.2 and values of Δx^+ and $\lambda_{\min}/\Delta x$ in Table 8.1, it is observed that for $k^+ \leq 30$, the minimum wavelength meshing criterion is dominant whereas for $k^+ > 30$, the Reynolds number meshing criterion is dominant. The fact that the sample at $k^+ = 30$ is dominated by minimum-wavelength meshing is inherent in its topography. However, the minimum Fourier wavelength of the sample decreases proportionately due to shrinking and tiling; for example $(\lambda_{\min})_{k^+=15} = (\lambda_{\min})_{k^+=30}/2$ and hence all samples for $k^+ < 30$ are also dominated by the minimum-wavelength mesh requirement.

8.2 Influence on the mean flow statistics

It is known that, in general, the effect of roughness, and hence ΔU^+, increases with k^+. Table 8.2 shows the values of ΔU^+ along with mean centreline velocity, U_c^+, and mean streamwise bulk velocity, U_b, for all cases in the Reynolds number dependence study. The current ΔU^+ values have been computed based on smooth-wall simulations with domain size $12\delta \times 6\delta$ (as mentioned in Section 4.1). As roughness decreases (lower k^+) and the flow approaches smooth-wall conditions, statistics may become more sensitive to computational domain size. Hence, for the three smallest $k^+ = 15$, 7.5 and 3.75, which are all at $Re_\tau = 180$,

k^+	0	3.75	7.5	15	30	40	60	90	120
Re_τ	180	180	180	180	180	240	360	540	720
U_c^+	18.44	18.09	17.65	16.32	14.08	13.84	13.61	13.32	13.38
U_b	15.77	15.21	14.48	12.75	9.97	9.79	9.59	9.38	9.39
ΔU^+	0	0.35	0.79	2.12	4.36	5.28	6.52	7.92	8.72

Table 8.2: ΔU^+ values along with mean centreline, U_c^+, and mean streamwise bulk, U_b, velocities for the Reynolds number dependence study. The smooth-wall data, $k^+ = 0$, has been obtained using a domain size of $12\delta \times 6\delta$ (refer Section 4.1)

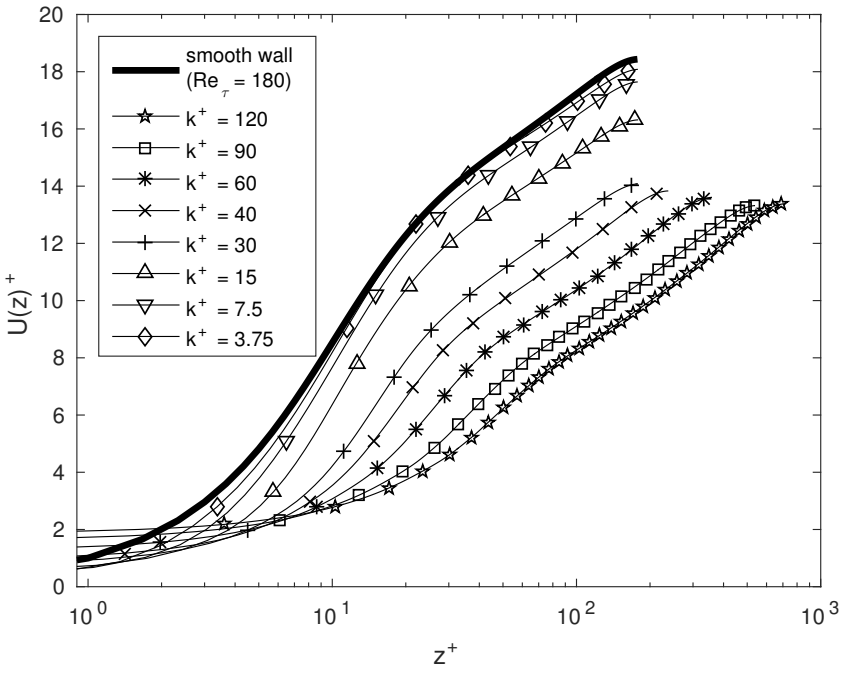

Figure 8.3: Mean streamwise velocity profiles, $U(z)^+$, for the Reynolds number dependence study. $z^+ = zu_\tau/\nu$ is the wall-normal distance in wall-units and $k^+ = ku_\tau/\nu$ is the roughness Reynolds number.

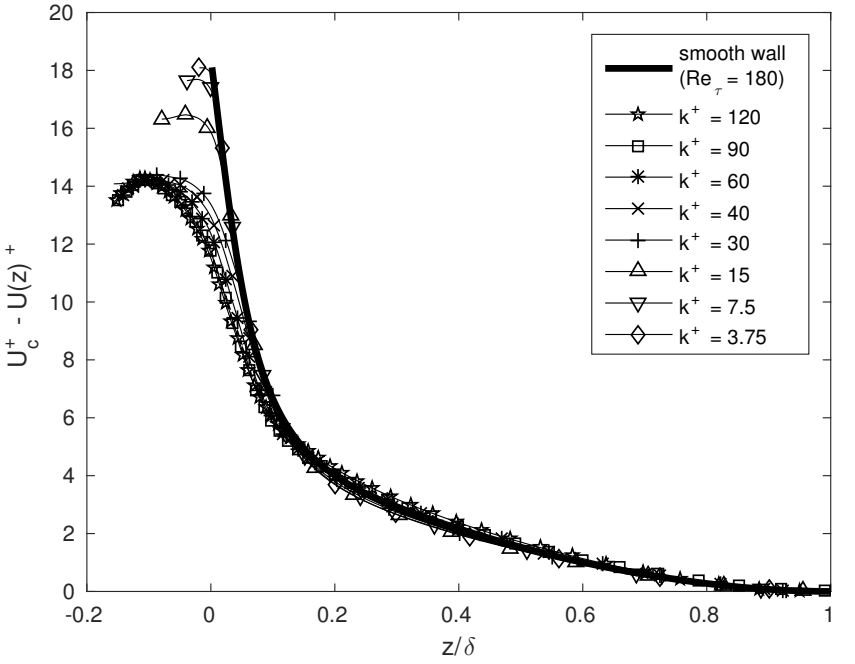

Figure 8.4: Mean streamwise velocity defect profiles for the Reynolds number dependence study. U_c^+ is the mean streamwise centreline velocity in wall-units, z/δ is the wall-normal distance and $k^+ = ku_\tau/\nu$ is the roughness Reynolds number.

ΔU^+ was also computed based on a smooth-wall simulation with the same domain size as the rough sample under consideration, $5.63\delta \times 2.815\delta$. Other parameters for this smooth-wall simulation were: $n_x \times n_y \times n_z = 128 \times 128 \times 224$ with $\Delta x^+ = 7.92$, $\Delta y^+ = 3.96$, $\Delta z^+_{\text{min}} = 0.667$ and $\Delta z^+_{\text{max}} = 4.6979$, $U_c^+ = 18.46$ and $U_b = 15.83$. A comparison with Table 8.2 shows a 0.02 difference in U_c^+, which, although changes ΔU^+ by the same amount, does not have a significant impact on the results.

From Table 8.2, for the two highest k^+ (90 and 120), U_b is very similar, with the difference being approximately 0.1%. This is an indication that the effective friction factor for these cases is approximately independent of k^+ and hence Re_τ, thus confirming their presence in the fully-rough regime (Busse et al. [2016]).

Figure 8.3 shows time-averaged mean streamwise velocity profiles, $U(z)^+$, against wall-normal distance in wall-units, z^+, on semilogarithmic axes. Also shown for reference is the smooth-wall profile for $Re_\tau = 180$. A clear roughness effect is seen at all k^+, except $k^+ = 3.75$ where the downward shift in the profile is almost unnoticeable. This is also evident from its value of $\Delta U^+ = 0.35$ (Table 8.2). The downward shift increases progressively with k^+. Figure 8.4 shows time-averaged mean streamwise velocity defect profiles, $U_c^+ - U(z)^+$, against wall-normal distance, z/δ. Also shown for reference is the smooth-wall velocity defect profile at $Re_\tau = 180$. Profiles for $k^+ \geq 30$ show a similar trend throughout. The effect of smaller roughness height for $k^+ \leq 15$ is seen in the lower part of the profiles as larger values of velocity defect are observed. All profiles collapse for $z/\delta \geq 0.1$, which indicates that outer-layer similarity is preserved and the Townsend [1976] hypothesis is satisfied for the mean flow. This is observed even for $k^+ \geq 30$, where all cases have a relatively small value of $\delta/k = 6$.

8.3 Influence on the roughness function

Figure 8.5 (top) shows the variation of ΔU^+ with k^+ on semilogarithmic axes along with the data of Nikuradse [1933], the fully-rough asymptote, given by

$$\Delta U^+ = \frac{1}{\kappa} \ln(0.3k^+_{s,eq}) \tag{8.1}$$

and the Colebrook interpolation formula, given by Jiménez [2004] as

$$\Delta U^+ = \frac{1}{\kappa} \ln(1 + 0.3k^+_{s,eq}). \tag{8.2}$$

In both the above equations, $\kappa = 0.4$ and $k_{s,eq}$ is the equivalent sand-grain roughness height.

The physical explanation of the behaviour in Figure 8.5 (top) is as follows. With increasing k^+, in general, the effect of roughness on the flow increases, as seen by the increase in ΔU^+. In the hydraulically smooth regime, k^+ is so small compared to the thickness of the viscous sublayer of the turbulent boundary layer that the flow does not feel any effect of the roughness. The drag in this regime is dominated by the viscous component. As k^+ increases with respect to the boundary layer thickness and the flow reaches the transitionally rough

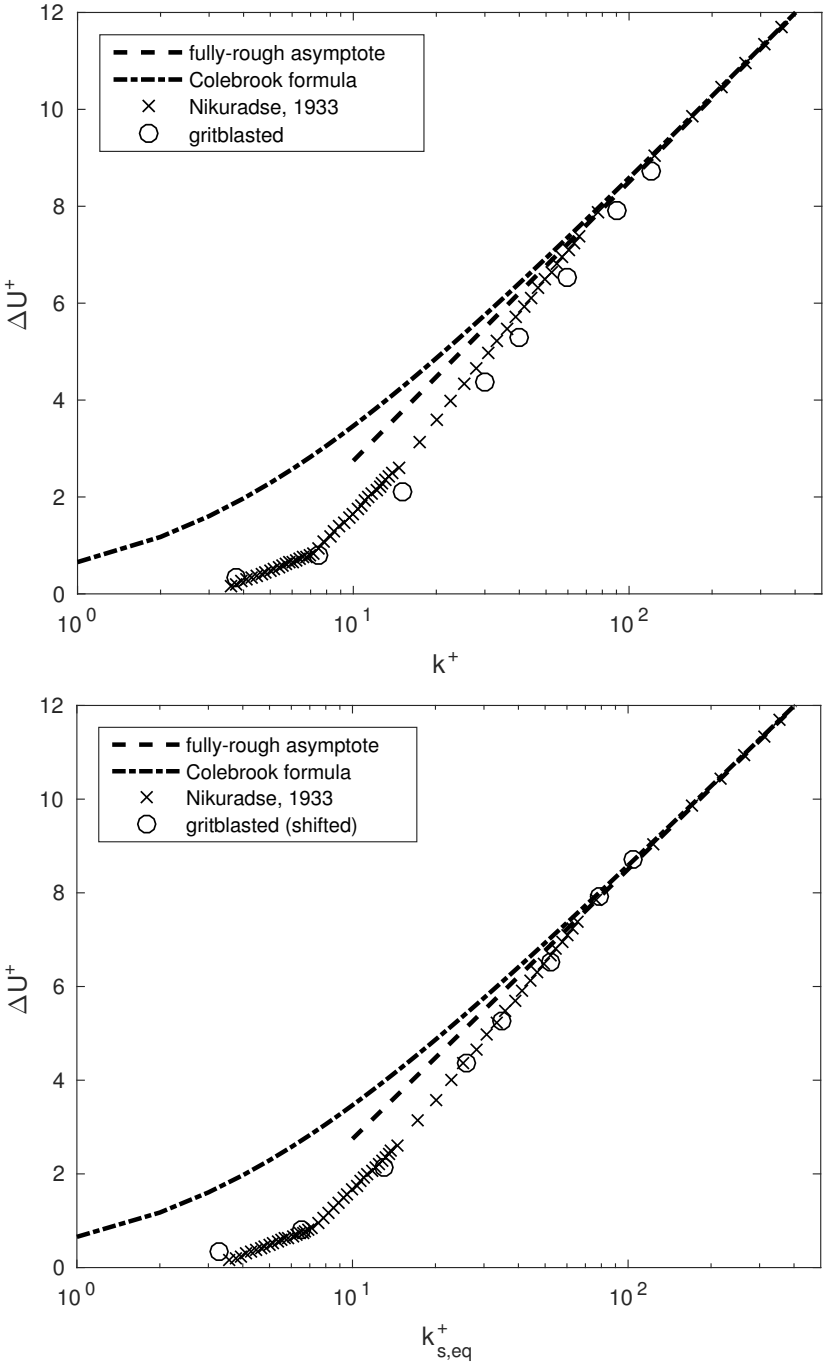

Figure 8.5: Variation of ΔU^+ with k^+ (top) and with $k^+_{s,eq} \approx 0.87k^+$ (bottom). Also shown are the fully-rough asymptote, Colebrook formula and the data of Nikuradse [1933].

regime (covered by data points $3.75 \leq k^+ \leq 90$ in Figure 8.5 (top)), the roughness has an increasing effect on the flow. In this regime, drag introduced by the roughness elements (which is a combination of viscous and pressure drag) progressively increases with k^+ and ΔU^+ depends on k^+ as well as the roughness topography. As k^+ further increases, the flow reaches the fully-rough regime, where the rate of increase of ΔU^+ with k^+ becomes constant ($k^+ > 90$ in Figure 8.5 (top)). In general, the drag in this regime is dominated by

k^+	3.75	7.5	15	30	40	60	90	120
$k^+_{s,eq} \approx 0.87k^+$	3.2625	6.525	13.05	26.1	34.8	52.2	78.3	104.4
ΔU^+	0.35	0.79	2.12	4.36	5.28	6.52	7.92	8.72

Table 8.3: k^+, equivalent sand-grain roughness height, $k^+_{s,eq}$ and ΔU^+ values for the Reynolds number dependence study.

pressure drag. However, for the current gritblasted surface, Busse et al. [2016] also observed an appreciable viscous drag component at the highest values of k^+. LES studies on irregular roughness conducted by De Marchis et al. [2010] also showed non-negligible viscous effects in their fully-rough cases at high k^+. It is clear that with increasing k^+, pressure drag increases whereas the viscous drag falls. Similar observations were first made by Nikuradse [1933] from his pipe-flow experiments on sand-grain roughness, based on the friction factor.

According to Jiménez [2004], $k_{s,eq}$ is a geometric property of a given rough surface, related to its skin-friction in the fully-rough regime. It can be used to characterise the Reynolds number of the flow and guarantees collapse of roughness functions for all types of roughness in the fully-rough regime which, according to Jiménez [2004], is reached when $k^+_{s,eq} \geq 50$. However, Nikuradse [1933] observed fully-rough conditions for $k^+_{s,eq} \geq 70$. This is the fully-rough flow criterion followed in the current study as the work of Nikuradse [1933] serves as an important comparison. Hence, for the current data, it leads to a second indication of $k^+ = 90$ and 120 clearly being in the fully-rough regime (refer $k^+_{s,eq}$ values in Table 8.3), along with the U_b criterion mentioned in Section 8.2. Also, the ΔU^+ for $k^+ = 90$ and 120, which are greater than 7, can be considered as a third indication of the fully-rough regime (Busse et al. [2016]). The fact that $k_{s,eq}$ collapses the roughness functions in the fully-rough regime can be used to compute the equivalent sand-grain roughness height for the gritblasted sample. To compute $k^+_{s,eq}$ from k^+, the sample data can be shifted in the horizontal direction to match with the reference curves in the fully-rough regime,

$$k^+_{s,eq} \approx 0.87k^+, \tag{8.3}$$

as shown in Figure 8.5 (bottom). Values of $k^+_{s,eq}$ are displayed in Table 8.3, along with k^+ and ΔU^+. Thus, $k_{s,eq}$ is approximately the same as the roughness height, k, for the gritblasted sample. This is a strong indication that the mean peak-to-valley height, $S_{z,5\times5}$, is a good measure of the roughness height as opposed to the average or rms roughness height, S_a or S_q (which have been used in previous studies on irregular roughness, for example Flack and Schultz [2010]).

Figure 8.6 shows the current data for the gritblasted sample along with the fully-rough asymptote, the Colebrook formula and the data of Nikuradse [1933]. Additionally, data from Ligrani and Moffat [1986], who conducted channel-flow experiments on roughness comprising of close-packed spheres, have been shown for comparison. Their data points have been scaled to have log-law constants that are consistent with the current study ($\kappa \approx 0.4$ and $A \approx 5.1$, from Jiménez [2004]). The gritblasted sample data show similar behaviour as

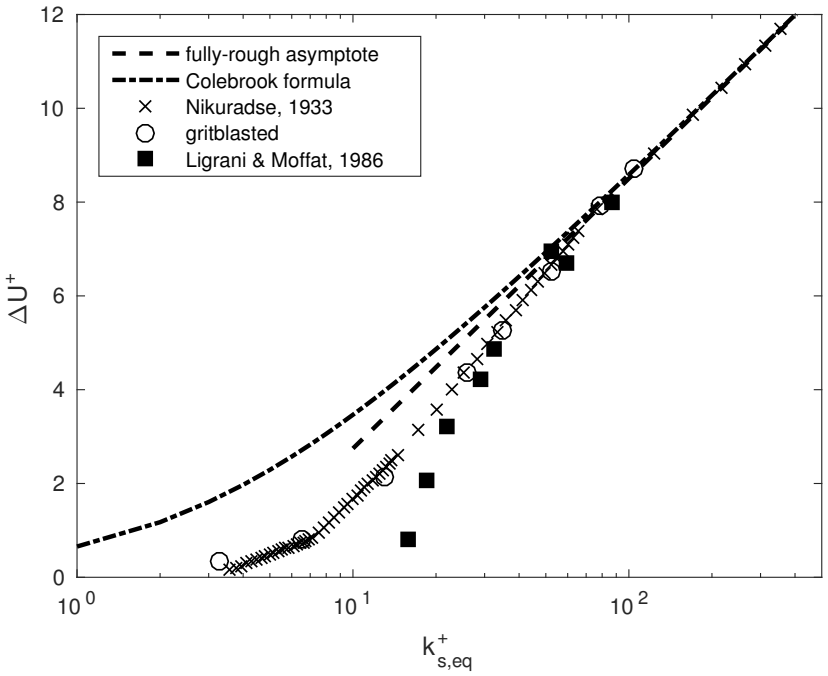

Figure 8.6: Comparison of the current Reynolds number range data with the study of Ligrani and Moffat [1986] (digitized from Jiménez [2004]). Data scaled to have consistent log-law constants with the current study.

Ligrani and Moffat [1986] in the upper part of the transitionally rough regime ($k^+_{s,eq} \geq 26.1$). Both sets of data also reach the fully-rough regime at about the same $k^+_{s,eq}$. In fact, the behaviour of the current data, the data of Ligrani and Moffat [1986] and Nikuradse [1933] all appear to be similar. Nikuradse [1933] used a single sand-grain size for a given experiment and, on careful consideration, it is understood that the sand grains can be approximated as spheres (though strictly speaking, Nikuradse's roughness is not classified as regular). Sphere diameter in the experiments of Ligrani and Moffat [1986] was 1.27mm with $\delta/k \approx 35$. The closest experiment of Nikuradse [1933] comprised of a sand-grain size of 1.6mm at $r/k = 30.6$ (where r is the pipe radius), so the difference is small. This similarity in the roughness of Nikuradse [1933] and Ligrani and Moffat [1986] is partially responsible for the similar behaviour of ΔU^+. The current data are also similar to both the above studies and in particular follow the Nikuradse [1933] data very closely. Although it is not completely clear exactly why the gritblasted sample data behave in this way, one reason could be the similarity between the Fourier filtering (Section 2.2.2) and the process of application of lacquer to hold the sand grains in place in Nikuradse's experiments. Since the lacquer was applied multiple times, to obtain better adherence of sand grains, it may have acted to effectively smooth out and hence eliminate the extremely small scales of roughness. The gritblasted sample data follow the data of Nikuradse [1933] remarkably well throughout the Reynolds number range, which is an important observation. This means that for the first time, roughness closely resembling Nikuradse's sand grains has been investigated from the hydraulically smooth to the fully-rough regime using DNS. The graphite sample study by Busse et al. [2016] also showed similar agreement with the Nikuradse [1933] data down to

$k^+ = 30$.

The length of the transitionally rough regime for the current data is quite wide, from $k^+_{s,eq} \approx 3.26$ to $k^+_{s,eq} \approx 78.3$, which is similar to that observed by Nikuradse [1933] ($k^+_{s,eq} \approx 5$ to $k^+_{s,eq} \approx 70$). The regular spherical roughness of Ligrani and Moffat [1986] showed a comparatively narrow transitionally rough regime, from $k^+_{s,eq} \approx 15$ to $k^+_{s,eq} \approx 55$. The reason for this was attributed by Ligrani and Moffat [1986] to the uniformity of the spheres, which caused a quicker change from smooth to fully-rough behaviour. An irregular distribution of sand grains would cause a more gradual transition with a wider transitionally rough regime and the same applies to the irregular gritblasted sample as well. According to Ligrani and Moffat [1986] and Flack et al. [2012], in general, the onset of roughness effects (beginning of the transitionally rough regime) as well as the beginning of the fully-rough regime are strongly dependent on the roughness type and topography.

Schultz and Flack [2007] conducted experiments on a honed surface which was geometrically similar to the honed pipe roughness of Shockling et al. [2006]. For a range of Reynolds number, comparisons were made with the data of Shockling et al. [2006], Nikuradse [1933] and Colebrook's interpolation formula. Schultz and Flack [2007] observed that their data displayed a Nikuradse-type behaviour, showing $\Delta U^+ \approx 0$ for low $k^+_{s,eq}$ (hydraulically smooth regime) with a slightly inflectional trend in the transitionally rough regime, similar to the behaviour observed by Shockling et al. [2006]. Flack et al. [2016] investigated skin-friction behaviour through experiments on surfaces grit-blasted with various grades of grit. Their data also showed Nikuradse-type behaviour in the Reynolds number range considered. The behaviour of the current gritblasted sample data is very similar to that observed in all three of the above studies. Bradshaw [2000] suggested that realistic surfaces should exhibit more Colebrook-type rather than Nikuradse-type behaviour owing to the large range of length scales present compared to the sand grains of Nikuradse [1933]. However, as observed by the three above mentioned studies and the current results, recent studies have contradicted this.

To further compare the current data and the experiments of Nikuradse [1933], a plot of Nikuradse's log-region velocity profile parameter, A, against the equivalent sand-grain roughness is shown in Figure 8.7. The experimental data has been digitised from Nikuradse [1933], Figure 16, whereas for the current data, A is computed using equation (16b) from Nikuradse [1933], which for channel flow takes the form

$$\frac{U_c}{u_\tau} = A + 5.75 \log\left(\frac{\delta}{k_{s,eq}}\right). \tag{8.4}$$

The values are tabulated in Table 8.4. To compare the data, A is plotted against $\log(k^+_{s,eq})$, just like in Nikuradse [1933], Figure 16. Physically, A is the Nikuradse [1933] analogue of ΔU^+. Depending on the behaviour of the curve, Nikuradse divided the plot into five different regions (indicated by vertical dashed lines in Figure 8.7), comprising three regimes. For $\log(k^+_{s,eq}) \leq 0.55$, the flow was classified in the hydraulically smooth regime whereas for $\log(k^+_{s,eq}) > 1.83$, the flow was in the fully-rough regime. The transitionally rough

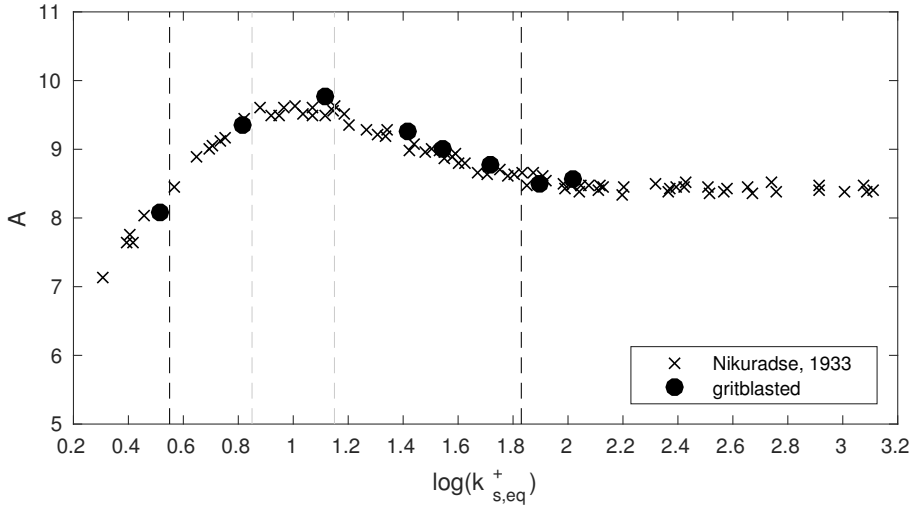

Figure 8.7: The log-region velocity profile parameter of Nikuradse [1933], A, compared between his experiments (data digitised from Nikuradse [1933], Figure 16) and the current data. Black vertical dashed lines indicate hydraulically smooth ($\log(k^+_{s,eq}) \leq 0.55$), transitionally rough ($0.55 < \log(k^+_{s,eq}) \leq 1.83$) and fully-rough regimes ($\log(k^+_{s,eq}) > 1.83$). Grey vertical dashed lines indicate further divisions of the transitionally rough regime, depending on the value of A, ($0.55 < \log(k^+_{s,eq}) \leq 0.85$), ($0.85 < \log(k^+_{s,eq}) \leq 1.15$) and ($1.15 < \log(k^+_{s,eq}) \leq 1.83$).

k^+	3.75	7.5	15	30	40	60	90	120
$k^+_{s,eq} \approx 0.87k^+$	3.2625	6.525	13.05	26.1	34.8	52.2	78.3	104.4
$\log(k^+_{s,eq})$	0.5136	0.8146	1.1156	1.4166	1.5416	1.7177	1.8938	2.0187
A	8.0702	9.3610	9.7642	9.2581	9.0116	8.7848	8.5011	8.5608

Table 8.4: k^+, $k^+_{s,eq}$ and the log-region velocity profile parameter of Nikuradse [1933], A, for the Reynolds number dependence study.

regime, $0.55 < \log(k^+_{s,eq}) \leq 1.83$, was further divided into three regions, depending on whether the value of A increases ($0.55 < \log(k^+_{s,eq}) \leq 0.85$), remains mostly constant ($0.85 < \log(k^+_{s,eq}) \leq 1.15$) or decreases ($1.15 < \log(k^+_{s,eq}) \leq 1.83$). Excellent agreement of A with the experimental data is observed, which further strengthens the agreement of ΔU^+ (Figure 8.6). Also, the fully-rough regime criterion of Nikuradse [1933], $\log(k^+_{s,eq}) > 1.83$, was based solely on $k^+_{s,eq}$. This adds further confirmation that the last two points in the current data ($k^+_{s,eq} = 78.3$ and 104.4) are in the fully-rough regime.

8.4 Data characterisation

Since ΔU^+ has been obtained for the entire range of Reynolds number, from hydraulically smooth to the fully-rough flow regime, the next logical step is to characterise the data by studying its behaviour and trends in the different regimes. Although the lowest value of $\Delta U^+ = 0.35$ at $k^+_{s,eq} \approx 3.26$ is still not low enough to be classified as hydraulically smooth, a reference point in this regime is available as $\Delta U^+ = 0$ at $k^+_{s,eq} = 0$ (which means no roughness). A similar approach as was adopted by Nikuradse [1933] is taken here, though

the limited amount of data in the current study limits the generality of the predictions to an extent. The data of Nikuradse [1933] were a result of studies at six different relative roughness ratios, r/k (where r was his pipe radius), each subject to a range of Reynolds number (refer Figure 15 in Nikuradse [1933]), which is extremely extensive compared to the current data set consisting of 8 data points. The relatively small number of points, however, are enough to make an investigation based on DNS data over the complete Reynolds number range. Also, the data for each Reynolds number have been statistically averaged for large times (refer Section 2.5), which makes the uncertainty in ΔU^+ small.

The data are characterised using least-squares curve fitting, using the plot of ΔU^+ against $k^+_{s,eq}$ on semilogarithmic axes. For fitting purposes, the data are classified into three sections: the lower transitionally rough regime, the upper transitionally rough regime and the fully-rough regime. Two separate fits, with different lower bounds on the upper transitionally rough regime, are made. The fully-rough regime, which is probably physically reached between $k^+_{s,eq} \approx 52.2$ and 78.3 (in agreement with the value of Nikuradse [1933], $k^+_{s,eq} \geq 70$), is taken as $k^+_{s,eq} > 78.3$ for both fits. Bounds are forced to lie on available data points, though possibilities may exist where they lie in between points. Data points in the lower transitionally rough regime are fitted such that the curve can be extended into the hydraulically smooth regime to give $\Delta U^+ = 0$ at $k^+_{s,eq} = 0$. The quality of the fit is determined by the rms error, σ, between the data points and the fit as well as the coefficient of determination, R^2. In general, a number of different types of curves (for example, polynomials, exponentials etc.) were fit for each section and those with the lowest value of σ, hence highest value of R^2 were selected.

Plots of both curve fits are shown in Figure 8.8, with corresponding equations for the

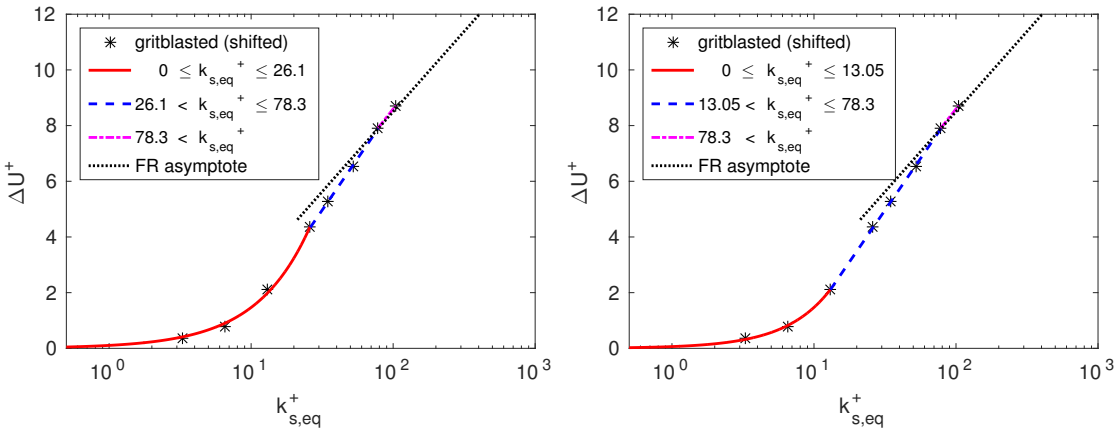

Figure 8.8: Data characterisation for the Reynolds number range showing the gritblasted sample data along with curve fits in three different regimes. In the left fit, $f1$, the lower and upper transitionally rough regimes are $0 \leq k^+_{s,eq} \leq 26.1$ and $26.1 < k^+_{s,eq} \leq 78.3$ respectively whereas in the right fit, $f2$, they are $0 \leq k^+_{s,eq} \leq 13.05$ and $13.05 < k^+_{s,eq} \leq 78.3$ respectively. The fully-rough regime is $k^+_{s,eq} > 78.3$ in both fits. The fully-rough (FR) asymptote is also shown for comparison.

regime	section	σ	R^2
lower transitionally rough	$0 \leq k^+_{s,eq} \leq 26.1$	0.1288	0.9966
upper transitionally rough	$26.1 < k^+_{s,eq} \leq 78.3$	0.0461	0.9994
fully rough	$k^+_{s,eq} > 78.3$	-	1

regime	section	σ	R^2
lower transitionally rough	$0 \leq k^+_{s,eq} \leq 13.05$	0.0446	0.9988
upper transitionally rough	$13.05 < k^+_{s,eq} \leq 78.3$	0.0378	0.9998
fully rough	$k^+_{s,eq} > 78.3$	-	1

Table 8.5: Best fit parameters for the curve fits, $f1$ (top), shown in Figure 8.8 (left) and $f2$ (bottom), shown in Figure 8.8 (right). σ = rms error of the fit and R^2 = coefficient of determination.

left fit, $f1$, as

$$0 \leq k^+_{s,eq} \leq 26.1 : \Delta U^+ = 0.11(k^+_{s,eq})^{1.14}, \tag{8.5}$$

$$26.1 < k^+_{s,eq} \leq 78.3 : \Delta U^+ = 3.22\ln(k^+_{s,eq}) - 6.17, \tag{8.6}$$

$$k^+_{s,eq} > 78.3 : \Delta U^+ = 2.78\ln(k^+_{s,eq}) - 4.21 \tag{8.7}$$

and for the right fit, $f2$, as

$$0 \leq k^+_{s,eq} \leq 13.05 : \Delta U^+ = 0.063(k^+_{s,eq})^{1.37}, \tag{8.8}$$

$$13.05 < k^+_{s,eq} \leq 78.3 : \Delta U^+ = 3.22\ln(k^+_{s,eq}) - 6.15, \tag{8.9}$$

$$k^+_{s,eq} > 78.3 : \Delta U^+ = 2.78\ln(k^+_{s,eq}) - 4.21. \tag{8.10}$$

The best fit parameters are shown in Table 8.5. Both fits in the lower transitionally rough regime, equations (8.5) and (8.8), satisfy the condition $\Delta U^+ = 0$ at $k^+_{s,eq} = 0$. In both plots, the data in the lower transitionally rough regime follow a power law behaviour whereas in the upper transitionally rough regime they follow a log-law behaviour. In the upper transitionally rough regime, $f1$ and $f2$ show very similar fitting coefficients (and hence similar quality) but they differ in the lower transitionally rough regime where the fit quality of $f2$ is better than that of $f1$ (Table 8.5), reducing the fit rms error by approximately 65%. Also, equations (8.5) and (8.8) depict the variation in fitting coefficients in the lower transitionally rough regime depending on section bounds. The data of Nikuradse [1933] in the range $14.13 \leq k^+_{s,eq} \leq 67.61$ gave $\Delta U^+ = 1.79\ln(k^+_{s,eq}) - 6$. Although equations (8.6) and (8.9), which are in a similar range, have a different slope than the preceding equation, the two data sets show good agreement in the range as seen from Figure 8.6. In the fully-rough regime, the last two data points are simply connected and hence the fits do not have any rms error and give $R^2 = 1$ (Table 8.5). The slope of the fully-rough asymptote is $1/\kappa = 1/0.4 = 2.5$, whereas the fits in the fully-rough regime, equations (8.7) and (8.10) both give a slope of 2.78, a difference of approximately 11%.

Bradshaw [2000] was unconvinced by the notion of a "critical roughness height" above which roughness effects start to appear, and stated that a power-law behaviour of the de-

parture of the smooth-wall additive constant, i.e. ΔU^+, was also plausible. On the basis of Stokes flow and Oseen's approximation, for sparse spherical roughness, he postulated that ΔU^+ may vary as $(k^+_{s,eq})^2$ for low values of equivalent sand-grain roughness. Although a specific regular roughness was considered in this approximation, in general, it could be applied to any type of roughness at low $k^+_{s,eq}$ and sufficiently high δ/k. As seen from equation (8.5), $\Delta U^+ = 0.11(k^+_{s,eq})^{1.14}$, and equation (8.8), $\Delta U^+ = 0.063(k^+_{s,eq})^{1.37}$, in the region of low $k^+_{s,eq}$, a power-law behaviour is indeed supported by the curve fits to the DNS data. However, the behaviour is closer to linear than quadratic in nature, as seen from the power of $k^+_{s,eq}$ in both equations. The differing behaviour may be due to several reasons. Firstly, Bradshaw [2000] made many simplifying approximations in his postulation: he assumed regular roughness, in the form of spheres, which were sparsely distributed, and also mentioned that his argument would be questionable for denser roughness. The current rough surface sample, although not strictly dense according to Jiménez [2004] (because its solidity is less than 0.15, from Table 3.2), is nevertheless denser than the roughness of Bradshaw [2000] and has a highly irregular topography (Figure 8.2 (left)) with a large number of length scales. Also, the argument of Bradshaw [2000] was entirely theoretical and, although based on well-established theories, could possibly be unreliable for more practical cases. The current data are based on DNS (the code for which has been thoroughly validated) and are considered very reliable. Secondly, and possibly more importantly, it is likely that the behaviour of ΔU^+ for low $k^+_{s,eq}$ depends on the rough surface under consideration. For $15 \leq k^+ \leq 120$, Busse et al. [2016] compared DNS results of the graphite sample (s7 from Table 3.1 and Figure 3.4 (g)) and the current gritblasted sample and observed differences in ΔU^+ between the two. The differences were possibly due to differing surface sample skewness; the graphite sample being positively skewed (peak-dominated) whereas the gritblasted sample being negatively skewed (valley-dominated). Based on surface skewness and other topographical properties (as shown in Table 3.2), it may be possible for different samples to exhibit differing behaviour in ΔU^+ at low $k^+_{s,eq}$. Although Busse et al. [2016] did not study the graphite sample at $k^+ = 3.75$ and 7.5, doing so and performing a similar data characterisation as the current section may be able to confirm the above-mentioned possibility. For irregular roughness, an experimental study on the onset of roughness effects in the transitionally rough regime conducted by Flack et al. [2012] suggested that the behaviour of ΔU^+ in the transitionally rough regime is topography dependent. Although they did not study the departure behaviour of ΔU^+ from its smooth-wall value, it is speculated that the preceding observation could have an influence on it.

8.5 Effects of tiling

In this section, the influence of sample tiling (to obtain $k^+ < 30$, as described in Section 8.1) on the flow is studied. Initially, the flow field is examined qualitatively. Since the sample is periodic in the streamwise and spanwise directions, the domain boundaries are also tile boundaries. These effects are studied for the 2×2 and 4×4 tiled cases, i.e. $k^+ = 15$ and 7.5 respectively. Figure 8.9 shows contours of instantaneous streamwise, u (left), and

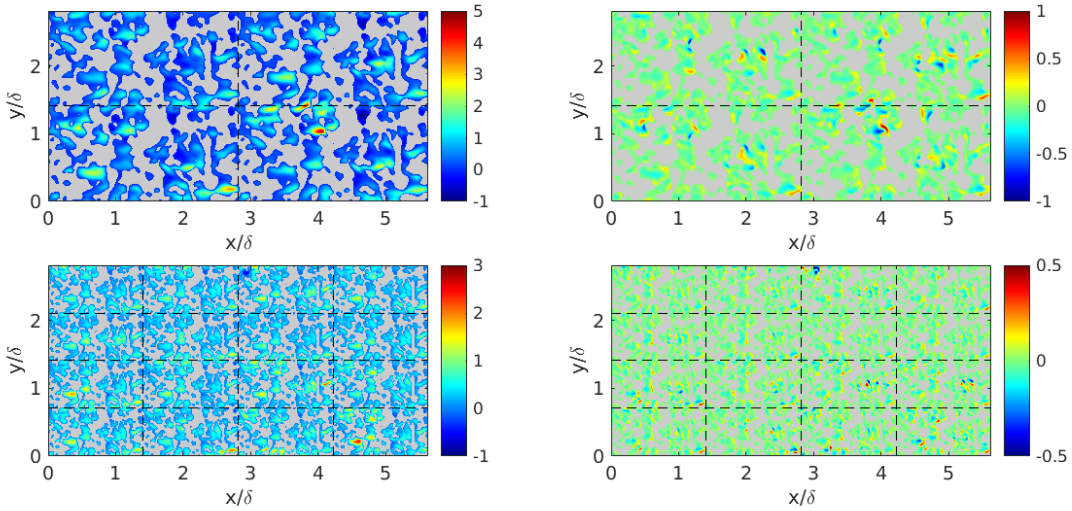

Figure 8.9: Contours of instantaneous flow velocities, u (left) and w (right), at $z^+ = 0$ for $k^+ = 15$ (top) and $k^+ = 7.5$ (bottom). Grey regions indicate the rough surface. Dashed lines denote tile boundaries in all plots. Flow is from left to right.

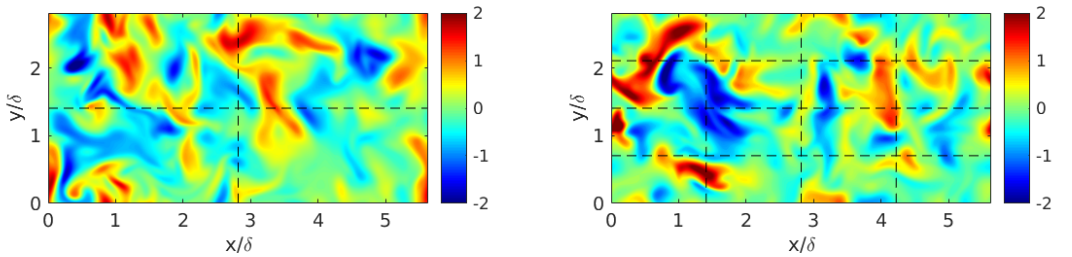

Figure 8.10: Contours of instantaneous wall-normal flow velocity, w, at $z^+ = 180$ for $k^+ = 15$ (left) and $k^+ = 7.5$ (right). Dashed lines denote tile boundaries in all plots. Flow is from left to right.

wall-normal velocities, w (right), at $z^+ = 0$ for $k^+ = 15$ (top) and $k^+ = 7.5$ (bottom). On close examination of individual tiles (for either k^+), the flow field shows some qualitatively similar features in each tile. However, this effect disappears at higher z^+, as seen from plots of w at the channel centre, $z^+ = 180$ (Figure 8.10). This will be quantified using velocity two-point correlation plots in subsequent paragraphs.

The time-averaged flow field behaves slightly differently. Figure 8.11 shows contours of time-averaged streamwise, $\overline{u}$ (left), and wall-normal velocities, $\overline{w}$ (right), at $z^+ = 18$ for $k^+ = 30$ (top), $k^+ = 15$ (middle) and $k^+ = 7.5$ (bottom). Since only a qualitative analysis is conducted at this stage, the colourbar range for each plot is adjusted to make the flow features clearly visible. For a given tiled case, the main features of the flow field on each tile appear to be similar to all other tiles for that case and resemble the flow features for $k^+ = 30$. This is seen quite clearly for $\overline{w}$ and the effect is stronger than seen in the instantaneous flow field (Figure 8.9). This is understandable, as the roughness topography of each tile for a tiled case is same as the roughness topography for $k^+ = 30$ (which is not tiled). The flow field in each tile also appears to be individually periodic in both streamwise and spanwise directions (especially for $\overline{w}$). The time-averaging interval for $k^+ = 30$, 15 and

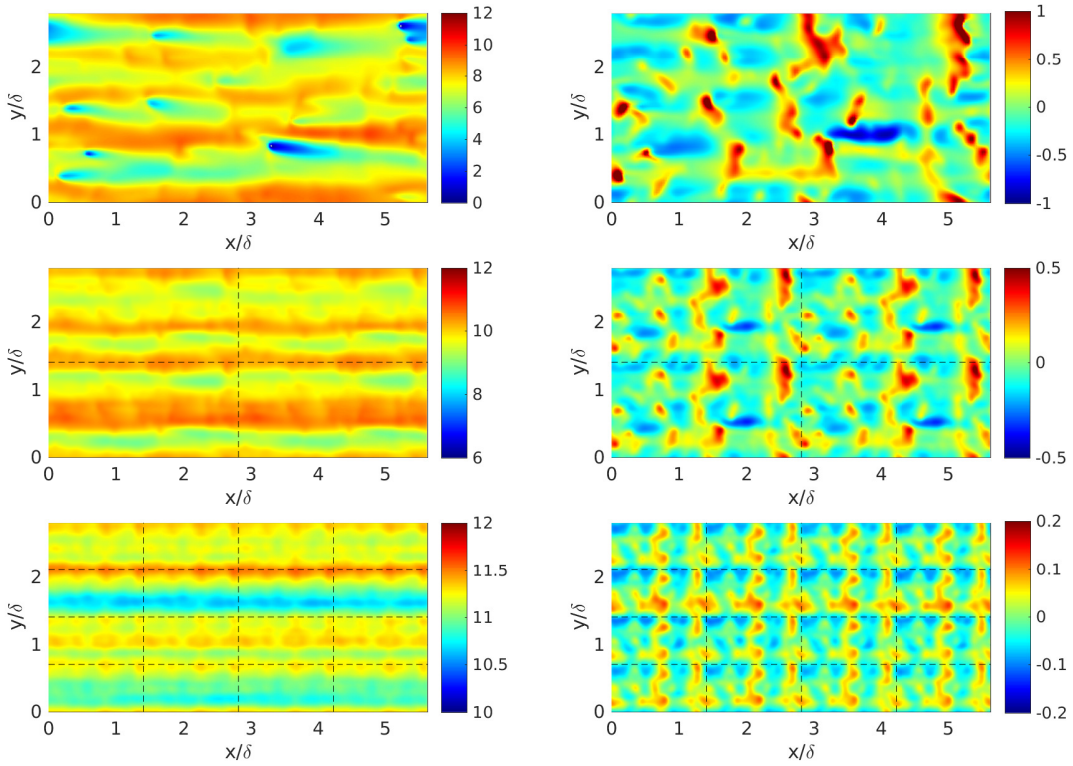

Figure 8.11: Contours of time-averaged flow velocity, $\overline{u}$ (left) and $\overline{w}$ (right), at $z^+ = 18$ for $k^+ = 30$ (top), $k^+ = 15$ (middle) and $k^+ = 7.5$ (bottom). Dashed lines denote tile boundaries in all plots. Flow is from left to right.

7.5 was also modified to check its effect on the flow field but the same time-averaged flow features were observed at $z^+ = 18$ irrespective of the averaging time (which in all cases was large enough to obtain converged statistics). These effects of tiling, however, also disappear for higher wall-normal distances. For example, Figure 8.12 shows plots of $\overline{w}$ at the channel centre, $z^+ = 180$, for $k^+ = 15$ (left) and $k^+ = 7.5$ (right). The flow field no longer appears to be similar in all tiles for a given k^+ and the individual tile periodicity appears to be seen only in the streamwise direction. Despite velocity variations being small, Figure 8.12 also shows streamwise coherent structures, which appear to be similar to the low momentum regions observed by Lee et al. [2011] in the outer regions of the rough-wall boundary layer from DNS studies over cubes.

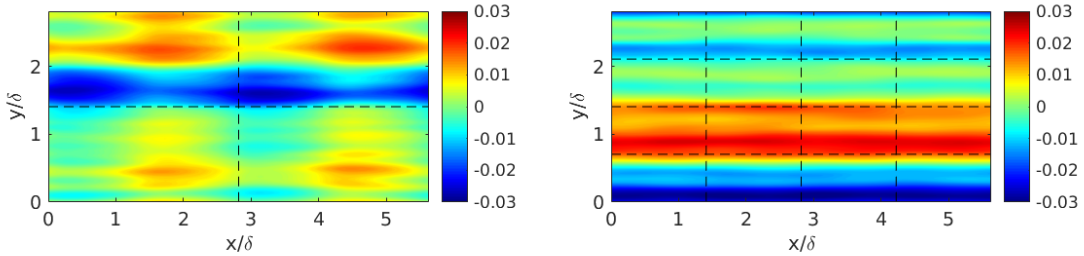

Figure 8.12: Contours of time-averaged wall-normal velocity, $\overline{w}$, at $z^+ = 180$ for $k^+ = 15$ (left) and $k^+ = 7.5$ (right). Dashed lines denote tile boundaries in all plots. Flow is from left to right.

Contour plots of the time-averaged flow field, spatially averaged in the streamwise direction, are studied to indicate any secondary flow features that might be caused due to the tiling, especially near the tile boundaries. Figure 8.13 shows $\overline{u}$ (left) and $\overline{w}$ (right), both spatially averaged in the streamwise direction for $k^+ = 30$ (top), $k^+ = 15$ (middle) and $k^+ = 7.5$ (bottom). The colourbar range for $\overline{w}$ is adjusted to make the flow features clearly visible. Plots of $\overline{u}$ resemble smooth-wall flow with decreasing k^+ but there is no evidence of any secondary flow features near tile boundaries. Plots of $\overline{w}$ show certain flow features near tile boundaries for $k^+ = 15$ and 7.5, which may at first appear to be secondary flow features due to tiling. However, for a feature to be regarded as a direct effect of tiling, it must be present at all tile boundaries in a plot of time- and spatially-averaged velocity. The above-mentioned flow features, although qualitatively present at all tile boundaries, differ

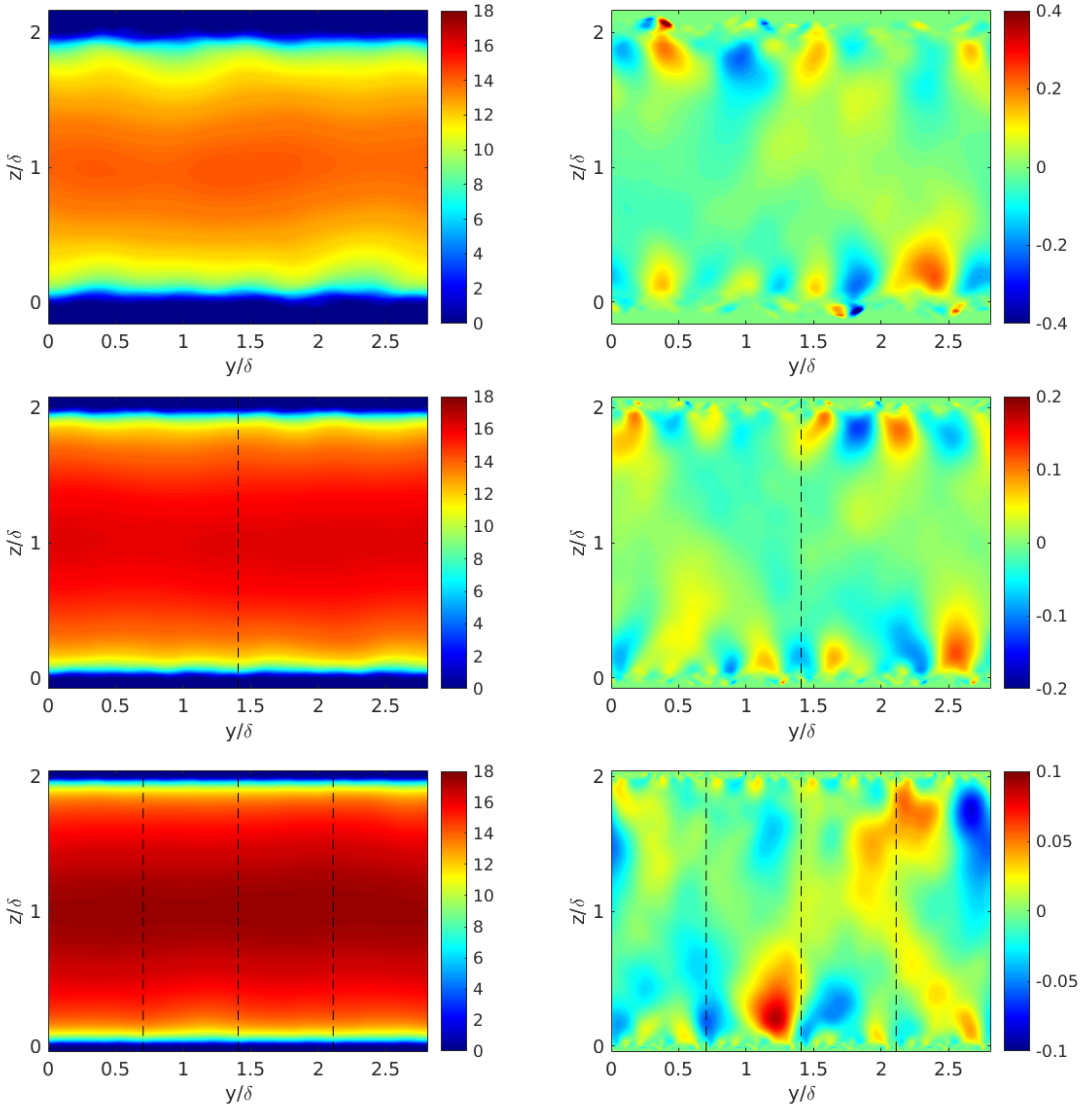

Figure 8.13: Contours of time-averaged flow velocities, $\overline{u}$ (left) and $\overline{w}$ (right), spatially averaged in the streamwise direction for $k^+ = 30$ (top), $k^+ = 15$ (middle) and $k^+ = 7.5$ (bottom). Dashed lines denote tile boundaries in all plots. Flow is into the page.

in size and magnitude. Hence they cannot be regarded as a direct effect of tiling and are simply flow features arising due to the roughness.

Plots of the velocity two-point correlation are studied in order to obtain further insight into the effect of tiling. If f is an array consisting of N elements then, in general, its two-point correlation with itself for separation index Δ, is given as

$$R_{ff}(\Delta) = \frac{\sum_{i=1}^{N-\Delta} (f_i - \overline{f})(f_{i+\Delta} - \overline{f})}{\sum_{i=1}^{N} (f_i - \overline{f})^2}, \tag{8.11}$$

where f_i is the i^{th} element of f and $\overline{f}$ is the arithmetic mean of f, given by $\overline{f} = \frac{1}{N}\sum_{i=1}^{N} f_i$. In the following, for all separation indices, $\Delta = [0 \;\; N]$, equation (8.11) is computed for each row of a two-dimensional flow field in a $y - z$ plane. Hence only spanwise separations are considered. Each row will thus provide an array of values for the two-point correlation, which are then stacked to obtain a matrix. The spanwise periodicity of the flow must also be taken into account. This matrix is used to visualize a two-dimensional contour plot of the two-point correlation. The contour plot is thus a collection of one-dimensional two-point correlations because only a single type of separation, i.e. spanwise, is considered.

Figure 8.14 shows contour plots of the above-mentioned two-point correlation for $k^+ =$

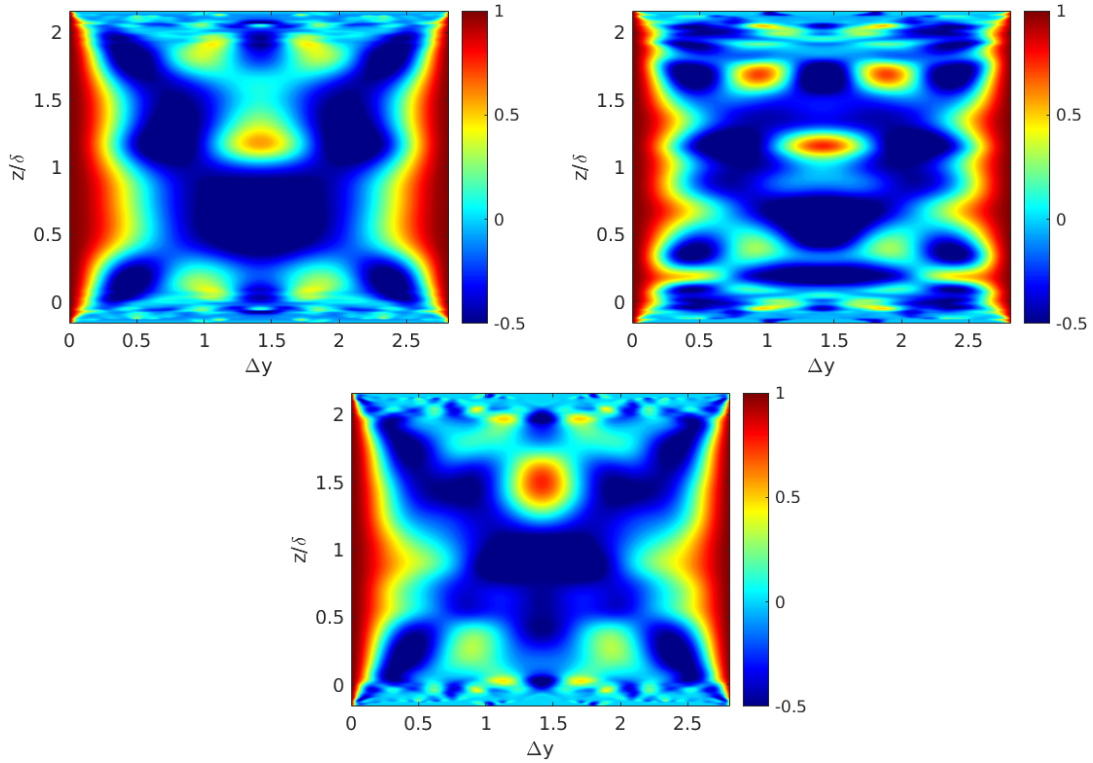

Figure 8.14: Two-point correlation (spanwise separations) of time-averaged flow velocity, spatially averaged in the streamwise direction, for $k^+ = 30$. R_{uu} (top left), R_{vv} (top right) and R_{ww} (bottom).

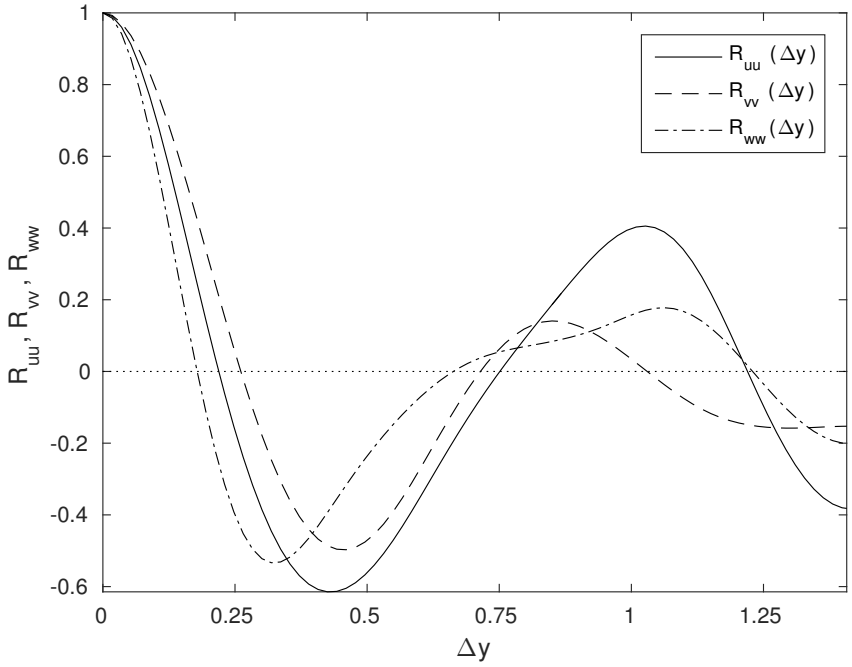

Figure 8.15: Two-point correlations (spanwise separations) for $k^+ = 30$ at $z/\delta = 0.1$ ($z^+ = 18$) from Figure 8.14. Since the flow field is periodic in the span, only half the total number of separations, Δy, are shown.

30. For the time-averaged flow velocity, spatially averaged in the streamwise direction, it is computed considering spanwise separations. Since this case is not tiled, it serves as reference for comparison when similar plots will be made for $k^+ = 15$ and 7.5. Additionally, Figure 8.15 shows two-point correlations for the same case but at $z/\delta = 0.1$ ($z^+ = 18$), which is very close to the roughness peak for this sample. It is observed that the correlations do not drop to zero, which may suggest the computational domain size is small for the given case. However, it was mentioned in Section 4.3 on domain size validation that domain restrictions for rough walls are less stringent than smooth walls as roughness is known to produce relatively more isotropic turbulence near the wall. Relatively small domain sizes have also been used in the computational studies of the graphite sample (s7 from Table 3.1 and Figure 3.4 (g)) by Busse et al. [2015] and of cube roughness by Coceal et al. [2007] and Coceal et al. [2006]. An important conclusion of these studies was that relatively small domains are enough to study mean and turbulent statistics, which is the main purpose of this study. The comparative study of Busse et al. [2016] as well as the surface correlations study of Thakkar et al. [2017] also used the gritblasted sample with the same domain extents as used in the current chapter (Figure 8.2 (left)). Relatively small domains have also been used in smooth-wall simulations in the past, for example, Lozano-Durán and Jiménez [2014] used a domain size ($L_x/\delta \times L_y/\delta$) of ($\pi \times \pi/2$).

According to Kim et al. [1987], who carried out smooth-channel numerical studies at $Re_\tau = 180$, the spanwise separation at which the minimum R_{uu} occurs provides an estimate of the mean separation between high- and low-speed fluid. The mean spanwise spacing between vortical streaks should be about twice this distance. From Figure 8.15, minimum

R_{uu} occurs at $\Delta y \approx 0.425$ or $\Delta y^+ \approx 76$, which means the spanwise streak spacing should be roughly $\Delta y \approx 0.85$ or $\Delta y^+ \approx 153$. This is confirmed by all plots in Figure 8.14 with higher correlation value (green) regions visible at approximately $0 \leq z/\delta \leq 0.5$. It is worth noting that streak spacing in the spanwise direction and distance from the wall are also governed by the roughness height and topography. Kim et al. [1987] also mentioned the spanwise separation at which the minimum of R_{ww} occurs gives the mean diameter of the streamwise vortical structure. From Figure 8.15, minimum R_{ww} occurs at $\Delta y \approx 0.319$ or $\Delta y^+ \approx 57$. This approximate vortex diameter is confirmed by the R_{ww} plot in Figure 8.14 with higher correlation value (green) regions visible around $\Delta y = 1$ and $0 \leq z/\delta \leq 0.5$.

Figure 8.16 shows similar contour plots for $k^+ = 15$ and 7.5. The observations that follow are made for all R_{uu}, R_{vv} and R_{ww}. In general, since the flow is periodic in the

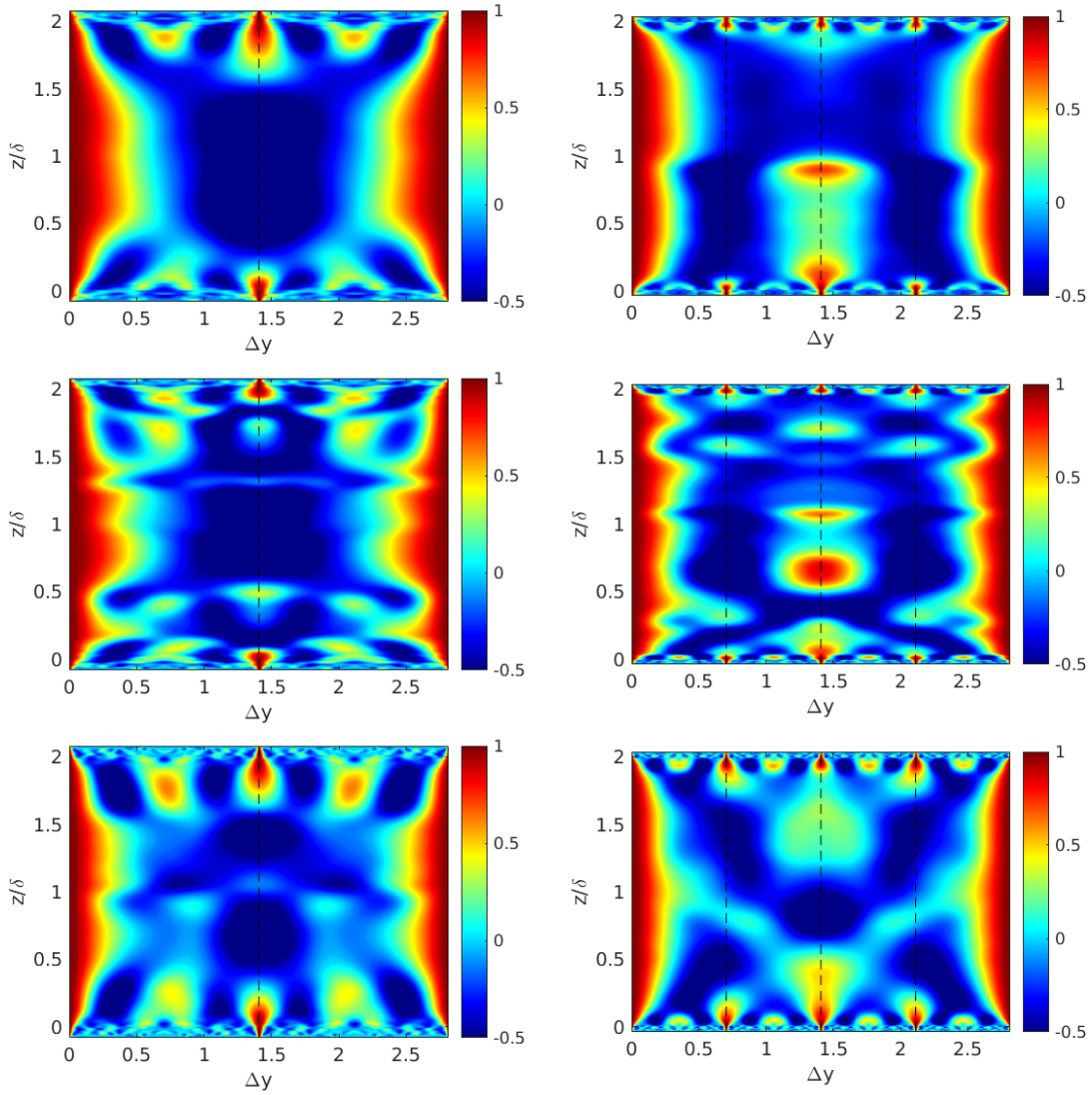

Figure 8.16: Two-point correlations (spanwise separations) of time-averaged flow velocity, spatially averaged in the streamwise direction for $k^+ = 15$ (left) and 7.5 (right). R_{uu} (top), R_{vv} (middle) and R_{ww} (bottom). Dashed lines denote tile boundaries in all plots.

span, the two-point correlations are symmetrical about the half-span separation (which is also a tile boundary). Additionally, since the individual tile periodicity is preserved up to a certain wall-normal distance, the two-point correlation appears symmetrical about tile boundaries up to $z/\delta \approx 0.25$ for $k^+ = 15$ and $z/\delta \approx 0.125$ for $k^+ = 7.5$. This means high values of correlation are observed near tile boundaries up to these wall-normal distances. A comparatively strong tiling effect is seen for $k^+ = 7.5$ at half-span separation, which appears to be sustained up to relatively large wall-normal distances (up to approximately the channel centre for R_{uu} and up to $z/\delta \approx 0.5$ for R_{ww}). These tiling effects, however, can be regarded as relatively small, as their presence is seen only in two-point correlation plots whereas the time-averaged velocity plots spatially averaged in the streamwise direction (Figure 8.13) do not show any significant effects. Also, near-wall flow features in each tile at $k^+ = 15$ and 7.5 are similar to those observed at $k^+ = 30$ (Figure 8.14). These features, however, decrease in size with decreasing k^+ and appear to be merging with each other. Plots in Figure 8.16 also show a lack of symmetry in the $z-$direction, which is stronger for $k^+ = 7.5$ than $k^+ = 15$. The normalisation of the two-point correlation could lead to this phenomenon. Variations in velocities used to obtain the plots in Figure 8.16 are small and when normalised by the variance, in equation (8.11), could amplify the asymmetry. As a check, Figure 8.17 shows plots of the non-normalised two-point correlations, R_{uu} (top left), R_{vv} (top right) and R_{ww} (bottom), for $k^+ = 7.5$, which show better symmetry in z

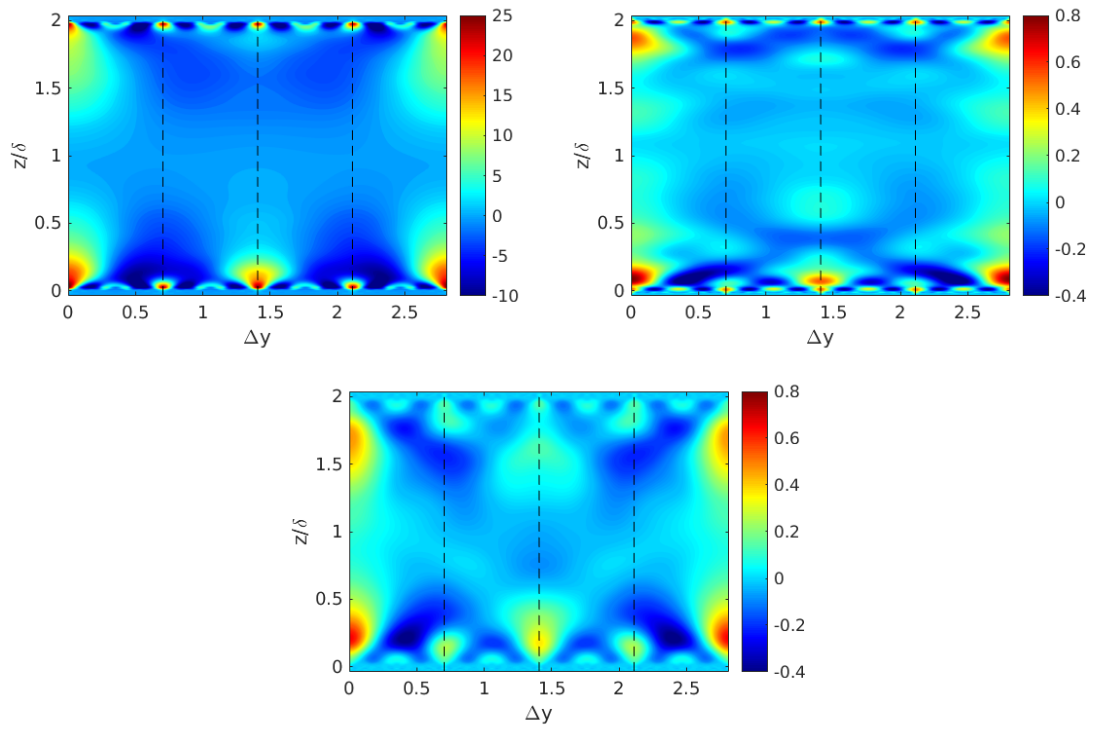

Figure 8.17: Non-normalised two-point correlations (spanwise separations) of time-averaged flow velocity, spatially averaged in the streamwise direction for k^+ =7.5. R_{uu} (top left), R_{vv} (top right) and R_{ww} (bottom). Dashed lines denote tile boundaries in all plots.

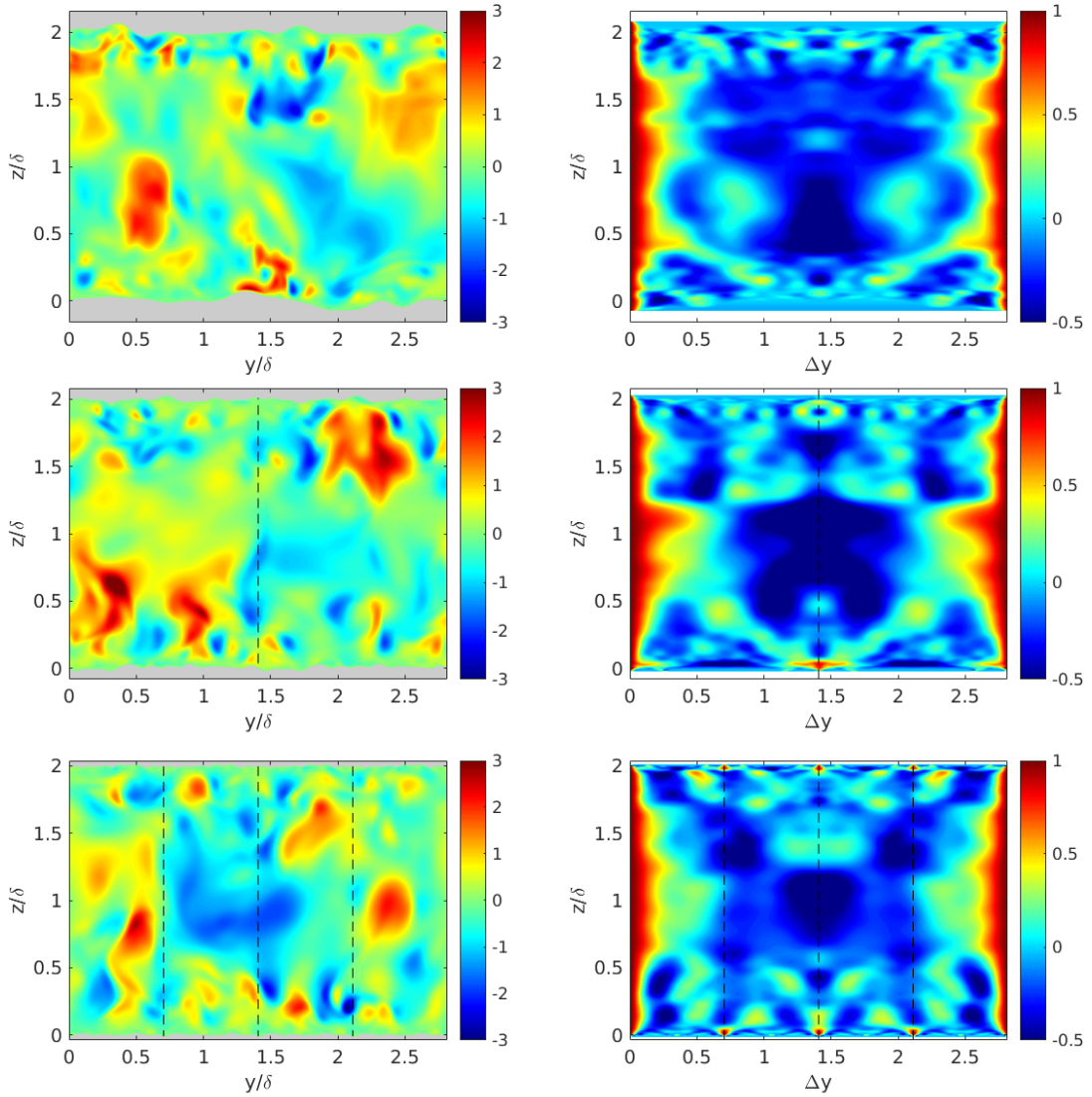

Figure 8.18: Instantaneous wall-normal velocity, w (left), and corresponding spanwise two-point correlation (right) at $x = L_x/4$ for $k^+ = 30$ (top), $k^+ = 15$ (middle) and $k^+ = 7.5$ (bottom). Flow is into the page. Grey regions in the left plots denote the rough surface. White regions in the right plots denote areas with non-existent correlation values due to zero velocities. Dashed lines denote tile boundaries in all plots.

compared to Figure 8.16.

Similar plots are also made for the instantaneous wall-normal velocity. Figure 8.18 shows contour plots of w (left) and the corresponding two-point correlation (right) at $x = L_x/4$ for $k^+ = 30$ (top), 15 (middle) and 7.5 (bottom). Individual tile periodicity in the correlation is observed for $k^+ = 15$ and 7.5, again up to a certain wall-normal distance. This distance ($z/\delta \approx 0.05$ for both $k^+ = 15$ and 7.5), however, is much smaller compared to that observed in the two-point correlations of Figure 8.16. This effect is seen, again, only in the correlation plots and not in the instantaneous velocity plots and hence can be regarded as small. Although the w flow field is plotted at different flow times for the three cases, this fact

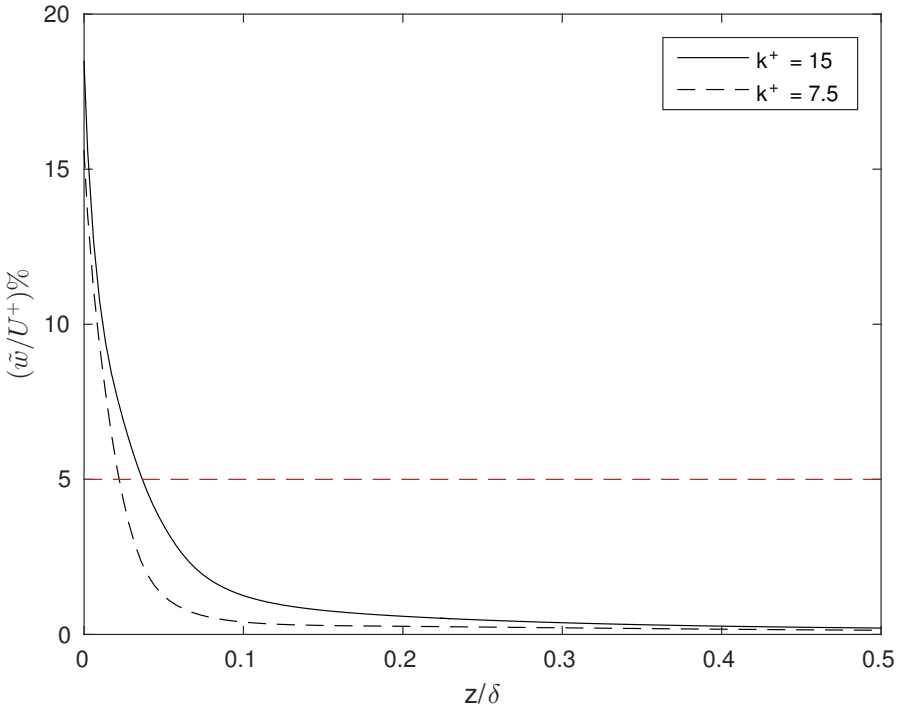

Figure 8.19: Standard deviation of $\overline{w}$ for each z/δ, normalized by the spatially-averaged $\overline{u}$. The red dashed line denotes a 5% threshold.

should not have a significant influence on the observations made above.

The final part of this section relates tiling effects to the dispersive stresses and hence thickness of the roughness sublayer. Busse et al. [2016] studied the thickness of the roughness sublayer by computing the standard deviation of $\overline{w}$ in each wall-normal plane, and normalising it by the time- and spatially-averaged streamwise velocity on the same plane. A similar approach is adopted here and the plot is shown in Figure 8.19 for $k^+ = 15$ and 7.5. The quantity on the y-axis, $\tilde{w}/U^+$, which is a representation of the wall-normal dispersive stress, decreases to below 5% close to the maximum roughness height for both cases. It drops to below 1% at $z/\delta \approx 0.3$ for $k^+ = 15$ and $z/\delta \approx 0.15$ for $k^+ = 7.5$. Effects of tiling are seen up to similar wall-normal distances for corresponding k^+ (as seen from the two-point correlation plots of Figure 8.16).

From this section, it can be concluded that, although tiling does affect the flow, the effects are confined to the near-wall regions close to tile boundaries and do not have a significant influence on the overall flow field. This is qualitatively demonstrated by the absence of secondary flow features near tile boundaries from plots of time-averaged streamwise and wall-normal velocity, spatially averaged in the streamwise direction. Close to the rough wall, the flow field is qualitatively periodic in each tile and this effect causes the velocity two-point correlation to be symmetric about tile boundaries. The time-averaged flow field is affected up to a greater wall-normal distance than the instantaneous flow field. Finally, plots of wall-normal dispersive stress for the time-averaged flow field at $k^+ = 15$ and 7.5 show that tiling effects are restricted to within the roughness sublayer.

Chapter 9

Closing remarks

9.1 Summary and conclusions

A direct numerical simulation study, investigating the physics of incompressible turbulent flow over irregular industrially relevant rough surfaces using an immersed boundary code, has been presented. A three-step numerical methodology, comprising surface data acquisition (which involves surface scanning using a variable focus microscope), surface preprocessing (which involves section selection, scaling and Fourier filtering) and conducting DNS of flow over the surface sample, is utilised. Seventeen rough surface samples with a wide range of topographical properties are considered.

Studies in the range $45 \leq Re_\tau \leq 95$ for the gritblasted sample indicate that the flow is laminar up to $Re_\tau = 89$. At $Re_\tau = 89.5$, small velocity fluctuations and quasi-periodic behaviour of the mean centreline velocity, $\langle U_c^+ \rangle$, with time, are observed. Thus the critical Reynolds number is in the range $89 \leq (Re_\tau)_{\text{crit}} \leq 89.5$. Fluctuations in the three velocity components continue to grow until $Re_\tau = 91$ and the flow is turbulent for $Re_\tau \geq 92$. Thus the transition Reynolds number is in the range $91 \leq (Re_\tau)_{\text{trans}} \leq 92$. Transition depends on the surface topography as some roughness peaks trigger fluctuations before others. The earliest wall-normal fluctuations close to the rough wall are not generated by the highest peak of the surface. Simulations are carried out with laminar and turbulent initial conditions and there is no evidence of hysteresis effects.

Following on, simulations for all seventeen surface samples are conducted at $Re_\tau = 180$, for which the flow is fully turbulent but transitionally rough. Investigations are carried out into the rough-wall flow physics, along with studies of the variation of selected flow properties with a range of surface topographical properties. All samples are scaled to the same physical roughness height such that $\delta/k = 6$. Nevertheless, a wide range of roughness function, ΔU^+, values is obtained, such that $1.28 \leq \Delta U^+ \leq 5.02$. Thus it is concluded that the roughness effect depends not only on the roughness height but also on the detailed surface topography. Mean streamwise velocity defect profiles for all samples collapse with the smooth-wall data away from the rough wall, thus satisfying the wall-similarity hypothesis of Townsend [1976] for the mean flow. Most samples show complete flow reversal deep within their roughness valleys, as indicated by the volume fraction of negative time-

averaged streamwise velocity. Some samples such as s6 (filed_2) and s9 (ground), however, do not show this behaviour because of their highly anisotropic topography. Second order statistics show considerable variation depending on the surface topography. ΔU^+ decreases with $\langle\overline{u'^2}\rangle_{\max}$ but increases with $\langle\overline{v'^2}\rangle_{\max}$. At $z/\delta = 0$, wall-normal fluctuations show an increasing trend with both, average and rms roughness heights, S_a and S_q. Close to the rough walls, $\langle\overline{u'^2}\rangle$, $\langle\overline{v'^2}\rangle$ and $\langle\overline{w'^2}\rangle$ are greater than the corresponding smooth-wall values because rough wall fluctuations can occur very close to the roughness features, including for $z/\delta \leq 0$, which is not possible for the smooth wall. Roughness increases the shear stress significantly and the Reynolds shear stress profiles at $z/\delta = 0$ show a decreasing trend with the streamwise effective slope, ES_x. Behaviour of the turbulent kinetic energy (TKE) profiles is very similar to that of $\langle\overline{u'^2}\rangle$. Values of normal components of the Reynolds stress anisotropy tensor, $b_{i,j}$, at peak values of $\langle\text{TKE}\rangle$ and $\langle\overline{u'_i u'_j}\rangle$ show that the streamwise fluctuations have the greatest contribution to the TKE. Comparison with the corresponding smooth-wall values of $b_{i,j}$ shows reduced flow anisotropy for all rough surface samples. Most samples have dispersive stresses that are less than the corresponding Reynolds stresses. Streamwise anisotropic samples, such as s2 (composite_1) and s6 (filed_2), however, show much higher values of streamwise dispersive stress compared to streamwise Reynolds stress because they promote large regions of high $\overline{u}$. Peak streamwise dispersive stress, $\langle\tilde{u}^2\rangle_{\max}$, shows an increasing trend with L_x^{cor} Samples such as s2 (composite_1) and s9 (ground) show relatively large values of wall-normal dispersive stress, $\langle\tilde{w}^2\rangle$, at the channel centre, possibly due to the relatively low δ/k ratio and their anisotropic topography. Results at $Re_\tau = 180$ along with respective surface topographical properties form the simulation database of rough surface samples.

Further studies on the variation of flow properties with surface topography at $Re_\tau = 180$ show that ΔU^+ correlates well with the Sigal-Danberg parameter of van Rij et al. [2002]. An improvement in the fit is obtained by formulating a new parameter based on the surface properties of four outlier data points. Subsequently, based on all topographical properties from the simulation database, a thorough surface parametrisation is conducted for ΔU^+ and $\langle\text{TKE}\rangle_{\max}$. A newly formulated method, that determines which surface topographical properties are important and how new properties can be added to an empirical model, is tested. Optimised models with several roughness properties are systematically developed. In determining ΔU^+, besides the known properties of surface solidity, S_f/S, and skewness, S_{sk}, it is shown that the streamwise correlation length, L_x^{cor}, and rms roughness height, S_q, are also significant. Although the models cannot currently be used to predict the equivalent sand-grain roughness height, $k_{s,eq}$, since the underlying data are in the transitionally rough regime, they determine precisely which properties influence ΔU^+, and it is likely that the same properties contribute to the determination of $k_{s,eq}$ in the fully-rough regime. $\langle\text{TKE}\rangle_{\max}$ is determined by S_{sk} and S_q, along with the mean forward-facing surface angle, $\overline{\alpha}$, and spanwise effective slope, ES_y.

Lastly, to show that a Reynolds number sweep of a highly irregular rough surface is feasible using DNS and to subsequently determine the equivalent sand-grain roughness

height, simulations are conducted on the gritblasted sample for a range of Reynolds number, such that $180 \leq Re_\tau \leq 720$, while the roughness height in viscous units varies in the range $3.75 \leq k^+ \leq 120$. ΔU^+ increases with k^+ and it is shown that the fully-rough regime is reached between $k^+ = 60$ and 90. Excellent agreement of the simulation data with the experimental data of Nikuradse [1933] is observed, with $k^+_{s,eq} \approx 0.87k^+$. Thus, for the first time, roughness closely resembling the sand-grain roughness of Nikuradse [1933] has been investigated using DNS in the entire Reynolds number range, from hydraulically smooth to the fully-rough regime. The data is characterised in the range using high quality curve fits. Behaviour of the data for low $k^+_{s,eq}$ differs from that speculated by Bradshaw [2000] and it is postulated to be dependent on the surface topography. Sample tiling used to obtain $k^+ \leq 15$ affects the flow field very mildly. Qualitatively, very close to the rough wall, the flow in each tile is individually periodic (in both the streamwise and spanwise directions). This effect, however, is observed only at tile boundaries, is significant only in the velocity field two-point correlations compared to the velocity field itself, and is stronger for the time-averaged flow than the instantaneous flow. The effect rapidly disappears with increasing wall-normal distance. It is also shown that the effects of tiling are observed up to about the same distance from the rough wall as the wall-normal dispersive stress.

Outer-layer similarity of the mean flow is observed for all results, including cases at relatively low $\delta/k = 6$. This is an indication that the criterion proposed by Jiménez [2004], $\delta/k \geq 40$ for universal behaviour, might be too stringent for the mean flow (as also mentioned by Placidi and Ganapathisubramani [2015], who also studied roughness at relatively low $\delta/k \approx 10$). Overall, the objectives set out in Section 1.2 have been achieved. Furthermore, the extensive amount of data generated at $Re_\tau = 180$ could also be used in future studies or as validation data for other studies on roughness.

9.2 Key achievements

The key achievements of the current work are summarised as follows.

- With respect to laminar to turbulent transition over a selected rough surface sample, the critical Reynolds number at which earliest fluctuations are observed lies in the range $89 < (Re_\tau)_{\text{crit}} \leq 89.5$ and the transition Reynolds number at which the flow is turbulent lies in the range $91 < (Re_\tau)_{\text{trans}} \leq 92$. Thus the flow is laminar for $Re_\tau \leq 89$ and turbulent for $Re_\tau \geq 92$.

- An extensive database of direct numerical simulation results (at $Re_\tau = 180$) and surface topographical properties has been developed, covering a relatively wide range of irregular, realistic and industrially relevant roughness, consisting of seventeen surface samples.

- A deeper understanding of irregular rough-wall flow physics has been achieved, including:

  - Complete flow reversal is observed deep within the roughness valleys.

  - ΔU^+ decreases with the peak streamwise fluctuations whereas it increases with the peak spanwise fluctuations.
  - Samples with streamwise anisotropic topographies exhibit streamwise dispersive stress values higher than corresponding streamwise Reynolds stresses.
  - Peak streamwise dispersive stress shows an increasing trend with the streamwise correlation length of the samples.

- The key surface properties influencing ΔU^+ (in decreasing order of influence) are surface solidity, S_f/S, streamwise correlation length normalized by the mean peak-to-valley height, $L_x^{\mathrm{cor}}/S_{z,5\times5}$, rms roughness height normalized by the mean peak-to-valley height, $S_q/S_{z,5\times5}$ and surface skewness, S_{sk}.

- The key surface properties influencing peak profile turbulent kinetic energy, $\langle \mathrm{TKE} \rangle_{\mathrm{max}}$, (in decreasing order of influence) are mean forward-facing surface angle, $\overline{\alpha}$, skewness, S_{sk}, rms roughness height normalized by the mean peak-to-valley height, $S_q/S_{z,5\times5}$ and spanwise effective slope, ES_y.

- Remarkable agreement is found between the data of the gritblasted sample and that of Nikuradse [1933], in terms of ΔU^+ and Nikuradse's log-region velocity profile parameter, A. This implies that, for the first time, roughness closely resembling Nikuradse's sand grains has been investigated in the entire Reynolds number range using direct numerical simulations.

- An understanding of the behaviour of ΔU^+ with the equivalent sand-grain roughness height, $k_{s,eq}^+$, through data characterisation over the entire Reynolds number range (from hydraulically smooth to the fully-rough regime), with excellent quality curve fits throughout.

- A collapse of the velocity defect profiles away from the wall with the corresponding smooth-wall data is seen for all simulations (including cases at relatively low channel half-height to roughness height ratio of $\delta/k = 6$), thus satisfying the wall-similarity hypothesis of Townsend [1976] for the mean flow.

9.3 Future work

Based on the outcomes of the present work, the following ideas are recommended for further work in the future.

- A straightforward extension of the work would be to expand the simulation results database (Chapter 6) with more number of rough surfaces and, especially, with cases in the fully-rough regime. Since the current database of 17 surfaces represents a relatively small class of roughness, the addition of further types of roughness, with an even wider range of topographical properties, would serve to establish further confidence in the surface parametrisation (Chapter 7). Additional results could be

numerical as well as experimental and need not be restricted to irregular roughness. For example, the studies of Flack et al. [2016] and De Marchis et al. [2010] could be valuable additions. New surfaces could also be obtained by artificially modifying surface properties, as done previously by Yuan and Piomelli [2014], or by constructing entire surfaces artificially, as done by Napoli et al. [2008] and by most studies on regular roughness. Additionally, conducting systematic parametric studies of certain surface properties, which have been proved important in literature (for example, surface solidity, skewness and effective slope), would provide a useful insight into the topographical aspect of roughness. These studies would serve to establish the importance of specific properties over others in the relevant context, most importantly in influencing the equivalent sand-grain roughness height. Such studies, among others, have been conducted by Placidi and Ganapathisubramani [2015] (who systematically varied the solidity), Chan et al. [2015] (varied the roughness height and wavelength) and Schultz and Flack [2009] (varied the roughness height and effective slope). Flow quantities other than ΔU^+ and TKE could also be considered (such as other turbulent statistics, for example, $\overline{u'^2}$, or $\overline{w'^2}$ as done by Orlandi and Leonardi [2006]). Carrying out the above mentioned ideas would lead to a much more robust parametrisation of roughness.

- Despite advances in the use of massively parallel, high performance computing, limitations on computational cost prevent the application of DNS to industrially relevant Reynolds numbers. Mesh resolution for DNS scales approximately with the cube of the Reynolds number and smaller time steps are required as the mesh becomes finer. An alternative is to use LES which is much cheaper (because only the large scales of motion are resolved), but leads to challenges in the near-wall region because of the importance of small scales in that region. Hence many LES in practise end up being wall-resolved, wherein the mesh resolution requirements are much less stringent compared to DNS but a strong scaling with Reynolds number remains. Another option is wall-modelled LES, which has better scaling characteristics, but relies heavily on wall treatment, which must be of reduced order and thus compromises on accuracy. Thus, LES is also impractical to be routinely applied to industrial problems. To circumvent the mesh resolution and Reynolds number scaling problems, a new approach, based on a combination of LES for the bulk flow and an array of non-space-filling quasi-DNS, which sample the response of near-wall turbulence to large scale forcing, has been proposed and evaluated by Sandham et al. [2017]. The quasi-DNS blocks are able to locally respond to changes in the outer-layer, provided by the LES. In return, the wall shear stress required by the LES as a boundary condition is provided by the quasi-DNS. The biggest advantage of this method is the reduction in mesh resolution requirements, as the main flow is treated with a coarse-grid LES, with the near-wall sampled quasi-DNS acting as wall-functions. The method was formulated and validated for turbulent incompressible smooth-channel flow at $Re_\tau = 4200$ (the current highest Re_τ for DNS of channel flow), using a tiny fraction of the mesh size required

for conventional DNS at such a high Reynolds number. Extension to rough walls seems logical due to the abundance of roughness seen in engineering applications. In order to study universal roughness behaviour, the roughness height must be small compared to the macroscopic length scale of the flow (channel half-height, for example), as suggested by Jiménez [2004]. Combining this with the high Reynolds numbers required to achieve fully-rough conditions puts strict requirements on the mesh resolution, especially in the near-wall region. Additionally, when irregular roughness is introduced in the mix, the computational cost further rises. Thus, to study universal roughness behaviour for irregular roughness at fully-rough conditions, the above method combining LES and quasi-DNS would be quite beneficial.

Appendix A

Parameters for the characterisation of rough surfaces

A large number of surface parameters are used to characterise the rough surfaces in the current study. Mainsah et al. [2001] give a very extensive range of metrological parameters that may be used to describe rough surfaces. The following are computed for the filtered samples.

The mean reference plane of a sample is set at $z = 0$ and hence the mean roughness height of the sample, $\overline{h}$, is assumed to be zero.

$$\overline{h} = \frac{1}{MN} \sum_{i,j}^{M,N} h_{i,j} = 0,$$

where $h_{i,j}$ are the coordinates of the roughness height obtained after filtering and M, N are the number of points discretising the surface in x, y respectively.

A.1 Amplitude parameters

Amplitude parameters are computed based on the distribution of roughness amplitude. The roughness height in this study is defined by the mean-peak-to-valley height, $S_{z,5\times5}$. To compute this quantity, a sample is first partitioned into 5×5 sections of equal size and the maximum and minimum height for each section is computed. $S_{z,5\times5}$ is then the difference between the mean of the maxima and mean of the minima. In the case of samples that are comprised of smaller tiled samples (for instance, the sample at $k^+ = 15$ from Chapter 8), the $S_{z,5\times5}$ of each tile, which is the same, represents the overall roughness height of the

sample. Other common measures for roughness height are,

$$\text{average roughness height: } S_a = \frac{1}{MN}\sum_{i,j}^{M,N}|h_{i,j}|,$$

$$\text{RMS roughness height: } S_q = \sqrt{\frac{1}{MN}\sum_{i,j}^{M,N}h_{i,j}^2}.$$

The maximum peak-to-valley height is given as

$$S_{\text{z,max}} = \max(h_{i,j}) - \min(h_{i,j}).$$

Other amplitude parameters, which describe the shape of the rough surface, include,

$$\text{surface skewness: } S_{sk} = S_q^{-3}\frac{1}{MN}\sum_{i,j}^{M,N}h_{i,j}^3,$$

$$\text{surface flatness (or kurtosis): } S_{ku} = S_q^{-4}\frac{1}{MN}\sum_{i,j}^{M,N}h_{i,j}^4.$$

A.2 Spacing parameters

Roughness spacing parameters characterise the spacing of the roughness features. They are computed from the areal autocorrelation function,

$$R_h(l,m) = S_q^{-2}\langle h_{i+l,j+m}h_{i,j}\rangle.$$

The shortest correlation length is defined as

$$S_{al} = \min\left\{\sqrt{(l\Delta s)^2 + (m\Delta s)^2}|R_h(l,m) \leq 0.2\right\}$$

and the longest correlation length is defined as

$$S_{sl} = \max\left\{\sqrt{(l\Delta s)^2 + (m\Delta s)^2}|R_h(l,m) \geq 0.2 \cap (l,m) \in \text{central lobe}\right\}.$$

The central lobe of the areal autocorrelation function is the simply connected area where $R_h > 0.2$ that contains $(0,0)$. The surface texture aspect ratio, S_{tr} is given by the ratio of the shortest to longest correlation lengths,

$$S_{tr} = \frac{S_{al}}{S_{sl}}$$

Surfaces with $S_{tr} \geq 0.5$ are in general regarded as isotropic. Surfaces with $S_{tr} < 0.3$ are considered anisotropic (refer Mainsah et al. [2001]). The surface correlation lengths are

given as

$$\text{streamwise correlation length: } L_x^{\text{cor}} = \min\{l\Delta s | R_h(l,0) \leq 0.2\},$$
$$\text{spanwise correlation length: } L_y^{\text{cor}} = \min\{m\Delta s | R_h(0,m) \leq 0.2\}.$$

A parameter called S_{tr}^{flow}, which depends on the streamwise and spanwise correlation lengths, has been defined as

$$S_{tr}^{\text{flow}} = \frac{L_y^{\text{cor}}}{L_x^{\text{cor}}}.$$

A.3 Aerodynamic parameters

In the context of aerodynamics, several other geometric parameters for the characterisation of rough surfaces have been defined. With respect to two-dimensional roughness, Napoli et al. [2008] introduced the streamwise effective slope, ES. For three-dimensional surfaces,

$$\text{streamwise effective slope: } ES_x = \frac{1}{L_x L_y} \int_0^{L_x} \int_0^{L_y} \left| \frac{\partial h(x,y)}{\partial x} \right| dxdy,$$
$$\text{spanwise effective slope: } ES_y = \frac{1}{L_x L_y} \int_0^{L_x} \int_0^{L_y} \left| \frac{\partial h(x,y)}{\partial y} \right| dxdy.$$

The solidity or frontal area ratio has been used extensively in literature and is an indication of roughness density. It is given by the ratio of the total frontal area of all roughness elements to the planform area of the sample, S_f/S. In the context of the present work, a roughness element is defined as the smallest discretised unit of roughness of the filtered sample.

The generalised Sigal-Danberg parameter as defined by van Rij et al. [2002] is given as

$$\Lambda_s = \left(\frac{S}{S_f}\right)\left(\frac{S_f}{S_w}\right)^{-1.6},$$

where $S = L_x L_y$ is the planform area of the corresponding smooth surface. S_f is the total frontal area of all roughness elements and is given as

$$S_f = \int_0^{L_x} \int_0^{L_y} \left| r_x \frac{\partial h}{\partial x} + r_y \frac{\partial h}{\partial y} \right| W(x,y) dxdy.$$

Hence S/S_f represents the inverse of the solidity. S_w is the total area of all roughness elements wetted by the flow, given as

$$S_w = \int_0^{L_x} \int_0^{L_y} \sqrt{\left[\left(\frac{\partial h}{\partial x}\right)^2 + \left(\frac{\partial h}{\partial y}\right)^2 + 1\right]} W(x,y) dxdy.$$

The function $W(x,y)$ indicates whether or not a local infinitesimal surface element is wetted

with respect to a given flow direction, $\overline{r} = (r_1, r_2, 0)$ (where $|\overline{r}| = 1$).

$$W(x,y) = \left\{ \begin{array}{lll} 1 & \text{for} & \overline{r} \cdot \overline{n} < 0 \\ 0 & \text{for} & \overline{r} \cdot \overline{n} \geq 0 \end{array} \right\}, \text{ where } \overline{n}(x,y) = \left(-\frac{\partial h}{\partial x}, -\frac{\partial h}{\partial y}, 1 \right).$$

Since x is the streamwise direction in this study, $\overline{r} = (1, 0, 0)$.

For the definition of ES_x, ES_y and Λ_s, it has been assumed that an analytic and differentiable representation of the rough surface, $h(x, y)$, is known, since the expressions then take a simpler form. The expressions from above can be reformulated for a discrete rough surface, $h_{i,j}$, by replacing the integrations with summations and using finite difference approximations for the derivatives.

Bons [2005] defined a local streamwise forward-facing surface angle, denoted by α. Since a rough surface sample can be constructed as streamwise traces of roughness height for each spanwise coordinate, the local streamwise forward-facing surface angle, α_j is computed for each streamwise trace. For roughness elements facing the flow ($W(x, y) = 1$ from above),

$$\alpha_j = \tan^{-1} \left(\frac{h_{j+1} - h_j}{\Delta s} \right),$$

where Δs is the streamwise spacing of the roughness elements and the required condition for forward facing elements is $h_{j+1} > h_j$. The sum of all roughness elements having a definite value of α_j gives the total number of forward-facing elements, n_f. The mean streamwise forward-facing surface angle, $\overline{\alpha}$ is then given as

$$\overline{\alpha} = \frac{1}{n_f} \sum_{k=1}^{n_f} \alpha_k$$

and its root-mean-square value is given as

$$\alpha_{rms} = \sqrt{\frac{1}{n_f} \sum_{k=1}^{n_f} \alpha_k^2}.$$

Appendix B

Procedure to carry out a rough surface simulation using the immersed boundary DNS code

This appendix describes in detail the steps to be followed in order to conduct a simulation of a rough surface sample using the immersed boundary DNS code. It has been written to serve as a step-by-step guide for a new user of the code. A description of the simulation process along with the relevant parameters will be provided with respect to an example rough surface. A scanned gritblasted surface is chosen as the example. Steps following the scanning stage are described. The appendix roughly follows Chapter 2.

A number of Fortran and Matlab routines are required for pre-processing before each stage of the simulation process. Their names will be written in the `courier` font for clarity. They are mentioned at the beginning of each stage below in the order in which they will be used. For stages 4 and 5, the Fortran source code contains a large number of files and only the ones requiring user input will be mentioned. Commands will be described for a Linux environment.

B.1 Stage 1: Raw surface data pre-processing

Fortran routines	`rewrite_wrl.F90`
Matlab routines	`reform.m`, `read_zgrid.m`, `trim_edge.m`, `substract_linear_mean_plane.m`

The first stage involves processing of the raw surface data obtained from the microscope, which is in the form of a *.wrl* file. The first step is to convert this to a binary, *.bin*, file using the `rewrite_wrl.F90` routine. After compiling the Fortran program (using a suitable Fortran compiler, `gfortran` was used for this work) in a Linux terminal, it is executed from within its directory as

→ `./rewrite_wrl` *input_file output_file*,

where `rewrite_wrl` is the name of the executable after compiling the program, *input_file*

is the *.wrl* file (provided with the file extension) and *output_file* is the required *.bin* file (provided with the file extension).

The next step is to extract the surface coordinate data from the binary file and save it as a Matlab *.mat* file for ease of future access. This is done in Matlab using the `reform.m` routine as

→ *output_data* = `reform('output_file')`,

where *output_data* is the Matlab structure that can be saved as a *.mat* file and `reform('output_file')` is the Matlab command with the *output_file* binary file from the previous step as a string input argument. The routines `read_zgrid.m`, `trim_edge.m` and `substract_linear_mean_plane.m` are part of `reform.m` and are used to perform various auxiliary operations. The final data after this stage contains raw surface x and y coordinates along with corresponding absolute roughness height values.

EXAMPLE: for the gritblasted surface under consideration, the file obtained from the microscope is called *gritblasted.wrl*. The following steps are then performed on it.

(1) In a Linux terminal, after compiling `rewrite_wrl.F90`

(i) `./rewrite_wrl` *gritblasted.wrl gritblasted.bin*.

(2) In Matlab

(i) *gritblasted_data* = `reform('gritblasted')`.

(ii) Save *gritblasted_data* as a *.mat* file, *gritblasted_data.mat*.

B.2 Stage 2: Section selection and filtering

Fortran routines	-
Matlab routines	`select_section.m`, `best_section.m`, `spike_detection.m`, `substract_linear_mean_plane.m`, `get_coeff.m`, `write_coeff.m`, `mean_peak_to_valley_height.m`

The next stage involves selecting an appropriate subsection from the surface scan, scaling the data from the physical into the computational domain and filtering the roughness height data in Fourier space. The only Matlab routine to be run in this stage is `select_section.m` and all others perform auxiliary functions from within it. The first step is to determine an appropriate size for the subsection in terms of indices of the surface scan data. This is a manual process and is done based on the theory described in Section 2.2.1.

The next step is to determine a suitable location for the sub-section on the surface scan (based on minimum rms error in absolute roughness height at the lateral boundaries), again in terms of indices of the scanned data. The `best_section` function is utilised for this purpose. This function also calls `spike_detection`, which detects and discards sections containing possibly unphysical features, such as spikes. Since spikes are determined based on the roughness height gradient between neighbouring points, a gradient threshold value must be provided in `spike_detection`.

The factor that scales the sample from physical to computational domain is obtained as the ratio of the computational streamwise domain length to the physical streamwise domain length.
$\rightarrow$ *fact* = *xl_target/xl_sel*,
where *fact* is the scaling factor, *xl_target* is the computational streamwise domain length and *xl_sel* is the physical streamwise domain length. In order to obtain the sample in the computational domain, the lateral coordinates and the roughness heights in physical domain are multiplied by the scaling factor.

Filtering in Fourier space is the next step. In order to do this, the value of the maximum streamwise wavenumber (which is also a measure of the Fourier filter width), $k_c L_x$ must be decided. Since filtering will directly affect the roughness height, k (which is $S_{z,5\times5}$), and the roughness height scales directly with the streamwise computational domain length, L_x/δ, the maximum streamwise wavenumber must be determined in conjunction with L_x/δ. The most important criterion to fix the value of $k_c L_x$ is the difference between the filtered and unfiltered values of the average and rms roughness heights, S_a and S_q, of the sample, which should not be greater than 8%. Keeping the streamwise domain length at a reasonable value (example, $L_x/\delta = 5$ for the example surface), $k_c L_x$ is fixed to satisfy the above condition. Then L_x/δ is adjusted such that the required value of the k/δ ratio (computed in the `mean_peak_to_valley_height` routine) is obtained. This process may involve some trial and error with different values of $k_c L_x$ and L_x/δ to obtain the required set of parameters but with some experience, the user should be able to accomplish it fairly quickly. The Fourier coefficients are computed using the `get_coeff` routine. Then using the `write_coeff` routine, they are written to a file for use in subsequent stages of the simulation process.

A number of other tasks (such as plotting the surface) can be performed in order to monitor the progress of the routine and check the obtained parameters.

EXAMPLE: the *gritblasted_data.mat* file serves as the start point for following operations in the `select_section.m` Matlab routine.

(1) The following parameters must be set in `select_section.m`.

   (i) Streamwise and spanwise section extents: $xsl = 1199$ and $ysl = 599$.

   (ii) Streamwise and spanwise domain lengths: *xl_target* = 5.630 and *yl_target* = 2.815.

   (iii) Maximum streamwise wavenumber: *kxmax* = 24.

(2) In `spike_detection`, set the slope threshold as *s_threshold* = 24 for this particular surface. As each rough surface has its own characteristics, this value cannot be generalized and would be different for each surface considered. Some knowledge of the surface topography in terms of physical roughness heights and gradients would be required to set this value appropriately.

(3) On running `select_section.m`,

   (i) Start indices in x and y of the subsection as obtained from `best_section` are $xst = 743$, $yst = 1568$.

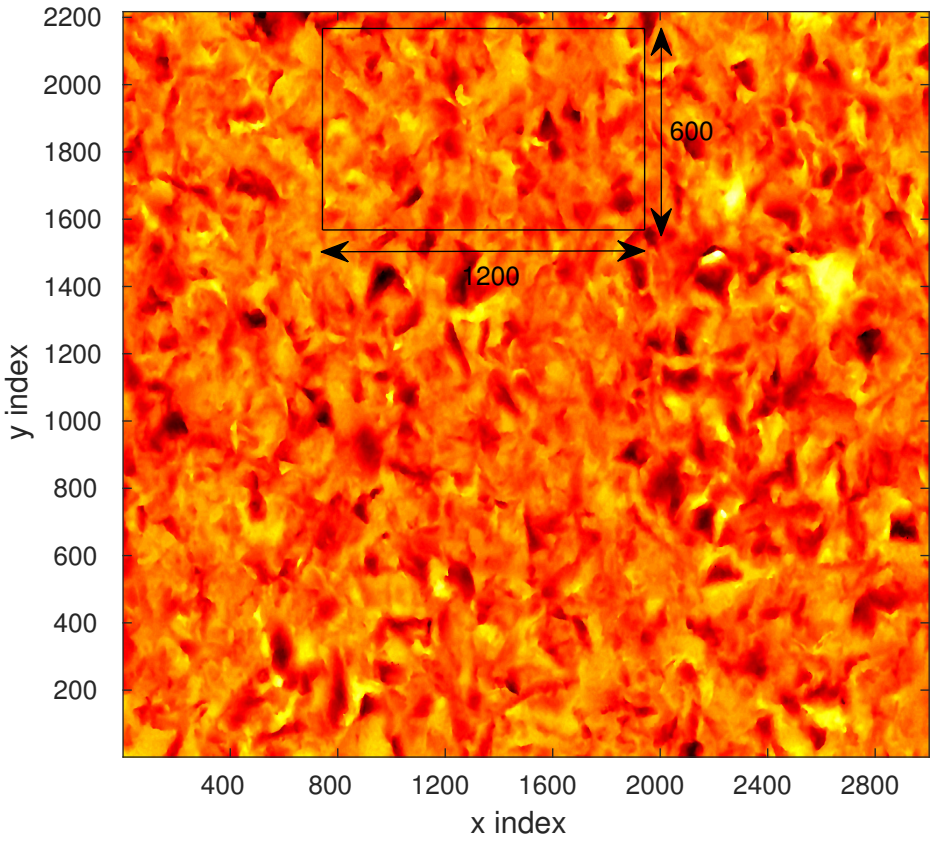

Figure B.1: Roughness height contour plot of the full gritblasted surface (top view) showing the optimum section as obtained from the `best_section` Matlab routine. Every alternate point is plotted. Section size in terms of streamwise and spanwise indices is also shown. Plot coloured by absolute roughness height. Colourbar: black to yellow - lower to higher roughness heights.

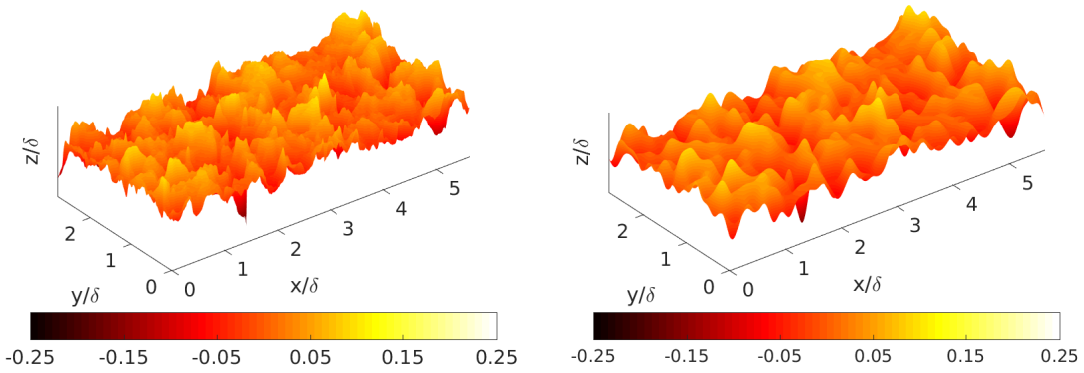

Figure B.2: Gritblasted sample unfiltered data (left) and filtered data (right). Plots coloured by roughness height, k/δ. Scale of plots increased in wall-normal direction for clarity.

(ii) Fourier coefficients are obtained in the Matlab variable *coeff_filt*, which are then written to file as
`write_coeff('gritblasted_Fouriercoeff.dat', coeff_filt,xl_target,yl_target)`,
where `'gritblasted_Fouriercoeff.dat'` is the name of the output file (with the *.dat* extension) provided as a string input argument to `write_coeff`.

(iii) For ease of future access, the unfiltered and filtered surface data are saved as Matlab *.mat* files as *sel_data.mat* and *filt_data.mat*.

(4) The optimum section obtained from `best_section` on the full surface scan is shown in Figure B.1. Surface plots of the unfiltered and filtered samples are shown in Figure B.2.

B.3 Stage 3: Meshing in the wall-normal direction

Fortran routines	-
Matlab routines	`init_zface_coor.m`, `gridfunction.m`, `stretchalpha.m`

The computational mesh is cartesian. In this stage, the wall-normal meshing parameters are finalised. A uniform mesh is used in the region of the roughness features, $\min(h(x,y)) < z < \max(h(x,y))$ (which is also the minimum mesh spacing) and a stretched mesh is used away from the rough walls with maximum mesh spacing at the channel centre. A hyperbolic tangent function is used for stretching.

The main Matlab routine in this stage is `init_zface_coor.m` and the others perform auxiliary functions from within it. The input parameters required for this function are i) z distance of the lower and upper ends of the computational domain, *zmin* and *zmax*, ii) z distance where the uniform grid spacing terminates at the lower and upper walls, *zseam1* and *zseam2*, iii) the desired minimum grid spacing, *dzmin* and iv) the number of wall-normal grid points, n_z. All wall-normal distances are measured from the bottom mean reference plane. The desired grid spacings are $\Delta z^+_{\min} < 1$ in the region of roughness features and $\Delta z^+_{\max} \leq 5$ at the channel centre. *zmin* can be directly obtained from the filtered data as the minimum roughness height of the lower wall. *zseam1* can be obtained from the filtered data as the maximum roughness height of the lower wall. Since the upper wall is a reflection of the lower wall and the total non-dimensionalised channel height is 2, the other required parameters are obtained as $zmax = 2 + |zmin|$ and $zseam2 = 2 - zseam1$. $\Delta z^+_{\min} = 0.667$ for all cases and hence the parameter $dzmin = 0.667/Re_\tau$. After setting these parameters, the number of grid points, n_z are adjusted such that the grid stretching towards the channel centre obtains a $\Delta z^+_{\max} \leq 5$. The routine is executed from within Matlab as,
→ `init_zface_coor(nz, zmin, zmax, zseam1, zseam2, dzmin)`.
The wall-normal mesh coordinates are saved in a binary, *.bin*, file which is subsequently provided as an input file in the next stage of the simulation process. The wall-normal domain length is obtained as $L_z = zmax + |zmin|$. A schematic of the channel with the

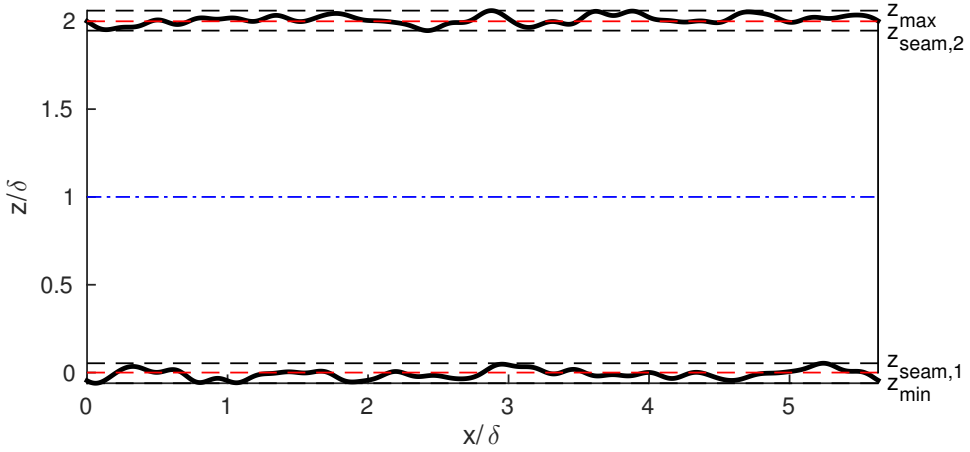

Figure B.3: Schematic diagram ($x - z$ view) of the channel showing various wall-normal meshing parameters. Black solid lines (thick): rough surface boundary, red dashed lines: bottom and top mean reference planes, blue dash-dot line: channel centreline

various wall-normal meshing parameters is shown in Figure B.3. A schematic of the wall-normal mesh is shown in Figure 2.5.

EXAMPLE: no input files are required for this stage as only the wall-normal meshing parameters are provided as inputs to `init_zface_coor`.

(1) From the filtered data file (saved in the previous stage), we obtain

(i) $zmin = -0.1622$ and $zmax = 2 + |zmin| = 2.1622$.

(ii) $zseam1 = 0.1052$ and $zseam2 = 2 - zseam1 = 1.8948$.

zmin and *zseam1* include a small tolerance over the actual values obtained from the filtered data. This is done to be sure the wall-normal mesh covers the lowest and highest roughness features.

(2) The simulation will be run at $Re_\tau = 180$ and hence $dzmin = 0.667/Re_\tau \approx 0.00371$.

(3) Set $n_z = 288$.

(4) From Matlab, execute the `init_zface_coor` function as
`init_zface_coor(288, -0.1622, 2.1622, 0.1052, 1.8948, 0.00371)`.
After execution, the function provides the maximum wall-normal mesh spacing, $\Delta z_{\max} = 0.020644$. Hence $\Delta z^+_{\max} = \Delta z_{\max} \times Re_\tau = 3.7159 \leq 5$.

This process also generates a *zgrid.bin* file containing the wall-normal mesh coordinates, which serves as input in the next stage. Also, the wall-normal domain length is obtained as $L_z = zmax + |zmin| \approx 2.3244$.

B.4 Stage 4: Streamwise/spanwise meshing and initialisation of the immersed boundary

Fortran routines	`incl.F90`, `user_module.F90`
Matlab routines	-

The streamwise and spanwise mesh spacing is uniform. The two criteria that need to be satisfied for the mesh in the streamwise and spanwise directions (refer Section 2.3.2) are

- The Reynolds number criterion: $\Delta x^+ = \Delta y^+ \leq 5$, which gives $n_x \geq \frac{L_x/\delta}{5} Re_\tau$.
- The minimum roughness wavelength criterion: $\Delta x = \Delta y \approx \lambda_{\min}/12$, which gives $n_x \geq 12(k_c L_x)$.

The two routines which require user input in this stage are `user_module.F90` and `incl.F90` which are part of the immersed boundary initialisation source code. The main input to `user_module.F90` is the *.dat* file containing the list of Fourier coefficients as obtained from stage 2. The `incl.F90` file contains all other input parameters to the simulation; the ones requiring user input in this stage are: number of mesh cells, domain lengths and domain decomposition parameters for parallelisation, all in x-, y- and z-coordinate directions. Other parameters from both these Fortran routines (explained below) can be left at their default values.

The main Fortran program is called `init_imb.F90`. It must be compiled using a parallel Fortran compiler (the Intel `mpif90` compiler was used in this study) and run in batch mode on a high performance computing cluster (Iridis4 at the University of Southampton was used for this study). Using a minimization algorithm, the program computes the signed distance function for every point in the mesh.

EXAMPLE: The *gritblasted_Fouriercoeff.dat* file generated in stage 2 and the *zgrid.bin* file generated in stage 3 serve as input files to initialise the immersed boundary.

(1) Since $L_x/\delta = 5.63$, $Re_\tau = 180$ and $k_c L_x = 24$,

(i) The Reynolds number criterion gives $n_x \geq 203$.

(ii) The minimum wavelength criterion gives $n_x \geq 288$.

Hence the minimum wavelength criterion is dominant. Before finalizing the values of n_x and n_y, it is important to note that there are 2 restrictions on their values.

- They must be set in conjunction with the domain decomposition parameters, $(n_x)_{\text{procs}}$ and $(n_y)_{\text{procs}}$, which represent the number of processor cores in the x- and y-coordinate directions. n_x and n_y must be exactly divisible by $(n_x)_{\text{procs}}$ and $(n_y)_{\text{procs}}$. In this study, $(n_x)_{\text{procs}} = 4$ and $(n_y)_{\text{procs}} = 4$ (these values are used in the current stage only and can be changed before execution of the DNS run in the next stage).

- Since the code employs a multigrid method to solve the pressure correction equation, n_x and n_y should also be exactly divisible by the multigrid preconditioning parameter (`mgpc_levels` in `incl.F90`). In this study, 3 coarse grid levels are used and the mesh size is halved at each level. Hence n_x and n_y should also be divisible by $2^3 = 8$.

On combining the above restrictions, n_x must be divisible by $(n_x)_{\text{procs}} \times 2^3$ and n_y must be divisible by $(n_y)_{\text{procs}} \times 2^3$. Only the appropriate n_x needs to be computed to satisfy these requirements as $n_y = n_x/2$ always. Hence the number of cells in the streamwise and spanwise directions are finalised as $n_x = 320$, $n_y = 160$. The above restrictions apply to n_z as well but in this stage, domain decomposition in the wall-normal direction is not permitted by the `init_imb` program. Hence $n_z = 288$ (as finalized in stage 3).

(2) The following parameters are set in `incl.F90`.

(i) `stdouterr_verbose = .FALSE.` This flag produces an output log from only the root processor. If output is desired from all processors, set to `.TRUE.` (normally done during debugging runs).

(ii) `nx = 320`, `ny = 160`, `nz = 288`.

(iii) `nxprocs = 4`, `nyprocs = 4`, `nzprocs = 1`. These can be changed before the DNS run in the next stage.

(iv) `xl = 5.63d0`, `yl = 2.815d0`, `zl = 2.3244d0`. These are the domain lengths in streamwise, spanwise and wall-normal directions.

All other parameters in `incl.F90` can be left at their default values.

(3) The following parameters are set in `user_module.F90`.

(i) `functional_representation = .TRUE.` This parameter indicates that the rough surface is represented by a mathematical function (in this case, a Fourier series).

(ii) `function_type = 0`. This value indicates the function varies in x and y. Set this value to 1 if the function varies only in x and 2 if the function varies only in y.

(iii) `surface_configuration = 0`. This value indicates mirror symmetry between the lower and upper rough walls. Set this value to 1 if different functions are used to represent the lower and upper walls, 2 if only the lower wall is rough (smooth upper wall) and 3 if only the upper wall is rough (smooth lower wall).

(iv) `comp_depth = nz`. This parameter indicates for which wall-normal mesh coordinates the signed distance function will be computed. In general, for `comp_depth` $\geq$ `nz`, the signed distance is computed for all wall-normal mesh coordinates. If `comp_depth` $<$ `nz`, the signed distance will not be computed for all wall-normal mesh coordinates, it will depend on the value of `comp_depth` and `surface_configuration`. A lower value of `comp_depth` will lead to quicker program execution. However, `comp_depth` must still be assigned such that the signed distance is computed close to the rough wall. In general, `comp_depth = nz` works in all cases.

(v) `offset = (/nx/2,ny/2/)`. This parameter determines the streamwise and spanwise shift of the upper rough wall relative to the lower wall, in terms of n_x and n_y. It takes effect only if `surface_configuration = 0`. The given values indicate the upper wall will be shifted by half the total number of streamwise and spanwise mesh cells relative to the lower wall, which ultimately implies half the streamwise and spanwise domain lengths.

(vi) In the `set_user_functions` subroutine, the call to `read_fourier_series` takes the *.dat* file containing the Fourier coefficients describing the rough wall as an input.
`call read_fourier_series('gritblasted_Fouriercoeff.dat')`.
The Fourier series initialisation takes place after this as,
`fun_lower_wall` $\implies$ `fourier_series_lower`,
`fun_upper_wall` $\implies$ `fourier_series_upper`,
where `fun_lower_wall` and `fun_upper_wall` are Fortran procedure pointers to the respective functions defining the lower and upper wall. The mean wall location of the lower wall is set in `fourier_series_lower` to 0 and of the upper wall in `fourier_series_upper` to 2, assuming that a_0 of the Fourier series is 0.

(4) Compile the `init_imb` program by using the `make` functionality (a makefile is provided) for the `mpif90` compiler. It is recommended to use `make clean` before compiling.

(5) Prepare a script file to launch the initialisation procedure in batch mode on an HPC cluster. The total number of processors provided in the script file must be consistent with the product `nxprocs` $\times$ `nyprocs` $\times$ `nzprocs` $=$ `16` (obtained from `incl.F90`). In the example script file, `init_imb.pbs` (prepared for Iridis4 at the University of Southampton), the command defining number of processors is
`#PBS -l nodes=1:ppn=16`.

(6) The *gritblasted_Fouriercoeff.dat* and *zgrid.bin* files must be placed within the same directory.

(7) Submit the batch job. The example script file is submitted on Iridis4 as,
`qsub init_imb.pbs`

After program execution, an *imb_psi.bin* file is obtained which contains the signed distance function. It also contains normal vectors to the surface, pointing into the solid domain.

B.5 Stage 5: Running the main DNS code

Fortran routines	`incl.F90`
Matlab routines	-
Other files	*par_file* (for `chres_da_mod.F90`), *run.log*, *flow.in*, *local_profiles.in* (optional)

In this stage, a number of different parameters and input files need to be prepared before the DNS can be run. Hence the table above has an extra row named 'Other files'. The `incl.F90` file is part of the DNS source code as well. Since many parameters in this file overlap between stages 4 and 5, it can be simply copied over from the immersed boundary initialisation source code. The extra parameters requiring input in this file are explained in the example below. This is the only Fortran file requiring user input in this stage.

The main Fortran program is called `flow_main.F90`. It must be compiled using a parallel Fortran compiler (the Intel `mpif90` compiler was used in this study) and run in batch mode on a high performance computing cluster (Iridis4 at the University of Southampton was used for this study).

An initial flow field must be provided to the code for the first run. Subsequent runs would use the restart file, generated by the previous run, as the initial flow field. The `chres_da_mod.F90` routine can be used to generate the first initial flow field. It requires a previously generated restart file, its corresponding *zgrid.bin* file and the *zgrid.bin* file for the current case under consideration. It also requires the meshing parameters and domain sizes of the previous and current cases. This routine interpolates the flow field from the restart file onto the new mesh. For the selection of the previous case, it is generally good practise to select a case with mesh and domain size similar to the current mesh and domain size. However, this may not always be possible.

The two important run-time files for the simulation are called *flow.in* and *run.log*. The *flow.in* file contains the value of simulation time step, number of time steps and the frequency of diagnostics computation and output. The *run.log* file contains information about whether the simulation is a first or restart run and the corresponding name of the first flow field or number in case of restart file. It contains only two lines,

`starttype: instrt` OR `starttype: restrt`
`restrt_no: start.field` `restrt_no: <number>`

The version on the left is for the first simulation run where `start.field` is the name of the initial flow field whereas the version on the right is for a restart run where `<number>` is the corresponding number of the restart file. The `starttype` keyword is `instrt` for the first run and is updated automatically to `restrt` at the end of the run. It remains the same for all subsequent runs. At the end of a run, `restrt_no` is also updated to reflect the generated restart file (for instance, at the end of the very first run, `restrt_no: 1`).

EXAMPLE: From previous stages, the *imb_psi.bin* and *zgrid.bin* files are required.

(1) The following parameters are set in `incl.F90`.

(i) `stdouterr_verbose = .FALSE.`

(ii) `nx = 320`, `ny = 160`, `nz = 288`.

(iii) `nxprocs = 8`, `nyprocs = 4`, `nzprocs = 4`.
A check on the domain decomposition and meshing parameters in this stage shows they are compatible with the restrictions described in stage 4.

(iv) `xl = 5.63d0`, `yl = 2.815d0`, `zl = 2.3244d0`.

(v) `visc = 1.d0/180.d0`. Since the governing equations are non-dimensionalised by δ and u_τ, viscosity is reduced to the inverse of Re_τ.

(vi) `ImmersedBoundary = .TRUE.` This flag confirms the use of an immersed boundary initialisation (which is the case for a rough-wall simulation). In case a smooth-wall simulation needs to be performed, set this flag to `.FALSE.`

(vii) The following describe parameters for diagnostics.

- `ndiagk_meanvel = 16`. The number of wall-normal locations where the time series for mean velocity statistics are computed.
- `nk_corr = 16`. The number of wall-normal locations where streamwise and spanwise velocity correlation field is computed. It is recommended to set this to the same value as `ndiagk_meanvel`.
- `kidx_corr = (/16,32,48,64,80,96,112,128,144,174,192,208,224,240, 256,272/)`. These represent the indices of the wall-normal locations where streamwise and spanwise velocity correlation field is computed. The number of values must be consistent with `nk_corr`. A more or less uniform distribution of indices is used in the current study.

(viii) `timeav_flag = .FALSE.` This flag determines the computation of field time averaging. It should be set to `.FALSE.` during the start of a simulation and changed to `.TRUE.` once the initial transients have passed and a fully developed flow state is attained.

(ix) The following describe parameters for the multigrid preconditioner.

- `mgpc_gamma = 2`. This parameter defines a W-cycle for multigrid. In case a V-cycle is required, it must be changed to 1.
- `mgpc_cycles = 1`. The number of multigrid cycles used.
- `mgpc_levels = 3`. The number of coarse multigrid levels.

All other parameters in `incl.F90` can be left at their default values.

(2) Compile the `flow_main` program by using the `make` functionality (a makefile is provided) for the `mpif90` compiler. The LAPACK library is required (loaded on Iridis4 as `module load intel/mkl/2013.2` for this study). It is recommended to use `make clean` before compiling.

(3) In order to obtain an initial flow field, `chres_da_mod.F90` must be provided with the input file *par_file*. It contains the following parameters.

```
zgrid_files          zgrid_OLD.bin   zgrid.bin
infile               field.012.bin
domain(input)        5.63d0          2.815d0     2.3244d0
resolution(input)    320             160         288
outfile              start.field
domain(output)       5.63d0          2.815d0     2.3244d0
resolution(output)   320             160         288
boundary_cond        1               1
```

where,
- `zgrid_files`: the previous and current *zgrid.bin* files,
- `infile`: name of the previous restart file,
- `domain(input)`: domain size of the previous case in x, y and z,
- `resolution(input)`: mesh size of the previous case in x, y and z,
- `outfile`: name of the initial flow field output file,
- `domain(output)`: domain size of the current case in x, y and z,
- `resolution(output)`: mesh size of the current case in x, y and z,
- `boundary_cond`: boundary condition on lower and upper wall. 1 indicates no slip.

The *field.012.bin* and both *zgrid.bin* files must be present in the directory. Compile the `chres_da_mod.F90` program using a serial Fortran compiler (`gfortran` was used in this study) and execute it as

```
./chres_da_mod par_file
```

where `chres_da_mod` is the name of the executable after compiling. A number of temporary files (*.tmp* extension) will be produced (which may be deleted) along with the *start.field* file, which is the initial flow field.

(4) The *run.log* file is prepared as follows.

```
starttype:  instrt
restrt_no:  start.field
```

(5) The *flow.in* file is prepared as follows.

```
time_step            3.d-4
numberofsteps        32000
Meandiagnostic       20
Detaileddiagnostic   20      1600
meanpressuregrad     1
gradp                -1.d0   0.d0   0.d0
zwallbc              1       1      1      1
zwallslen            0.d0    0.d0   0.d0   0.d0
```

where,
- `time_step`: the simulation time step,
- `numberofsteps`: number of time steps in the current run,
- `Meandiagnostic`: frequency of calls to the mean flow diagnostics (every 20^{th} time step),

- `Detaileddiagnostic`: frequency of calls to the profile and correlation statistics (called every 20^{th} time step and written to disk every 1600 calls to the diagnostic),
- `meanpressuregrad`: mean flow condition for constant mean streamwise pressure gradient. For constant mass flow rate, it must be changed to 2,
- `gradp`: value of the mean pressure gradient. This line is not present if `meanpressuregrad` is 2,
- `zwallbc`: boundary condition on lower and upper wall (must remain at default value, as in the current example),
- `zwallslen`: slip length on lower and upper wall (must remain at default value, as in the current example).

(6) The code may be instructed to compute some optional diagnostics such as line profiles averaged in time only, or averaged in time and in one of the coordinate directions (streamwise or spanwise). These can be activated through a *local_profiles.in* file. The existence of this file in the directory with other input files triggers the computation of these profiles. An example of the contents of this file is given below.

```
4
1.0  1.0
1.0  2.0
2.0  1.0
2.0  2.0
2
1.0
2.0
2
1.0
3.0
```

All profiles are obtained as a function of wall-normal coordinates. The first line represents the number of time-averaged (only) line profiles required, with the corresponding x- and y-coordinates in subsequent lines. The sixth line represents the number of time- and spanwise-averaged line profiles, with corresponding x-coordinates in subsequent lines. The ninth line represents the number of time- and streamwise-averaged line profiles required, with corresponding y-coordinates on subsequent lines. The data order and input format of this file must be maintained as shown.

(7) Prepare a script file to launch the DNS code in batch mode on an HPC cluster. The total number of processors provided in the script file must be consistent with the product `nxprocs` $\times$ `nyprocs` $\times$ `nzprocs` $=$ `128` (obtained from `incl.F90`). In the example script file, `flow_main.pbs` (prepared for Iridis4 at the University of Southampton), the command defining number of processors is
`#PBS -l nodes=8:ppn=16`.

(8) The *imb_psi.bin*, *zgrid.bin*, *start.field*, *run.log* and *flow.in* files must be placed within the same directory.

(9) Submit the batch job. The example script file is submitted on Iridis4 as,
`qsub flow_main.pbs`

During the run, several diagnostics are written to *.dat* files. These include diagnostics related to correlation statistics, mean forces, mean velocities, spatially averaged quantities and line profiles (if the *local_profiles.in* file is present). Details of computation of all diagnostics are in the `diagnostics.F90` file. At the end of the run, a restart file called *field.001.bin* is also written to disk.

B.6 Stage 6: Basic post-processing

All post-processing has been done in Matlab for the current study. Some basic post-processing scripts have been provided.

- Data from the *meanforce.XXX.dat* files can be extracted using the `meanforce.m` Matlab script. *XXX* represents the number of the restart file which was used to start the run. In case of the very first run, *XXX* is 000.
- Data from the *meanvel.XXX.dat* files can be extracted using the `meanvel.m` Matlab script.
- Data from the *stats.XXX.YYY.dat* files can be extracted using the `stats_mean_itc.m` Matlab script. The convention on *XXX* is same as above whereas *YYY* depends on the value of the second parameter from `Detaileddiagnostic` in *flow.in*.
- The velocity and pressure data from the *field.XXX.bin* files can be extracted using the `readflowmainbin.m` Matlab function. For the very first restart file, *XXX* is 001.

Additional post-processing files are required when time averaging is switched on (using `timeav_flag = .TRUE.` in `incl.F90`). This will produce an additional *.bin* field file called *time_av_field_new.XXX.bin*, where *XXX* again represents the number of the restart file which was used to start the run. The file represents time-averaged quantities over the current run. To obtain statistical convergence, several of these files need to be averaged. This can be done using the `ave_tav.F90` routine along with its required input file *ave_par*. Profiles in the wall-normal direction (averaged in the streamwise and spanwise directions) can then be obtained using the `compute_prof.m` Matlab routine. Since an immersed boundary is employed, a correction factor must be applied due to the spatial averaging in this routine. This is obtained from the `compute_cfact.F90` routine with the *cfact_par* input file. The *imb_psi.bin* file must be present in the directory from which `compute_cfact.F90` is executed.

The post-processing routines (in both Matlab and Fortran) and their corresponding input files are relatively self-explanatory and the user should be able to understand them fairly easily.

Appendix C

Data statement

(1) The following data for the 17 samples are available (in *.csv* format) from the University of Southampton repository at http://dx.doi.org/10.5258/SOTON/392562.

   (i) Figures 3.4 and 3.5 - roughness height maps after filtering.

   (ii) Table 3.2 - surface topographical properties.

   (iii) Table 6.1 - simulation parameters including values of ΔU^+ and peak profile TKE at $Re_\tau = 180$.

(2) The data at $Re_\tau = 180$ for the 17 samples from the following figures are available (in *.csv* format) from the University of Southampton repository at http://doi.org/10.5258/SOTON/D0118.

   (i) Figure 6.1 - mean streamwise velocity profiles.

   (ii) Figure 6.2 - mean streamwise velocity defect profiles.

   (iii) Figures 6.5, 6.8, 6.11 and 6.14 - profiles of the Reynolds streamwise, spanwise, wall-normal and shear stress.

   (iv) Figure 6.17 - profiles of the turbulent kinetic energy.

   (v) Figures 6.19, 6.23, 6.26 and 6.30 - profiles of the dispersive streamwise, spanwise, wall-normal and shear stress.

References

Acharya, M., Bornstein, J., and Escudier, M. P. (1986). Turbulent boundary layers on rough surfaces. *Expts. Fluids*, 4:33–47.

Antonia, R. A. and Krogstad, P.-A. (2001). Turbulence structure in boundary layers over different types of surface roughness. *Fluid Dyn. Res.*, 28:139–157.

Arnfield, A. J. (2003). Two decades of urban climate research: A review of turbulence, exchanges of energy and water, and the urban heat island. *Int. J. Climatol.*, 23(1):1–26.

Ashrafian, A. and Andersson, H. I. (2006). The structure of turbulence in a rod-roughened channel. *Int. J. Heat and Fluid Flow*, 27:65–79.

Ashrafian, A., Andersson, H. I., and Manhart, M. (2004). DNS of turbulent flow in a rod-roughened channel. *Int. J. Heat and Fluid Flow*, 25:373–383.

Bons, J. P. (2002). St and c_f augmentation for real turbine roughness with elevated freestream turbulence. *J. Turbomach.*, 124(4):632–644.

Bons, J. P. (2005). A critical assessment of Reynolds analogy for turbine flows. *J. Heat Transfer*, 127:472–485.

Bons, J. P., Taylor, R. P., McClain, S. T., and Rivir, R. B. (2001). The many faces of turbine surface roughness. *J. Turbomach.*, 123(4):739–748.

Bottema, M. (1997). Urban roughness modelling in relation to pollutant dispersion. *Atmospheric Environment*, 31(18):3059–3075.

Bradshaw, P. (2000). A note on "critical roughness height" and "transitional roughness". *Phys. Fluids*, 12:1611–1614.

Brent, R. P. (1973). *Algorithms for Minimization without Derivatives.* Prentice Hall, Englewood Cliffs, NJ.

Britter, R. E. and Hanna, S. R. (2003). Flow and dispersion in urban areas. *Annu. Rev. Fluid Mech.*, 35:469–496.

Busse, A., Lützner, M., and Sandham, N. D. (2015). Direct numerical simulation of turbulent flow over a rough surface based on a surface scan. *Comp. Fluids*, 116:129–147.

Busse, A. and Sandham, N. D. (2012). Parametric forcing approach to rough-wall turbulent channel flow. *J. Fluid Mech.*, 712:169–202.

Busse, A., Thakkar, M., and Sandham, N. D. (2016). Reynolds number dependence of the near-wall flow over irregular rough surfaces. *J. Fluid Mech.*, 810:196–224.

Busse, A., Tyson, C. J., and Sandham, N. D. (2013). DNS of turbulent channel flow over engineering rough surfaces. In *International Symposium On Turbulence and Shear Flow Phenomena (TSFP-8)*, Poitiers, France.

Cardillo, J., Chen, Y., Araya, G., Newman, J., Jansen, K., and Castillo, L. (2013). DNS of a turbulent boundary layer with surface roughness. *J. Fluid Mech.*, 729:603–637.

Chan, L., MacDonald, M., Chung, D., Hutchins, N., and Ooi, A. (2015). A systematic investigation of roughness height and wavelength in turbulent pipe flow in the transitionally rough regime. *J. Fluid Mech.*, 771:743–777.

Chung, D., Chan, L., MacDonald, M., Hutchins, N., and Ooi, A. (2015). A fast direct numerical simulation for characterising hydraulic roughness. *J. Fluid Mech.*, 773:418–431.

Clauser, F. H. (1954). Turbulent boundary layers in adverse pressure gradient. *J. Aeronaut. Sci.*, 21:91–108.

Clauser, F. H. (1956). Turbulent boundary layer. *Adv. Appl. Mech.*, 4:1–51.

Coceal, O., Dobre, A., Thomas, T. G., and Belcher, S. E. (2007). Structure of turbulent flow over regular arrays of cubical roughness. *J. Fluid Mech.*, 589:375–409.

Coceal, O., Thomas, T. G., Castro, I. P., and Belcher, S. E. (2006). Mean flow and turbulence statistics over groups of urban-like cubicle obstacles. *Boundary-Layer Meteorol.*, 121:491–519.

Darcy, H. (1857). *Recherches experiméntales relatives au mouvement de l'eau dans les tuyaux*. Paris: Mallet-Bachelier.

De Marchis, M., Napoli, E., and Armenio, V. (2010). Turbulence structures over irregular rough surfaces. *J. Turbul.*, 11(3):1–32.

Dobre, A., Arnold, S., Smalley, R., Boddy, J., Barlow, J., Tomlin, A., and Belcher, S. (2005). Flow field measurements in the proximity of an urban intersection in London, UK. *Atmospheric Environment*, 39:4647–4657.

Downs III, R. S., White, E. B., and Denissen, N. A. (2008). Transient growth and transition induced by random distributed roughness. *AIAA J.*, 46(2):451–462.

Fadlun, E. A., Verzicco, R., Orlandi, P., and Mohd-Yusof, J. (2000). Combined immersed-boundary finite-difference methods for three-dimensional complex flow simulations. *J. Comput. Phys.*, 161(1):35–60.

Finnigan, J. (2000). Turbulence in plant canopies. *Annu. Rev. Fluid Mech.*, 32:519–571.

Flack, K. A. and Schultz, M. P. (2010). Review of hydraulic roughness scales in the fully rough regime. *J. Fluids Eng.*, 132:041203–1 – 041203–10.

Flack, K. A., Schultz, M. P., Barros, J. M., and Kim, Y. C. (2016). Skin-friction behaviour in the transitionally-rough regime. *Int. J. Heat and Fluid Flow*, 61:21–30.

Flack, K. A., Schultz, M. P., and Rose, W. B. (2012). The onset of roughness effects in the transitionally rough regime. *Int. J. Heat and Fluid Flow*, 35:160–167.

Floryan, J. M. (2006). Three-dimensional instabilities of laminar flow in a rough channel and the concept of a hydraulically smooth wall. *Eur. J. Mech. B-Fluid*, 26:305–329.

Grass, A. J. (1971). Structural features of turbulent flow over smooth and rough boundaries. *J. Fluid Mech.*, 50(2):233–255.

Grimmond, C. S. B. and Oke, T. R. (1998). Aerodynamic properties of urban areas derived from analysis of surface form. *J. Appl. Meteorol.*, 38:1262–1292.

Hagen, G. (1854). Über den Einfluss der Temperatur auf die Bewegung des Wassers in Röhren. *Math. Abh. Akad. Wiss. Berlin*, pages 17–98.

Hu, Z., Morfey, C. L., and Sandham, N. D. (2006). Wall pressure and shear stress spectra from direct simulations of channel flow. *AIAA J.*, 44(7):1541–1549.

Hwang, Y. (2013). Near-wall turbulent fluctuations in the absence of wide outer motions. *J. Fluid Mech.*, 723:264–288.

Jiménez, J. (2004). Turbulent flow over rough walls. *Annu. Rev. Fluid Mech.*, 36:173–196.

Jiménez, J. and Moin, P. (1991). The minimal flow unit in near-wall turbulence. *J. Fluid Mech.*, 225:213–240.

Kim, J., Moin, P., and Moser, R. (1987). Turbulence statistics in fully developed channel flow at low reynolds number. *J. Fluid Mech.*, 177:133–166.

Kirschner, C. M. and Brennan, A. B. (2012). Bio-inspired antifouling strategies. *Ann. Rev. Mater. Res.*, 42:211–229.

Klebanoff, P. S. and Tidstrom, K. D. (1972). Mechanism by which a two-dimensional roughness element induces boundary-layer transition. *Phys. Fluids*, 15:1173–1188.

Kline, S. J., Reynolds, W. C., Shraub, F. A., and Runstadler, P. W. (1967). The structure of turbulent boundary layers. *J. Fluid Mech.*, 30:741–773.

Krogstad, P.-A. and Antonia, R. A. (1999). Surface roughness effects in turbulent boundary layers. *Exp. Fluids*, 27:450–460.

Lee, J. H., Sung, H. J., and Krogstad, P.-A. (2011). Direct numerical simulation of the turbulent boundary layer over a cube-roughened wall. *J. Fluid Mech.*, 669:397–431.

Ligrani, P. M. and Moffat, R. J. (1986). Structure of transitionally rough and fully rough turbulent boundary layers. *J. Fluid Mech.*, 162:69–98.

Ligrani, P. M., Oliveira, M. M., and Blaskovich, T. (2003). Comparison of heat transfer augmentation techniques. *AIAA J.*, 41(3):337–362.

Lozano-Durán, A. and Jiménez, J. (2014). Effect of computational domain on direct simulations of turbulent channels up to Re = 4200. *Phys. Fluids*, 26:011702.

Mainsah, E., Greenwood, J. A., and Chetwynd, D. G. (2001). *Metrology and Properties of Engineering surfaces*. Kluwer Academic, Dordrecht, Netherlands.

Mejia-Alvarez, R. and Christensen, K. T. (2010). Low-order representations of irregular surface roughness and their impact on a turbulent boundary layer. *Phys. Fluids*, 22:015106.

Mohajeri, S. H., Grizzi, S., Righetti, M., Romano, G. P., and Nikora, V. (2015). The structure of gravel-bed flow with intermediate submergence: A laboratory study. *Water Resour. Res.*, 51:9232–9255.

Musker, A. J. (1980). Universal roughness functions for naturally occurring surfaces. *Trans. Can. Soc. Mech. Eng.*, 6(1):1–6.

Napoli, E., Armenio, V., and De Marchis, M. (2008). The effect of the slope of irregularly distributed roughness elements on turbulent wall-bounded flows. *J. Fluid Mech.*, 613:385–394.

Nikuradse, J. (1933). Strömungsgesetze in Rauhen Rohren. *VDI-Forschungscheft 361*. (English translation - Laws of flow in rough pipes, NACA Technical Memorandum 1292 (1950)).

Orlandi, P. (2011). DNS of transitional rough channels. *J. Turbul.*, 12(29):1–20.

Orlandi, P. and Leonardi, S. (2006). DNS of turbulent channel flows with two- and three-dimensional roughness. *J. Turbul.*, 7(53):N73.

Orszag, S. A. (1971). Accurate solution of the Orr-Sommerfeld equation. *J. Fluid Mech.*, 50(4):689–703.

Pailhas, G., Touvet, Y., and Aupoix, B. (2008). Effects of Reynolds number and adverse pressure gradient on a turbulent boundary layer developing on a rough surface. *J. Turbul.*, 9(43):1–24.

Peskin, C. S. (1972). Flow patterns around heart valves: a numerical method. *J. Comput. Phys.*, 10:252–271.

Placidi, M. and Ganapathisubramani, B. (2015). Effect of frontal and plan solidities on aerodynamic parameters and the roughness sublayer in turbulent boundary layers. *J. Fluid Mech.*, 782:541–566.

Press, W. H., Teukolsky, S. A., Vetterling, W. T., and Flannery, B. P. (2007). *Numerical Recipes: The Art of Scientific Computing*. Cambridge University Press, Cambridge, UK.

Sadeh, W. Z., Cermak, J. E., and Kawatani, T. (1971). Flow over high roughness elements. *Bound-Lay. Meteorol.*, 1:321–344.

Sandham, N. D., Johnstone, R., and Jacobs, C. T. (2017). Surface-sampled simulations of turbulent flow at high Reynolds number. *Int. J. Numer. Meth. Fl.* DOI: 10.1002/fld.4395.

Schlichting, H. (1936). Experimentelle untersuchungen zum rauhigkeitsproblem. *Ingeneur-Archiv*, 7:1–34. (English translation - Experimental investigation of the problem of surface roughness, NACA Technical Memorandum 823 (1937)).

Schultz, M. P. and Flack, K. A. (2007). The rough-wall turbulent boundary layer from the hydraulically smooth to the fully rough regime. *J. Fluid Mech.*, 580:381–405.

Schultz, M. P. and Flack, K. A. (2009). Turbulent boundary layers on a systematically varied rough wall. *Phys. Fluids*, 21:015104–1 – 015104–9.

Seddighi, M., He, S., Pokrajac, D., O'Donoghue, T., and Vardy, A. E. (2015). Turbulence in a transient channel flow with a wall of pyramid roughness. *J. Fluid Mech.*, 781:226–260.

Sherrington, I. and Howarth, G. W. (1988). Approximate numerical models of 3-d surface topography generated using sparse frequency domain descriptions. *Int. J. Mach. Tools Manufact.*, 38:599–606.

Sherrington, I. and Smith, E. H. (1988a). Modern Measurement techniques in Surface Metrology: Part I; Stylus intruments, Electron microscopy and Non-optical comparators. *Wear*, 125:271–288.

Sherrington, I. and Smith, E. H. (1988b). Modern Measurement techniques in Surface Metrology: Part II; Optical Instruments. *Wear*, 125:289–308.

Shockling, M. A., Allen, J. J., and Smits, A. J. (2006). Roughness effects in turbulent pipe flow. *J. Fluid Mech.*, 564:267–285.

Sigal, A. and Danberg, J. E. (1988). Analysis of turbulent boundary-layer over rough surfaces with application to projectile aerodynamics. Technical Report BRL-TR-2977, Army Ballistic Research Lab, Aberdeen Proving Grounds MD.

Sigal, A. and Danberg, J. E. (1990). New correlation of roughness density effect on the turbulent boundary layer. *AIAA J.*, 28(3):554–556.

Smalley, R. J., Leonardi, S., Antonia, R., Djenidi, L., and Orlandi, P. (2002). Reynolds stress anisotropy of turbulent rough wall layers. *Exp. Fluids*, 33(1):31–37.

Thakkar, M., Busse, A., and Sandham, N. D. (2017). Surface correlations of hydrodynamic drag for transitionally rough engineering surfaces. *J. Turbul.*, 18(2):138–169.

Townsend, A. A. (1976). *The Structure of Turbulent Shear flow*. Cambridge University Press, Cambridge, UK.

Townsin, R. L. (2003). The ship hull fouling penalty. *Biofouling*, 19:9–15.

van Rij, J. A., Belnap, B. J., and Ligrani, P. M. (2002). Analysis and experiments on three-dimensional, irregular surface roughness. *J. Fluids Eng.*, 124(3):671–677.

Vreman, A. W. and Kuerten, J. G. M. (2014). Comparison of direct numerical simulation databases of turbulent channel flow at $Re_\tau = 180$. *Phys. Fluids*, 26:015102.

Wahl, M. (1989). Marine epibiosis. I. Fouling and antifouling: some basic aspects. *Mar. Ecol. Prog. Ser.*, 58:175–189.

Waigh, D. R. and Kind, R. J. (1998). Improved aerodynamic characterisation of regular three-dimensional roughness. *AIAA J.*, 36(6):1117–1119.

Wieringa, J. (1993). Representative roughness parameters for homogeneous terrain. *Bound-Lay. Meteorol.*, 63:323–363.

Wu, Y. and Christensen, K. T. (2006). Reynolds-stress enhancement associated with a short fetch of roughness in wall turbulence. *AIAA J.*, 44(12):3098–3106.

Wu, Y. and Christensen, K. T. (2007). Outer-layer similarity in the presence of a practical rough-wall topography. *Phys. Fluids*, 19:085108.

Xie, Z. T., Coceal, O., and Castro, I. P. (2008). Large-eddy simulation of flows over random urban-like obstacles. *Bound-Lay. Meteorol.*, 129:1–23.

Yang, J. and Balaras, E. (2006). An embedded-boundary formulation for large-eddy simulation of turbulent flows interacting with moving boundaries. *J. Comput. Phys.*, 215:12–40.

Yang, X. I. A., Sadique, J., Mittal, R., and Meneveau, C. (2016). Exponential roughness layer and analytical model for turbulent boundary layer flow over rectangular-prism roughness elements. *J. Fluid Mech.*, 789:127–165.

Yuan, J. and Piomelli, U. (2014). Estimation and prediction of the roughness function on realistic rough surfaces. *J. Turbul.*, 15(6):350–365.